

UNIVERSITÀ DI PISA

Department of Chemistry and Industrial Chemistry



Doctoral School in Chemistry and Materials Science

XXXIII Cycle

PhD thesis

**Mechanistic studies on the interaction
between small molecules and biosubstrates:
a multitechnique approach**

Candidate:

Francesca Macii

Supervisor:

Dr. Tarita Biver

2020

Table of Contents

Abstract	1
1. Nucleic acids and proteins as biotargets for small molecules	3
1.1 Interaction between small molecules and long chain nucleic acids	3
1.1.1 Natural double helix DNA	3
1.1.2 Synthetic homopolymeric DNA: polyG·polyC and polyA·polyT	6
1.1.3 Double and triple helix RNA.....	7
1.1.4 Types of binding to long chain nucleic acids	10
1.2 Interaction between small molecules and DNA G-quadruplex structures	15
1.2.1 DNA G-quadruplex structures.....	15
1.2.2 Types of binding to G-quadruplexes	17
1.3 Interaction between small molecules and serum albumin protein.....	20
1.3.1 Bovine serum albumin.....	20
1.3.2 Types of binding to BSA.....	21
2. Spectroscopic techniques as essential tools for providing information on the binding modes	27
2.1 Nucleic acids binding studies	27
2.1.1 Absorbance titrations.....	28
2.1.2 UV Melting experiments	35
2.1.3 Fluorescence titrations.....	39
2.1.4 Competitive fluorescent displacement experiments	42
2.1.5 FRET melting experiments.....	45
2.1.6 Circular dichroism spectroscopy	48
2.2 Proteins binding studies.....	55
2.2.1 Fluorescence quenching experiments	56
2.2.2 Competitive fluorescent displacement for binding site determination	61
3. Materials and methods	63
3.1 Materials.....	63

3.2 Experimental methods	68
3.2.1 Spectrophotometric and spectrofluorimetric titrations	68
3.2.2 UV melting experiments.....	69
3.2.3 FRET melting experiments.....	70
3.2.4 Circular Dichroism	71
3.2.5 Isothermal Titration Calorimetry	71
3.2.6 Viscometry	73
3.2.7 Micellar Enhanced UltraFiltration.....	74
3.3 Computational methods.....	76
3.3.1 Time Dependent - Density Functional Theory (TD-DFT) calculations .	76
3.3.2 Molecular dynamic (MD) simulations.....	77
3.3.3 Docking	79
4. The perylene diimide derivative PZPERY	81
4.1 Introduction	81
4.2 Spectroscopic characterization	84
4.3 Binding to polynucleotides.....	85
4.3.1 Spectrophotometric titrations	86
4.3.2 Circular dichroism	93
4.3.3 Ethidium bromide displacement assay	94
4.3.4 Isothermal Titration Calorimetry.....	95
4.3.5 DFT calculations.....	98
4.4 Binding to oligonucleotides.....	101
4.4.1 FRET melting experiments.....	101
4.4.2 UV melting experiments.....	103
4.4.3 Spectroscopic and calorimetric titrations.....	105
4.4.4 Molecular dynamics simulations	109
4.5 Conclusions	114
5. The phthalocyanine ABTP.....	117
5.1 Introduction	117
5.2 Spectroscopic characterization	120

5.3 Binding to polynucleotides.....	123
5.3.1 Spectrophotometric titrations	123
5.3.2 Melting experiments	127
5.3.3 Circular Dichroism	129
5.4 Binding to oligonucleotides.....	131
5.4.1 Spectroscopic titrations	131
5.4.2 Melting experiments	136
5.5 Conclusions	139
6. The molecular rotor BTATPE	143
6.1 Introduction	143
6.2 Synthesis.....	147
6.3 Spectroscopic characterization	149
6.4 Binding studies	152
6.5 UV Melting experiments	166
6.7 Conclusions	168
7. The pollutants	171
7.1 Introduction	171
7.2 1-PyNH ₂ , carbendazim and carbaryl binding to DNA	174
7.3 Herbicides.....	184
7.3.1 Spectroscopic characterization	184
7.3.2 DNA binding	186
7.3.3 BSA binding	191
7.3.4 Micellar Enhanced Ultra-Filtration (MEUF) tests on surfactants and liposomes.....	198
7.4 Conclusions	201
8. Conclusions	205
Appendices	209
Bibliography	227

List of abbreviations, acronyms and symbols

Δ	variation of
ε	molar extinction coefficient
ϕ	proportion coefficient between fluorescence and concentration
λ	wavelength
A	adenine nucleotide
ABTP	Alcian Blue-tetrakis(methylpyridinium) chloride
BSA	bovine serum albumin
BTATPE	1,2-bis{4-[(triethylammonium)butoxy]phenyl}-1,2-tetraphenylethene dibromide
C	cytosine nucleotide
CD	circular dichroism
ct-DNA	calf thymus deoxyribonucleic acid
CuPCTS	copper phthalocyanine-3,4',4'',4'''-tetrasulfonic acid tetrasodium salt
DFT	density functional theory
DNA	deoxyribonucleic acid
DQ	diquat dibromide
DTAC	dodecyl trimethyl ammonium chloride
EEC	enthalpy-entropy compensation
FAM	aminofluorescein
FRET	fluorescence resonance energy transfer
G	guanine nucleotide
G4	guanine quadruplex
GAFF	generalized amber force field
IB	ibuprofen
ITC	isothermal titration calorimetry

LiCac	lithium cacodylate
logP	logarithm of partition coefficient
MD	molecular dynamic
MEUF	micellar enhanced ultrafiltration
NaCac	sodium cacodylate
NTO	natural transition orbital
PB	phenylbutazone
PCM	polarizable continuum model
PDB	protein databank
PDI	perylene diimide
POP	persistent organic pollutants
POPC	1-palmitoyl-2-oleoyl-sn-glycero-3-phosphocholine
PQ	paraquat dichloride hydrate
PZPERY	N,N'-bis(2-(1-piperazino)ethyl)-3,4,9,10- perylenetetracarboxylic acid diimide dichloride
QM/MM	quantum mechanics/ molecular mechanics
RESP	restrained electrostatic potential
RMSD	root mean square deviation
RNA	ribonucleic acid
SDS	sodium dodecyl sulphate
T	thymine nucleotide
TAMRA	carboxytetramethylrhodamine
TD-DFT	time dependent - density functional theory
Tel	telomere
Tm	melting temperature
U	uracil nucleotide

Abstract

The analysis of equilibria in solution have impacted many research fields, including the study of the interaction between small molecules and biosubstrates. The availability of simple tools provides easy access to these data and often several tricky aspects are not carefully considered in the design of the tests. Therefore, the number of low quality results increased and the published data do not always satisfy the required quality standards. In this context, renewed attention in the research approaches is required for a deeper comprehension of the physico-chemical properties of the systems.

One of the main aspect of this thesis is to produce and offer to the scientific community mechanistic studies on the interaction between small molecules and biosubstrates for complex selected systems of high biomedical interest. For every system, we highlight and discuss the critical aspects for correctly designing the experiments and treating the data.

Most data on these kind of systems come from *in vivo* analysis, whereas structure/behaviour relationships are not always fully explored and mechanistic insights into the interaction with biosubstrates are not always available. It also happens that serious experimental problems are not carefully taken into account in the spectroscopic tests. However, the robust knowledge of the details of the molecular interactions could be very important to develop new efficient therapeutic agents and sensors and to get insight into the activity of some toxic species.

In fact, the binding of small molecules to biosubstrates deserves interest from two apparently opposite point of views. On one side, the development of new efficient anticancer agents. On the other hand, the analysis of the effects of possible tumour-genic species. For the first aspect, although the many studies

involved, there are still many unsolved problems mainly related to drug resistance and detrimental effects on the patients. Concerning the second aspect, and in the context of our participation to National Antarctic Research Program (PNRA), our attention has been focused on Persistent Organic Pollutants (POPs), which were demonstrated to enhance tumour morbidity.

On the whole, we provided detailed discussions on the binding modes of the selected systems, by employing a combination of experimental and computational techniques. We characterized the interaction of a water soluble perylene diimide derivative, which resulted to intercalate into natural DNA (ct-DNA), while groove binding was evidenced in the presence of synthetic both duplex and triplex RNA polynucleotide. The molecule does interact with G-quadruplex DNA (G4) and an analysis of the binding geometries was done. A copper phthalocyanine was investigated for affinity to ct-DNA, duplex and triplex RNAs and G4 DNA with different conformations: in the case of ct-DNA, the experimental evidences indicated intercalation, while, in the case of RNAs, external binding occurred. Among the G4s, a slightly preference for the antiparallel form was observed.

The binding features of a new synthesized tetraphenylethene derivative were investigated with a focus on its molecular rotor properties. The different behaviour showed towards ct-DNA or RNA (high affinity for the former and none for the latter polynucleotide) makes this molecules very promising to be exploited as a fluorescent sensor.

Detailed information on the binding mode to biosubstrates of some POPs was also obtained. The polycyclic aromatic hydrocarbon and the carbamate pesticides resulted to intercalate into the ct-DNA base pairs. Oppositely, the studied herbicides showed no affinity for ct-DNA, but they do bind serum albumin.

Chapter I

1. Nucleic acids and proteins as biotargets for small molecules

1.1 Interaction between small molecules and long chain nucleic acids

1.1.1 Natural double helix DNA

Deoxyribonucleic acid is a polymer whose monomeric repeating units (nucleotides) are composed of a pentose sugar (deoxyribose), a phosphate group and a purine or pyrimidine nucleobase (guanine (G), adenine (A), cytosine (C) or thymine (T)) (Figure 1.1). Nucleotides associate through 5' → 3' phosphodiester bonds to form polynucleotides. Overall, DNA results negatively charged due to the mono-deprotonated phosphate groups. The sequential order of the nucleotide units represents the genetic information and drives the synthesis of the corresponding biologic materials through the processes of transcription and translation.

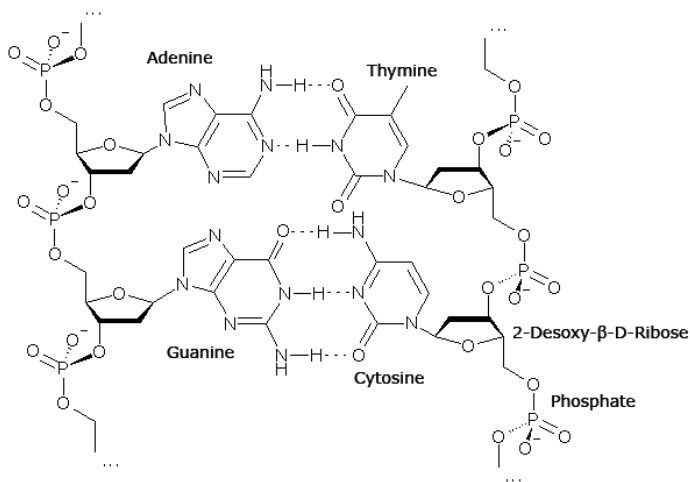


Fig. 1.1. DNA base pairs structures

DNA can be typically arranged in three different conformations, labelled as A-DNA, B-DNA and Z-DNA (Figure 1.2).^[1]

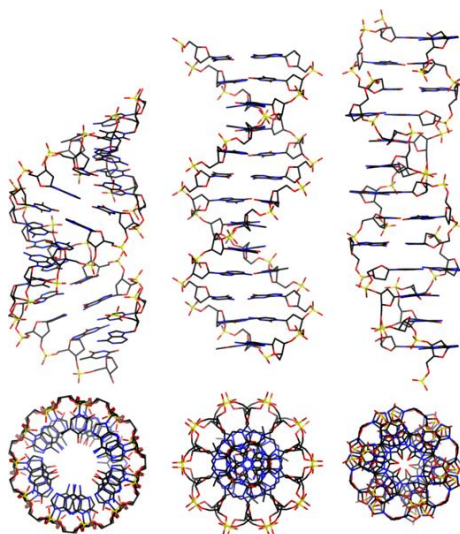


Fig. 1.2. DNA conformations: (A) A-DNA; (B) B-DNA; (C) Z-DNA
(<https://commons.wikimedia.org/wiki/File:Dnaconformations.png>)

In 1953 *J. Watson and F. Crick* unravelled for the first time the classical B-DNA structure by X-ray crystallographic measurements.^[2] Antiparallel single strands couple one another to form a double helix structure with a diameter of 20 Å, in which the sugar-phosphate groups constitute the backbone and the nucleobases lie perpendicular to the helix axis, being 3.4 Å far from the next ones.^[3] The structure is stabilized by the formation of hydrogen bonds between complementary nucleobases: the guanine-cytosine pair is bound through 3 H-bonds while 2 H-bonds connect the adenine-thymine couple.^[4] Additional stabilization comes from π stacking between the nucleobases. The arrangement of the glycosylic bonds with respect to the hydrogen bonds results in the formation of a major and a minor groove of different sizes.^[5] Major groove is wider (11.7 Å) than the minor groove (5.7 Å), although their depths are almost identical (major 8.5 Å vs. minor 7.5 Å).^[6] The B-form is the most stable structure for a random-sequence DNA molecule under physiological conditions and is therefore the standard reference for studying the properties of DNA.

The A-form is instead favoured in solutions that are relatively devoid of water, but the actual presence of A-DNA in cells is still uncertain.^[7] The A-DNA is arranged in a right-handed double helix, but the helix is wider with a diameter of 26 Å and the number of base pairs per helical turn is 11 (one each 2.6 Å),^[4] rather than 10.5 as in B-DNA.^[8] The base pairs are not completely perpendicular to the helix axes, thus deepening and narrowing the major groove while making the minor groove broader and shallower.^[9]

Z-form DNA was first observed in 1979 by *A. H. J. Wang et al.* through single-crystal X-ray diffraction experiments.^[10] Z-DNA is a more radical departure from the B structure. The most obvious distinction is the left-handed helical rotation. There are 12 base pairs per helical turn, and the structure appears more slender (18 Å of diameter) and elongated (being 3.7 Å the distance

between adjacent base pairs).^[4] The DNA backbone takes on a zigzag appearance. Z-DNA arrangement is favoured *in vitro* at high salt contents and in presence of multivalent cations,^[11] whereas *in vivo* Z-DNA is a transient form of DNA, only occasionally existing in response to certain types of biological activity.^[12] Scientists have discovered that some proteins bind very strongly to Z-DNA, suggesting that Z-DNA plays an important biological role in protection against viral diseases.^[13]

1.1.2 Synthetic homopolymeric DNA: polyG·polyC and polyA·polyT

Polydeoxyguanylic·polydeoxycytidylic acid (polyG·polyC) acid and polydeoxyadenylic·polydeoxythymidylic acid (polyA·polyT) are synthetic double stranded DNAs that are commonly used for probing the selectivity towards the DNA base pairs. These polynucleotides are composed of homopolymeric strands of complementary nucleobases and exhibit conformations different from each other.

Crystallographic analyses on polyG·polyC provides a double helical structure similar to that of A-DNA (Figure 1.3A). The double helix has a broad, shallow minor groove and a deep, water-filled major groove. Adjacent guanine bases on the same strand stack in a staggered way, while in the opposite strand cytosine bases practically do not show any overlap.^[14] Upon addition of salt excess and raising the relative humidity above 90%, polyG·polyC incompletely transforms from A-DNA to B-DNA; on the contrary, natural DNA totally undergoes this transition.^[15] PolyG·polyC tracts were found to be implicated in the initiation of RNA transcription in the genomes of various organisms.^[16]

The polyA·polyT polymer exhibits instead a B-type structure both in water solution^[6] and in the crystal structure^[17] (Figure 1.3B). The X-ray crystallographic analysis highlighted the presence of a high propeller twist, which is stabilized by the formation of bifurcated hydrogen bonds on the floor of the major groove. Compared to natural DNA, the base pairs of the synthetic polynucleotide are not perpendicular to the helix axis. Further investigations also revealed the narrower feature of the minor groove with respect to the analogous groove in B-DNA.^[18]

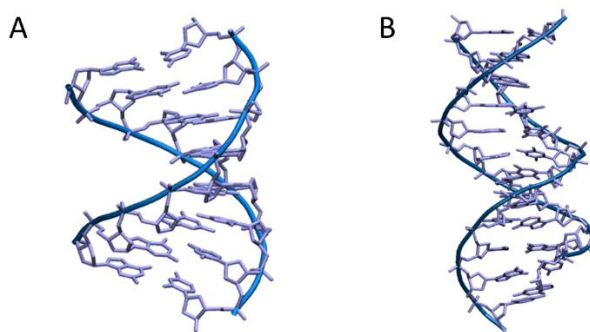


Fig. 1.3. (A) Structure of *d(G-G-G-G-C-C-C-C)* (PDB id 2ANA, defined as a model for *poly(dG)·poly(dC)*)^[14] and (B) *poly(dA)·poly(dT)*

1.1.3 Double and triple helix RNA

Ribonucleic acid is a polymeric biomolecule whose monomeric units are composed of a ribose sugar with a phosphate in 3' position and a purine or pyrimidine nucleobase in 1' position (guanine (G), adenine (A), cytosine (C) or uracil (U)). RNA plays several important biological roles such as coding, decoding, regulation and expression of genes.^[19] Unlike DNA, RNA is usually

found in nature as a single strand folded onto itself, rather than paired double strands.

Sometimes, RNA is instead arranged in double helix composed of two complementary strands (G coupled with C and A coupled with U).^[20] Nowadays, it is known that the RNA double helix serves as a structural framework for many molecules, including tRNA and ribozymes.^[21] Double stranded RNA represents the genetic material of some viruses (dsRNA viruses).^[22] Furthermore, it has been found that the RNA double helix is involved in the phenomenon of RNA interference (RNAi), which triggers the destruction of homologous messenger RNA (mRNA).^[23]

Synthetic RNA double helix (polyA·polyU, Figure 1.4) is exploited to study ligand-RNA binding mechanisms.^[24] PolyA·polyU is constituted of homopolymeric strands whose repeating units are composed of a rebose-phosphate group and a nitrogenous base. Under physiological condition, the geometry of this double helix is very similar to that of A-DNA.^[25] PolyA·polyU is commercially available or easily formed by a spontaneous reaction in solution between equimolar amounts of polyA and polyU.^[26]

A third strand can fit in the major groove of a duplex RNA, thus giving rise to the formation of a triple helical RNA that must have homopurine-homopyrimidine sequences.^[27] RNA triple helix can easily penetrate the cell and modify the double stranded DNA, resulting in the inhibition of transcription processes.^[27] Triple helical RNA structures are also involved in the catalytic activity of the telomerase enzyme.^[28] Furthermore, RNA triplex is supposed to be an important structural motif of microRNAs (miRNAs), that the therapeutic agents may target for gene regulation.^[29]

Synthetic triple helices (polyA·2polyU) can be obtained in aqueous solution from the combination of polyriboadenilic (polyA) and polyribouridylic (polyU) acids in presence of bivalent cations,^[30] as well as from the

association of equal amounts of double stranded polyA·polyU and single stranded polyA.^[31] For triplex RNA, the base-plane tilt results smaller (7-13 Å) than the double helical tilt (16-19 Å). Moreover, the dislocation of the helix axis is reduced from 4.4 Å in duplex to 2.8 Å in triplex; this change is due to the presence of the third chain, which can be fitted with reasonable geometry to the duplex only if the helix axis is approximately in the centre of the base triplets.^[6]

Because of the involvement in such many biological roles, double and triple stranded RNA have been gaining increasing attention as biotargets for potential therapeutic agents.^[32]



Fig. 1.4. *Space-filling model of polyA·polyU based on X-ray fiber diffraction data*
(T. V. Chalikian, 1999)^[33]

1.1.4 Types of binding to long chain nucleic acids

The helical structure results in the partial exposure of the nucleobases, thus representing suitable binding sites for small molecules. The binding of a ligand to a polynucleotide can occur through covalent or non-covalent interactions. Covalent interactions are mostly established by metal ions, whose binding was exploited in the development of the oldest class of anticancer agents. The common chemotherapeutic agent cisplatin covalently binds DNA at site N7 of the guanines.^[34]

The here presented work concerns non-covalent interactions, with a focus on the major approaches employed to their characterization. Typically, three main non-covalent binding modes are defined as intercalation, groove binding and electrostatic binding.^[35] Anyway, the binding process could be quite complex and could involve a combination of different types of interactions as well. The relevant abundance of one on the other will depend on different conditions such as salt content, temperature and reactant concentration.



Fig. 1.5. *Non-covalent binding modes: (A) intercalation, (B) groove binding, (C) electrostatic binding (adapted from Ihmels et al., 2004)^[36]*

Intercalation (Figure 1.5A) is identified with the insertion of a ligand between two adjacent polynucleotide base pairs.^[37] It is typically related to small planar molecules that do not bear steric hindrance. Intercalation requires the formation of an intercalation pocket, into which the ligand can lie, followed by the formation of additional molecular interactions (π stacking, hydrogen bonding, Van der Waals forces).

Aromatic rings and positive charges can promote the interaction thanks to π - π interactions with the nucleobases and electrostatic attraction with the phosphate groups. Classical examples of intercalators (Figure 1.6 A, B, C and D) are ethidium bromide,^[38] acridinium salts including proflavines,^[39] quinoline^[40] and pyrene^[41] derivatives. Intercalation typically corresponds to a strong interaction with binding constant values of $K = 10^4 \div 10^6 \text{ M}^{-1}$ under physiological conditions.^[42]

Intercalation reactions are usually driven by large favourable enthalpy variation (ΔH) with an entropy contribution (ΔS) close to zero.^[43] Favourable enthalpy arises from stabilizing interactions such as π stacking between the ligand and the nearby bases. The entropic effect is much more difficult to explain. On one hand, there is an entropic penalty related to the formation of a rigid bimolecular complex which loses translational and rotational degrees of freedom.^[44] On the other hand, the binding of a positive molecule causes the release of bounded cations and the insertion produces a release of solvent molecules (the hydration shell of the intercalating species), both aspects corresponding to a favourable entropic contribution.^[45] The combination of these effects may explain the ΔS signature.

Intercalating agents distort the polynucleotide structure to a great extent, resulting in the unwinding and lengthening of the double helix.^[46] The conformational changes can affect and inhibit DNA biological functions with effects on duplication and replication processes and transcription events, thus

leading to the death of the cell.^[47] Therefore, ligands that can intercalate into the DNA base pairs with selectivity for malignant cells are often studied as anticancer or antibacterial agents.^{[48],[49]}

Groove binding (Figure 1.5B) consists in the formation of an external complex in which the ligand lies on the groove of the double helix. Groove binders are usually curved-shape molecules composed of a series of flexible moieties that possess rotational freedom and match well with the topology of the double helix.^[50]

Groove binding molecules interact with base pairs edges either in major or minor grooves. Small crescent shaped molecules have been claimed to bind DNA via minor grooves,^[51] whereas larger molecules such as proteins^[52] and oligonucleotides^[53] have been found to be placed in the major groove. Classical examples of groove binding agents (Figures 1.6 E, F, G and H) are DAPI,^[54] netropsin,^[55] Hoechst 33258,^[56] distamycin^[57] and hairpin polyamides.^[58]

Groove binding does not perturb the DNA secondary structure to any great extent, but it significantly affects the flexibility of the double helix.^[59]

Groove binding reactions are typically entropically driven.^[43] The explanation for the more favorable entropy variation (ΔS) is that it results from the water release upon complex formation, by the displacement of the hydration sphere of both the groove and the ligand.^[60]

Electrostatic binding (Figure 1.5C) arises from the electrostatic interaction between positively charged species and the negative charges of the nucleotide phosphate groups. Despite being weaker than intercalation,^[61] this process has shown to have important implications in the ligand-polynucleotide interaction.^{[62],[63]} As far as electrostatic attraction is involved, the binding becomes very sensitive to the ionic strength.^[35] This does occur also for the

former binding modes as, from a detailed reaction mechanism point of view, the first step of the binding is always the approach of the partners, likely driven by electrostatic forces. In this light, the binding of a small molecules to a complex biosubstrate is the same of the two-steps complex formation mechanism proposed by *M. Eigen* (1962).^[64]

Self-aggregation of the ligands, using the negative phosphate residues backbone as a template, can also occur.^[65] If this is the case, external binding will be stabilised much by ligand-ligand π - π interactions that may go until formation of extended stacks on the helix.

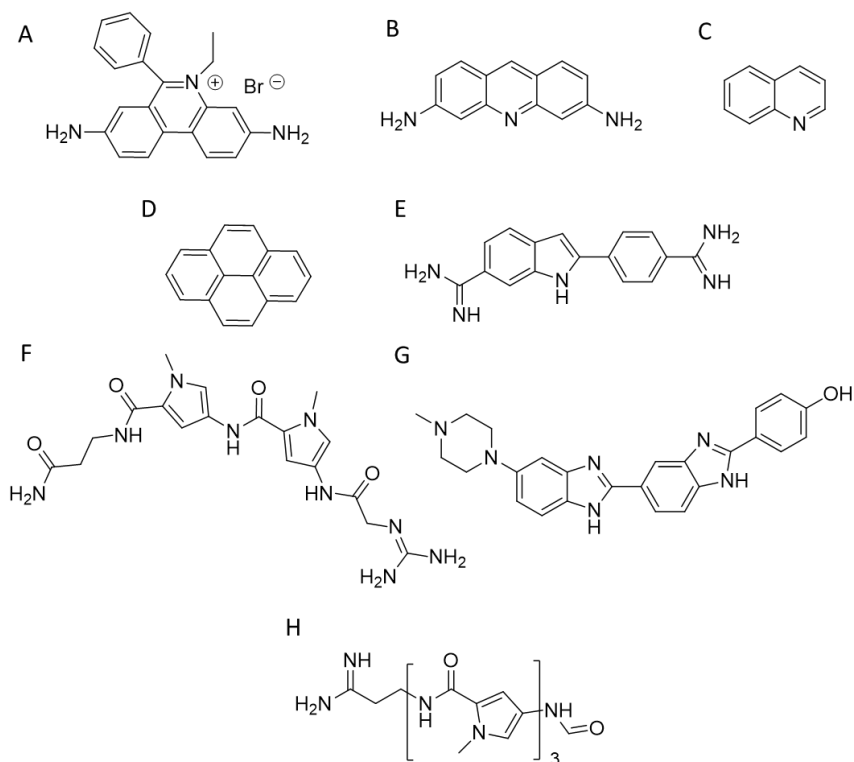


Fig. 1.6. Examples of DNA binders: (A) ethidium bromide, (B) proflavine, (C) quinoline, (D) pyrene, (E) DAPI, (F) netropsin, (G) Hoechst 33258, (H) dystamycin

The interaction of a molecule with a polynucleotide can depend on the sequence of the nucleobases at each binding site.

Concerning the ligand, the polarity, the charge and the dimension of the system can cause sequence selectivity.^{[66],[67]} Groove binders are considered to be more specific than intercalators in the recognition of the DNA base pairs.^[68] Different grooves' dimensions are especially crucial for the recognition and have been thought to be responsible for the selectivity of the typical groove binder netropsin towards the A-T base pair.^[69] The higher polarity of G-C compared to A-T base pair is also important in the determination of the preferential binding site, as observed for some heteroaromatic compounds^[70] and actinomycin derivatives.^[71] Some ligands show also different binding type depending on the nucleobases' sequence: methylene blue has been found to intercalate into polyG·polyC, while groove binding has appeared to be the main binding mode for polyA·polyT.^[72]

However, the primary structure of the biosubstrate is not the only parameter affecting the binding, as the secondary structure of the polynucleotide leads the interaction as well. In fact, it is known that some molecules, such as actinomycin D, are able to discriminate between DNA and RNA, binding to the former but not to the latter polynucleotide.^[73]

1.2 Interaction between small molecules and DNA G-quadruplex structures

1.2.1 DNA G-quadruplex structures

G-quadruplex (G4) is a four-stranded DNA structure with stacked guanine tetrads (G-tetrads) held together by hydrogen bonds (Figure 1.7).^[74] These structure are typically formed in G-rich DNA strands. Potential quadruplex sequences have been identified at the end of telomeric DNA in eukaryotic chromosomes^[75] as well as in gene promoter regions.^[76]

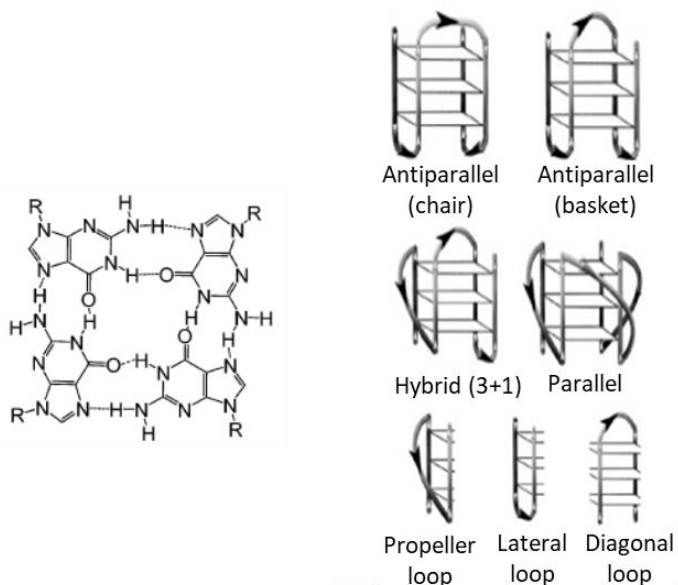


Fig. 1.7. *G-tetrad and structural conformations of G4 (adapted from C. Platella et al., 2017)^[77]*

G4 can arise from the folding of a single strand (*intramolecular G4*). Formation of these quadruplex structures in human chromosomes is possible since the terminal nucleotides of telomeric DNA are single-stranded.^[78] On the other hand, G4 can be formed by the combination of two or more separated strands (*intermolecular G4*).

G4 can display a wide variety of topologies, as a consequence of several possible combinations of strand direction (intended as 5' → 3'), number of G-tetrads, as well as variations in the size and the disposition of the loops (arising from the nucleotides not involved in the G-tetrads). G-quadruplexes can be classified as *parallel* if the strands are all oriented in the same direction (4 ↑ or ↓).^[79] On the contrary, *antiparallel* structures derive from strands directed in different ways (2↑ + 2↓).^[80] These G4 can be arranged as *chair* or *basket type* structures depending on the loops' position. If the structure is instead formed by 3 parallel and 1 antiparallel strands, G-quadruplex is defined as *hybrid* (3↑ + 1↓ or 3↓ + 1↑).^[81]

The formation, the stability and the conformation of the quadruplexes are dependent on monovalent cations (M⁺).^[82] M⁺ ions can conveniently fit into the central channel of the G-tetrads, according to the strong negative electrostatic potential created by the guanine oxygen atoms.^[83] The precise location of the cation depends on the nature of M⁺. Na⁺ ions have been found as centred in the plane of a G-tetrad as well as in the space between two successive G-tetrads; K⁺ ions are instead always equidistant between each G-tetrad plane and form a symmetric tetragonal bipyramidal configuration with the eight oxygen atoms.^[74] Because K⁺ is much more abundant than Na⁺ in cellular environments, the knowledge of the human telomeric G4 structure in K⁺ solution is really important. K⁺ ions have been found to induce hybrid-type conformations for human telomeric G4, whereas Na⁺ ions tend to promote antiparallel structures.^[84]

Ligand-G4 interactions are extensively investigated since G4 are involved in important biological processes, especially concerning cancer cells.^[85] In healthy human somatic cells, the telomers progressively shorten during the replication process and this means that each cell cannot divide indefinitely.^[86] In contrast, in more than 80% of cancer cells, an enzyme called telomerase is active and catalyses the synthesis of telomeric DNA, resulting in an everlasting proliferative potential.^[87] G4 structures inhibit the telomerase activity because G4 cannot function as a substrate for this enzyme (Figure 1.8).^[88] Therefore, ligands that stabilize or induce the formation of G4 structures can be considered as promising anticancer agents.^[89]

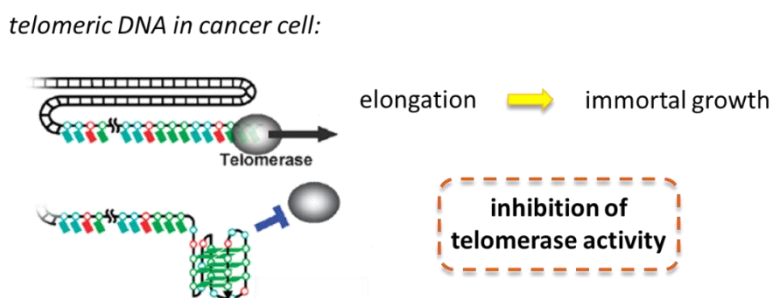


Fig. 1.8. Schematic representation of telomerase activity and inhibition by G4 in cancer cells (adapted from H. Yaku et al., 2012)^[90]

1.2.2 Types of binding to G-quadruplexes

Detailed NMR spectroscopic and crystallographic studies, together with computational investigations, have provided a clear understanding of quadruplex DNA structures. On this basis, it has been possible to develop a

rational approach to the design of quadruplex DNA binding ligands with potential anticancer activity.^[91]

Good G4 binders should present extended π -planar structures able to stack the external G-tetrads. Moreover, positively charged substituents promote the affinity with the grooves and the loops of G4, thanks to the electrostatic attraction with the negatively charged phosphate backbone. Lastly, a partial positive charge can lie in the centre of the guanine quartet and this has been found to increase G4 stabilisation by substituting the cationic charge of the potassium or sodium that would normally occupy this site.^[92]

Optimal ligands should clearly be selective for G4 over double helix DNA, since the double-stranded helix constitutes the major component of the human genome and its binding can prelude general cellular toxicity.^[93] G4 selectivity can arise, at least in part, from the difference between the large, highly accessible surface area of a terminal quartet compared with the much smaller, less accessible G-C or A-T base pair surfaces of a typical duplex DNA.^[94]

Many potential G4 binding agents have been extensively studied and here there are reported just the most typical examples (Figure 1.9). Common G4 binders are macrocyclic ligands such as porphyrins, phthalocyanines and their metal complexes.^[95] Meso-5,10,15,20-Tetrakis-(N-methyl-4-pyridyl)porphine (TMPyP₄) represents the most commonly studied example for the porphyrin class.^[96] Metal-salphen and metal-salen complexes have shown strong affinity and high selectivity for G4s as well.^[97] Square-planar Ni(II)-salphen complexes have been found to inhibit the telomerase activity by stabilizing G4 structures.^[98] Aromatic molecules that bear charged peripheral chains (such as perylene diimide and phenantroline derivatives) are able to bind G4 through π -stacking interaction between the aromatic core and the G-tetrads along with electrostatic interactions between the substituents and the G4 backbone.^[99] Investigations on non-planar metal complexes are rarer,

but some examples are reported in the literature anyway. For example, the binding properties of dinuclear $[\text{Ru}(\text{II})(\text{phen})_2(\text{dppz})]^{2+}$ complexes have been successfully investigated.^[100]

Concerning the disposition of the ligand, intercalation of small molecules between the quadruplex tetrads is thought to be difficult because G4 structures are extremely stable and rigid and their distortion requires a very high energy cost. Thus, stacking of the ligand on the outer surface of G4 as well as its disposition on the grooves appear to be a more energetically favourable and probable binding mode.^[101]

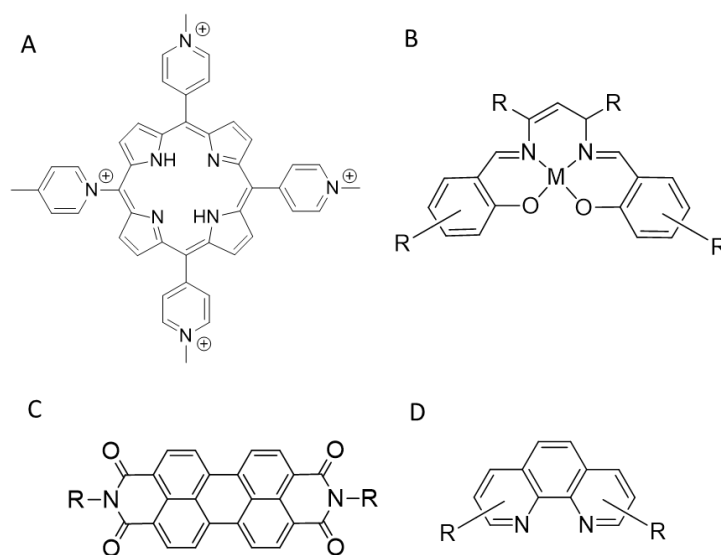


Fig. 1.9. Examples of G4 binders: (A) *TmpyP₄*, (B) *metal salen complex*, (C) *peryene diimide derivative*, (D) *phenantroline derivative*

1.3 Interaction between small molecules and serum albumin protein

1.3.1 Bovine serum albumin

Serum albumins represent the major protein content of the circulatory system.^[102] Albumins are involved in the regulation of blood osmotic pressure and the maintenance of blood pH.^[103]

However, from the point of view of this work, the most important function of serum albumins is their involvement in the transport, distribution and metabolism of exogenous and endogenous substances.^[104] Many reactants establish stable but reversible bonds with albumins and it clearly affects their life-time, solubility, toxicity as well as their bioavailability in the blood.^[105]

The influence of albumins in the pharmacokinetics and pharmacodynamics of drugs has been gaining widespread interest for the development of new therapeutic agents.^[106] Furthermore, plasma proteins have been studying for their carrying role for toxic substances such as pesticides.^[107]

Bovine serum albumin (BSA, Figure 1.10) is one of the most extensively studied albumins, thanks to its structural homology with human serum albumin (HSA). BSA is composed of 583 aminoacids, whose sequence corresponds to that of HSA for more than 75%.^[108] Bovine serum albumin is postulated to have a heart-shaped structure with high α -helical content (67%).^[109] BSA is divided into three main domains (I, II and III); each domain is composed of two subdomains (A and B).^[110] BSA contains two tryptophan residues: Trp-134, located on the surface of domain IA, and Trp-212, embedded within the hydrophobic pocket of domain IIB.^[111] The presence of these residues, along with tyrosines and phenylalanines, lends light emission properties to the protein.

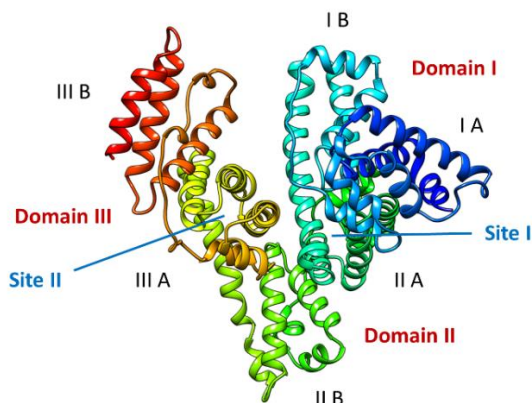


Fig. 1.10. Structure of bovine serum albumin (from PDB file 4F5S)

1.3.2 Types of binding to BSA

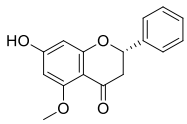
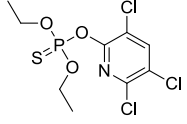
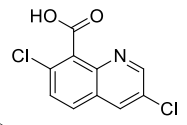
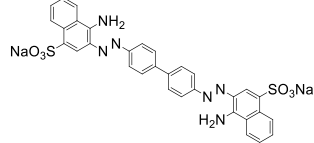
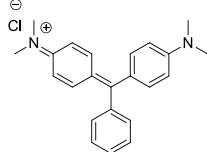
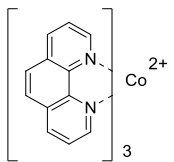
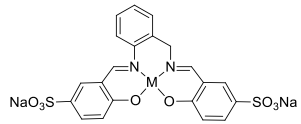
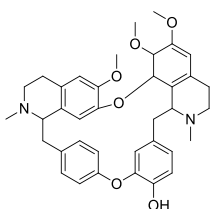
X-ray crystallographic studies have revealed that bovine serum albumin possess two principal binding site: site I is situated in the hydrophobic pocket of subdomain IIA, whereas site II is located into the hydrophobic cavity of subdomain IIIA.^[112] Site I is relatively larger in size and it is mainly bound by neutral, bulky and heterocyclic compounds through hydrophobic interactions. On the contrary, site II is smaller and the interaction commonly occurs through a combination of hydrophobic, hydrogen bonding and electrostatic forces.^[113] When ligands bind to proteins, the intramolecular forces responsible for maintaining the secondary and tertiary structures of the protein can be altered, resulting in conformational changes.^[114] The quenching of the fluorescence may indicate that the ligand-protein interaction has changed the microenvironment of the tryptophan residues and the tertiary structure of the

protein.^[115] Changes in the secondary structure can be enlightened by the means of infrared absorption spectroscopy.^[116]

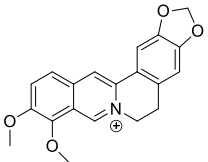
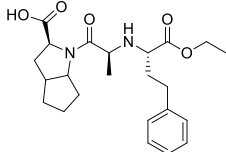
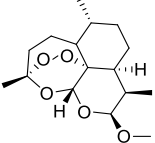
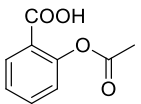
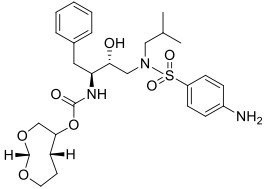
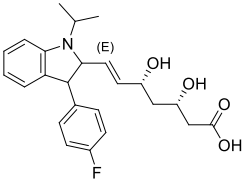
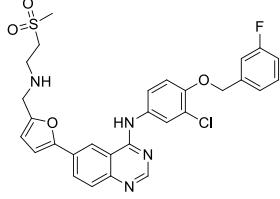
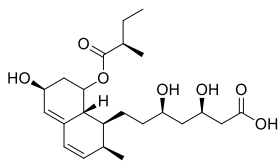
Small molecules can bind to proteins through H-bonds, van der Waals, electrostatic and hydrophobic interactions^[117] and the thermodynamic parameters of the interaction are considered as indicative of the binding mode. In particular, *P.D. Ross and S. Subramanian* (1981) have characterized the thermodynamic signature for each binding type.^[118] Positive values for ΔH and ΔS indicate the presence of hydrophobic forces. Negative ΔH and ΔS values concern the existence of hydrogen bonding and/or van der Waals forces. The contribution of electrostatic forces is instead highlighted by negative values for ΔH and positive values for ΔS .

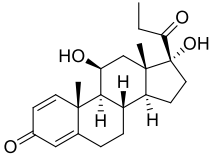
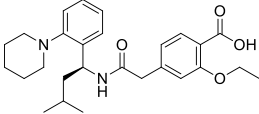
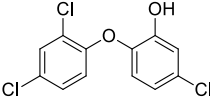
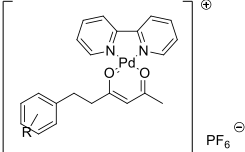
Table 1 reports some examples of BSA binders, together with their preferential binding site and type.

Tab. 1.1. Examples of small molecules which are claimed to show selective binding for one of the sites of BSA

MOLECULE	SITE	MODE	REF		
	Alpinetin	Plant extract	I	hydrophobic	[119]
	Chlorpyrifos	Pesticide	I	electrostatic	[120]
	Quinclorac	Herbicide	I	van der Waals / H bond	[121]
	Congo Red	Carcinogenic dye	I	hydrophobic / H bond	[122]
	Malachite green	Commercial stain Antimicrobial agent	I	van der Waals / H bond	[123]
	Co(II) 1,10-phenanthroline	Metal complex possible anti tumor agent	I	electrostatic / hydrophobic	[124]
	Schiff base complexes of Mg(II), Mn(II), Zn(II)	Anticancer agents	I	hydrophobic	[125]
	Berbamine	Calcium channel blocker	I	van der Waals / H bond	[126]

Chapter I

	Berberine	Alkaloid	I	electrostatic	[127]
	Ramipril	Commercial drug	I	van der Waals / H bond	[128]
	Artemether	Commercial drug	I/II	van der Waals / H bond	[129]
	Aspirin	Commercial drug	II, small quantity I	van der Waals / H bond	[130]
	Darunavir	Commercial drug	II	van der Waals / H bond	[131]
	Fluvastatin	Commercial drug	II	van der Waals / H bond	[132]
	Lapatinib	Commercial drug	II	van der Waals / H bond	[133]
	Pravastatin	Commercial drug	II	van der Waals / H bond	[132]

	Prednisolone	Commercial drug	II	van der Waals / H bond	[134]
	Repaniglide	Commercial drug	II	hydrophobic	[113]
	Triclosan	Antibacterial agent	II	van der Waals / H bond	[135]
	Pd(II) hispolon derivatives complexes	Therapeutic agent	II	-	[136]

Chapter 2

2. Spectroscopic techniques as essential tools for providing information on the binding modes

2.1 Nucleic acids binding studies

Over the last 60 years, researchers have focused their attention on the binding of small molecules to biosubstrates. The purpose of such an effort is to understand the mechanisms of the toxic and/or therapeutic activity of the binding agents.

Nucleic acids represent an attractive target for small molecules, especially those with planar chromophores.^[137] The formation of complexes between nucleic acids and small molecules is thought to be responsible for carcinogenic and mutagenic effects. On the other hand, selective drugs can recognize specific nucleic sequences and induce the apoptosis of the cancer cells, avoiding detrimental effects on the healthy systems.

Binding studies involve the use of many different techniques, ranging from calorimetry,^[138] viscometry,^[139] mass spectrometry,^[140] electrophoresis,^[141] dialysis,^[142] X-ray crystallography,^[143] nuclear magnetic resonance (NMR)^[144] or electron paramagnetic resonance (EPR) spectroscopy.^[145] Sometimes these techniques may be complicated or peculiar and may require specific expertise. Besides, UV-vis spectroscopies represent a relatively simple tool for investigating the binding of small molecules to nucleic acids. Acridine dyes, and especially aminoacridines,^[146] have been the first molecules that attracted the interest of researchers during the earliest

spectroscopic studies on small molecules binding to polynucleotides. In 1961 *L. S. Lerman* proposed the “*intercalation hypothesis*” in a publication on the physico-chemical behaviour of DNA in the presence of small amounts of proflavine and acridine orange.^[147] Since then, many investigations on small molecules binding to nucleic acids have been performed and the knowledge of the mechanistic aspects as well as the mastery of the experimental techniques have considerably advanced. Notwithstanding, many questions are still unsolved.

In this chapter, the principal spectroscopic methods are presented with a focus on their own advantages and drawbacks. On the whole, and even more for complex systems as those involving biosubstrates, it is the combination of different approaches that better provides significant and valuable results.

2.1.1 Absorbance titrations

Complexation between ligands and biomolecules may lead to optical changes that can be used to monitor the binding process. Within this context, ultraviolet-visible (UV-Vis) absorption spectrometry constitutes a relatively simple approach that can provide important information on the structural changes induced by the binding agents and on the mode of interaction.^[148]

The spectrophotometric titration technique was firstly developed in 1918 by *A. Tingle*^[149] and since then has found universal application, also in polynucleotide-ligand binding studies. In an absorbance titration, essentially, a thermostated cuvette is filled with a solution of the ligand and the progressive absorbance changes are recorded upon the addition of serial and known amounts of the polynucleotide solution.

When the ligand does absorb in the visible region (i.e. far from the UV band of the biosubstrates), the addition of the polynucleotide as titrant species enables the signal of the free dye to be better distinguished from that of the adduct. If the ligand is conversely used as the titrant, the signal of the complex would be overcome from that of the free dye as its concentration is raised. Under these circumstances, the spectral changes due to adduct formation would be hardly identified. In addition, it would be difficult to determine the end of the titration, as the signal would continuously increase because of the progressive addition of the dye.

Clearly, the choice of the absorption wavelength at which the analysis will be performed deserves careful attention. As both ligands and biosubstrates usually show characteristic absorption bands in the UV range of the spectrum, the superimposition of the signals makes the analysis of the data quite difficult, requiring an estimation of the separate contribution of the dye and the biosubstrate. The first point is to try to avoid any superimpositions, which is quite easy in the lucky event of visible-absorbing ligands. If this is not the case, the researcher may try to overcome this problem by means of differential titrations, performed with a double-ray spectrophotometer by adding the same amount of titrant both into the sample and into the reference cuvette. Therefore, the contribution of the free polynucleotide will be subtracted from the recorded signal. Anyway, this process may lead to significant bias, as the spectrophotometer setup does not always guarantee indisputable corrections of the signal. In particular, when the free titrant's absorption turns out to be much higher than that of the titrand, its contribution cannot be subtracted correctly. Moreover, differential titrations are quite expensive as their performance requires high amounts of biosubstrate, and the availability of the titrant often limits the applicability. Hence, sometimes a purely mathematical correction shall be preferred.

Overall, the superimposition of the UV signal represents a complex problem that can be difficult to overcome and it should be avoided in the design of the experiment. A valuable solution could arise from displacement experiments (see Paragraph 2.1.4).

As already discussed, ligands that possess absorption bands lying in the visible range are thus more easily tested by spectroscopic studies. This feature makes the observation of the spectral changes much easier and enables the binding analysis to be fairly performed. Among others, aromatic dyes and extended π conjugated systems profitably show electronic transitions in the visible range. Upon the binding, the ligand will be placed in a different environment with respect to the free state in solution. In fact, the pH in the grooves is significantly lower than that of the surrounding solution^[150] and the interior of DNA is proposed to exhibit a lower dielectric constant.^[151] Moreover, the electronic distribution of the dye is distorted upon interaction. All of these factors contribute to change the absorption features of the bound molecule as compared to that free in solution.

The spectral changes are usually more evident for intercalative binding modes. When π stacking interactions are established between the ligand and the nucleobases, electronic delocalization occurs and the HOMO-LUMO gap of the adduct is reduced.^[152] Therefore, intercalation typically produces the shift of the absorption band to longer wavelengths (*bathochromic effect* or *red shift*) together with a decrease of the band intensity (*hypochromic effect*).^[153] For example, the visible band of an intercalating Pt-proflavine complex was found to decrease in intensity as well as to shift to longer wavelengths upon the addition of polyA·polyU.^[24] Bathochromic and hypochromic effects were also observed for the intercalation of auramine O into the DNA base pairs.^[154] Nonetheless, such modifications of the absorbance are not exclusively due to intercalation and cannot be employed alone to identify the binding mode.

The presence of a not-well defined isosbestic point (i.e. the intersection point of a set of absorption curves) suggests that two or more complexes are formed.^[155] This can be related to the involvement of different binding modes depending on the C_P/C_D ratio as well as to auto-aggregation phenomena. Just to cite few examples, the non-perfect isosbestic point of the Pd(II)-5,10,15,20-tetrakis(1-methyl-4-pyridyl)porphyrin/DNA system was ascribed to dye aggregation on the DNA surface.^[156] Instead, the lack of a well-defined isosbestic point for a pyridinimino complex of Pt(II) binding to DNA indicated that the presence of different binding modes which, finally, were found to be both groove binding and intercalation, the prevailing one being dependent on the reagents concentrations.^[157]

One should also take into account that the measurement of the absorbance intensity can be affected by experimental artefacts. The baseline of the signals can be altered because of light scattering problems. Light scattering can occur for very concentrated solution, because the precipitates as well as the aggregates can diffract the light beam. In this case, the spectra should be corrected according to *S. J. Leach and H. A. Scheraga (1960)*.^[158] A logarithmic plot of the experimental data ($\log(\lambda)$ vs. $\log(A_\lambda)$) should be linear in the range where the scattering occurs and should depart from linearity in the wavelength region of absorption. Hence, the extrapolation of the linear portion ($\log(\lambda) = m \cdot \log(A_\lambda) + q$) will indicate the scattering contribution and can be subtracted from the total absorbance intensity in order to obtain the pure absorption effect (Equation 2.1).

$$A_{\text{corr}} = A_{\text{obs}} - (10^{\text{intercept}} \times \lambda^{\text{slope}}) \quad (2.1)$$

However, it should be remembered that every mathematical manipulation may result in a loss of information or at least in a deviation from the actual behaviour.

Reliable quantification of binding constants requires that the optical behaviour of the dye is linear over the range of concentrations used in the test. Thus, the *Lambert and Beer* law has to be obeyed and this has to be checked before any subsequent evaluation. Non-linear concentration dependencies of absorbance may result from polymerisation, aggregation or simple precipitation. In general, quantitative analyses are not recommended for situations in which linear concentration dependence cannot be ensured.

As for the analysis of the binding process, many refined methods can be employed, differing for the host/guest model. The choice of the best treatment mainly depends on the system under study.

For a simple 1:1 complex, the data can be fitted according to the model proposed in 1949 by *H. A. Benesi and J. H. Hildebrand* during their spectroscopic studies on benzene-iodine solutions (Equation 2.2).^[159] A more detailed description of this equation is reported in Appendix I.

$$\frac{C_D}{\Delta A} = \frac{1}{K\Delta\epsilon} \cdot \frac{1}{[P]} + \frac{1}{\Delta\epsilon} \quad (2.2)$$

Here, C_D is the total molar concentration of the dye (ligand), K is the binding constant, ΔA denotes the changes in the optical variable, $\Delta\epsilon$ represents the variation in the extinction coefficient and $[P]$ is the molar concentration of the free polynucleotide (or protein).

It has to be noted that the binding analysis requires the determination of the free polynucleotide concentration, which is not aprioristically known. One can suppose that, at the end of the titration, the free polynucleotide is in large

excess with respect to the limiting dye and its total molar concentration (C_P) can be approximated to that of the free form ($C_P \cong [P]$). However, the correct approach consists in an iterative fitting procedure: for each step a better estimation of the free polynucleotide concentration is obtained and employed for the determination of the binding constant until convergence.

For multiple binding sites, the data can be fitted on the basis of the equation presented by *G. Scatchard* in 1949 in his binding studies between proteins and small ligands (Equation 2.3, see Appendix II for the details).^[160]

$$\frac{r}{[D]} = -K_{SC}r + K_{SC}B \quad (2.3)$$

where r is $[PD]/C_P$, $[D]$ represents the free dye concentration, the *Scatchard* constant K_{SC} is employed to obtain the binding constant as $K = K_{SC} \times B$ and B is a constant related to the site size n by the relationship $n = 1/B$. The site size is a parameter which, for nucleic acids with concentration expressed in base pairs, corresponds to the number of adjacent base pairs inactivated by the binding of one ligand.

The *Scatchard* model assumes a linear relationship for $r/[D]$ vs. r , that is rarely obeyed. A substitute model is called *excluded site model* (or neighbour exclusion) and was developed by *J. D. McGhee and P. H. von Hippel* in 1974 on the basis of cooperativity and probabilistic studies (Equation 2.4).^[161] This model introduces a cooperative factor $f(r)$ to consider the interactions between the bound molecules. The authors also demonstrated that B is related to the binding site size through the relationship $n = (1+1/B)/2$.

$$\frac{C_D}{\Delta A} = \frac{1}{K\Delta\varepsilon} \cdot \frac{1}{C_P f(r)} + \frac{1}{\Delta\varepsilon} \quad (2.4)$$

On the whole, although the absorbance titration technique represents an easy-to-use method for providing information on the binding, one has to consider that these measurements are not exempt from drawbacks. The reliability of the titrations should be always checked by repeating the measurements and other complementary techniques could be useful to confirm the obtained results.

Note that all the equations above and much of those which will be discussed below are referred to an absorbance (or fluorescence) read at fixed wavelength. Nowadays, different software are available, which work over a wide wavelength range and use multivariate fitting to reproduce the spectroscopic trend during the titration and provide binding constants for a certain model. This is certainly a modern and powerful approach but that has to be used carefully. First and obviously, high attention has to be given to the way the experimental data are uploaded in the software. Second, different attempts have to be made (starting values for parameters, different types of model) to ensure that the final values provided are robust. Last but not least, an important point is that these software very often are based on a starting model where the reactants interact according to a given stoichiometric ratio. The stoichiometry is here intended as an integer number. This is not strictly occurring in the case of biosubstrates, where the complexity of the system may lead to a mediated fractional number.

2.1.2 UV Melting experiments

UV melting experiments represent a suitable tool for providing information on the nature and the strength of the binding modes to polynucleotides.

The main principles of this experiment were firstly presented in 1951 by *R. Thomas*, who noted that the actual absorbance intensities of nucleic acids appeared 30% lower than those calculated by summing the individual absorbances of their constituent nucleotides.^[162] The hypochromicity of native nucleic acids as compared to the mixture of their components was explained as a consequence of interactions between nucleobases.^[163] In fact, increases in the absorbance intensity were observed upon mild treatments (thermal denaturation, pH variation) that caused effects on the secondary structure of nucleic acids, but neither on the phosphodiester backbone nor in the degree of polymerization.^[164]

Certainly, only with the elucidation of the DNA structure by *J. Watson and F. Crick* (1953)^[2] nucleic acids denaturation could have been considered as a useful tool for providing information on the secondary structures. Since then, this method has been applied for decades, initially on simple polynucleotides,^[165] then even on unusual DNA structures such as triplexes^[166] or quadruplexes.^[167]

Thermal denaturation can be easily monitored by means of absorbance spectroscopy, by observing the absorbance changes as a function of temperature.^[168] As the temperature increases, the secondary structure of the polynucleotide unfolds, this usually leading to hyperchromism. However, the absorbance spectra of nucleic acids correspond to different $\pi \rightarrow \pi^*$ and $n \rightarrow \pi^*$ transitions, depending not only on the intrinsic transition moments of each base, but also on the relative moment of the interacting bases (base-paired

or stacked).^[169] Such complexity makes the accurate prediction of hypo or hyper-chromic effects a difficult task.

Absorbance spectra of folded and unfolded polynucleotides are recorded above and below the melting temperature and the values of absorbance are plotted against temperature. The inflexion point of the obtained sigmoidal curve represents the melting temperature (T_m). T_m corresponds to the temperature at which 50% of the polynucleotide is unfolded while the rest is still folded.^[168]

In most cases, the thermal denaturation of nucleic acids is studied by following the increase of the signal at $\lambda = 260$ nm. However, in some cases it may be preferable to perform the analysis at other wavelengths, for which more significant variations are observed. For example, G4 denaturation does not lead to large variation in absorbance at $\lambda = 260$ nm, but it is possible to follow the process at $\lambda = 295$ nm.^[167] The hypochromic effect observed upon denaturation might be the result of the significant contribution of $n \rightarrow \pi^*$ transition moments at this wavelength: as these transition moments are parallel to the helix axis, increased stacking resulting from the formation of a folded structure may result in hyperchromism.^[170]

The melting temperature strongly depends on the composition of the polynucleotide, since the thermal energy required to break the 3 H-bonds between G-C is higher than that needed for the 2 A-T H-bonds.^[171]

The thermal denaturation of nucleic acids is also affected by the salt content and the buffered solvent conditions. For example, higher salt concentrations generally result in higher T_m values, since the negative charges on the phosphate backbone are stabilized through electrostatic forces.^[172]

As the studies are performed in aqueous solvents and given evaporation and bubbles formation problems, measurements become hardly feasible above 90-95°C. Also, the spectrophotometer itself may in principle suffer if the cell-

holder is not properly isolated from the optical part. The relationship between T_m and ionic strength can be therefore exploited to change T_m to a more convenient and lower temperature range, simply by reducing the salt content. UV melting tests offer convenient insights into the effects of ligands-nucleic acids interactions: as more energy is required to denature the stabilized secondary structure relative to the untreated polynucleotide, the melting temperature increases. On the other hand, lower T_m are observed for destabilized structures.^[173] Although the stronger is the binding the higher is the ΔT_m , it is complicated to directly correlate ΔT_m with the binding constant. In fact, ΔT_m not only depends on the affinity, but also on the number of the binding sites, on possible cooperativity between them, as well as on the affinity for the unfolded forms.^[174]

Different ligand/biosubstrate (C_D/C_P) ratios should be explored in order to obtain reliable results, but the ratio should also be correctly adjusted. A significant amount of adduct has to be formed in order to observe variations in T_m , meaning that either high binding constants or appropriate concentrations are required. In fact, if just a small fraction of the polynucleotide is bound to the ligand, the obtained melting temperature will quite uniquely reflect that of the free polynucleotide. On the other hand, excessive concentrations might lead to precipitation problems. On the whole, the best option may be to repeat melting tests at increasing C_D , trying to reach the saturation of the substrate i.e a plateau in the T_m vs C_D/C_P plot.

The binding modes are characterized by different stabilization extents.^[175] Intercalation into DNA base pairs typically provides the most significant ΔT_m , as the double helix is strongly stabilised by π - π stacking interactions.^[176] In this respect, $\Delta T_m > +5$ °C is usually associated with intercalation.^[177] The classical intercalator ethidium bromide markedly increases the T_m of both polyA·polyT and polyA·polyU of +7.2°C and +17.3°C respectively.^[178]

Ibuprofen's intercalation into the DNA base pairs stabilizes the double helix of $\Delta T_m = +6.2^\circ\text{C}$.^[179] Low positive or negative ΔT_m are usually associated with groove binding or weak electrostatic interactions.^[180] However, this feature does not provide indisputable insights into the binding modes. For instance, the typical groove binder distamycin was found to induce $\Delta T_m = +21^\circ\text{C}$ on polyA·polyT double helix.^[178]

Melting studies can be also exploited to investigate the effect of the ligand on the nucleic acids folding. For example, absorption melting profiles revealed that the antibiotic coralyne tends to promote the disproportionation of the double stranded polyA·polyU into the triplex polyA·2polyU and a single-strand of polyA.^[181] Melting experiments also indicated that ethidium bromide facilitates the triplex polyA·2polyU melting and hinders the following thermal denaturation of the duplex polyA·polyU instead.^[31]

Beside the melting temperature, other relevant information can be also extracted from UV melting experiments. In contrast to proteins,^[182] the denaturation of nucleic acids is generally a reversible process.^[183] The reversibility of the thermal denaturation of natural DNA was firstly observed in 1961 by *J. Marmur and P. Doty*.^[184]

Melting curves obtained by heating and cooling the sample can be compared. The superimposition of the melting profiles indicates that the observed reaction is fast relative to the steps of the temperature gradient and this most likely confirms intramolecular folding. On the contrary, hysteresis suggests that the structural transition is slow as compared to the temperature gradient and this usually occurs for intermolecular folding.^[185]

Among other interesting and more recent structural studies, *J.L. Mergny et al.* (2005) have pointed out that thermal difference spectra (TDS) represent a specific signature for nucleic acids conformations.^[186] A thermal difference spectrum can be easily obtained by the difference between the absorbance

spectra of the unfolded and folded polynucleotide (i.e. at T well above and below its melting temperature). The TDS has a particular shape that is specific for each type of nucleic acid, reflecting the subtlety of base stacking interactions that occurs uniquely for each type of conformation. TDS provides a simple, inexpensive and rapid tool to obtain structural insights into nucleic acid structures, which is usually and successfully applied for studying G4 conformations.

2.1.3 Fluorescence titrations

During the past 20 years there has been a remarkable growth in the use of fluorescence spectroscopy for biochemical studies.

Fluorescence is defined as the emission of light during the irradiation of a substance with electromagnetic radiation and concerns the return to the electronic ground state from the first electronic excited state. Fluorescence emission typically occurs for molecules with aromatic moieties, which also constitute optimal features for binding to nucleic acids.

The interaction with polynucleotides may lead to optical changes on the fluorescent ligand, which can modify the emission signal as well as can cause the appearance of new bands. These features have been successfully exploited in the development of new efficient “switch on” fluorescent probes for nucleic acids.^[187] Fluorescence is indeed strongly influenced by the microenvironment surrounding the fluorophore (*solvatochromism*), as the energy of the excited state is very sensitive to dielectric constant and the hydrogen-bonding capacity of the medium.^[188] Moreover, quenching effects due to the dissipation of energy to the solvent molecules can be prevented by the polynucleotide’s double helix.^[189] At first sight, this light emission

enhancement effect would seem to enable the discrimination between intercalation and groove binding, since in the former case the fluorophore is buried deep into the helix, whereas in the latter case it is more exposed. Unfortunately, this is not straightforward. Upon binding to DNA, the fluorescence intensity of the groove binder Hoechst 33258 was found to dramatically increase.^[190] The same effect was observed for Cyan2 intercalating into polyA·polyT and polyG·polyC.^[191]

Indirect fluorescence quenching assays could better provide information on the binding mode. Collisional quenching by oxygen was used to study the behaviour of several DNA-binding molecules. The quenching constant k_q of the intercalated proflavin was found to be less than $0.1 \times 10^{10} \text{ M}^{-1}\text{s}^{-1}$, whereas for the groove binder Hoechst 33258 the value increases up to $1.1 \times 10^{10} \text{ M}^{-1}\text{s}^{-1}$; the intermediate value of $k_q = 0.17 \times 10^{10} \text{ M}^{-1}\text{s}^{-1}$ for coronene is ascribable to partial intercalation into the double helix.^[192]

In solution, some particular molecules called molecular rotors exhibit dynamic motions that serve as a non-radiative decay pathway for the excited form. Clearly, the interaction with the polynucleotide could limit the mobility of the ligands and this could result in an enhancement of their emissive features. For instance, thiazole orange was observed to become fluorescent when buried into the hydrophobic cavity of DNA.^[193] Addition of DNA gives rise to a new emission band and causes a dramatic enhancement on the fluorescence signal of the weak emitter thioflavin T.^[194]

It is worth recalling also the existence of aggregation induced emission (AIE) properties, which often arise from dye-dye interaction.^[195] Interaction with nucleic acids can act as physical constraint as well, restricting the intramolecular rotations and enabling light emission.

Spectrofluorimetric titrations are performed on the same basis of the absorbance titrations but together with some advantageous features.

As fluorescence spectroscopy is more sensitive than absorption, much diluted solutions (up to $10^{-7} - 10^{-6}$ M) can be employed. Therefore, aggregation and precipitation phenomena are conveniently limited and small amounts of sample are required.

Anyway, the linear correlation between fluorescence intensity and concentration has to be checked before the experiments, more thoroughly than for absorption. For absorbing species, the direct proportionality between signal and molar concentration is obeyed (within the *Lambert and Beer* law limits and unless the dye form is modified). Concerning fluorescence spectroscopy instead, the mathematical dependence of the signal on concentration is exponential and results to be approximable to directly proportional to concentration only for low values of the molar absorption coefficient and/or at low concentrations of the fluorophore.^[192] More details on the concept are reported in Appendix III. In principle, the lowest is the concentration, the better the linearity will be followed. Therefore, from this point of view, it would be better to use the more diluted species possible. However, the optimal concentrations will be also a function of the minimum signal read possible (and therefore fluorophore quantum yield) and of the binding constants involved (the ligand-BSA complex need to form).

The superimposition of the signals is avoided as nucleic acids are not fluorescent, but the choice of the working wavelengths plays a crucial role.

In fact, fluorescence experiments can be affected by a variety of tricky non-molecular mechanisms (inner filter effects), which thereby distort the obtained fluorescence data.^[196] The inner filter effect due to absorption of the incident ray as well as the emitted light can decrease the fluorescence intensity. As the concentration of the absorbing species varies at each step of the titration, this

effect cannot be neglected. The inner filter effect causes a downward curvature in the binding isotherm that is not ascribable to the ligand-biosubstrate interaction.

Regardless of the ligand being used, it is important to determine if the inner filter effects are significant or not. Limited inner filter effects ($A < 0.1$) can be corrected according to *Lakowicz*^[192] as follows (Equation 2.5):

$$F_{\text{corr}} = F_{\text{obs}} \times 10^{\left(\frac{A_{\lambda\text{em}} + A_{\lambda\text{exc}}}{2}\right)} \quad (2.5)$$

where F_{corr} and F_{obs} are respectively the corrected and the observed fluorescence intensities, while $A_{\lambda\text{em}}$ and $A_{\lambda\text{exc}}$ are the absorbance values respectively at the emission and excitation wavelengths for the absorbing species.

2.1.4 Competitive fluorescent displacement experiments

Competitive fluorescence displacement assays are indirect titration techniques used to determine the binding affinity of non-fluorescent DNA-binding ligands with the help of a fluorescent probe.^[173] Among others, the ethidium bromide (EtBr) displacement assay represents the most popular test. Ethidium bromide is an intercalating agent, which binds strongly and specifically to double helix DNA and RNA.^[38] Under physiological conditions, the equilibrium constant for the formation of the EtBr-DNA complex was estimated to be $K_{\text{eq}} = 2.6 \times 10^5 \text{ M}^{-1}$ (NaClO_4 0.1 M, NaCac 10 mM, EDTA 0.25 mM, pH 7.0, 24°C).^[197]

In aqueous solutions, the emission properties of EtBr solvated dye are dramatically reduced due to the quenching mechanism of the water molecules.

Upon binding to nucleic acids, the fluorescence intensity is strongly enhanced, because intercalation prevents the exposure to the solvent effect.^[198] By irradiating the system at approximately $\lambda_{\text{exc}} = 540 \text{ nm}$, the maximum of the fluorescence emission spectrum is found at $\lambda_{\text{em}} = 590 \text{ nm}$.^[199]

The use of the EtBr intercalator as fluorescent probe to evaluate binding affinities was originally proposed by *A. R. Morgan* in 1979.^[200] The procedure consists in saturating all the binding sites of the nucleic acid with the intercalating agent. Excessive amounts of EtBr should be avoided in order to limit the contribution of the free dye to the competitive assay. There should be approximately one EtBr molecule every two base pairs,^[201] but the yield is dependent on the experimental conditions and should be always checked. A spectrofluorimetric titration is therefore performed by adding the non-fluorescent ligand to the EtBr-DNA mixture. The interaction will be confirmed by the displacement of the intercalated EtBr, resulting in a decrease of the fluorescence signal (Figure 2.1).

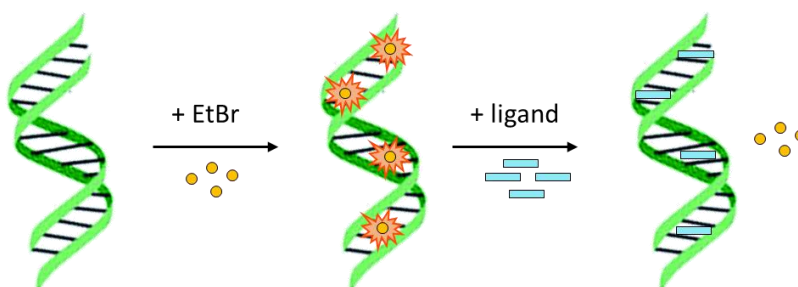


Fig. 2.1. Schematic representation of EtBr displacement assay

The exchange constant between the ligand and EtBr can be calculated according to Equation 2.6:^[202]

$$\frac{(C_{EB} - [PEB])^2}{[PEB]} = K_{ex}(C_D - C_{EB} + [PEB]) \quad (2.6)$$

where C_D and C_{EB} are the total analytical ligand (dye) and EtBr concentrations respectively, K_{ex} is the equilibrium exchange constant, whereas $[PEB]$ is calculated as $C_{EB}^\circ \times F/F^\circ$.

For a simplified 1:1 stoichiometry model, the equilibrium binding constant for the ligand-DNA complex can be expressed as $K_b = K_{ex} \times K_{EB}$, K_{EB} being the EtBr-DNA binding constant.^[202] The presented model represents a purely qualitative approach as several approximations have to be done in particular on the stoichiometric ratio of the exchange process which is both non-straightforward and in principle may also be a function of the polynucleotide saturation (i.e. variable during the exchange experiment).

The exploitation of the visible wavelengths related to EtBr limits inner filter effects (most aromatic dyes strongly absorb in the UV region) and enables the use of fluorescence spectroscopy even for non-fluorescent species. However, the measurements should be evaluated with caution.

The decrease of the fluorescence intensity can be obviously caused by intercalating ligands, which exchange with EtBr molecules; but also the distortion of the DNA structure, due for instance to groove binding or external stacking, results in a greater exposure of the intercalated EtBr with the consequent fluorescence quenching.

On the other hand, the quenching effect is sufficient to confirm that the interaction does occur, but not mandatory at all. If the binding constant of the studied ligand is lower than that of EtBr, the fluorescent probe might not be

displaced, but it does not mean that the ligand does not possess affinity for DNA. To check this possibility, larger amounts of ligand should be employed in order to promote the interaction, but the experimental conditions (volume, precipitation, availability) might limit this approach.

Hence, the competitive fluorescent displacement assay clearly represents a valuable approach, but it may lead to uncertainties in the determination of the type and the strength of the binding and should be supported by other tests.

2.1.5 FRET melting experiments

Fluorescence Resonance Energy Transfer (FRET) concerns the transfer of energy from a fluorescent donor molecule to an acceptor molecule coupled through a dipole-dipole interaction.^[192] This process occurs when the emission spectrum of the fluorophore overlaps with the absorption spectrum of the acceptor. However, it must be underlined that FRET is not the result of emission from the donor being absorbed by the acceptor: there is no intermediate photon, but a pure energy transfer through non-radiative dipole-dipole coupling.

As a consequence of the energy transfer, the excited fluorophore does not decay through a radiative path and no fluorescence is observed.

The extent of energy transfer (k_T , Equation 2.7) is determined by the distance between the donor and acceptor, according to *T. Förster* (1948):^[203]

$$k_T = \frac{1}{\tau_D} \left(\frac{R_0}{r} \right)^6 \quad (2.7)$$

where τ_D is the lifetime of the donor in the absence of energy transfer, R_0 corresponds to the distance at which the efficiency of the energy transfer is 50%, and r is the distance between the donor and acceptor.

The efficiency of the energy transfer is expressed as Equation 2.8:

$$E = \frac{R_0^6}{R_0^6 + r^6} \quad (2.8)$$

Generally, the maximum distance between the acceptor and the donor is equal to 60 Å, comparable with the dimension of biological macromolecules.^[192] For this reason, FRET is often used as a spectroscopic tool for measuring distances in proteins.^[204]

The dependence on donor-acceptor distance is the key factor for the use of FRET-based methods in binding studies. Since the original work of *T. Simonsson and R. Sjöbak* (1999)^[205] demonstrating that the energy transfer could be used to study G4s, FRET has been exploited to measure the stabilizing effects and the selectivity of G4 ligands.^[206] Among others, in recent years, challenging studies on G4 folding and binding have been performed by *J. L. Mergny* and his research group.^{[207],[208]}

The polynucleotide is tagged with a donor and an acceptor chromophore at 5' and 3' site respectively.^[209] Typically, aminofluorescein (FAM) is employed as donor ($\lambda_{exc} = 492$ nm, $\lambda_{em} = 516$ nm) and carboxytetramethylrhodamine (TAMRA) as acceptor species.^[210] In contrast to the absorbance measurements, the FRET melting assay can avoid the superimposition of the UV bands, as just the signal of the tag is monitored.

Melting experiments can be performed by following the changes of the fluorescence intensity, as the distance between the chromophores increases with temperature. In the folded G4 conformation, the chromophores are placed

at a distance for which the fluorescence energy transfer is allowed and hence no FAM fluorescence is observed (TAMRA is non-emissive). On the contrary, in the unfolded structure the two chromophores are distant and the FAM fluorophore can emit light upon excitation (Figure 2.2).

The addition of a binding molecule can affect the melting temperature and the ΔT_m can provide significant information on the nature and strength of the interaction, as previously described for UV melting experiments (Paragraph 2.1.2).

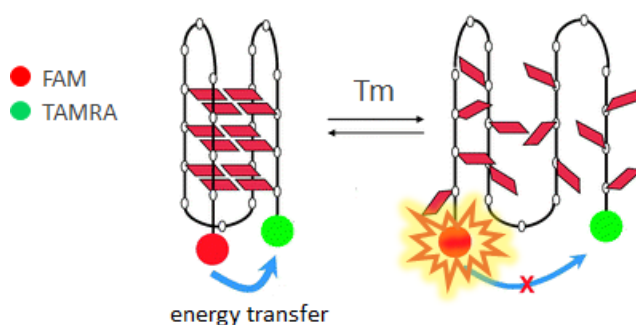


Fig. 2.2. Schematic representation of labelled G4 melting process (adapted from P. Murat, 2011)^[211]

The FRET measurement is carried out by means of Real Time PCR machines.^[206] This approach enables the simultaneous analysis of 96 independent samples to be performed. Different C_D/C_P ratios can be explored and each condition can be easily tested in replicate, guaranteeing the reliability of the results. Moreover, different biotargets can be tested at the same time, enabling the ligand's selectivity to be rapidly evaluated.

This technique conveniently requires small amounts of sample, typically 25 μL , at very low concentrations within the order of $10^{-7} - 10^{-6}$ M. Nevertheless, the labelled oligonucleotides are very expensive and the low concentrations might not lead to the formation of appropriate amounts of adduct in presence of scarcely affine ligands.

2.1.6 Circular dichroism spectroscopy

The binding features of non-covalent adducts between nucleic acids and small ligands can be also characterized by means of chiroptical spectroscopies. Linear dichroism (LD),^[212] fluorescence detected circular dichroism (FD CD)^[213] and circularly polarized luminescence (CPL)^[214] have been exploited for this purpose.

Within the aim of this work, we have considered the use of electronic circular dichroism spectroscopy (ECD, or simply CD).

Circular dichroism is defined as the difference between the absorption of left and right circularly polarized lights (A^l and A^r , respectively) (Equation 2.9).^[215]

$$\text{CD} = A^l - A^r \quad (2.9)$$

The definition of Equation 2.9 immediately suggests that CD is a signed quantity because A^l can be larger or smaller than A^r .

A useful derived quantity is the *g-factor*, called anisotropy or dissymmetry factor, defined as follows (Equation 2.10):

$$g = \frac{A^l - A^r}{A} = \frac{\Delta\varepsilon}{\varepsilon} \quad (2.10)$$

where A represents the conventional absorbance of non-polarized light.

Note that g is independent on the dye concentration and on the path length of the cell.

Differences in absorption between left and right circularly polarized lights were firstly observed in 1895 by *A. Cotton* during his studies on Cu(II) and Cr(III) coordination compounds.^[216] The basic theory of circular dichroism spectroscopy was then presented by *L. Rosenfeld* in 1928, who showed that, in order to understand the optical activity, it was not sufficient to consider only the electric transition dipole as in absorption.^[217]

Although the description of the interaction between light and matter goes far beyond our purpose, it is useful to recall that for each electronic transition one can define an electric and a magnetic transition dipole. They are related to the electron cloud redistribution taking place during the transition: if the initial and the final states are labelled as i and j respectively, a linear charge displacement leads to a non-vanishing electric transition dipole $\vec{\mu}_{ij}$, whereas a rotation of electrons induces a magnetic transition dipole \vec{m}_{ij} .^[218]

For chiroptical spectroscopies both the dipole moments play a crucial role: only electronic transitions associated with non-orthogonal $\vec{\mu}_{ij} \neq 0$ and $\vec{m}_{ij} \neq 0$ can provide CD signals, according to the *Rosenfeld* equation (Equation 2.11). The scalar product of the electronic and the magnetic transition dipoles

is proportional to the intensity of the CD and is defined as *rotational strength* R_{ij} .

$$R_{ij} = \int \Delta\epsilon d\nu = \vec{\mu}_{ij} \times \vec{m}_{ij} \quad (2.11)$$

The simplest source of CD signal is therefore represented by an electronic displacement through a helical path.^[219]

The rotational strength results to be non-vanishing only for chiral chromophoric molecules. Chiral molecules may absorb left and right circularly polarized light with different extents and two enantiomers are characterized by opposite CD signs with the same intensities.

In addition, it should be considered that CD is sensitive not only to the absolute configuration, but also to conformational features. Perturbations on the microenvironment of the chromophore can affect position, intensity and sign of the CD signal.^[220]

Circular dichroism is widely exploited for structural studies on non-racemic chiral systems, including biopolymers such as proteins and nucleic acids.

Concerning nucleic acids, the nucleobases are achiral and only small chiral perturbations arise from the sugar-phosphate backbone. However, the helical conformation of the polynucleotides introduces chirality, especially for double stranded DNA and RNA whereby the helical axis is almost perpendicular to the base pairs plane.^[221]

In this situation, CD derives from the so-called exciton coupling mechanism between the various $\pi \rightarrow \pi^*$ transitions of the regularly arranged nucleobases. Generally, this phenomenon can arise when two chromophores with strong transition dipoles are located near in space and their electric transition dipoles possess a skewed mutual orientation (not coplanar or collinear).^[220] The

dipolar coupling can concern either degenerate/near-degenerate electronic transitions (equal chromophores as for the DNA itself) or non-degenerate transitions (different chromophores) (Figure 2.3).

As a consequence of the degenerate coupling, the two otherwise degenerate excited states split into two levels divided by a discrete quantity, called *Davydov* splitting. The splitting in the excited states results in a bisignate CD signal in which the crossover point is centred in correspondence of the chromophore's transition. The sign of the CD couplet (which is defined as the sign of the low-energy component) is determined by the mutual orientation of the electric transition dipoles, whereas the intensity depends on the interchromophoric distance as well as on the dipole strength.

In the case of B-DNA, exciton coupling gives rise to a positive band at approximately $\lambda = 280$ nm and a negative one at $\lambda = 245$ nm.^[221]

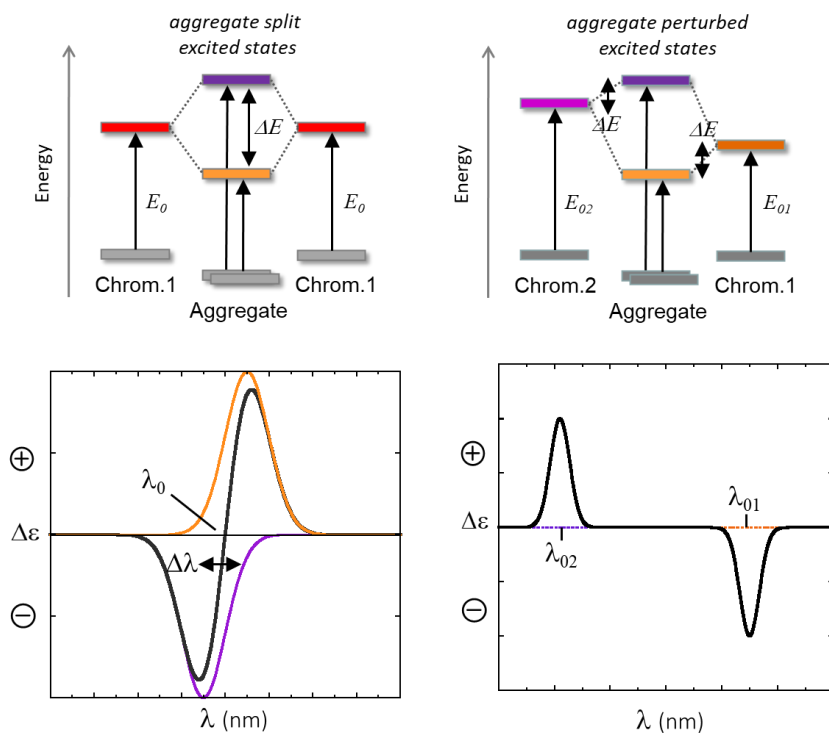


Fig. 2.3. Exciton couplet mechanism in its degenerate (left) and non-degenerate (right) version (T. Smidlehren et al., 2018)^[222]

As the polynucleotide secondary structure is possibly affected by the binding of small molecules, analysis of its typical CD bands can provide information on the binding features and strength.

Small DNA binders often possess achiral chromophores and thus do not exhibit any CD in solution. However, their interaction with chiral systems, such as polynucleotides and proteins, may produce induced CD signals (ICD) centred on the achiral ligand transitions (Figure 2.4).^[223]

ICD can arise from the non-degenerate exciton coupling between the electric transition dipoles of the ligand and the polynucleotide base pairs.^[224] ICD is

therefore sensitive to the orientation of the transition dipole of the dye with respect to that of the nucleobases. However, a general correlation between ICD and binding mode it is not easy to obtain because many factors can affect the appearance of the signal.

P. E. Schipper et al. (1980) proposed a model that directly correlates the ICD sign and the degree of alignment between the ligand and the DNA helix axis plane.^[225] For an intercalator with a transition dipole oriented along its long axis, the ICD signal is typically positive if the ligand transition dipole is oriented parallel to the long axis of the adjacent base pairs and negative if perpendicular.^[226] In general, the magnitude of ICD in an intercalator is relatively low, with a $|\Delta\epsilon|$ less than $10 \text{ M}^{-1}\text{cm}^{-1}$.^[148] Intercalation into polyG·polyC was found to induce a negative ICD signal of approximately $\Delta\epsilon = -10 \text{ M}^{-1}\text{cm}^{-1}$ for tetrakis(4-N-methylpyridyl)-porphine.^[227]

It should be noted that, in the case of complex molecules bearing different intercalating moieties, decreasing CD amplitudes are expected because these intercalators will probably assume different orientations around the helix axis and the rotational strength averages to zero for random distributions.^[228]

In the case of groove binding, the model is different and more complex than that used for intercalation, as the mutual orientation of the transition dipoles is described by two angles: (I) that between the transition moment and the helix axis and (II) that between the projection of the dipole on the plane perpendicular to the helix axis and the distance vector.^[148]

Despite this complexity, if the transition moment of the ligand is oriented along a groove forming an angle of approximately 45° with the bases, then the ICD is expected to be positive.^[222] The intensity and sign of the ICD signal for a ligand bound in the major groove is more variable because of the greater number of possible orientations permitted by the width of the major groove. Generally, the ICD of groove binders is an order of magnitude higher than that

of intercalators.^[224] For example, the common groove binder DAPI was found to show a strong positive band centred at $\lambda = 365$ nm when bound to DNA.^[214] Interactions with the negative phosphate backbone do not significantly disturb the secondary structure of the polynucleotides, so that CD signals are almost unaffected by a purely electrostatic binding. However, ICD signals can also be observed as a result of the supramolecular chirality (chiral orientation relative to each other) induced by the helical structure, which gives rise to a degenerate exciton coupling among the ligand molecules.^[229] This is generally taken as an evidence of external stacking, although it can be also observed as a consequence of interactions between ligands intercalated into adjacent base pairs. The positive couplet (negative band at $\lambda = 430$ nm and positive band at $\lambda = 475$ nm) observed for proflavine in presence of DNA was for example interpreted as an exciton effect due to the presence of dye-dye aggregation on the DNA surface.^[230] The positive couplet (negative band at $\lambda = 468$ nm and positive band at $\lambda = 510$ nm) of acridine orange were instead thought to be induced from the interaction between dye molecules bound to adjacent DNA binding sites.^[231]

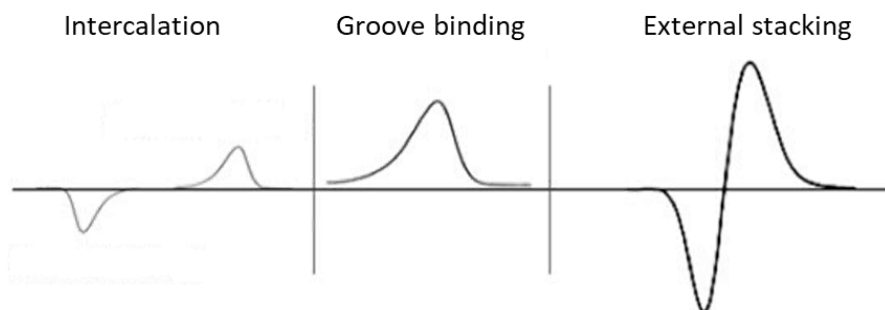


Fig. 2.4. Overview of ICD expected for the principal binding modes (T. Biver, 2012)^[148]

On the whole, chiroptical spectroscopies are particularly useful thanks to the specificity of the chiroptical response. By one side, the induced CD signal is sensitive only to the complex and ensures the formation of the adduct. On the other hand, the polynucleotide CD signal is not affected by the contribution of the free ligand. This is in contrast to UV-Vis absorbance spectra, in which both the bound and unbound ligand provide detectable signals, usually in similar regions of the spectrum.

2.2 Proteins binding studies

The binding of small molecules to proteins is commonly investigated, as proteins are involved in several important biological functions. Biomedical studies are often performed *in vivo*,^{[232],[233]} but the availability of lyophilized proteins enables *in vitro* experiments to be performed.

Among others, bovine serum albumin represents the most common model protein used for binding studies, thanks to the low cost and the analogy to human serum albumin.

Many solution-equilibria techniques as for instance differential scanning calorimetry (DSC),^[234] equilibrium dialysis,^[235] liquid chromatography,^[236] electrophoresis^[237] and ultrafiltration^[238] methods are typically employed for studying the binding affinity. Furthermore, the optical properties of the protein can conveniently be exploited for the application of affordable and easy-to-use spectroscopic techniques. Besides absorbance^[239] and circular dichroism^[240] spectroscopies, fluorescence experiments represent a very popular approach. This is our focus on this work.

2.2.1 Fluorescence quenching experiments

If the ligand molecule possesses its own fluorescence band in the visible range, far away from the BSA range, spectrofluorimetric titrations can be conveniently performed by following the dye's signal, as a BSA excess can be added with no inner-filter problem on the recorded emission. Unfortunately, it often occurs that the ligand is a non-fluorescent species with absorbance in the UV-range only. This is true for instance in the case of a plenty of metal complexes that deserve high biomedical interest.^[241]

Under these circumstances the signal to be followed is necessarily that of BSA fluorescence. Fluorescence emission properties of BSA are provided by the presence of tryptophan, tyrosine and phenylalanine aminoacids. As the relative ratio of fluorescence intensity for these residues has found to be Trp : Tyr : Phe = 100 : 9 : 0.5, it is likely that the emission of BSA mainly arises from the two tryptophan residues (Trp134 and Trp 212).^[242]

By exciting the system at $\lambda_{\text{exc}} = 280$ nm, the fluorescence is mainly contributed by Trp and Tyr residues, whereas only Trp residues are excited at $\lambda_{\text{exc}} = 295$ nm.^[243] The emission spectrum of BSA broadens from $\lambda_{\text{em}} = 300$ nm to $\lambda_{\text{em}} = 450$ nm with a maximum at approximately $\lambda_{\text{em}} = 345$ nm.

The fluorescence can be quenched by a ligand when the distance between the ligand and the protein's fluorophore is smaller than 10 nm.^[108]

Therefore, in order to study the interaction between small molecules and BSA, spectrofluorimetric titrations are commonly performed. A decrease in the fluorescence intensity of BSA upon the addition of ligand may indicate that the interaction does occur. Moreover, shifts in the emission maximum are related to changes in the hydrophobicity of the environment around the tryptophan residues.^[244] No change in the position of the emission signal indicates no alteration in the local dielectric environment of BSA.^[245]

Note that the inner filter effects previously described for the nucleic acids binding studies might affect the quenching measurements as well and should be carefully taken into account. Also, light emission decrease is non-necessarily an indication of a ligand-BSA interaction. It is worth recalling that fluorescence quenching can be due to the formation of ligand-protein complexes with lower fluorescence yields, but the fluorophore can also return to the ground state due to diffusive collisions with the quencher and in this case the molecules are not chemically altered.^[192] Note that complex formation is usually the main contributor to what is called static quenching, as well as collisional quenching is the main process in dynamic quenching. However, the picture is complicate and the exact equivalence complex/static and collision/dynamic is not straightforward (for a detailed discussion, out of the scope of the present text, refer for instance to ^{[246],[247]}).

The quenching process can be described by using the *Stern-Volmer* equation (Equation 2.12):^[247]

$$\frac{F_0}{F} = 1 + k_q \tau_0 [Q] = 1 + K[Q] \quad (2.12)$$

where F_0/F corresponds to the ratio between the BSA fluorescence intensity in the absence and in the presence of the quencher respectively (F values must be corrected for the dilution contribution and, if necessary, for inner filter effects), $[Q]$ is the total molar concentration of the quencher (ligand), k_q is the bimolecular quenching constant, τ_0 corresponds to the average lifetime of the protein in the absence of quencher. It is known that the average life-time of a protein is within the nanosecond order.^[248]

The slope K represents the *Stern-Volmer* constant: in the case of ground-state complex formation, K is called K_{SV} and corresponds to the equilibrium

constant for the formation of the complex, but only if the adduct is not fluorescent at all.^[249] Moreover, [Q] needs to be considered as [Q_{free}] (the molar concentration of free quencher). The correct use of the amount of quencher added is a check that is not considered in many papers and that may produce biased results. C_Q (total molar concentration of the quencher added) is not necessarily equal to [Q_{free}] and they will coincide only in the presence of Q excess.

Linear correlation of F₀/F and [Q] indicates that only one type of quenching is involved, whereas upward curving *Stern-Volmer* plots reveal the concomitant contribution of both static and dynamic quenching processes.^[250] The *Stern-Volmer* equation can be thus modified as Equation 2.13:

$$\frac{F_0}{F} = (1 + K_s[Q])(1 + K_d[Q]) \quad (2.13)$$

where K_s and K_d are the quenching constants for the static and the dynamic quenching respectively.

Downward curvatures in the *Stern-Volmer* plots can instead occur when a system contains fluorophores within different environments or binding sites with different accessibility to the quencher.^[251] The modified *Stern-Volmer* (or *Lehrer*) equation can be expressed as follows (Equation 2.14):^[252]

$$\frac{F_0}{\Delta F} = \frac{1}{f_a K_{SV}[Q]} + \frac{1}{f_a} \quad (2.14)$$

where ΔF corresponds to the difference between the fluorescence intensity in absence and in presence of quencher (F₀ – F) and f_a is the fraction of initial fluorescence that is accessible to the quencher (Q).

Different quenching types are characterized by different typical values of the bimolecular quenching constants k_q . As the collisions between solvated species are limited by the diffusion coefficient of the medium, a constant value of $k_q = 1 \div 3 \times 10^{10} \text{ M}^{-1}\text{s}^{-1}$ is considered as the largest possible value for collisional quenching in aqueous solution.^[253] On the other hand, the average life-time of a protein is in the nanosecond order:^[192] for tryptophan in BSA $\tau_0 = 7 \text{ ns}$.^[254] This means that, roughly, $k_q\tau_0 \leq 200$. Even if supposing that this threshold may undergo some distortion in very peculiar conditions,^{[255],[256]} a slope of *Stern-Volmer* plots of 1000 or even higher would necessarily be related to the presence of some non-collisional quenching. Therefore, high values of the slope of the Stern Volmer's plot indicate complex formation.^{[257],[258],[259]}

The anticancer agent diacetyl malsinic acid was found to bind BSA and $K_{SV} = 2.56 \times 10^3 \text{ M}^{-1}$.^[260] Complex formation was also proved for dyes such as malachite green ($K_{SV} = 5.45 \times 10^4 \text{ M}^{-1}$)^[123] and congo red ($K_{SV} = 1.92 \times 10^5 \text{ M}^{-1}$).^[122] K_{SV} values from 1.5 to $2.0 \times 10^5 \text{ M}^{-1}$ were found for hydrazone complexes of Ni(II), Co(II) and Cu(II) with significant antioxidant activity.^[261] The potential therapeutic agent N'-(2-hydroxynaphthalenemethylene)-4-(2-hydroxynaphthalenemethylenamine)benzoylhydrazine-Zn(II) complex binds BSA with K_{SV} of $3.6 \times 10^5 \text{ M}^{-1}$, whereas K_{SV} values ca. $1 \times 10^5 \text{ M}^{-1}$ were observed for the antitumoral Zn(II) dinuclear complexes with polypyridyl ligands.^[262] Platinum(II) and palladium(II) complexes containing adamantane weakly bound to BSA with K_{SV} values from 2 to $9 \times 10^3 \text{ M}^{-1}$.^[263]

Complex formation and collisional-only quenching can be also distinguished by their different dependence on temperature, viscosity of the medium^[250] or by life-time measurements.^[264] From the point of view of this work, only the former case will be taken into account. The titrations have thus to be repeated

at different temperatures and the obtained *Stern-Volmer* constant's values have to be compared. Higher temperatures result in faster diffusions and hence larger amounts of collisional events. K increase with temperature indicates collisional quenching.^[265] On the contrary, dissociation of weakly bound complexes is typically promoted by higher temperatures. Smaller amounts of quenching are observed and thereby K_{SV} values decrease when the temperature increases.^[266]

If complex formation is confirmed, the relevant thermodynamic parameters can be calculated by the modified *Scatchard* equation (Equation 2.15):^[267]

$$\log \frac{F_0 - F}{F} = \log K + n \log [Q] \quad (2.15)$$

where K_b is the binding constant and n is the number of the binding sites.

Generally, the binding of a ligand to serum albumins should be strong enough to ensure that a significant amount of adduct is actually formed but, simultaneously, weak enough to permit the ligand's release once the biotarget is reached. Such optimal K_b range is considered between 10^4 and 10^6 M^{-1} .^[242] For example, the aromatic dye p-aminobenzene was found to bind BSA with $K_b = 8.89 \times 10^4 \text{ M}^{-1}$,^[268] whereas for the flavonoid hesperdin a binding constant of $K_b = 5.15 \times 10^4 \text{ M}^{-1}$ was observed.^[269] Anticancer drugs such as gefitinib, lapatinib and sunitinib bind BSA with a binding constant value of $8.32 \times 10^4 \text{ M}^{-1}$, $2.24 \times 10^5 \text{ M}^{-1}$ and $1.32 \times 10^5 \text{ M}^{-1}$ respectively.^[133]

The number of involved binding site is usually $n = 1$. If this does occur, other equations based on a 1:1 complex model can be exploited for the calculation of the binding constant. *Hildebrand-Benesi* equation (see also Paragraph 2.1.1 and Appendix I) is expressed as follows (Equation 2.16):

$$\frac{C_{\text{BSA}}}{\Delta F} = \frac{1}{K_b \Delta\phi} \cdot \frac{1}{[Q]} + \frac{1}{\Delta\phi} \quad (2.16)$$

where C_{BSA} is the molar concentration of protein, K_b is the binding constant, $\Delta\phi$ represent the difference between the fluorescence coefficient of BSA and the ligand-BSA adduct and $[Q]$ is the molar concentration of the free quencher (ligand).

2.2.2 Competitive fluorescent displacement for binding site determination

It is worth recalling that serum albumin possess two main binding site: site I, is situated in the hydrophobic pocket of subdomain IIA, and site II, located into the hydrophobic cavity of subdomain IIIA (Chapter I, Paragraph 1.3.2).^[112] In order to determine the preferential binding site of the studied ligands, competitive spectrofluorometric studies are usually performed. In the most simple approach, firstly the protein is saturated with a specific probe. Phenylbutazone^[270] and warfarin^[271] are often used to mark BSA at site I, whereas ibuprofen,^[270] diazepam and flufenamic acid^[272] for site II. Displacement experiments are then carried out by adding increasing amounts of the ligand to the labelled-BSA solutions.^[133] The equilibrium constant for binding to BSA alone, probe I-BSA and probe II-BSA are thereby compared. Significant variations of K_b for the free and the marked protein indicate that the ligand and the probe compete for the same binding site, therefore this can be determined. Just to cite few examples, berberine selectively binds BSA at site I^[106] as well as chlorpyrifos,^[120] whereas repaglinide was found to compete with ibuprofen for site II;^[113] other noticeable examples are cited in Chapter I (Paragraph 1.3.2, Table 1.1).

The qualitative meaning of such a practical comparison is quite straightforward, however these experiments may not be as simple as it might seem at first sight. The detailed analysis of the exchange process needs more complicated solution equilibria studies.^{[273],[274]} Also, experimentally, the addition of high amounts of quencher may produce too high bias in the measured fluorescence (which is often already lowered by the addition of the probe) if the already discussed inner filter effects are strongly at play. Another critical point, which is often not well described in many papers, concerns the details and rationale of the probe-BSA mixture preparation. A robust estimation of values to be used as binding constant is not easily found in the literature, given the different experimental conditions/buffers together with different techniques and mathematical equations used.^[275] Under diluted conditions for both BSA and probe concentrations (often 1-10 μM range), the percentage of probe-BSA complex formation could be low. Thus, being most of the target sites still free, the exchange experiment might be less effective. The attentive preparation of the test would better first consider a titration of the probe-BSA system under the same experimental conditions used for the subsequent addition of the studied ligand. The binding affinity for both single probe-BSA and ligand-BSA systems will be known and a high percentage of site labelling can be ensured. Species distribution diagrams confirming probe-BSA complex formation (and describing the process for the addition of increasing amounts of ligand over a certain range) can be a useful additional tool (software such as HySS^[276] are freely available online).

Chapter 3

3. Materials and methods

3.1 Materials

N,N0-bis(2-(1-piperaziny)ethyl)-3,4,9,10-perylenetetracarboxylic acid diimide dichloride (PZPERY) was received from the group of Prof. A. Pucci.^{[277],[278]} Briefly, perylene-3,4,9,10-tetracarboxylic dianhydride (PTCDA) (1 g, 2.55 mmol) was dissolved in 20 mL of 1-(2-aminoethyl)piperazine at 160°C and stirred for 22 h under nitrogen. After cooling to room temperature, the solution was treated with 100 mL of 2 M HCl. The dark violet solution was stirred for 12 h. The hydrochloride salt reaction products, precipitated in acetone, were separated by filtration and then washed thoroughly with distilled water until the pH of the washings was neutral. The dried product 1.3 g (1.92 mmol, yield: 75.6%) was a deep-red solid. PZPERY peripheral chains are composed by piperazine rings (first pKa = 9.1 – 9.2 for alkyl piperazines^[279]), that are considered fully charged in the selected physiological conditions.

FT-IR spectra were recorded with the help of a PerkinElmer Spectrum One spectrometer on dispersions in KBr. FT-IR: 2926 cm⁻¹ (νCH aliph), 1695, 1656, 1593 cm⁻¹ (νCO imide), 1508, 1441, 1401, 1362 cm⁻¹ (νCC ring).

¹H and ¹³C NMR spectra were recorded on Varian Gemini 200 MHz spectrometer at 20 °C. Samples were prepared using D₂O solutions containing 5–10% CF₃COOD (Aldrich, 99.5 atom% D). In the ¹H NMR spectrum, two doublets with the same coupling constant (J=15 Hz) were present at 8.8-8.9

ppm, and hence attributed to the aromatic protons of PZPERY. In the lower spectral region, two multiplet signals were recognized and attributed to CH₂ groups of the linking chain adjacent to the PDI moiety (Nimm-CH₂, 4.7-4.9 ppm) and near the piperazine fragment (Npip-CH₂, 4.4-4.5 ppm). Remaining multiplet signal integrating for 16 protons was assigned to piperazine moiety ring protons (4.0 ppm). In the ¹³C NMR spectrum, signals at 31.2, 37.8, 45.5, and 52.8 ppm were attributed to carbon nuclei of CH₂ groups, while signal at 117.5, 120.4, 122.5, 125.4, 129.3, and 132.5 ppm to carbons belonging to the central aromatic core. Carbons of the carbonyl function (imide) was clearly identified at 162.5 ppm.

Elemental analysis: calcd. (C₃₆H₃₈Cl₂N₆O₄): 62.9% C, 5.3% H, 12.2% N; found: 63.5% C, 5.7% H, 12.4% N.

Solid **Alcian Blue-tetrakis(methylpyridinium) chloride** (ABTP, purity ≥ 85%) was purchased from Sigma, as well as **copper phthalocyanine-3,4',4'',4'''-tetrasulfonic acid tetrasodium salt** (CuPCTS, purity ≥ 85%). Stock solutions (ca. 1 mM) were prepared by dissolving known amounts of the solid in water.

1,2-bis{4-[(triethylammonium)butoxy]phenyl}-1,2-tetraphenylethene dibromide (BTATPE) was synthesised in collaboration with Prof. A. Pucci, through a McMurry coupling on 4-(4-bromobutoxy)benzophenone, followed by a quaternization reaction with trimethylamine (see Chapter VI, Paragraph 4.2).

Paraquat dichloride hydrate (PQ, purity ≥ 98%) and **diquat dibromide monohydrate** (DQ, purity ≥ 95%) were supplied by Sigma. Stock solutions (ca. 1 mM) were obtained by dissolving known amounts of the solid in water.

Calf thymus DNA (from now on ct-DNA or simply DNA) is the most commonly used DNA extracted from *calf thymus* tissue and consists of 41.9 mol % G–C and 58.1 mol % A–T base pairs.^[280] Lyophilised sodium salt from Sigma-Aldrich was dissolved in water and sonicated (MSE-Sonyprep sonicator, 7 cycles of 10 s sonication + 20 s pause at an amplitude of 14 μm , solution kept in ice bath).^[281] Gel electrophoresis was used to determine the length of the fragments, being approximately 500 base pairs (100 bp DNA ladder is used as the reference). Stock solutions of ct-DNA were standardized spectrophotometrically ($\epsilon = 13200 \text{ M}^{-1}\text{cm}^{-1}$ at $\lambda = 260 \text{ nm}$, $I = 0.10 \text{ M}$, $\text{pH} = 7.0$);^[282] concentrations of ct-DNA are expressed in molarity of base pairs.

Dried DNA oligonucleotides, labelled as **Tel23**, **CTA22** and **c-myc** (sequences reported in Table 3.1), were purchased from Metabion for the G-quadruplexes (G4s) binding tests. Stock solutions (ca. 1 mM) were prepared in 2.5 mM lithium cacodylate (LiCac) buffer containing 0.1 M KCl at $\text{pH} = 7.0$. The formation of the G4 structures was carried out by heating the oligonucleotide solutions up to 90°C for 6 min and slowly cooling down to room-temperature. The solutions were then stored overnight at 4°C .

Lyophilised **doubly marked oligonucleotides** (aminofluorescein (FAM) as donor fluorophore, carboxytetramethylrhodamine (TAMRA) as acceptor fluorophore) were provided by Eurogentec. Their sequences are reported in Table 3.1. 100 μM stock solutions were prepared in water. Appropriate amounts of stock solutions were annealed in lithium cacodylate buffer at $\text{pH} 7.4$ supplemented with potassium, in order to obtain work solutions 0.2 μM in 10 mM KCl + 90 mM LiCl + 10 mM LiCac.

Tab. 3.1. Sequences of the oligonucleotides used in the present study (*F* = FAM probe, *T* = TAMRA probe)

Name	G4 Type/origin	Tetrads	Sequence (5' to 3')	Ref
Tel23	hybrid DNA human telomere	3	TAGGGTTAGGGTTAGGGTTAGGG	[81]
CTA22	antiparallel DNA human telomere	3	AGGGCTAGGGCTAGGGCTAGGG	[80]
cmyc	proto-oncogen	3	dTGAGGGTGGGTAGGGTGGGTAA	[283]
dx	DNA intramolecular duplex	3	F-TATAGCTAT-hexaethyleneglycol- TATAGCTATA-T	
Tel21	hybrid DNA human telomere	3	F-GGGTTAGGGTTAGGGTTAGGG-T	[284]
RTel21	parallel RNA human telomere	3	F-GGGUUAGGGUUAGGGUUAGGG-T	
CEB25	parallel DNA minisatellites	3	F- AAGGGTGGGTGTAAGTGTGGGTGGGT- T	[285]
CTA21	antiparallel DNA human telomere	3	F-GGGCTAGGGCTAGGGCTAGGG-T	[80]
TBA	antiparallel DNA aptamer	2	F-GGTTGGTGTGGTTGG-T	[286]
BOM17	antiparallel DNA <i>bombyx</i> telomere	2	F-GGTTAGGTTAGGTTAGG-T	[93]

Polydeoxyguanylic·polydeoxycytidylic (polyG·polyC) and **polydeoxyadenylic·polythymidylic** (polyA·polyT) acids were provided by Merck as sodium salts. Stock solutions ca. 1 mM were prepared in water by weighting and dissolving knowing amount of solid.

Polyriboadenylic·polyriboutydylic (polyA·polyU) and **polyribouridylic** (polyU) acids were purchased from Sigma as potassium salts and stock solutions ca. 1 mM were prepared by dissolving suitable amounts of solid in water. The standardization of the synthetic RNA stock solutions was attained spectrophotometrically ($\epsilon = 14900 \text{ M}^{-1}\text{cm}^{-1}$ at $\lambda = 260 \text{ nm}$ for polyA·polyU and $\epsilon = 8900 \text{ M}^{-1}\text{cm}^{-1}$ at $\lambda = 260 \text{ nm}$ for polyU, at $I = 0.1 \text{ M}$, $\text{pH} = 7.0$).^[287]

PolyA·2polyU was obtained in buffer by quantitative reaction between equimolar amounts of polyU and polyA·polyU.^[288] The analytical concentration of polyU, polyA·polyU and polyA·2polyU are expressed in molarity of single bases, base pairs and base triplets respectively.

Bovine serum albumin (BSA) was provided by Sigma-Aldrich as crystallized and lyophilized powder ($\geq 98 \%$, agarose gel electrophoresis and $\leq 0.005 \%$ fatty acids). Known amounts of lyophilised solid were dissolved in water and the molar concentration of the protein (ca. 0.1 mM) was determined by measuring light absorption using absorptivity ($\epsilon = 45000 \text{ M}^{-1}\text{cm}^{-1}$ at $\lambda = 278 \text{ nm}$).^[289]

Phenylbutazone (from Sigma) and **ibuprofen** (from Sigma) were employed respectively as binding site I and II markers for protein BSA. Stock solutions of approximately 1 mM were prepared by weighting and dissolving known amounts of solid in ethanol.

Concerning the MEUF experiments, **sodium dodecyl sulphate** (SDS – from Sigma), was dissolved in water to obtain 0.2 M stock solution ($\text{CMC} =$

$8.0 \times 10^{-3} \text{ M}^{[290]}$). **Dodecyl trimethyl ammonium chloride** (DTAC - from Fluka) was also dissolved in water to obtain 0.2 M stock solution (CMC = $1.0 \times 10^{-2} \text{ M}^{[291]}$). **TritonX-100** (Merck) 0.2 M stock solution was prepared by appropriate dilution of the pure liquid in water (CMC = $2 \times 10^{-4} \text{ M}^{[291]}$). Working solutions of any surfactant were well all above the critical micellar concentration. **1-palmitoyl-2-oleoyl-sn-glycero-3-phosphocholine** was purchased from Sigma-Aldrich and liposomes solutions were prepared as discussed in Chapter 3.2.7.

The experiments were usually performed under physiological conditions at 0.1 M NaCl for ct-DNA, synthetic RNA and BSA, while 0.1 M KCl was used for G4s. Sodium cacodylate ($(\text{CH}_3)_2\text{AsO}_2\text{Na}$ (NaCac) 2.5 mM was the pH = 7.0 buffer, whereas lithium cacodylate ($(\text{CH}_3)_2\text{AsO}_2\text{Li}$ (LiCac) was employed in the presence of G4 structures. Ultra-pure grade water from a SARTORIUS Arium-pro water purification system was used as reaction medium. All reactants not specifically mentioned were analytical grade and were used without further purifications. The stock solutions of every reactant were stored in the dark at 4°C or -20°C and the stability was always checked.

3.2 Experimental methods

3.2.1 Spectrophotometric and spectrofluorimetric titrations

A *Shimadzu UV-2450* and a *Perkin Elmer Lambda 35* double ray spectrophotometers were used to record absorption spectra and to perform spectrophotometric titrations. Both the instruments were equipped with a tungsten lamp for the visible light and a deuterium lamp for the UV range.

The fluorescence experiments were carried out by employing a *Perkin Elmer LS 55* spectrofluorimeter. The excitation light is provided by a pulsed Xenon lamp (50 Hz).

The instruments were equipped with jacketed cell holders, providing temperature control to be within $\pm 0.1^\circ\text{C}$. The measurements were performed by employing quartz cells of minimum content needed equal to 500 μL or 1000 μL , with an optical path length of 1.0 cm.

In the spectroscopic titrations, increasing amounts of the titrant were added directly in the cuvette containing the dye and a spectrum was recorded upon each addition. The precise and accurate addition of very volumes was done owing to a glass syringe connected to a Mitutoyo micrometric screw (one complete turn of the screw is 8.2 μL , 1/50 of a turn is the minimum possible addition).

3.2.2 UV melting experiments

The thermal denaturation processes were followed with the help of a *Shimadzu UV-2450* spectrophotometer communicated with a Peltier thermostat. The melting experiments were carried out by heating the working solution (different concentrations depending on the substrate) from 25°C to 90°C with a scan rate of $+5^\circ\text{C}/\text{min}$ every 6.5 minutes. After keeping the temperature constant for 6.5 min to allow the system reach the equilibrium, an absorbance spectrum was recorded.

Thermal denaturation plots were obtained by monitoring absorbance changes at fixed wavelengths; the melting temperature (T_m) was extrapolated as the inflexion point. Duplex DNA and RNA denaturation was investigated by considering the absorbance at $\lambda = 260 \text{ nm}$, whereas quadruplex melting was

followed at $\lambda = 295 \text{ nm}$.^[186] The difference between T_m of ligand+polynucleotide and T_m of the polynucleotide alone represents the ΔT_m value. The experiments were repeated at different ligand/polynucleotide ratios.

In order to evaluate the reversibility of the denaturation process, further experiments were performed by cooling down the heated solution from 90°C to 25°C with a scan rate of $-5^\circ\text{C}/\text{min}$ every 6.5 minutes.

3.2.3 FRET melting experiments

FRET melting experiments on G4s were carried out with a 7500 Real Time PCR System (Applied Biosystems). G4 oligonucleotides were labelled in 5' position with FAM as donor molecule and in 3' position with TAMRA as acceptor molecule.

The sigmoidal fit of normalised FAM fluorescence against temperature provides the melting temperature as the inflexion point of the curve. H_2O and was used for control experiments.

Experimentally, 8-well optical tube strips were filled with $25 \mu\text{L}$ each ($20 \mu\text{L}$ G4 + $5 \mu\text{L}$ ligand) providing G4 and ligand concentrations to be $0.2 \mu\text{M}$ and $2 \mu\text{M}$ respectively ($C_D/C_P = 10$). The sample were heated from 25°C up to 95°C at $1^\circ\text{C}/\text{min}$ rate. FAM fluorescence intensity ($\lambda_{\text{exc}} = 492 \text{ nm}$, $\lambda_{\text{em}} = 516 \text{ nm}$) was recorded every 0.4°C . The experiments were performed in 10 mM KCl + 90 mM LiCl + 10 mM LiCac.

3.2.4 Circular Dichroism

CD spectra were recorded on a MOS-450 spectrophotometer (Bio-Logic SAS, Claix, France) with a xenon light source. Equal amounts of left and right circularly polarized light of a selected wavelength are alternately radiated on the sample with a frequency of 50 kHz. The read is provided as molar ellipticity. The measurements were performed at $T = 25.0 \pm 0.1$ °C, using 1.0 cm path-length cells. The buffer baseline was collected and subtracted from each sample spectra.

In the CD titrations, increasing amount of the ligand were added directly into the cell containing the biosubstrate and a CD spectrum was recorded for each step.

3.2.5 Isothermal Titration Calorimetry

The Isothermal Titration Calorimetry (ITC) experiments were performed with a Nano ITC (TA Instruments, Newcastle, USA). The instrument is composed of two identical cells (sample and reference) enclosed into an adiabatic jacket (Figure 3.1). An automatic syringe provides the addition of the titrant directly into the sample cell. The equipment measures the amount of thermal energy per second (J/s or W) required to keep the two cells at the thermic equilibrium ($\Delta T = 0$) during the whole experiment. The experimental raw data consists of a series of spikes of heat flow, with every spike corresponding to one titrant injection.

Working solutions were degassed for 30 min in a degassing station (TA, Waters LLC, New Castle, USA) in order to avoid the formation of bubbles during the titrations. The reference cell was filled with degassed solvent. Approximately every 300 s the syringe injected the ligand (25 injections of

2.02 μL) into the sample cell (187 μL) containing the polynucleotide solution in buffer. The temperature was set up at $T = 25.0^\circ\text{C}$ and the stirring speed was maintained constant at 250 rpm. Control experiments were carried out in order to subtract the contribution of the dilution heat of the ligand.

The resulting thermograms (integrated area of the calorimetric peak normalized for the moles of injectant vs. $[\text{ligand}]/[\text{polynucleotide}]$ ratio) were treated with a model equation for an independent mode of binding using the Nano Analyze Software (TA Instruments, New Castle, USA).

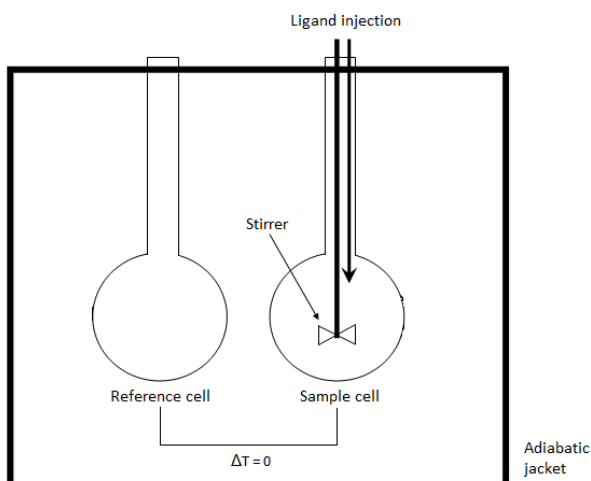


Fig. 3.1. Schematic representation of an ITC instrument
(<https://en.wikipedia.org/wiki/File:ITC1.png>)

3.2.6 Viscometry

The viscosity of the solutions was measured with an Ubbelohde viscometer immersed in a controlled temperature bath (Figure 3.2). The temperature was kept constant at $T = 25.0 \pm 0.1$ °C. 3.0 mL of ct-DNA solution approximately 2.0×10^{-4} M were introduced into the reservoir (A). The liquid was sucked in the measuring tube (B) with the help of an aspirating syringe, while the tube (C) was kept plugged. Once filled half of the second bulb, the tube (C) was opened. The solution flowed due to gravity through the capillary (D) and the flow time from the initial point (i) to the final point (f) was measured with a digital chronometer. Flow times of ligand/DNA mixtures at different C_D/C_P ratios were recorded by adding increasing volumes of ligand through tube (B) directly into the polynucleotide solution. The systems were carefully mixed by sucking and blowing the liquid inside tube (B). Control experiments were performed by adding the same volumes of buffer solution in order to take into account possible dilution contributions on the DNA viscosity. The flow time of the solvent was measured as well. All the measurements were repeated at least 5 times.

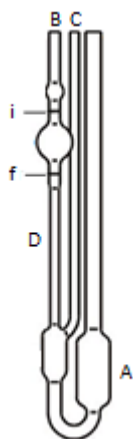


Fig. 3.2. Schematic representation of an Ubbelohde viscometer

The relative viscosity of the polynucleotide was calculated as follows (Equation 3.1, detailed description in Appendix IV):

$$\frac{\eta_{\text{sample}}}{\eta_{\text{reference}}} = \frac{t_{\text{sample}} - t_{\text{solvent}}}{t_{\text{reference}} - t_{\text{solvent}}} \quad (3.1)$$

where t_{sample} , $t_{\text{reference}}$ and t_{solvent} are respectively the observed flow times for the small molecule/DNA mixtures, DNA alone and the buffer solution.

The relative viscosity is connected to the polynucleotide elongation by Equation 3.2:

$$\frac{L}{L_0} = \left(\frac{\eta}{\eta_0}\right)^{\frac{1}{3}} \quad (3.2)$$

where L is the length of the bound polynucleotide and L_0 is the length of the free one.

3.2.7 Micellar Enhanced UltraFiltration

Ultrafiltration experiments were performed on 10.0 mL of an aqueous solution containing the analyte and the surfactant (at a concentration higher than the CMC), which was introduced in a 50 cm³ cell (Figure 3.3) and then stirred at 300 r/pm under a nitrogen pressure of 40 psi. The cell was equipped with a cellulose membrane (YM3, Millipore) of 4.5 cm diameter, with effective area 13.4 cm² and a molecular weight cut-off of 3000 Da. The membranes were treated and stored as recommended by Millipore. The ultrafiltration experiments were conducted in NaCl 0.1 M, NaCac 2.5 mM buffer at pH 7.0 and were repeated at least 3 times.

For liposomes preparation, known amounts of 1-palmitoyl-2-oleoyl-sn-glycero-3-phosphocholine (monomer) were dissolved in 10 mL methanol. The solution was dried under nitrogen stream, until the complete evaporation of the solvent. The obtained thin bilayer lipid film was hydrated by water addition of the buffer. The hydrated lipid sheets detached during agitation and self-closed to form large multilamellar vesicles (LMV). Liposomes stock solutions were stored at 4°C and employed without further purifications.

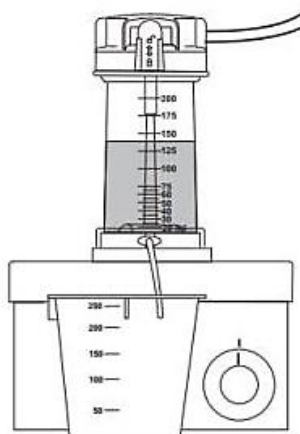


Fig. 3.3. Schematic representation of an ultrafiltration stirred cell
(<https://www.sigmaaldrich.com/technical-documents/articles/biology/amicon-stirred-cells.html>)

3.3 Computational methods

3.3.1 Time Dependent - Density Functional Theory (TD-DFT) calculations

All TD-DFT calculations were personally performed by using the Gaussian 16 package.^[292] The coordinates of ct-DNA are extracted from the PDB file 108D.^[293] The QM description was used for both the ligand and the DNA fragments constituting the pockets. The models used in the calculations represent: (I) a single molecule of ligand in water solution; (II) a system where the ligand is placed in the intercalation pocket of DNA.^[193] All geometry optimizations were performed without imposing constraints on the ligand, whereas, in the case of the intercalated system, the DNA structure was kept fixed.

The Integral Equation Formalism (IEF) version^[294] of the Polarizable Continuum Model (PCM)^[295] was used to describe the implicit effects of the solvent (water) both in the ground and in the excited state. PCM cavities were described as a series of interlocking spheres centred on atoms with universal force field (UFF) radii multiplied by a cavity size factor of 1.2. In the case of the intercalation pocket, a cavity size factor of 1.9 was used in order to fill the space between the base pairs in the double stranded DNA helix. Both absorption and emission energies in the PCM solvent were obtained within the corrected linear response (cLR) scheme.^[296]

The ground state structures of the ligand/DNA adduct were preliminarily optimized *in vacuo* by employing the semi-empirical method PM6 and then further refined using Density Functional Theory (DFT). The ground state geometry optimizations were performed using the B3LYP functional and the 6-31G(d) basis set. The excited state geometries and the absorption and

emission energies were calculated with the CAM-B3LYP functional and the 6-31+G(d) basis set. In the case of the intercalated system, the excited state optimizations were performed with the CAM-B3LYP functional using the 6-31+G(d) basis set to describe the ligand and the 6-31G basis set for the DNA structure.

The Natural Transition Orbitals^[297] were calculated by applying unitary transformations to occupied and unoccupied orbitals, in order to obtain a new set of orthogonal orbitals, defined as “natural”. The transition density matrix expressed in terms of the new orbitals is diagonal. The eigenvalues of this matrix represent the probability to find the electron in the natural orbital.

The absorption shape of PZPERY and perylene diimide was computed in the linear vibronic coupling approximation. A normal-mode analysis of PZPERY *in vacuo* was performed at the B3LYP/6-31G(d) level, followed by a gradient calculation for the excited state at the CAM-B3LYP/6-31G(d) level. The excited-state gradient was projected onto the normal modes to finally obtain the Huang-Rhys factors. The latter were used to finally compute the absorption profile in the second-order cumulant expansion formalism.^[298]

3.3.2 Molecular dynamic (MD) simulations

All the MD simulations were personally performed. The structure of the Tel23 G4 in K⁺/water solution was obtained from the Protein Data Bank (PDB), with PDB id 2JPZ. In detail, the first, the second and the last residues of the G4 chain of the PDB file (a 26-mer hybrid) were removed and two K⁺ atoms were added between the tetrads by using the Maestro software (Maestro, version 10.2, Schrödinger, LLC, New York, NY, 2015), in order to generate the same Tel23 sequence of the experimental studies. The starting molecular structure

of PZPERY was obtained by full geometry optimization through DFT calculations, as reported above. The starting structures of the PZPERY/Tel23 system were extracted from the docking calculations described below.

For MD simulations, GAFF parameters were used for PZPERY, and the corresponding atom-types were assigned with the ACPYPE software (AnteChamber PYthon Parser interfacE).^{[299],[300]} The Amber99SB force field ParmBSC1 nucleic acid parameters were used for the G4 model.^[301] Atomic partial charges of PZPERY were obtained as RESP charges by Hartree-Fock (HF/6-31G(d)) calculations and using the Antechamber package. A triclinic box (1.0 nm depth on each side) of TIP3P water was generated around the PZPERY/Tel23 system, for a total of about 5500 solvent molecules; 39 K⁺ ions and 17 Cl⁻ ions were added to neutralize the negative charges of the G4 sugar-phosphate backbone and to set the solution ionic strength to approximately 0.15 M.

Explicit solvent MD simulations for the PZPERY/G4 system were performed by using the Gromacs 5.0.4 software package,^{[302],[303]} at 300 K in the canonical NPT ensemble (whose number of particles (N), pressure (P) and temperature (T) are constant), under control of a velocity-rescaling thermostat.^[304] The particle Mesh-Ewald method was used to describe long-range interactions.^[305] Preliminary energy minimizations were run for 5000 steps with the steepest descent algorithm, during which the equilibration of the PZPERY/Tel23 system were harmonically restrained with a force constant of 1000 kJ/mol·nm², gradually relaxed in five consecutive steps of 100 ps each, to 500, 200, 100 and 50 kJ/mol·nm².

Root Mean Square Deviation (RMSD) plots were used to assess the stability of the G4 model and of the binding site. Clustering analysis was performed with the g-cluster tool to determine the most recurrent structures at equilibrium.

3.3.3 Docking

The starting structures of the PZPERY/Tel23 system analysed with the MD simulations were personally obtained by docking the ligand on the G4 host with DOCK6 software.^[306] The blind docking procedure was performed by taking into account all the G4 surface. Spheres within a radius of 0.14 – 0.4 nm were used to define the binding site into a 1.2 nm large box. The grid-based score depends on the non-bonded terms of the molecular mechanics force field. The ligand charge for the docking was calculated using the AM1-BCC method.

In the case of PQ docked into the protein BSA, the binding sites were constructed on the actual position of the selected markers (see Chapter VII, Paragraph 7.3.3). For binding site I, PDB id 2BXC was employed as starting structure, whereas PDB id 2BXG was used for binding site II. Spheres of 0.14 – 0.4 nm of radius were created in the place of the ligands into a 0.7 nm large box.

Chapter IV

4. The perylene diimide derivative PZPERY

4.1 Introduction

Perylene diimides (PDIs) derivatives are aromatic dyes which show intense visible light absorption, excellent photostability and high quantum yields. The low reduction potential of PDIs^[307] makes them electron acceptors and semiconductors in photoinduced charge transfer reactions; that's why they are studied for applications in the fields of photovoltaics,^[308] luminescent solar concentrators,^[309] OLEDs,^[310] and nano-sensors.^[277] PDIs undergo auto-aggregation phenomena and the aggregates show interesting new properties arising from π - π coupling.^[311] From the biochemical point of view, PDIs can interact with double-helix DNA both by the formation of extended aggregates on the external DNA backbone^[312] or by intercalating between the DNA base pairs.^{[313],[314]} PDIs derivatives might have anti-tumour properties, as they were found to be involved in the inhibition of the telomerase activity by stabilizing DNA G-quadruplex (G4) structures.^[315] For instance, N,N'-bis-(2-(1-piperidino)ethyl)-3,4,9,10-perylene tetracarboxylic acid diimide (PIPER, Figure 4.1A) and N,N'-bis-(3-(4-morpholino)-propyl)-3,4,9,10-perylene tetracarboxylic acid diimide (Tel01, Figure 4.1B) were proposed to be promising G4 binders.^[316] N,N'-bis-{4-[1-oxo-6-biotinamidoethyl]piperidin-4-yl}-1,6,7,12-tetrakis[3,5-bis(hydroxycarbonyl) phenoxy]-perylene-3,4,9,10-tetracarboxylic diimide (PDI2B, Figure 4.1C) was found to interact

with G4 structures with high selectivity, as no affinity towards double helix DNA was displayed.^[93]

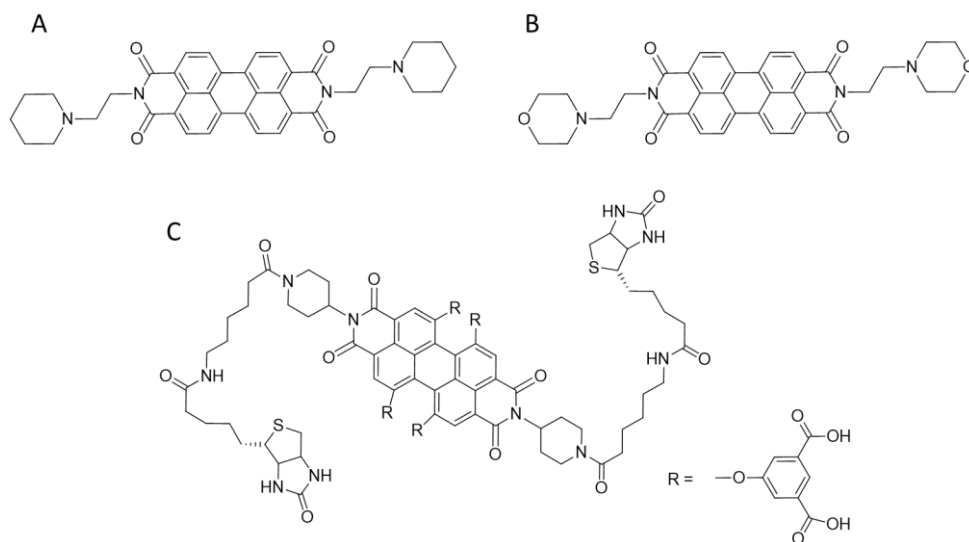


Fig. 4.1. Molecular structures of (A) PIPER, (B) Tel01 and (C) PDI2B

Moreover, PDI derivatives have been found to promote the formation of G4 structures from certain duplex oligonucleotides.^[317] *L. Rossetti et al.* (2002) characterized the role of different PDI side-chains in the G4 binding process.^[318] The positive charges emerged to be significantly involved in the G4 stabilization, as the PDI derivative bearing positively charged substituents was found to inhibit the telomerase activity to a greater extent with respect to the neutral equivalents.^[319] Also, the distance between the charged nitrogen atoms in the side-chains and the aromatic moiety of PDI is known to be an important parameter, in particular, to optimize the interactions with the

negatively charged sugar-phosphate backbone. This evidence is in agreement with the binding model proposed by *H. Hurley* and co-workers (2001), according to whom planar ligands are generally stacked on the terminal G-tetrad of the quadruplex.^[320] However, the G-tetrad may also be hindered, and different conformations will drive formation of adducts with different geometries and ligand/DNA binding stoichiometries larger than 1:1.^[321]

On the whole, PDI's structure/behaviour relationships are not always fully explored and mechanistic insights into the direct interaction with biosubstrates are not always available. The robust knowledge of the details of the molecular interactions could be very important to develop new efficient therapeutic agents and sensors. This study represents an innovative example of a spectroscopic and theoretical-combined analysis of a PDI derivative binding to nucleic acids. At the best of our knowledge, just few examples of MD simulations for G4 binding are reported in the literature,^{[93],[322],[321]} whereas no DFT calculation on DNA/PDI derivatives is reported at all. Concerning MD simulations, the PDB entries used often refer to parallel or anti-parallel G4 structures with inner G-tetrad accessibility^{[323],[324]}; as this accessibility may not always be ensured in real systems it might be interesting to check what happens in the case of more hindered conformations.

The binding to double helix RNA is scarcely investigated,^{[325],[326]} while information on the binding to triple helix RNA is missing at all; data on intercalation are often based on qualitative approaches.^{[313],[314]}

On this basis, the newly synthesized water soluble N,N'-bis(2-(1-piperazino)ethyl)-3,4,9,10-perylenetetracarboxylic acid diimide dichloride (PZPERY, Figure 4.2) is here tested to get information on the mechanistic aspects of its binding to double-stranded DNA, G4 DNAs and RNA both in double and triple helix forms.

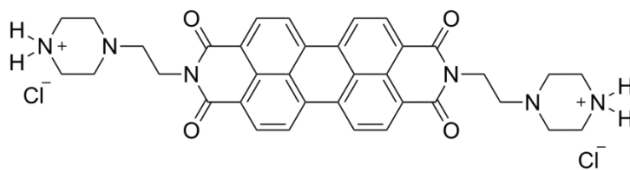


Fig 4.2 Molecular structure of *N,N'*-bis(2-(1-piperazino)ethyl)-3,4,9,10-perylenetetracarboxylic acid diimide dichloride (PZPERY)

4.2 Spectroscopic characterization

Before any subsequent test, the solution properties of PZPERY under physiological conditions (NaCl 0.1 M, NaCac 2.5 mM, pH 7.0) were measured. Absorbance spectra at different dye concentrations were recorded. Upon increasing concentrations, the absorbance profile changes and the absorbance ratio plot against C_{PZPERY} is not constant (Figure 4.3). This behaviour is indicative of the formation of superimposed aggregates of the H-type.^{[307],[327]} The well resolved shape with three peaks typical of PDIs monomers is never observed, in agreement with the presence of auto-aggregation phenomena.^{[328],[329],[330],[331],[332]} No CD signal is observed for these solutions (Figure 4.4). No aggregation phenomena could be observed by Isothermal Titration Calorimetry with 1.0 and 3.0 mM PZPERY in the syringe. A possible explanation may due to the difficulty to reach the opportune measurable heat/concentration/aggregation constant (K_{agg}) balance needed in ITC experiments, being likely K_{agg} high.^[333]

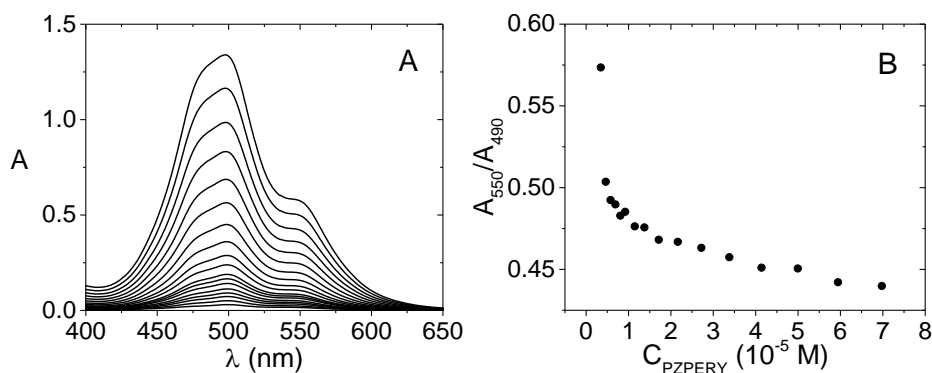


Fig. 4.3. (A) Absorbance spectra of PZPERY and (B) absorbance ratio A_{550}/A_{490} (C_{PZPERY} from 1.16×10^{-6} to 6.98×10^{-5} M, NaCl 0.1 M, NaCac 2.5 mM, pH 7.0, 25.0°C)

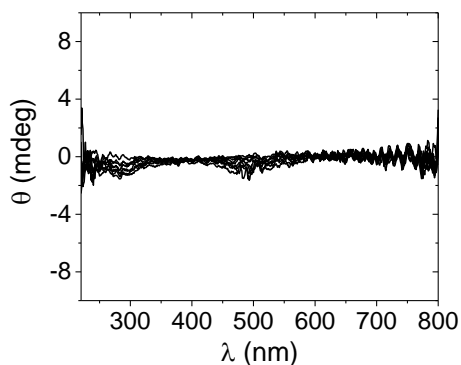


Fig. 4.4. CD spectra of PZPERY (C_{PZPERY} from 0 to 1.15×10^{-4} M, NaCl 0.1 M, NaCac 2.5 mM, pH 7.0, 25.0°C)

4.3 Binding to polynucleotides

PZPERY was tested for affinity to ct-DNA and RNA both in double (polyA·polyU) and triple helix (polyA·2polyU) forms. The different conformation of the polynucleotides for sure plays a major role on driving the

binding features. It is known that natural DNA adopts a conformation called B-DNA, while RNAs structure (both in the double and triple helix form) closely corresponds to a geometry called A-DNA.^{[137],[178]} In RNA duplexes, the displacement of the base pairs from the helical axis is considerable, with the base plane tilted away from the plane vertical to the axis; thus, intercalation of a large molecule should be disfavoured. The A-DNA form is characterized by a broad shallow minor groove and a deep narrow major groove, and the phosphate groups locate closer than those of B-DNA.^{[137],[334]}

4.3.1 Spectrophotometric titrations

Figure 4.5 shows the absorbance spectra recorded during a spectrophotometric titration where known amounts of ct-DNA were added to a PZPERY solution.

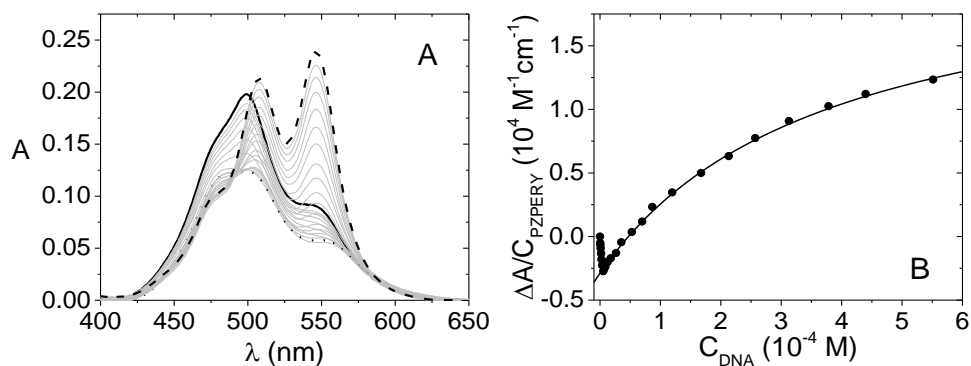


Fig. 4.5. (A) Spectrophotometric titration of PZPERY/ct-DNA and (B) corresponding binding isotherm at $\lambda = 550 \text{ nm}$ ($C_{\text{PZPERY}} = 1.16 \times 10^{-5} \text{ M}$, C_{DNA} from 0 (solid) to $5.57 \times 10^{-4} \text{ M}$ (dash), NaCl 0.1 M, NaCac 2.5 mM, pH 7.0, 37.0 °C). The spectrum corresponding to the minimum of the binding isotherm is evidenced as dotted line

The spectral behaviour is quite complicated and suggests that several bound forms are involved in the interaction. The first branch of the binding isotherm corresponds to points under conditions of dye excess and would likely be connected to the cooperative dye aggregation on the DNA template.^{[335],[336]} However, as the ct-DNA content is raised, the dye would dilute itself over a high quantity of polynucleotide's binding sites. Under these circumstances, aggregates break and monomer binding to DNA occurs. The latter binding process is the more interesting (and the more likely to occur) from a biochemical point of view and is that on which we focus on. The loss of aggregation is confirmed by the rise of well resolved bands, peaked at ca. 485, 510 and 550 nm, which very much resemble the spectrum of PDI monomers (see below theoretical calculations and ^{[307],[328],[329]}).

A general reaction scheme can be that below (Equation 4.1 and 4.2).



This system might be expressed by the apparent reaction (Equation. 4.3):



where P is the polynucleotide (in base pairs), D_f considers any form of free dye ($[D_f] = [D] + m[D_m]$), PD_T is the total of bound species ($[PD_T] = [PD] + [PD_m]$) and K_{app} is the binding constant related to this model.

In order to perform an analysis of the DNA binding, only the points related to polynucleotide excess are taken into account. Under these circumstances $[PD_m]$ can be supposed to be minority and $K_{app} = \alpha_D \times K$ where $\alpha_D = [D]/[D_f]$ is the monomer fraction and K is the equilibrium constant for monomer binding only (Equation 4.1). K_{app} can be evaluated by interpolating the data points at $C_{DNA} \geq C_{PZPERY}$ using Equation 4.4 (see Appendix I):

$$\frac{\Delta A}{C_D} = \frac{\Delta \varepsilon \cdot K_{app} \cdot [P]}{1 + K_{app} \cdot [P]} + c \quad (4.4)$$

where $[P]$ is the free polynucleotide content, $\Delta A = A - \varepsilon_D C_D$ is the amplitude of the binding isotherm, and c is an offset. Initially, the total concentration of the polymer is introduced in Equation 4.4 in place of $[P]$ to obtain a first K_{app} estimation that can be used to calculate $[P] = CP - [PD]$. Then, K_{app} is re-evaluated and the procedure is repeated until convergence is reached. The continuous line in Figure 4.4B is relevant to the fitting procedure.

We obtain $K_{app} = (2.8 \pm 0.9) \times 10^3 \text{ M}^{-1}$ at 37.0°C .

The titration is repeated at different temperatures (Figure 4.6): the dependence of K_{app} on T is complex, due to the superimposition of both dis-aggregation and binding. Overall, no significant dependence of K_{app} on temperature is observed, likely due to some enthalpy compensation between endothermic dis-aggregation and exothermic DNA binding processes.

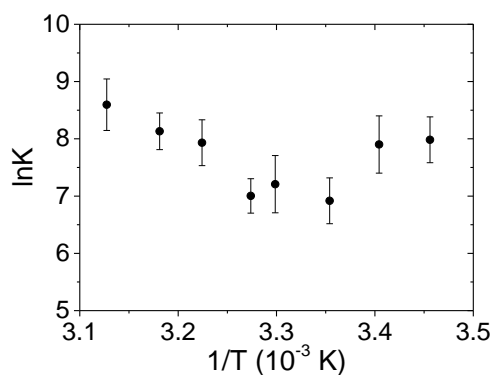


Fig. 4.6. *Van't Hoff plot for PZPERY/ct-DNA (NaCl 0.1 M, NaCac 2.5 mM, pH 7.0)*

Figure 4.7 shows that the interaction is favoured at lower ionic strength (steeper second branch) in agreement with the electrostatic attraction between the DNA phosphate groups and the positive PZPERY. These experiments also evidence changes in the absorbance profile of PZPERY at different salt content which confirm the different extent of auto-aggregated forms. Ionic strength's increase promotes intermolecular interactions for charged molecules: the absorbance profile is less resolved at NaCl 1.0 M + NaCac 2.5 mM with respect to NaCac 2.5 mM only.

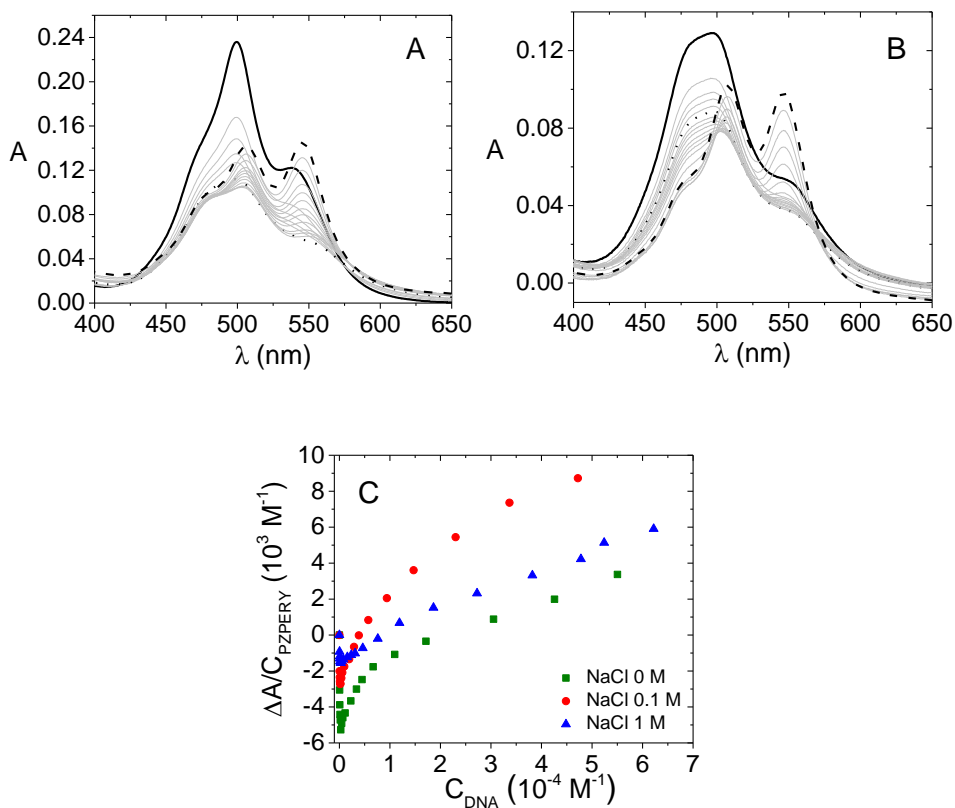


Fig. 4.7. Spectrophotometric titrations of PZPERY/ct-DNA: (A) $C_{PZPERY} = 1.00 \times 10^{-5} \text{ M}$, C_{DNA} from 0 (solid) to $5.50 \times 10^{-4} \text{ M}$ (dash), NaCac 2.5 mM, pH 7.0, 41.0°C; (B) $C_{PZPERY} = 1.00 \times 10^{-5} \text{ M}$, C_{DNA} from 0 (solid) to $6.22 \times 10^{-4} \text{ M}$ (dash), NaCl 1.0 M, NaCac 2.5 mM, pH 7.0, 41.0°C; (C) corresponding binding isotherms at $\lambda = 550 \text{ nm}$. The spectra corresponding to the minimum of the binding isotherm are evidenced as dotted line

For RNAs, some scattering effects were found to occur and the shown spectra (Figure 4.8) were corrected according to the *Leach and Scheraga* approach.^[158] The binding to RNAs is different with respect to ct-DNA, both for polyA·polyU duplex and polyA·2polyU triplex, which behave in a similar way. Under the same experimental conditions, the signal change upon binding is still evident but much more limited and the second branch of the titration cannot reach a curvature. Therefore, K_{app} could not be robustly evaluated for RNAs.

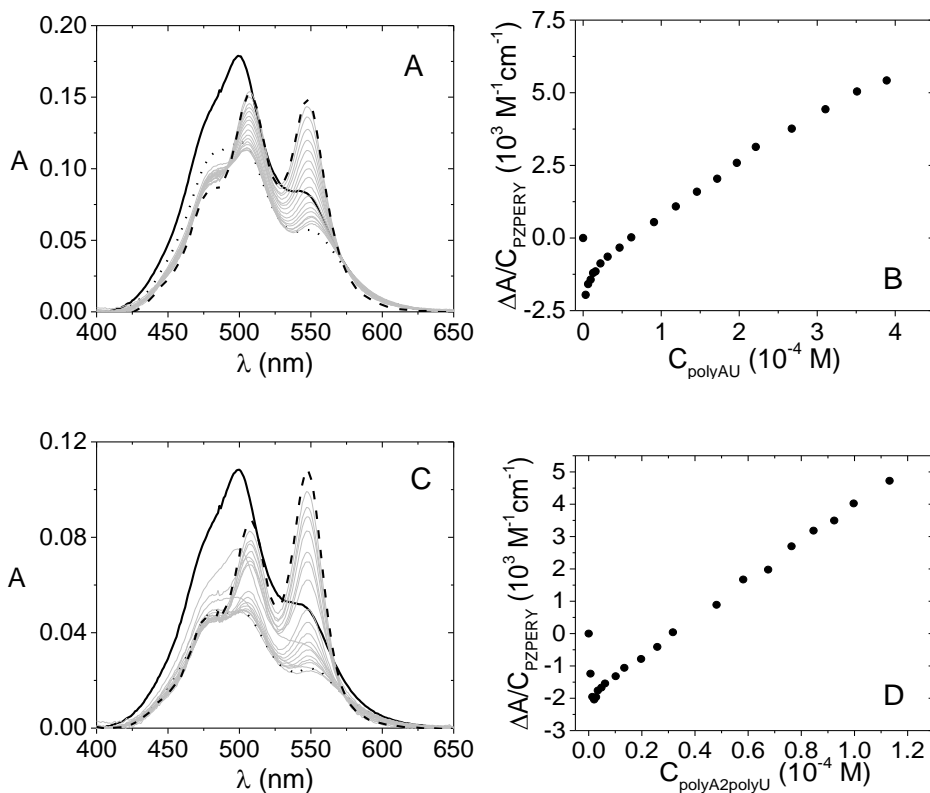


Fig. 4.8. (A-B) Spectrophotometric titration of PZPERY/polyA-polyU and corresponding binding isotherm at $\lambda = 550$ nm ($C_{\text{PZPERY}} = 1.19 \times 10^{-5}$ M, C_{polyAU} from 0 (solid) to 3.89×10^{-4} M (dash); (C-D) Spectrophotometric titration of PZPERY/polyA-2polyU at 37°C and relevant binding isotherm at $\lambda = 550$ nm ($C_{\text{PZPERY}} = 1.20 \times 10^{-5}$ M, $C_{\text{polyA2polyU}}$ from 0 (solid) to 1.13×10^{-4} M (dash)). NaCl 0.1 M, NaCac 2.5 mM, pH 7.0, 37.0°C. The spectrum corresponding to the minimum of the binding isotherm is evidenced as dotted line

4.3.2 Circular dichroism

Circular Dichroism (CD) titrations confirm the different behaviour of double-helix DNA vs. double- and triple-helix RNA (Figure 4.9).

The addition of increasing amounts of PZPERY to a ct-DNA solution provides a strong negative induced signal (ICD) in the visible part of the spectrum and a significant distortion of the CD bands of the DNA base pairs, suggesting intercalation of PZPERY into the polynucleotide. The amplitude of the ICD signal corresponds to $|\Delta\epsilon| = [\theta]/3300 = 7.7 \text{ M}^{-1}\text{cm}^{-1}$, which is compatible with an intercalative process ($|\Delta\epsilon| < 10 \text{ M}^{-1}\text{cm}^{-1}$).^[148] The CD signature is very different in the case of RNAs: here, the effect on the UV bands is opposite and the evident degenerate exciton coupling appears in the visible region. An analogous behaviour has been previously observed in the few studies on other PDIs binding to double stranded RNA.^{[325],[326]} Here, the induced (ICD) positive and negative bands point out groove binding as PZPERY/RNA binding mode for both duplex and triplex RNAs. In any case, as the changes in the intrinsic CD bands reveal, the conformational changes induced in the polynucleotide structure by PZPERY are too profound to arise from a simple electrostatic binding. Note that blank tests confirmed no ICD/background signal for PZPERY alone in buffer (Figure 4.4).

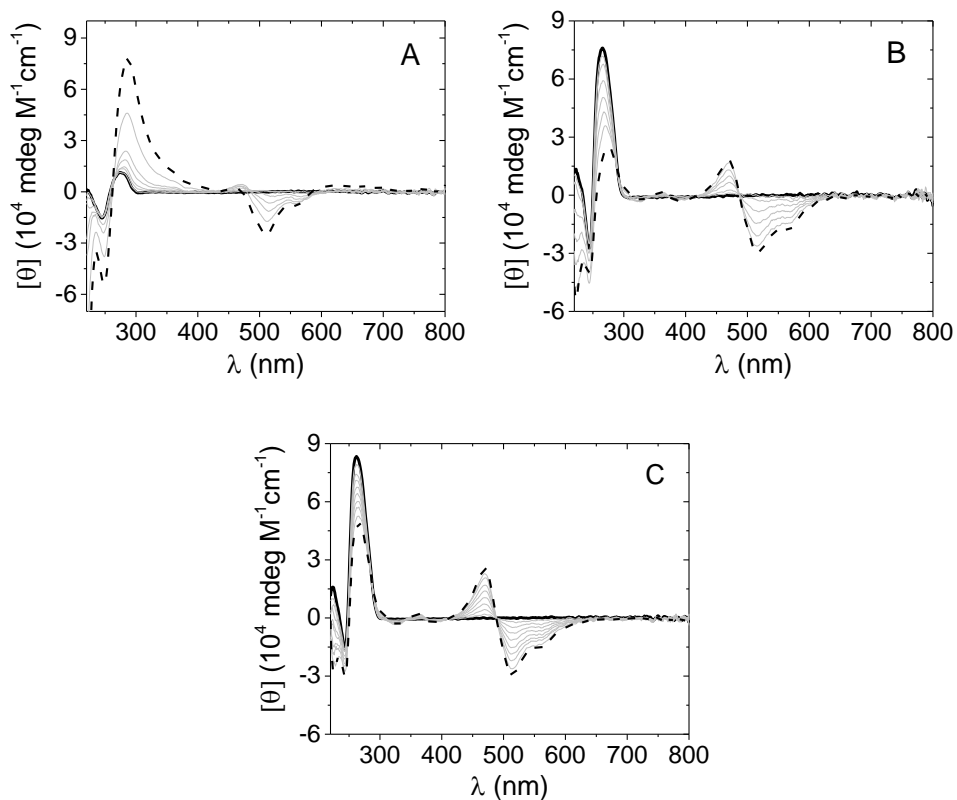


Fig. 4.9. CD spectra of (A) PZPERY/ct-DNA ($C_{DNA} = 7.00 \times 10^{-5} M$, C_{PZPERY} from 0 (solid) to $6.97 \times 10^{-5} M$ (dash); (B) PZPERY/polyA·polyU ($C_{polyAU} = 4.03 \times 10^{-5} M$, C_{PZPERY} from 0 (solid) to $4.03 \times 10^{-5} M$ (dash); (C) PZPERY/polyA·2polyU ($C_{polyA2U} = 6.50 \times 10^{-5} M$, C_{PZPERY} from 0 (solid) to $8.03 \times 10^{-5} M$ (dash)); NaCl 0.1 M, NaCac 2.5 mM, pH 7.0, 25.0°C

4.3.3 Ethidium bromide displacement assay

The hypothesis of PZPERY intercalation into ct-DNA is confirmed also by ethidium (EtBr) displacements assays (Figure 4.10). PZPERY addition to the probe-saturated nucleic acid produces a dramatic decrease of the light

emission of intercalated EtBr, indicating that an exchange reaction takes place and that PZPERY substitutes EtBr from its location in the intercalation pocket.

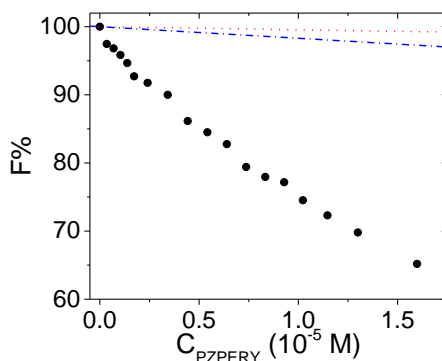


Fig. 4.10. PZPERY/ct-DNA ethidium bromide displacement test ($C_{\text{DNA}} = 1.69 \cdot 10^{-4} \text{ M}$, $C_{\text{EB}} = 6.40 \cdot 10^{-5} \text{ M}$), NaCl 0.1 M, NaCac 2.5 mM, pH 7.0, 25.0 °C, $\lambda_{\text{ex}} = 520 \text{ nm}$, $\lambda_{\text{em}} = 595 \text{ nm}$. The red line refers to blank test where solvent only is added, whereas the blue line refers to the typical behaviour of groove/external binders^[241]

4.3.4 Isothermal Titration Calorimetry

The Isothermal Titration Calorimetry technique allowed us to observe this complex system from the opposite point of view. In fact, in this case, the dye is added to the polynucleotide's solution and the aggregation step should be relevant just for the last additions. The ITC experiments (Figure 4.11, 4.12 and 4.13) enabled the determination of the thermodynamic parameters for the binding. There is a specific binding process accompanied by non-specific binding processes that could be related to the PZPERY stacking along the polynucleotides.

The thermodynamic parameters of the PZPERY interaction with the different substrates are collected in Table 4.1. Although all the binding reactions are

exothermic processes, they are entropically driven probably due to hydrophobic interactions and desolvation.^[337] The binding constant of PZPERY/ct-DNA is too small to be accurately determined by ITC and all data related to this system should be considered as qualitative only. However, K value is in good agreement with spectrophotometric results.

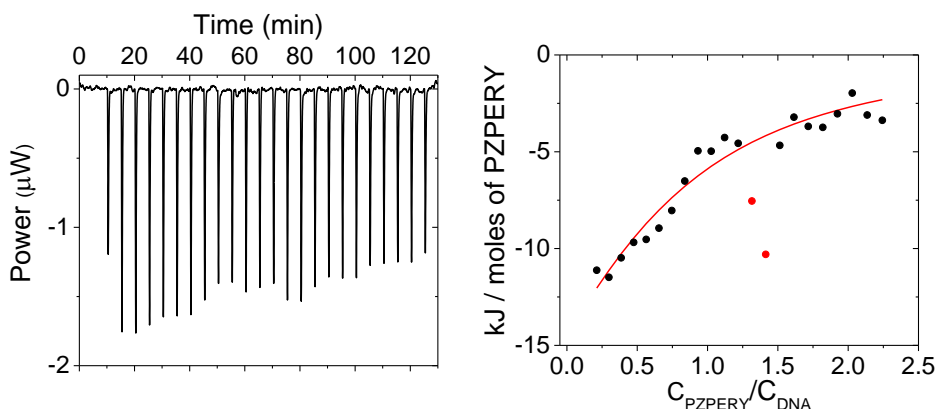


Fig. 4.11. ITC titration of ct-DNA with PZPERY ($C^{\circ}_{\text{DNA}} = 3.0 \times 10^{-4} \text{ M}$, $C^{\circ}_{\text{PZPERY}} = 3.0 \times 10^{-3} \text{ M}$, NaCl 0.1 M, NaCac 2.5 mM, pH 7.0, 25.0°C)

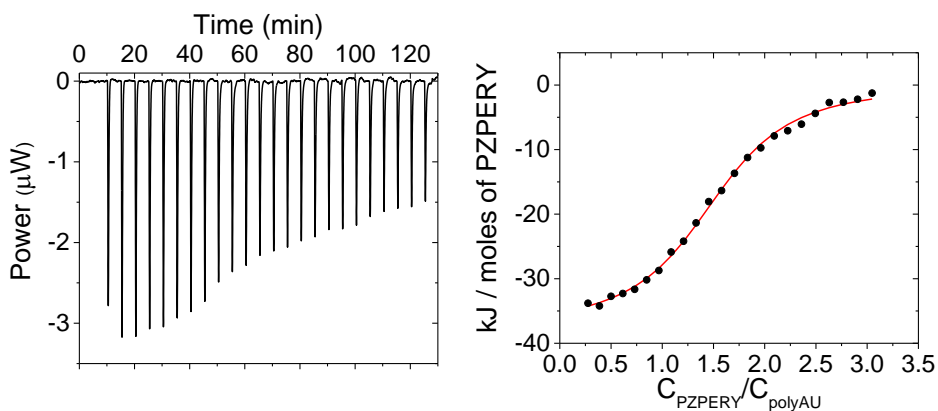


Fig. 4.12. ITC titration of polyA-polyU with PZPERY ($C^{\circ}_{\text{polyAU}} = 3.0 \times 10^{-4} \text{ M}$, $C^{\circ}_{\text{PZPERY}} = 3.0 \times 10^{-3} \text{ M}$, NaCl 0.1 M, NaCac 2.5 mM, pH 7.0, 25.0°C)

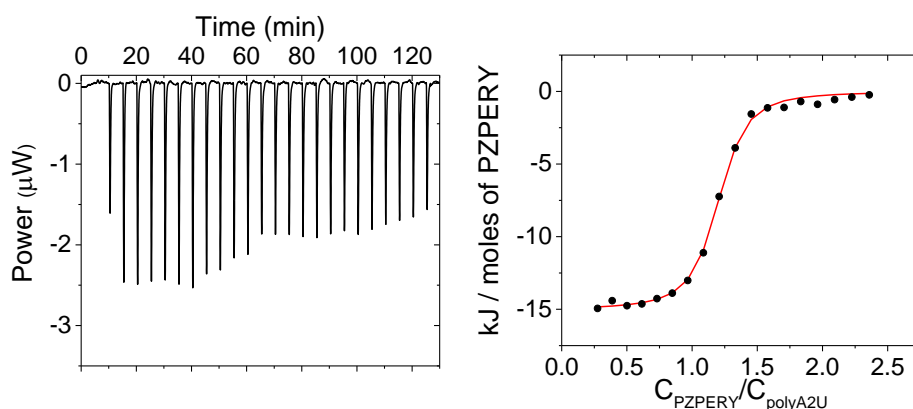


Fig. 4.13. ITC titration of polyA-2polyU with PZPERY ($C^{\circ}_{polyA2U} = 3.0 \times 10^{-4} M$, $C^{\circ}_{PZPERY} = 3.0 \times 10^{-3} M$, NaCl 0.1 M, NaCac 2.5 mM, pH 7.0, 25.0°C)

Tab. 4.1 Thermodynamic parameters obtained by ITC for the interaction between PZPERY and the quoted biomolecules (NaCl 0.1 M, NaCac 2.5 mM, pH 7.0, 25.0°C)

	<i>ct-DNA</i>	<i>polyA·polyU</i>	<i>polyA·2polyU</i>
K (M⁻¹)	$(2.7 \pm 1.8) \times 10^3$	$(3.3 \pm 0.1) \times 10^4$	$(3.5 \pm 0.8) \times 10^5$
ΔH (kJ/mol)	-5.6 ± 2.2	-6.1 ± 0.2	-2.5 ± 0.1
ΔS (J/mol·K)	46.9	65.9	97.8
n	0.9 ± 0.3	1.5 ± 0.1	1.1 ± 0.1

4.3.5 DFT calculations

Given that intercalation is found to be the active binding mode in the case of ct-DNA, QM calculations were performed in order to obtain a geometrical representation of the adduct. Firstly, the geometrical structures for both ground and excited states of the water solvated PZPERY were optimized by employing a time dependent - Density Functional Theory (TD-DFT) approach combined with a PCM description of the solvent. The superimposition of the ground state optimized conformation with the corresponding optimized excited state is shown in Figure 4.14.

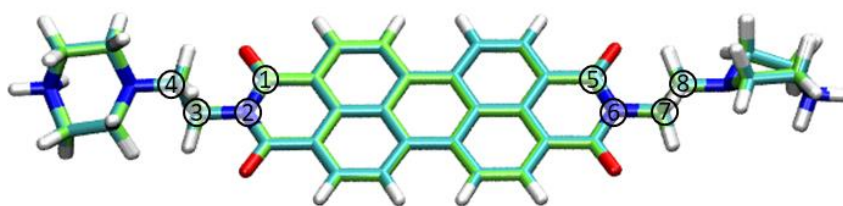


Fig 4.14. *Superimposition of optimized ground state (blue) and excited structures (green) of PZPERY (dihedral angles for Table 4.2 marked with numbers)*

Because of the large size of the system, we consider the double stranded DNA intercalation pocket as a simplified model, which limits the interactions between PZPERY and the polynucleotide to the first neighbours.^{[249],[338]} The DNA model is obtained by eliminating the entire backbone with the exception of two adjacent base pairs (GC and AT) and the sugar-phosphate groups connecting those bases. Twenty geometrical structures for each adduct were optimized by employing a semi-empirical method (PM6) as a rapid screening

procedure. The RMSD was considered as the parameter to compare the obtained results and the adducts with the same conformation are excluded from the subsequent TD-DFT analysis.

The superimposition of the TD-DFT optimized structures of the ground (in blue) and the corresponding excited state (in green) (Figure 4.15) shows at a glance that they are essentially equivalent. In the most favourable arrangement, the aromatic core of PZPERY establishes π -stacking interactions with ct-DNA base pairs, whereas the positive charged substituents lean towards the negative phosphate groups.

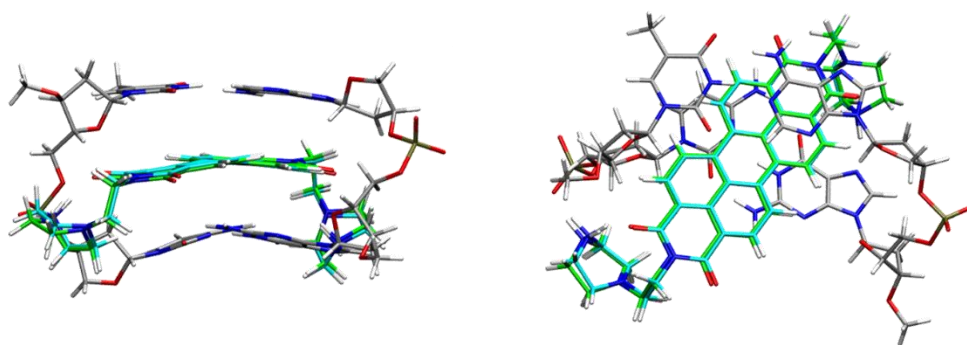


Fig. 4.15. *Ground state (blue) and excited state (green) optimized structures of PZPERY intercalated into the DNA double helix*

The Natural Transition Orbitals (NTO) provide a qualitative representation for the electronic transition density. The dominant NTO pair for the $S_0 \rightarrow S_1$ transition of the intercalated system (95% of contribution to the transition) is shown in Figure 4.16.

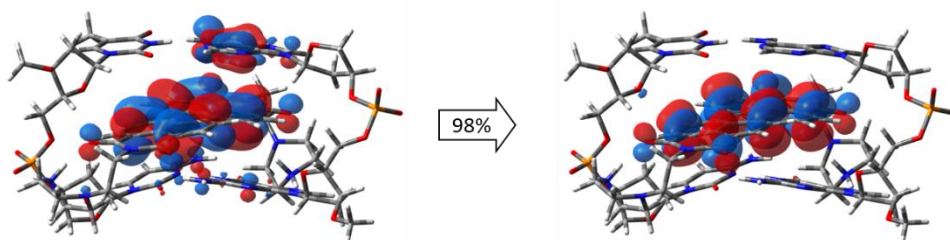


Fig. 4.16. NTO ($S_0 \rightarrow S_1$) for intercalated PZPERY (98% of contribution to the transition)

The dihedral angles (carbon atoms 1-2-3-4;5-6-7-8 of Figure 4.14), dipole moments, absorption and emission energies obtained with the TD-DFT calculations are summarized in Table 4.2. The calculated excitation energies of PZPERY do not significantly change as a result of the DNA binding. The significant spectral changes observed during the absorbance titrations can only be explained by simultaneous binding and dis-aggregation processes.

Tab. 4.2. Calculated properties for PZPERY solvated in water and intercalated into the DNA

	water	DNA
Dihedral angle GS	-87; 92	81; -81
Dihedral angle EXC	-87; 92	84; -81
Dipole moment GS (D)	7.03	$\mu_{GS} > \mu_{EXC}$
Dipole moment EXC (D)	7.04	
Oscillator Strength	1.07	0.54
ABS (eV)	2.52	2.40
FLUO (eV)	2.19	2.12

The simulated absorption spectrum of monomeric PZPERY is reported in Figure 4.17. The absorption spectrum of PZPERY is identical to that of its precursor perylene diimide for both shape and position, meaning that the charged substituents do not affect the spectral shape.^[307] The shape of the simulated spectrum is very similar to that obtained in large excess of ct-DNA, further confirming that the spectral changes observed upon binding reflect the dis-aggregation of the dye.

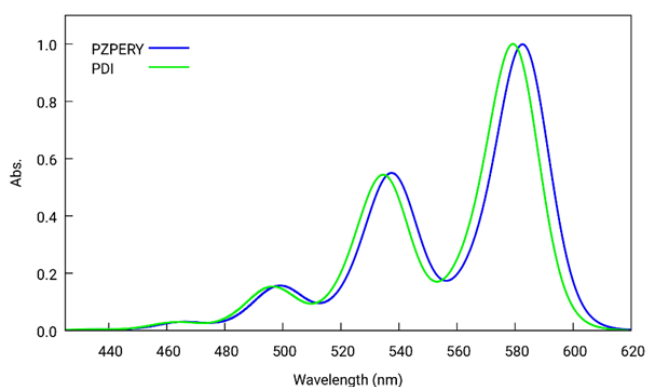


Fig. 4.17. *Calculated visible-light absorbance spectra for PZPERY and PDI (perylene diimide with no substituents)*

4.4 Binding to oligonucleotides

4.4.1 FRET melting experiments

To compare the affinity towards G4s against polynucleotides and evaluate possible selectivity rules, FRET melting experiments in KCl 10 mM, LiCl 90 mM, LiCac 10 mM, at pH 7.4 were performed. FRET melting tests were carried out on 2-tetrad (TBA and BOM17) and 3-tetrad G-quadruplexes

(Tel21, RTel21, 21CTA, TBA, 25CEB). This set contains antiparallel (21CTA, TBA and BOM17), parallel (RTel21 and 25CEB) and mixed/hybrid (Tel21) conformations. The FRET melting experiments reveal thermal stabilization of G4s by PZPERY to different extents, being the effect on double stranded DNA much lower with respect to what found for G4s (Figure 4.18). PZPERY thermally stabilized all 3-tetrads G4s in a greater extent than all the 2-tetrads G4s. Different factors may contribute to the stabilisation, but it can be speculated that such a behaviour agrees with a contribution of the length in the “groove-parallel” direction (extension of the lateral surface) in the binding features. The most stabilized G4s are the human telomeric G4, Tel21 (hybrid) and 21CTA (antiparallel); in fact, at $r = 10$ the melting temperature is beyond the limits of the technique. The least stabilized among the 3-tetrad structures are parallel G4. This pattern is similar to that reported by *M. Zuffo et al.* (2018) for core extended naphthalene diimides.^[339]

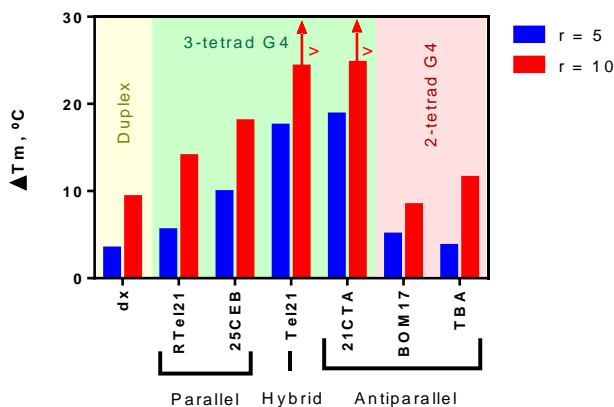


Fig. 4.18. Values of ΔT_m obtained from FRET melting experiments.

ΔT_m = difference in the melting temperature of the oligonucleotide with and without different concentrations of PZPERY, $r = [\text{PZPERY}]/[\text{G4}]$ ($C_{G4} = 0.2 \mu\text{M}$,

$\text{KCl } 10 \text{ mM}$, $\text{LiCl } 90 \text{ mM}$, $\text{LiCac } 10 \text{ mM}$, $\text{pH } 7.4$)

4.4.2 UV melting experiments

UV melting tests^[185] on hybrid (Tel23), antiparallel (CTA22) and parallel (c-myc) G4 structures were performed in KCl 0.1 M (KCl 10 mM for c-myc), LiCac 2.5 mM, pH 7.0. The results indicate that the thermal stabilisation on G4 induced by the addition of equimolar amounts of PZPERY is $\Delta T_m = 2 - 4$ °C (Figure 4.19A, 4.19B and 4.19C). Thermal difference spectra (TDS), i.e. the difference between final (unfolded) and initial (folded) spectrum during melting tests, constitute a signature for G4 structure.^[186] The TDS (Figure 4.18D) indicate that the G4 conformation is not significantly modified by the interacting species. Both aspects concur to hint lateral binding as concluded by FRET tests. Also, the behaviour of Tel23 and CTA22 is almost identical, as previously observed in the FRET experiments. The different extent of thermal stabilisation recorded with the two melting techniques might be ascribed to the different experimental conditions: it is known that K^+ atoms strongly stabilize G4 structures^[84] and the presence of high KCl content in the UV test might smooth the additional stabilising effect of the ligand.

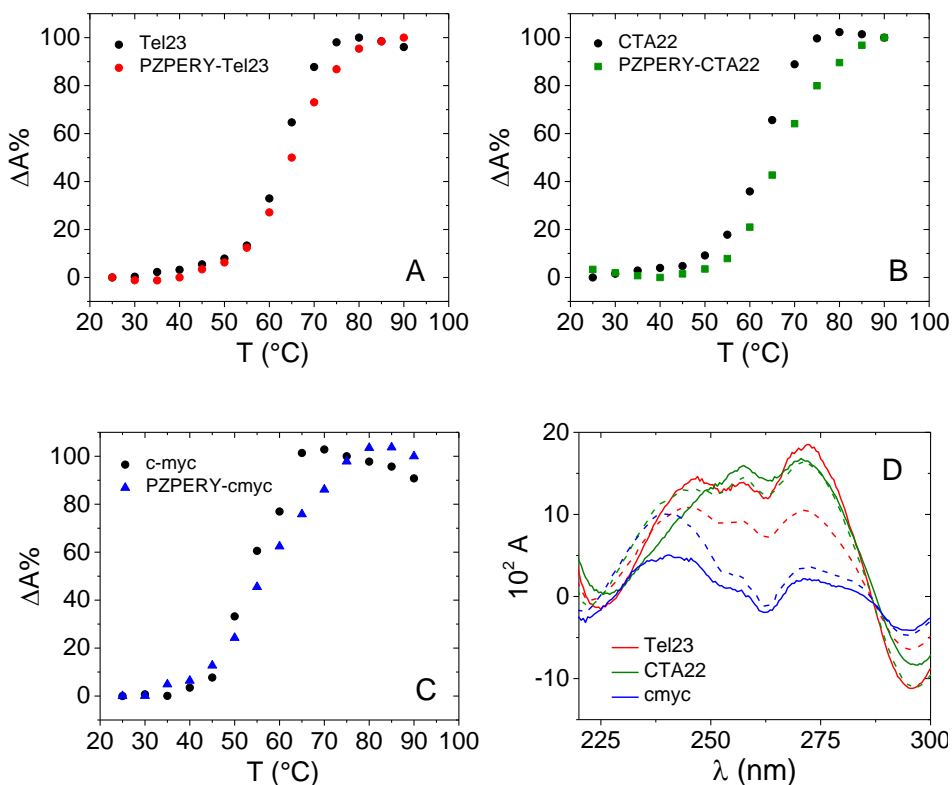


Fig. 4.19. Superimposition of melting curves of (A) PZPERY/Tel23 ($C_{\text{Tel23}} = 5.5 \times 10^{-6} \text{ M}$, $C_{\text{PZPERY}} = 5.8 \times 10^{-6} \text{ M}$); (B) PZPERY/CTA22 ($C_{\text{CTA22}} = 5.8 \times 10^{-6} \text{ M}$, $C_{\text{PZPERY}} = 5.8 \times 10^{-6} \text{ M}$); (C) PZPERY/c-myc ($C_{\text{cmyc}} = 5.8 \times 10^{-6} \text{ M}$, $C_{\text{PZPERY}} = 5.8 \times 10^{-6} \text{ M}$); (D) Thermal difference spectra (TDS) for PZPERY/Tel23 (red), PZPERY/CTA22 (green) and ABTP/c-myc (blue). Continuous lines are related to PZPERY/G4 heating process, dashed lines refer to G4 alone. KCl 0.1 M (KCl 10 mM for c-myc), LiCac 2.5 mM, pH 7.0

4.4.3 Spectroscopic and calorimetric titrations

The top G-tetrad stacked binding mode of PDI derivatives has already been elucidated in previous papers.^[340] Highly exposed tetrads constitute a major binding site which may not always be the most likely to occur in reality. Different papers underline the importance of quadruplex-polymorphism^{[99],[341]} and structural studies have shown that the hybrid-type intramolecular G4 structure is the major conformation formed in the human telomeric sequences.^[342] On this basis, and given the experimental results, we found it interesting to focus our studies on the hybrid G4 conformation.

Absorbance titrations with the Tel23 oligonucleotide at different temperatures were performed and the results are shown in Figure 4.20. The relevance of the spectral changes immediately suggests strong affinity for Tel23: the bands of the bound species are similar but much more prominent than in the DNA/RNAs cases. The binding isotherms show the steep shape that is indicative of a quantitative reaction. This result agrees with the high selectivity shown for some PDIs for G4 structures.^[93]

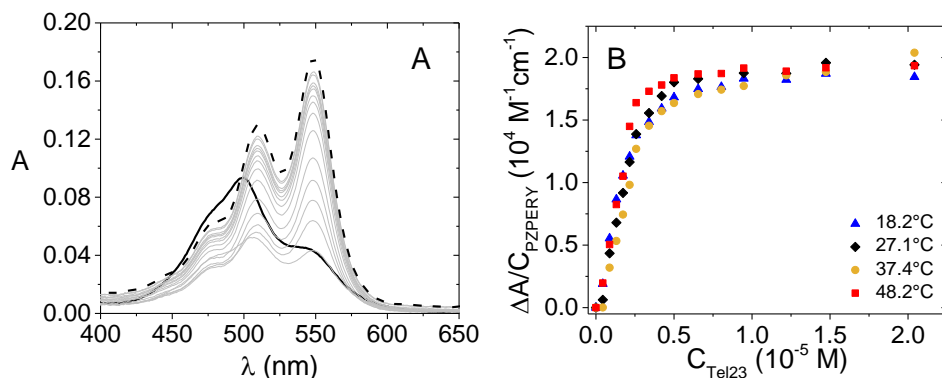


Fig. 4.20. (A) Spectrophotometric titration of PZPERY/Tel23 ($C_{PZPERY} = 6.51 \times 10^{-6}$ M, C_{Tel23} from 0 (solid) to 2.04×10^{-5} M (dash), KCl 0.1 M, LiCac 2.5 mM, pH 7.0, 37.4°C) and (B) binding isotherms at different temperatures ($\lambda = 550$ nm)

CD titrations where increasing amounts of PZPERY are added to the G4 showed the born of a positive ICD band (Figure 4.21). This behaviour occurs only in the presence of dyes monomers bound on the lateral surface; oppositely, sitting atop positions would reflect in no ICD^[343] whereas dye-dye interactions on the G4 would produce a bisignate ICD.^[321]

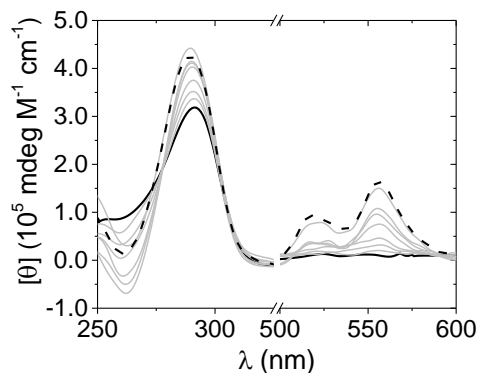


Fig. 4.21. CD spectra of PZPERY/G4 ($C_{\text{Tel}} = 2.70 \times 10^{-6} \text{ M}$, C_{PZPERY} from 0 (no ICD signal, solid line) to $1.39 \times 10^{-5} \text{ M}$ (dashed line)); KCl 0.1 M, LiCac 2.5 mM, pH 7.0, 25.0°C

ITC experiments highlight that PZPERY shows great affinity towards the human telomeric G-quadruplex DNA (Figure 4.22) (and the lowest towards ct-DNA) similarly to the well-known highly selective specific G4 ligands 360A-Br and PhenDC3.^[344] The highest affinity of positively charged perylene derivatives towards G4 with respect to triplex or duplex DNA has been previously described.^{[345],[346]} The $n = C_{\text{PZPERY}}/C_{\text{poly}} \neq 1$ value found in the case of Tel23 (Table 4.3) agrees with previous spectrophotometric findings.

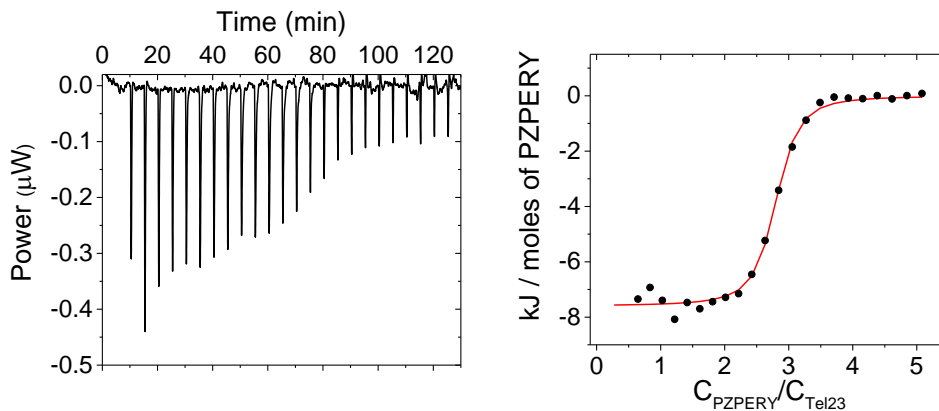


Fig. 4.22. ITC titration of *Tel23* with *PZPERY* ($C^{\circ}_{Tel23} = 6.0 \times 10^{-5} M$, $C^{\circ}_{PZPERY} = 3.0 \times 10^{-3} M$, KCl $0.1 M$, $LiCac$ $2.5 mM$, pH 7.0 , $25.0^{\circ}C$)

Tab. 4.3. Thermodynamic parameters obtained by ITC for the interaction between *PZPERY* and *Tel23* (KCl $0.1 M$, $LiCac$ $2.5 mM$, pH 7.0 , $25.0^{\circ}C$)

<i>Tel23</i>	
K (M⁻¹)	$(1.6 \pm 0.5) \times 10^6$
ΔH (kJ/mol)	-3.8 ± 0.1
ΔS (J/mol·K)	108.9
n	2.7 ± 0.1

4.4.4 Molecular dynamics simulations

The melting tests suggest the occurrence of an external binding mode to G4, but the actual position of the ligand is difficult to determine because of the complexity of the system. In principle, PZPERY could: (a) stack to the G4-tetrad (“tetrad-parallel” direction); (b) sit-atop the G4 by establishing π - π interactions with the bases in the loops (again “tetrad-parallel” direction); (c) interact with the quadruplex grooves mainly because of the electrostatic attraction between the positive substituents and the negatively charged sugar-phosphate backbone (“groove-parallel” direction). Preliminary docking calculations confirmed both (b) and (c) possibilities; given the choice of a hybrid conformation, where the G-tetrad is hindered by the loops, option (a) is here not probable and we will focus on the other alternatives. Also note that the ligand only very rarely intercalates within the G4 itself but rather stacks on the surface of the terminal G-tetrad, a binding mode that is sometimes classified as a threading intercalation in the case of G4s even if no intercalation really occurs.^[340]

Thus, the MD simulations were performed on hybrid Tel23, on the lateral position (binding site I) as it is the most frequently occurring structure, and on the sitting-atop position (binding site II) as it shows the best grid score.

Root Mean Square Deviation (RMSD) plots can be used to evaluate the stability of each binding site. RMSDs from the first frame are reported in Figure 4.23 for binding site I and Figure 4.24 for binding site II, but the convergence to the final structure was determined also by considering the RMSDs from the last frame (Figure 4.25 for binding site I and 4.26 for binding site II). The RMSDs of Tel23 (especially for the G-tetrads and the backbone) indicate that the oligonucleotide core does not undergo significant conformational changes during the MD. The RMSD for PZPERY was

calculated after aligning the guanine bases to the first frame, in order to measure the relative displacement of PZPERY in the reference frame of the G4 core.

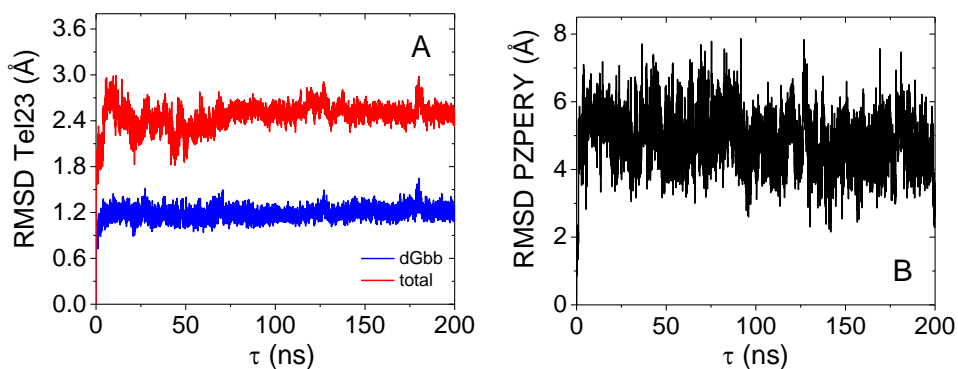


Fig. 4.23. RMSD plots from the first frame for binding site I related to (A) Tel23 (*dGbb* for guanine+backbone, in blue; total for the entire structure, in red) and (B) PZPERY

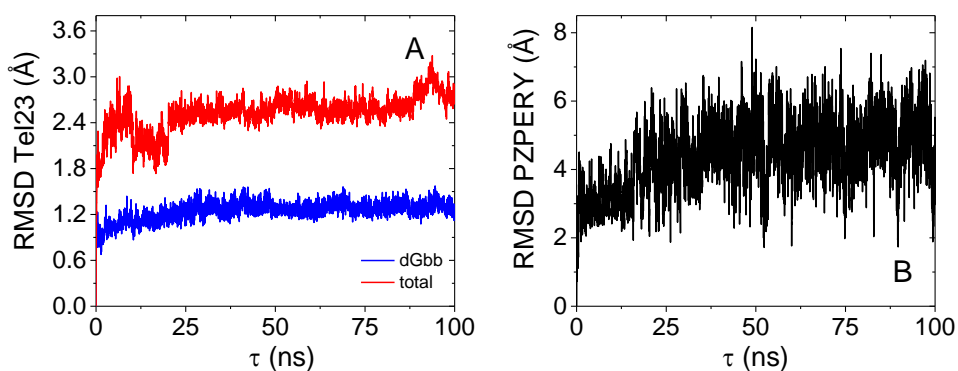


Fig. 4.24. RMSD plots from the first frame for binding site II related to (A) Tel23 (*dGbb* for guanine+backbone, in blue; total for the entire structure, in red) and (B) PZPERY

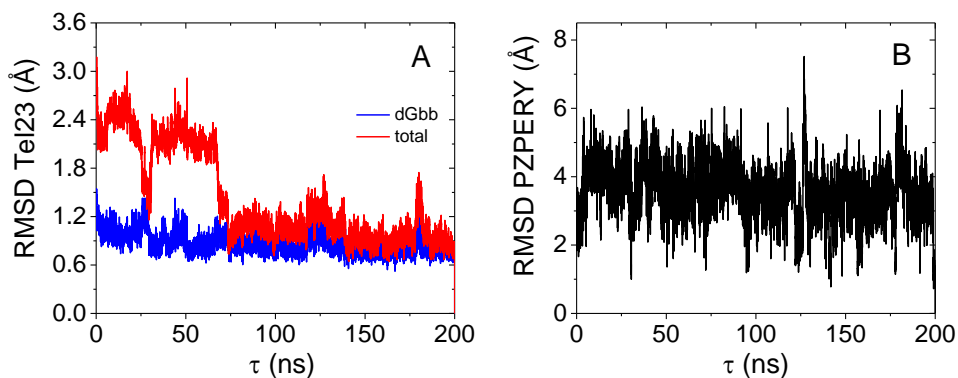


Fig. 4.25. RMSD plots from the last frame for binding site I related to (A) Tel23 (dGbb for guanine+backbone, in blue; total for the entire structure, in red) and (B) PZPERY

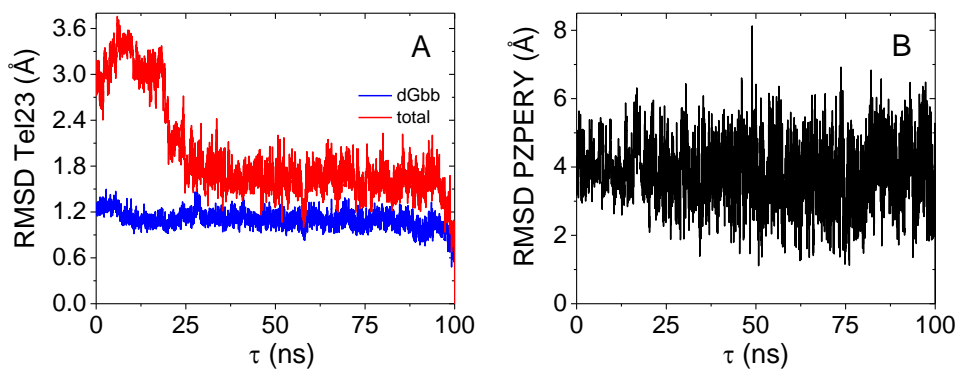


Fig. 4.26. RMSD plots from the last frame for binding site II related to (A) Tel23 (dGbb for guanine+backbone, in blue; total for the entire structure, in red) and (B) PZPERY

The analysis highlights that binding mode I is more flexible, as PZPERY is able to shift along the groove. However, the persistence of H-bonds suggests that a precise arrangement of PZPERY is preferred. Figure 4.27 reports the atoms involved in H-bonds together with the occurrence of the bond (as the fraction of frames in which the bond is formed with respect to the total MD frames) and the average distance between the donor and the acceptor atoms (for binding site I). On the contrary, for binding site II, no H-bond stabilizes the adduct. The high importance of hydrogen bonding in driving the different ability to interact with the G4 was already evidenced.^[347]

Acceptor	DonorH	Donor	%	AvgDist
LIG_26@O1	DG_22@H22	DG_22@N2	56.15	2.8579
DT_6@O4	LIG_26@H18	LIG_26@N3	15.51	2.8413
DG_2@O1P	LIG_26@H31	LIG_26@N6	3.25	2.8166
DT_6@O4	LIG_26@H17	LIG_26@N3	1.97	2.8519
LIG_26@O3	DA_1@H5T	DA_1@O5'	1.55	2.7265
DG_2@O1P	LIG_26@H32	LIG_26@N6	1.22	2.799
DT_5@O2P	LIG_26@H18	LIG_26@N3	1.07	2.8211

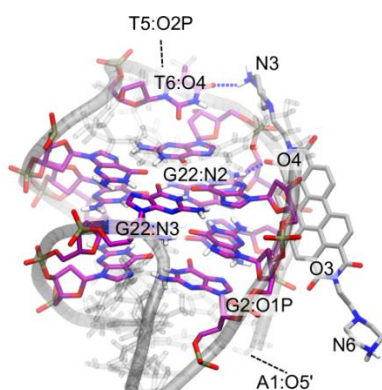


Fig. 4.27. H-bonds analysis of binding site I and graphical representation of the relevant bonds

The stability of binding site I was also characterized by considering the distance between PZPERY and Tel23. Figure 4.28 shows that the distance between the ligand and the G4 residues remains approximately constant during the MD trajectory, showing a flexible but persistent binding mode.

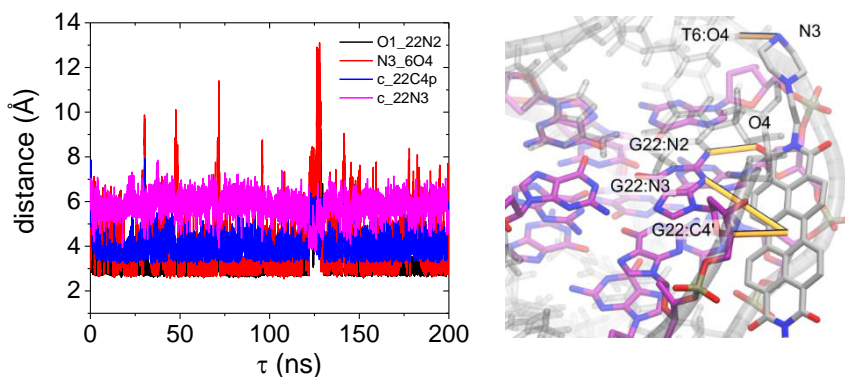


Fig. 4.28. Distances between Tel23 and PZPERY in binding site I and definition of the distances

In order to obtain a geometrical representation of the adducts, the PZPERY conformations explored in the last part of the MD (150 – 170 ns for binding site I, 65 – 85 ns for binding site II) were clustered with a cut-off of 0.2 nm. Figure 4.29A and Figure 4.29B represent the superimposition of the initial position of PZPERY (blue) and the one corresponding to a representative frame of the most populated cluster (cyan). For binding site I, in addition to the stabilising H-bond interaction, electrostatic attraction seems to be at play as the positively charged substituent lies towards the negatively charged phosphate groups. Furthermore, the perylene core fits well into the groove.

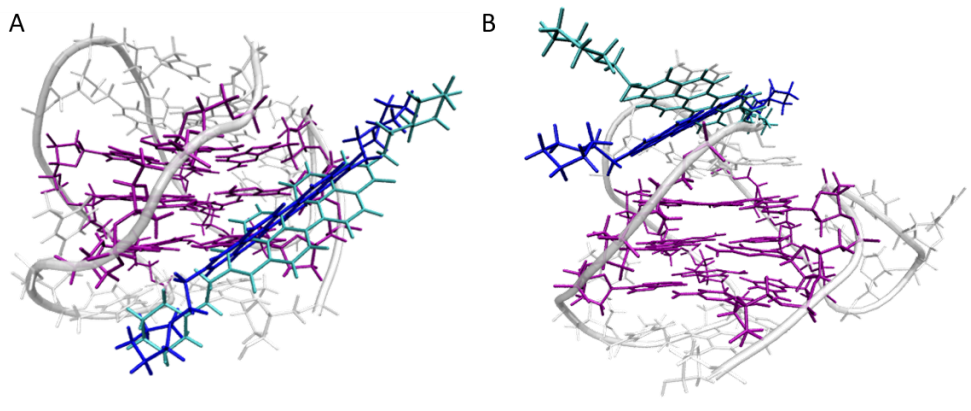


Fig. 4.29 PZPERY/Tel23 adduct for binding site I (A) and binding site II (B). Initial position coloured in blue, first cluster position in cyan.

4.5 Conclusions

A combined spectroscopic/thermodynamic analysis of the interaction of the water soluble perylene diimide PZPERY to different biosubstrates was carried out. In parallel, theoretical calculations were also performed and were crucial to highlight the details of the adduct structures. This study widens the few examples on MD simulations for G4 binding and reports on a first DFT calculation on DNA/PDI derivative.

PZPERY does bind to DNA and RNA polynucleotides but the affinity is not particularly high. The binding features are very different between DNA and RNAs as intercalation into calf-thymus DNA is found to occur, whereas groove binding is present for both double and triple helix RNAs. Natural *calf thymus* DNA is geometrically a B-DNA, while poly(A)·poly(U) duplex resembles A-DNA with a deeper but narrower major groove and wider and shallower minor groove;^{[137],[178],[334]} in the triplex the wide groove is furtherly hindered by the third strand. As often observed, the different geometries of the

helices play a crucial role in driving the affinity towards a particular binding mode.^[336]

DFT calculations on the DNA adduct confirm that intercalation itself cannot produce the dramatic changes in the absorbance profiles of the dye that were experimentally observed. Therefore, this feature is due to the combined effect of intercalation and of aggregates disruption driven by monomer intercalation. When the negative enthalpy intercalation change^[43] is balanced by the positive contribution of dis-aggregation,^{[307],[329]} the overall process has ΔH close to zero. The importance of the interplay between auto-aggregation and intercalation ability is quite straightforward and was observed for neutral PDIs.^[348]

PZPERY shows very good selectivity towards G4 tetrads. The MD simulations suggest that, in principle, both sitting-atop positions and lateral positions are possible. Planar ligands might prefer the “tetrad parallel” geometry for the adduct^[320] but this process usually produces a strong G4 stabilisation.^[349] This is observed by the FRET melting assays, but not in the UV melting tests. On the other hand, MD indicates formation of H-bonds and very favourable complementary geometry for lateral binding, whereas the same is not found in sitting atop structures. FRET assays seem to suggest an increase in the stabilisation by increasing the “groove-parallel” direction (lateral surface). More robustly, the presence of ICD bands in the PZPERY/G4 system indicates lateral binding. Therefore, both experiments and calculation would show that the two binding modes are possible, with no significant preference of one over the other. Also, both spectrophotometric and ITC titrations agree with a binding stoichiometry higher than 2:1, indicating that multiple binding modes may be simultaneously present.

Chapter V**5. The phthalocyanine ABTP****5.1 Introduction**

Phthalocyanines are aromatic compounds composed of four isoindole rings connected by nitrogen atoms which can form stable metal complexes upon the double deprotonation of the isoindole groups. The peripheral rings can also bear different substituents, whose features modulate the photophysical properties of the dye, together with the metal centre. Thus, the absorption and emission properties of phthalocyanines can be tuned to obtain different coloured dyes and pigments.

It is estimated that approximately 25% of all artificial organic pigments are phthalocyanine derivatives.^[350] Among others, Cu(II) phthalocyanines are widely exploited as bright blue pigments in paints, printing inks and textile dyeing.^[351] Moreover, these Cu(II) complexes have been historically used as markers in histologic staining methods. Alcian Blue (Figure 5.1A) is considered one of the most common dye for staining tissues, thanks to its affinity for polysaccharides.^[352]

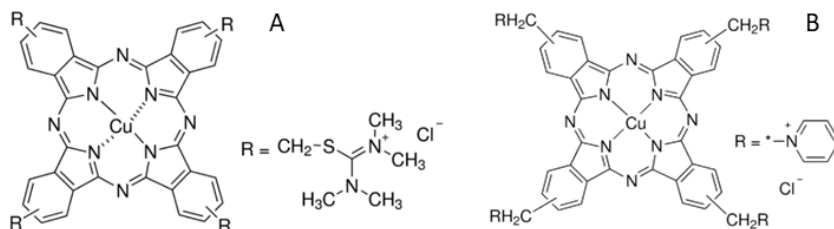


Fig. 5.1. Molecular structure of (A) Alcian Blue and (B) Alcian Blue-tetrakis(methylpyridinium) chloride (ABTP)

Although Alcian Blue undoubtedly presents suitable features (i.e. aromatic structure and cationic substituents) to bind polynucleotides, its interaction with DNA has been scarcely studied and, at the best of our knowledge, no information on the binding to RNA polynucleotides is reported in the literature. The very first obstacle was certainly the lack of structural information until 1973.^[353] Pioneering work by *J. E. Scott* (1972) affirmed that Alcian Blue does bind DNA through electrostatic forces, but the steric hindrance caused by the peripheral groups prevents the insertion of the dye into the stacked base pairs.^[354] Since then, at the best of our knowledge, no mechanistic study had been performed and detailed information on the reactivity towards bio-substrates is missing in the literature.

In addition to the hypothesis of *Scott*, it should be noted that Alcian Blue is highly prone to self-aggregate in water solution^[355] and the formation of supramolecular aggregates surely limits the direct interaction with the polynucleotide and complicates its analysis.

The lack of information clashes with the increasing biomedical role of phthalocyanines which have recently gained high interest as widely diffused therapeutical agents. For example, phthalocyanines are extensively studied and employed as photosensitizers for photodynamic therapy (PDT) thanks to

their suitable photophysical properties.^{[356],[357],[358]} Also, the recent researches have been focusing on the potential anticancer activity of these compounds.^{[359],[360],[361]} Among other non-canonical polynucleotides forms, G-quadruplex DNA structures (G4) have received widespread attention because of their involvement in the mortality of the cancer cells and ligands that stabilize or induce the formation of G4 structures can be considered as promising anticancer agents.^[85] The structural features of phthalocyanines should allow the molecules to bind to human G4 DNA with high affinity through π - π stacking interactions.^[90]

On the above basis, the here presented work concerns the study of the interaction between nucleic acids and Alcian Blue-tetrakis(methylpyridinium) chloride (ABTP, Figure 5.1B), which is a Cu(II) phthalocyanine derived from Alcian Blue. This variant is indicated as a superior alternative to Alcian Blue as for water solubility, staining performance and stability in histologic assays.^[362] Also, ABTP is expected to be an optimal G4 binder because of the large dimension of the π system and the presence of four positively charged peripheral substituents.

To evaluate the selectivity over double helix DNA (calf thymus DNA) and compare the affinity towards different G4 conformations, mixed/hybrid (Tel23^[363]), antiparallel (CTA22^[80]) and parallel (c-myc^[283]) conformations were taken into account as representative examples. The affinity towards synthetic RNAs (duplex and triplex forms) is in our opinion an interesting, but usually much less studied aspect: it is here investigated as well.

In Appendix V we deepen the effect of charged peripheral substituents on the interaction with the biosubstrates, reporting the binding analysis of another Cu(II) phthalocyanine, Cu(II)-phthalocyanine-3,4',4'',4'''-tetrasulfonic acid tetrasodium salt (CuPCTS), which, oppositely to ABTP, bears four negative charges.

5.2 Spectroscopic characterization

Given the known strong tendency of phthalocyanines to undergo auto-aggregation phenomena,^{[355],[364]} this feature was checked here for ABTP.

Under physiological conditions (NaCl 0.1 M, NaCac 2.5 mM, pH 7.0), absorbance profiles do not seem to change with dye concentration, the *Lambert and Beer* plots are linear, and the ratio between two absorbance values is independent of the dye content (Figure 5.2). No CD signal is observed for these solutions (Figure 5.3).

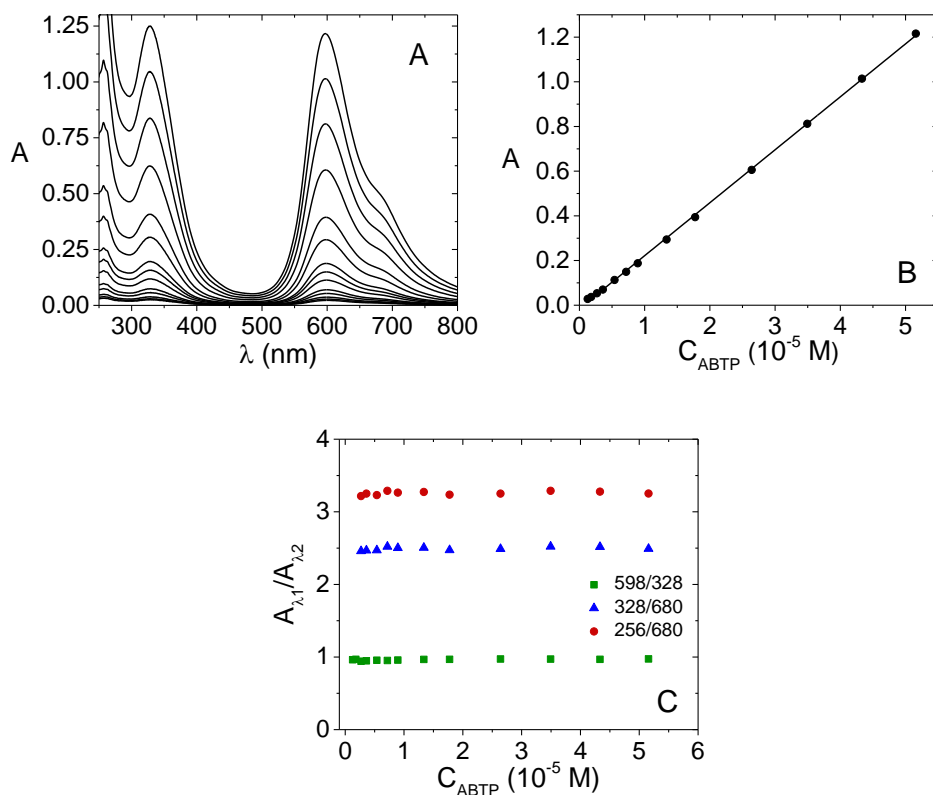


Fig. 5.2. (A) Absorbance spectra of ABTP, (B) Lambert Beer's plot at $\lambda = 598$ nm and (C) $A_{\lambda 1}/A_{\lambda 2}$ ratios (C_{ABTP} from 1.26×10^{-6} M to 5.16×10^{-5} M (NaCl 0.1 M, NaCac 2.5 mM, pH 7.0, 25.0°C))

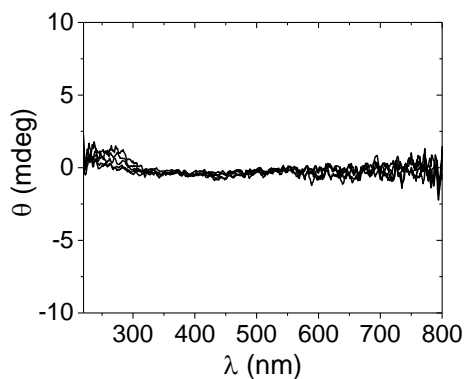


Fig. 5.3. CD Spectra of ABTP (C_{ABTP} from $1.01 \times 10^{-6} M$ to $4.93 \times 10^{-5} M$, NaCl 0.1 M, NaCac 2.5 mM, pH 7.0, 25.0°C)

This behaviour should in principle be against the formation of supramolecular structures related to auto-aggregation phenomena. However, it might also be that the aggregate is strongly majority over all the concentration range explored in the experiment. In fact, if the absorbance experiments are repeated in ethanol (lower dielectric constant), strong deformations in the shape of the spectrum and changes in the relevant abundance of the two major bands occur by increasing the ABTP content (Figure 5.4).

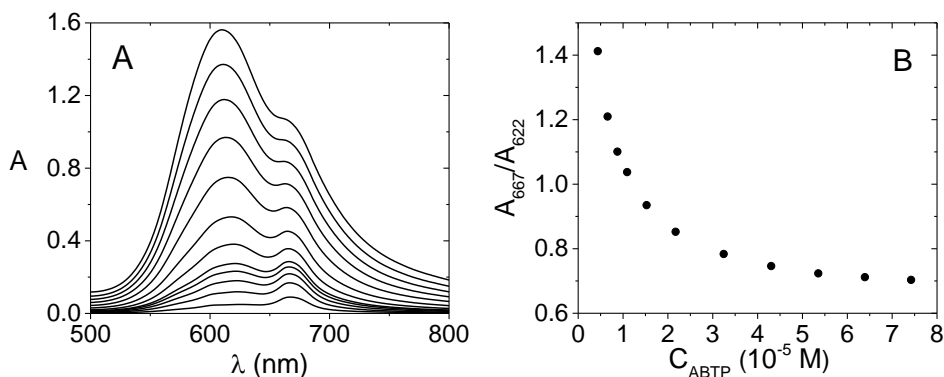


Fig. 5.4. (A) Absorbance spectra of ABTP in ethanol and (B) A_{667}/A_{622} ratios (C_{ABTP} form 2.19×10^{-6} M to 7.42×10^{-5} M, 25.0°C)

It can thus be concluded that the band at around $\lambda = 622$ nm corresponds to the aggregate, whereas that at about $\lambda = 667$ nm should be attributed to the monomer: co-facial H-aggregates are supposed to be formed. In water, the aggregation process is even stronger than in ethanol^[364] and the monomer can hardly be evidenced, even under the most diluted conditions. It is here confirmed that the chirality of these supramolecular structures can be turned-off, depending on the staggering angle.^{[365],[220]}

5.3 Binding to polynucleotides

5.3.1 Spectrophotometric titrations

ABTP was first investigated for affinity towards natural polynucleotide as ct-DNA through absorbance titrations under physiological conditions (NaCl 0.1 M, NaCac 2.5 mM, pH 7.0). Figure 5.5, 5.6 and 5.7 show the absorbance spectra together with the binding isotherm recorded by adding to ABTP solutions known amounts of ct-DNA, polyA·polyU and polyA·2polyU respectively. Some scattering effects were found to occur and the shown spectra were corrected according to *Leach and Scheraga*.^[158]

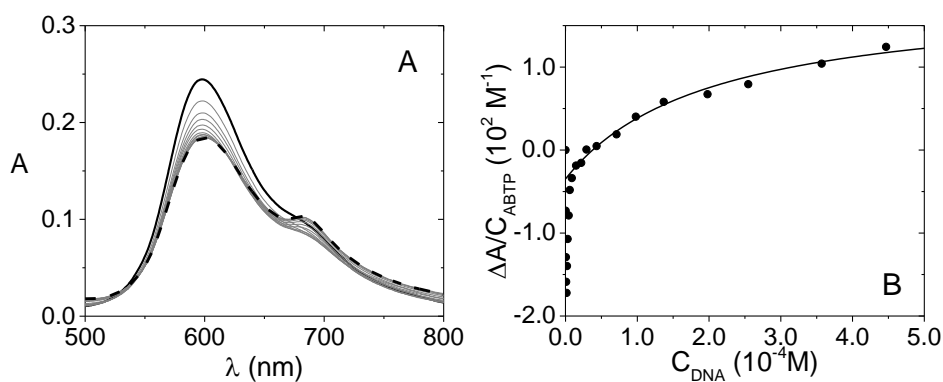


Fig. 5.5. (A) Spectrophotometric titration ABTP/ct-DNA and (B) corresponding binding isotherm at $\lambda = 682$ nm ($C_{ABTP} = 8.73 \times 10^{-6}$ M, C_{DNA} from 0 (solid) to 4.47×10^{-4} M (dash), NaCl 0.1 M, NaCac 2.5 mM, pH 7.0, 25.0°C)

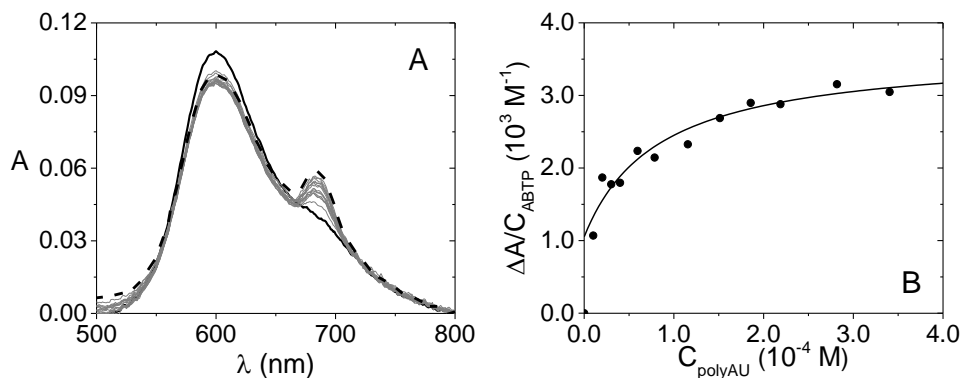


Fig. 5.6. (A) Spectrophotometric titration ABTP/polyA·polyU and (B) corresponding binding isotherm at $\lambda = 682 \text{ nm}$ ($C_{ABTP} = 4.32 \times 10^{-6} \text{ M}$, C_{polyAU} from 0 (solid) to $3.41 \times 10^{-4} \text{ M}$ (dash), NaCl 0.1 M, NaCac 2.5 mM, pH 7.0, 25.0°C)

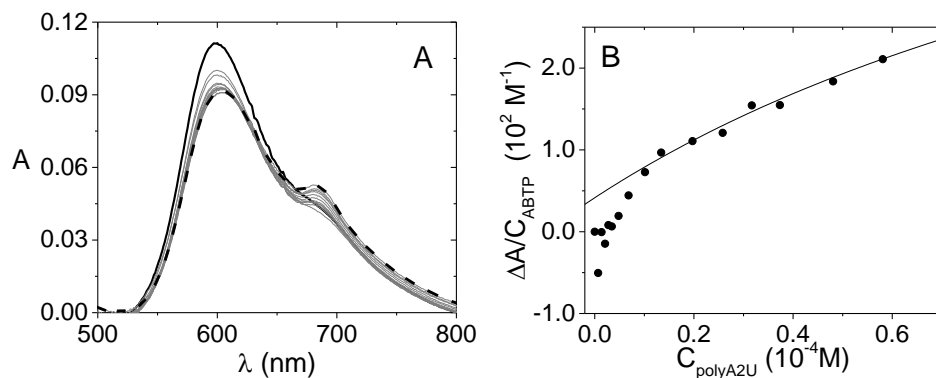


Fig. 5.7. (A) Spectrophotometric titration ABTP/polyA·2polyU and (B) corresponding binding isotherm at $\lambda = 682 \text{ nm}$ ($C_{ABTP} = 4.97 \times 10^{-6} \text{ M}$, C_{polyA2U} from 0 (solid) to $5.81 \times 10^{-5} \text{ M}$ (dash), NaCl 0.1 M, NaCac 2.5 mM, pH 7.0, 25.0°C)

Although the spectral changes are not very remarkable, the interactions are well confirmed by the appearance of a peak at $\lambda = 682$ nm. The similarity both in the shape and in the wavelength of this peak constitutes an indication that ABTP binds to the biosubstrate as a monomer and that binding favours aggregates disruption. A similar behaviour agrees with dye dilution over the helix and was found for the DNA binding of the monomer for other aggregating dyes.^{[335],[366]}

The binding isotherm of the titrations repeated at different temperatures are all biphasic, with a sharp initial change followed by a smoother curve. This is in keep with some aggregation of the dye on the polymer surface for the first points, i.e. those in the presence of high dye excess. Oppositely, when the polynucleotide is the major species, its interaction with the dye monomer is the predominant process. The second branch of titration, where $C_{\text{poly}}/C_{\text{ABTP}} > 1$, can thus be fitted according to Equation 5.1 to yield an estimate of the apparent binding constant of the monomer (K_{app}).^[336]

$$\frac{\Delta A}{C_D} = \frac{\Delta \varepsilon \cdot K_{\text{app}} \cdot [P]}{1 + K_{\text{app}} \cdot [P]} + c \quad (5.1)$$

For the detailed description of the equation refer to Chapter IV – Equation 4.4 and Appendix I.

We have $K_{\text{app}}(\text{ABTP}/\text{ct-DNA}) = (5.0 \pm 1.1) \times 10^3 \text{ M}^{-1}$,
 $K_{\text{app}}(\text{ABTP}/\text{polyA} \cdot \text{polyU}) = (1.2 \pm 0.6) \times 10^4 \text{ M}^{-1}$ and
 $K_{\text{app}}(\text{ABTP}/\text{polyA} \cdot 2\text{polyU}) = (6.2 \pm 3.2) \times 10^3 \text{ M}^{-1}$.

The apparent enthalpy ΔH_{app} and the entropy ΔS_{app} variations of the binding were obtained by the *Van't Hoff* equation (Equation 5.2, Figure 5.8):

$$\ln K_{\text{app}} = -\frac{\Delta H_{\text{app}}}{R} \cdot \frac{1}{T} + \frac{\Delta S_{\text{app}}}{R} \quad (5.2)$$

where K_{app} is the apparent binding constant, T is the temperature (K) and R is the universal constant of gas.

The processes are found to be exothermic with $\Delta H_{\text{app}} = -22 \pm 6$ kJ/mol for ABTP/ct-DNA, $\Delta H_{\text{app}} = -77 \pm 8$ kJ/mol for ABTP/polyA·polyU and $\Delta H_{\text{app}} = -44 \pm 14$ kJ/mol for ABTP/polyA·2polyU.

The slope of the *Van't Hoff* plot is higher for the RNAs. For all the polynucleotides, the order of magnitude for enthalpy changes lies at the boundaries between groove binding (low negative or positive ΔH) and intercalation (highly negative ΔH).^{[43],[367]}

We have to keep in mind that these parameters are apparent ones, due to the coupling with the aggregation process. However, they can still provide information on the binding process. Indeed, being aggregation contribution the same in all systems, they suggest different binding features in the case of RNA polynucleotides with respect to natural DNA.

The thermodynamic parameters will be further discussed below, as Figure 5.16 shows the enthalpy/entropy compensation (EEC) plot for the studied systems.

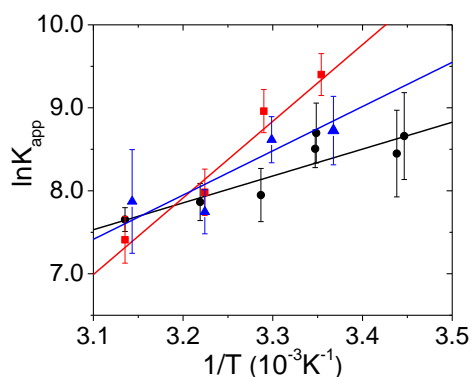


Fig. 5.8. Van't Hoff plot for (●) ABTP/ct-DNA, (■) ABTP/polyA·polyU and (▲) ABTP/polyA·2polyU systems (NaCl 0.1 M, NaCac 2.5 mM, pH 7.0)

5.3.2 Melting experiments

Different binding modes for DNA and RNAs emerged by melting experiments in NaCl 0.1 M, NaCac 2.5 mM, pH 7.0.

In the case of the ABTP/ct-DNA system, precipitation phenomena occurring by increasing the temperature above a certain threshold do not enable to register a complete melting curve. It might be speculated that the outside protruding part could constitute a bridge for some strand-strand aggregating process (being also the inter-DNA repulsion lowered by positive ABTP); these processes are enhanced at higher temperature^[368] and this might be the reason for precipitation during the ABTP/ct-DNA melting tests.

On the contrary, melting studies are possible for both ABTP/polyA·polyU and ABTP/polyA·2polyU, which showed significant helix stabilisation upon ABTP binding: at $C_{ABTP}/C_{poly} = 1.25$, $\Delta T_m > 14^\circ\text{C}$ for both ABTP/polyA·polyU and ABTP/polyA·2polyU systems (Figure 5.9 and Table 5.1). Even if the significant stabilisation of the RNAs could at first sight be against external/groove binding, similar ΔT_m can be found also for this

binding mode^[178] and would agree with the stabilising effect of a +4 charged species which presence strongly reduces phosphates repulsion.

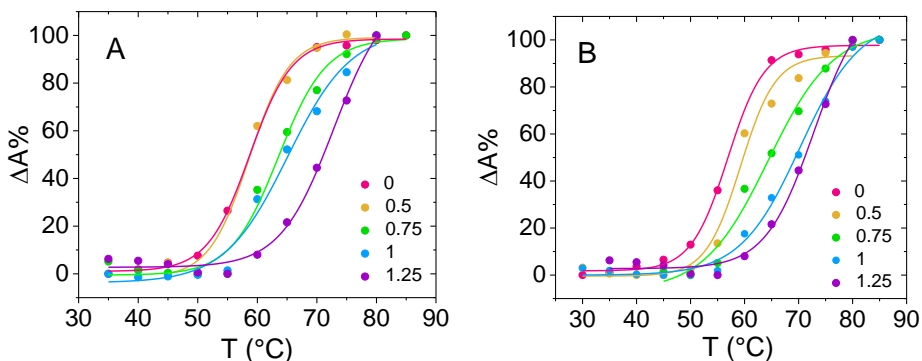


Fig. 5.9. Superimposition of melting curves of (A) ABTP/polyA-polyU and (B) ABTP/polyA-2polyU at different dye/polynucleotide ratios ($C_{poly} = 1.00 \times 10^{-5}$ M, NaCl 0.1 M, NaCac 2.5 mM, pH 7.0)

Tab. 5.1. Melting temperature of ABTP/polynucleotide mixtures ($C_{poly} = 1.00 \times 10^{-5}$ M, NaCl 0.1, NaCac 2.5 mM, pH 7.0)

C_{ABTP}/C_{poly}	ABTP/polyA-polyU		ABTP/polyA-2polyU	
	T_m (°C)	ΔT_m (°C)	T_m (°C)	ΔT_m (°C)
0	58.7 ± 0.5	-	56.9 ± 0.3	-
0.5	59 ± 1	0.3 ± 1.5	59.3 ± 0.8	2.4 ± 1.1
0.75	63.5 ± 0.8	4.8 ± 1.8	64 ± 1	7.1 ± 1.3
1.0	65 ± 1	6.3 ± 1.5	70.3 ± 0.8	13.4 ± 1.1
1.25	73 ± 1	14.3 ± 1.5	73 ± 1	16.1 ± 1.3

5.3.3 Circular Dichroism

Circular dichroism (CD) titrations (Figure 5.10) confirm different behaviours in the presence of DNA or RNAs.

For ct-DNA, a significant negative induced CD signal (ICD) appears in the visible region upon dye addition to the polymer, which indicates that the DNA interaction induces a supramolecular order on ABTP. Negative induced CD signal are proposed to be related to intercalation.^{[224],[227]} Moreover, the amplitude the ICD signal corresponds to $|\Delta\epsilon| = 4.7 \text{ M}^{-1}\text{cm}^{-1}$, a value which is compatible with an intercalative process ($|\Delta\epsilon| < 10 \text{ M}^{-1}\text{cm}^{-1}$).^[148] The geometrical constraints of ABTP support partial intercalation with the insertion of the aromatic substituents.

The interaction with RNAs does not produce the same effect: no ICD bands are present and the CD couplets of the RNAs base pairs are not affected by the addition of ABTP. The absence of induced CD signals suggests the lack of a precise orientation on the helix surface with ABTP randomly placed. Moreover, no distortion in RNAs base pairs' bands might indicate no dipolar interaction (non-degenerate exciton coupling) occurs between the transition moments of RNAs and ABTP, suggesting no penetration into the helices. This picture agrees with an external/groove binding interaction.

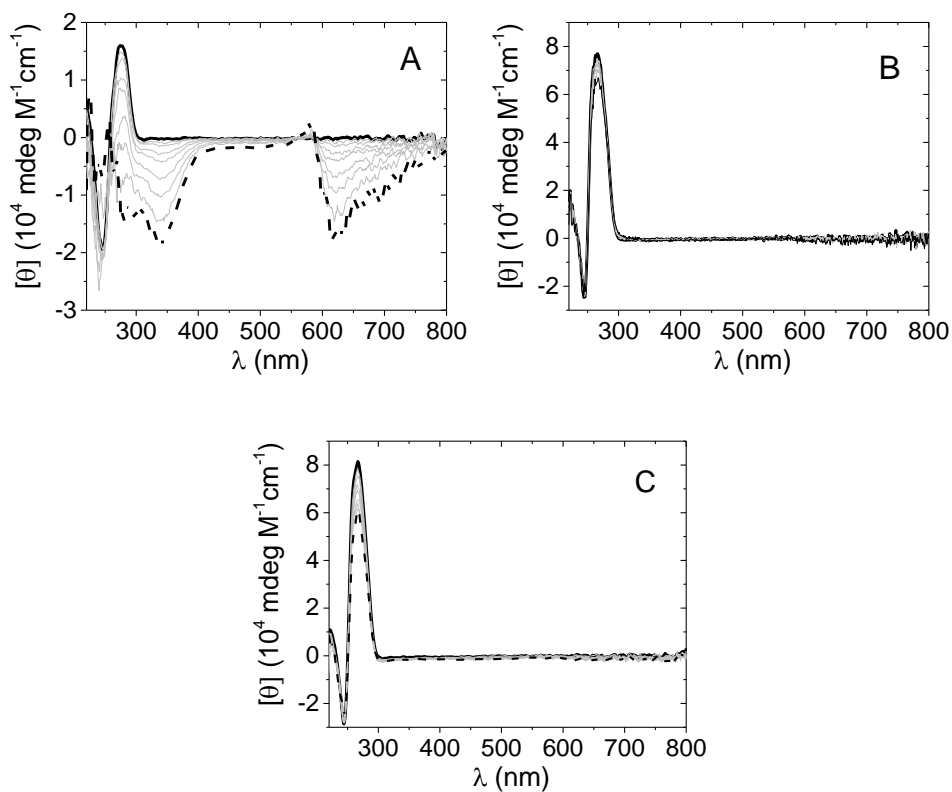


Fig. 5.10. CD spectra of (A) ABTP/*ct*-DNA ($C_{DNA} = 1.05 \times 10^{-4} M$, C_{ABTP} from 0 (solid) to $9.77 \times 10^{-5} M$ (dash)), (B) ABTP/*polyA*·*polyU* ($C_{polyAU} = 7.75 \times 10^{-5} M$, C_{ABTP} from 0 (solid) to $3.33 \times 10^{-5} M$ (dash)) and (C) ABTP/*polyA*·2*polyU* ($C_{polyA2U} = 6.50 \times 10^{-5} M$, C_{ABTP} from 0 (solid) to $8.75 \times 10^{-5} M$ (dash)); NaCl 0.1, NaCac 2.5 mM, pH 7.0, 25.0°C

5.4 Binding to oligonucleotides

ABTP was tested for affinity to different G-quadruplex (G4) structures. The selected G4 all contain three G-tetrads, but have different conformations, being this hybrid in the case of Tel23, antiparallel for CTA22 and parallel for c-myc.^[93] Note that G4s also exhibit different loops orientations (Figure 1.6, Chapter I) with CTA22 having the more exposed lateral surfaces. The aim was thus also to evaluate how the geometrical factors affect the determination of the binding mode.

5.4.1 Spectroscopic titrations

The absorbance titrations were performed in KCl 0.1 M, LiCac 2.5 mM, pH 7.0 at different temperatures. The relevance of the spectral changes immediately suggests strong affinity for all the G4 (Figure 5.11, 5.12 and 5.13) and the band of the adduct (peaked at around $\lambda = 690$ nm) is even much more prominent than in the case of the polynucleotides. Some scattering effects on the shown spectra were corrected according to *Leach and Scheraga*.^[158]

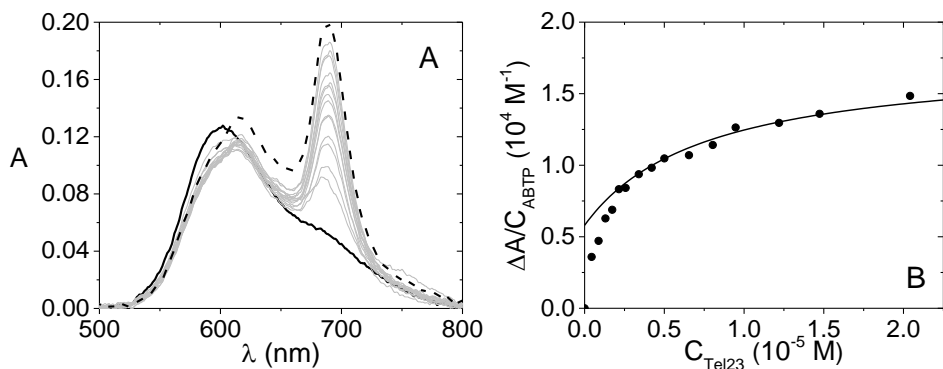


Fig. 5.11. (A) Spectrophotometric titration ABTP/Tel23 and (B) corresponding binding isotherm at $\lambda = 690$ nm ($C_{ABTP} = 5.46 \times 10^{-6}$ M, C_{Tel23} from 0 (solid) to 2.04×10^{-5} M (dash), KCl 0.1 M, LiCac 2.5 mM, pH 7.0, 25.0°C)

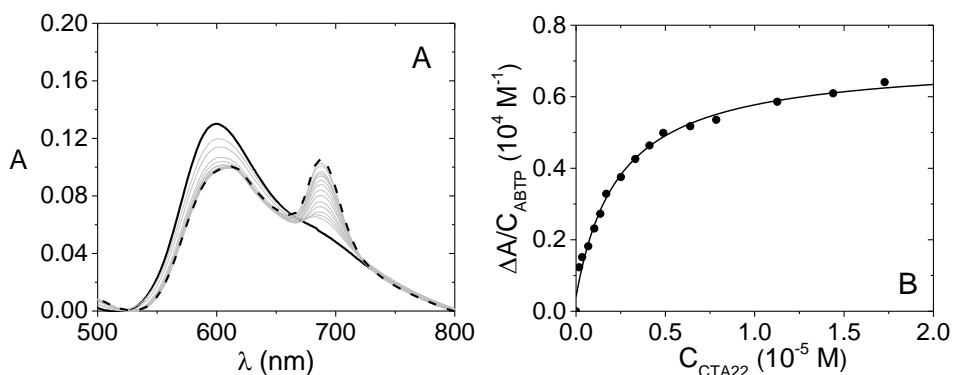


Fig. 5.12. (A) Spectrophotometric titration ABTP/CTA22 and (B) corresponding binding isotherm at $\lambda = 690$ nm ($C_{ABTP} = 5.46 \times 10^{-6}$ M, C_{CTA22} from 0 (solid) to 1.73×10^{-5} M (dash), KCl 0.1 M, LiCac 2.5 mM, pH 7.0, 25.0°C)

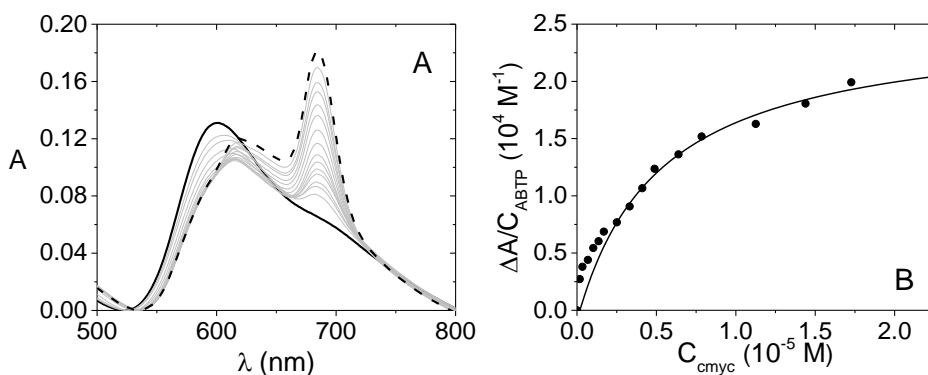


Fig. 5.13. (A) Spectrophotometric titration ABTP/cmymc and (B) corresponding binding isotherm at $\lambda = 690 \text{ nm}$ ($C_{\text{ABTP}} = 5.46 \times 10^{-6} \text{ M}$, C_{cmymc} from 0 (solid) to $1.73 \times 10^{-5} \text{ M}$ (dash)) KCl 0.1 M, LiCac 2.5 mM, pH 7.0, 25.0°C

Equation 5.1 can again be used to evaluate K_{app} for the binding processes: at 25.0 °C we have $K_{\text{app}}(\text{ABTP/Tel23}) = (3.7 \pm 1.2) \times 10^5 \text{ M}^{-1}$, $K_{\text{app}}(\text{ABTP/c-myc}) = (3.6 \pm 1.1) \times 10^5 \text{ M}^{-1}$ and $K_{\text{app}}(\text{ABTP/CTA22}) = (6.1 \pm 2.1) \times 10^5 \text{ M}^{-1}$.

Despite the high errors, it seems that the affinity for CTA22 is somewhat higher with respect to the other G4 forms. Also note that, at the end of titration (same $C_{\text{G4}}/C_{\text{ABTP}}$) the ratio between the two major peaks (A_{690}/A_{615}) is around 1.0 for ABTP/CTA22 and 1.5 for both ABTP/Tel23 and ABTP/c myc (Figure 5.14A). The spectrophotometric behaviour is the result of the type of binding and relevant affinity, together with the coupling with dye-dye aggregation effects. At constant temperature, given the identical starting dye content (C_{ABTP}) and similar biosubstrates, differences in the shapes of the spectrum of the bound species might suggest subtle differences in the bound forms. On the other hand, a significant increase of the binding isotherm amplitude on increasing temperature is observed for CTA22 (Figure 5.14B), which should

be correlated not only to the dependence of K_{app} on T , but also to the contribution of a different dye aggregation extent at the different T .

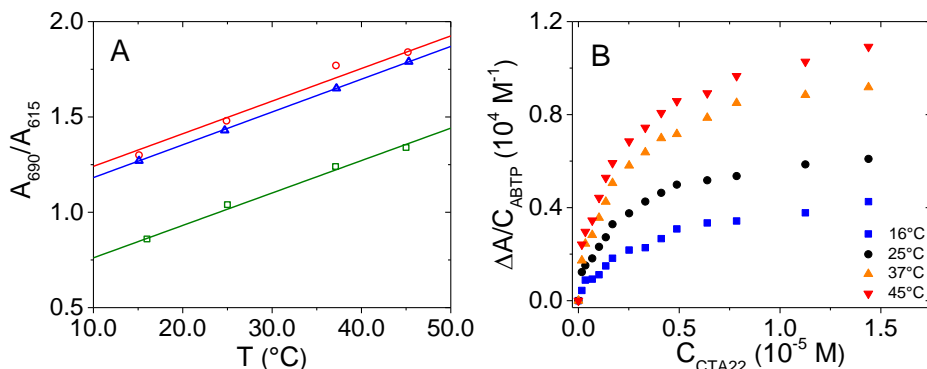


Fig. 15.14. (A) Ratio between the absorbance of the two main peaks of ABTP/Tel23 (\circ), ABTP/CTA22 (\square) and ABTP/c-myc (Δ) at the end of the spectrophotometric titration and (B) dependence of the binding isotherm amplitude ($\lambda = 690 \text{ nm}$) on temperature for ABTP/CTA22 (KCl 0.1 M, LiCac 2.5 mM, pH 7.0)

The *Van't Hoff* equation (Equation 5.2, Figure 5.15) yields $\Delta H_{app} = -7 \pm 3 \text{ kJ/mol}$ for ABTP/Tel23, $\Delta H_{app} = -23 \pm 6 \text{ kJ/mol}$ for ABTP/CTA22 and $\Delta H_{app} = -3 \pm 4 \text{ kJ/mol}$ for ABTP/c-myc. The interaction with G4 results to be less exothermic than that with ct-DNA.

These low values agree with a picture where the dye is externally bound. G4s are stable and rigid structures, which distortion requires a very high energy cost: stacking of the drug on the outer planes of tetrads is often a more probable mode for ligands whereas deep intercalation is a difficult event.^[101] In the case of CTA22, some slightly higher interaction with the internal bases might be at play (higher $|\Delta H_{app}|$), due to subtle differences in the geometrical factors.

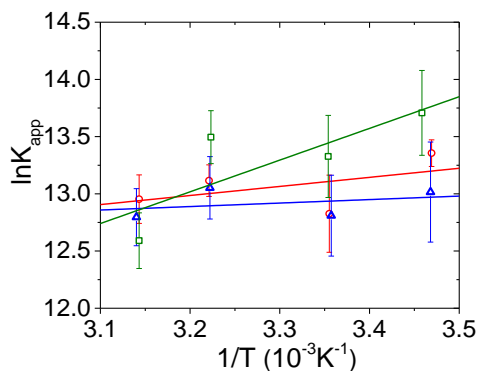


Fig. 5.15. Van't Hoff plot for (○) ABTP/Tel23, (■) ABTP/CTA22 and (△) ABTP/c-myc systems (KCl 0.1 M, LiCac 2.5 mM, pH 7.0)

Interestingly, the thermodynamic parameters for G4s are in line with the general EEC plot for ABTP (Figure 5.16). EEC has been widely observed and reported for protein-ligand interactions (see also Chapter VII, Paragraph 7.3.3) but also for other biosubstrates such as DNA.^{[369],[370]} EEC is typically explained by assuming that if a molecular change in the ligand leads to more and/or tighter van der Waals contacts and H-bonds with the substrate (giving a more negative ΔH), this inevitably leads to reduced mobility/flexibility in either or both components of the interaction, i.e., a reduction in the overall conformational entropy, and that change compensates the enthalpy decrease.^[371] The importance of the rearrangement of water molecules and different hydration has also been evidenced.^{[370],[371]} Despite the somehow high errors on the thermodynamic values, the correlation plot for the ABTP may be assumed to be linear. The slope close to one indicates that the enthalpy gain from the complexation is cancelled out by the entropic loss from the conformational changes caused upon binding (rigid hosts will correspond to

lower slopes).^[372] The intercept of the plot is associated with the degree of desolvation upon binding. Its value is high (around 30 kJ/mol) and very close to the value found in the case of the interaction of a zinc porphyrin to diamines.^[372]

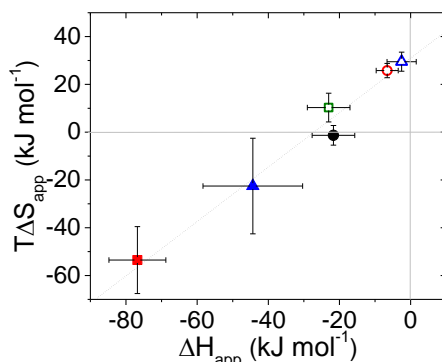


Fig. 5.16. Enthalpy-entropy compensation (EEC) plot for (●) ABTP/ct-DNA, (■) ABTP/polyA-polyU, (▲) ABTP/pola-2polyU (NaCl 0.1 M, NaCac 2.5 mM, pH 7.0, 25.0°C); (○) ABTP/Tel23, (■) ABTP/CTA22 and (△) ABTP/c-myc (KCl 0.1 M, LiCac 2.5 mM, pH 7.0, 25.0°C)

5.4.2 Melting experiments

External binding is also confirmed by the thermal denaturation tests. As c-myc is particularly stable because of its parallel conformation, these melting experiments were performed at KCl 10 mM, whereas Tel23 and CTA22 were tested in KCl 0.1 M, LiCac 2.5 mM, pH 7.0. The melting plots at $\lambda = 295$ nm are reported in Figure 5.20. No stabilisation is observed for the ABTP-G4 complex compared to that of G4 alone (Table 5.2), meaning that no relevant structural modification has occurred.

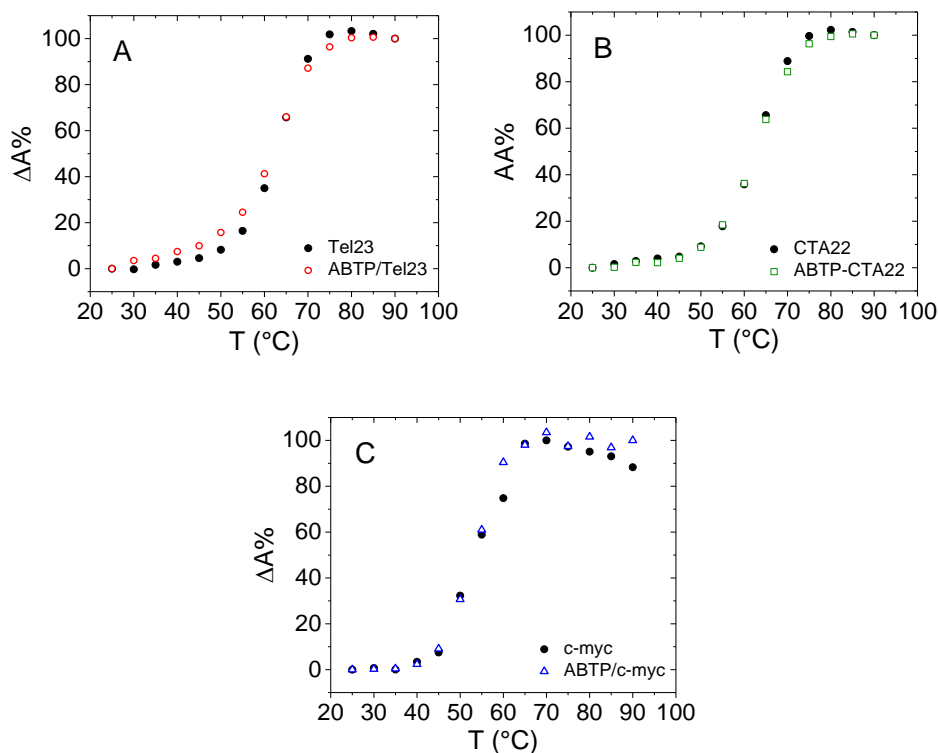


Fig. 5.17. Superimposition of melting curves of (A) ABTP/Tel23 ($C_{Tel23} = 5.49 \times 10^{-6} M$; $C_{Tel23} = 5.51 \times 10^{-6} M$, $C_{ABTP} = 5.45 \times 10^{-6} M$); (B) ABTP/CTA22 ($C_{CTA22} = 5.81 \times 10^{-6} M$; $C_{CTA22} = 5.23 \times 10^{-6} M$, $C_{ABTP} = 5.45 \times 10^{-6} M$); (C) ABTP/c-myc ($C_{c-myc} = 5.81 \times 10^{-6} M$; $C_{c-myc} = 5.23 \times 10^{-6} M$, $C_{ABTP} = 5.45 \times 10^{-6} M$); KCl 0.1 M (10 mM for c-myc), LiCac 2.5 mM, pH 7.0

Tab. 5.2. Melting temperatures of the studied systems (conditions for reactants concentrations as for Figure 5.17)

oligonucleotide	T_m (°C)	T_m (°C)
	$C_D/C_P = 0$	$C_D/C_P = 1$
Tel23	62.7 ± 0.3	62.0 ± 0.4
CTA22	62.6 ± 0.2	62.6 ± 0.2
c-myc	53.2 ± 0.6	53.1 ± 0.3

The melting process of the ABTP-G4 complexes turns out to be reversible, with perfect superimposition between the folding and the unfolding mechanism (Figure 5.18). This means that the presence of ABTP does not affect the G4 structures folding, which are able to come back to their starting conformation.

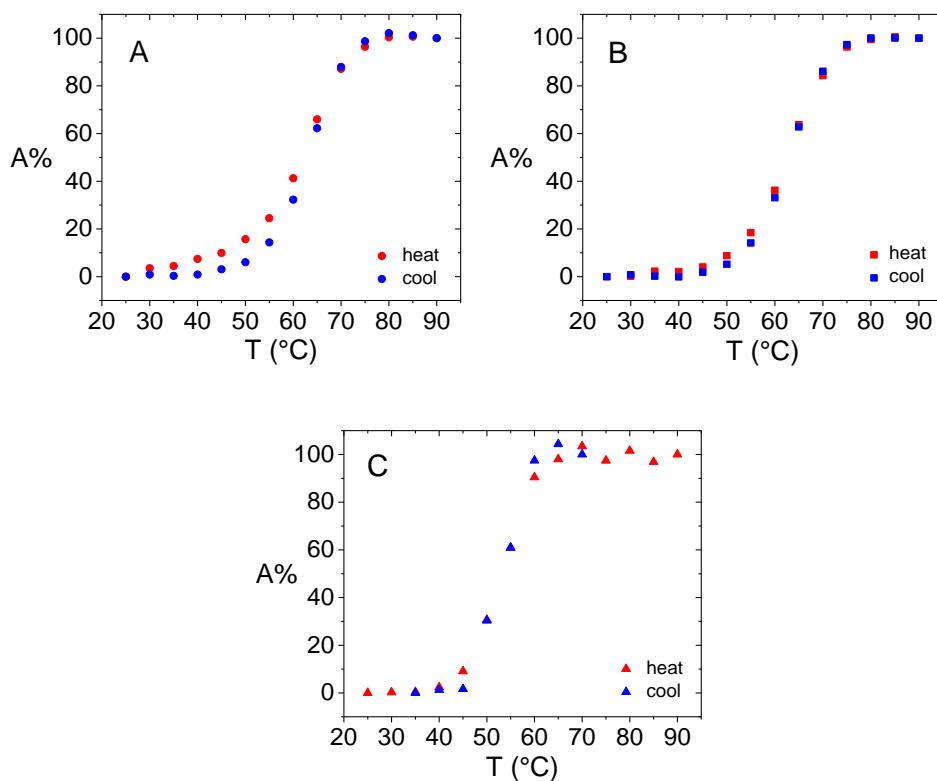


Fig. 5.18. Superimposition of the heating and the cooling curves of (A) ABTP/Tel23, (B) ABTP/CTA22 and (C) ABTP/c-myc (conditions for reactants concentrations as for Figure 5.17)

Figure 5.19 contains the thermal difference spectra (TDS) of the here analysed systems and confirms: (I) that the three G4 have different geometries; (II) that these geometries are not significantly modified in the presence of ABTP.

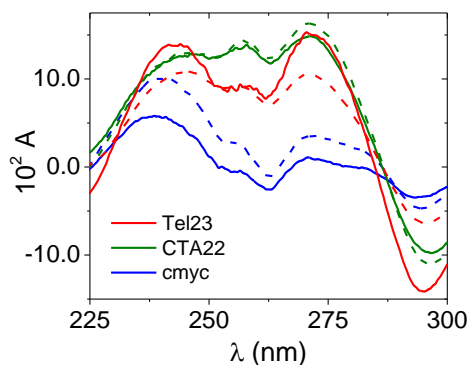


Fig. 5.19. Thermal difference spectra (TDS) for ABTP/Tel23 (red), ABTP/CTA22 (green) and ABTP/c-myc (blue). Continuous lines are related to ABTP/G4 heating process, dashed lines refer to G4 alone; conditions for reactants concentrations as for Figure 5.17

5.5 Conclusions

The here analysed systems are complicated by the superimposition of auto-aggregation effects for the ABTP phthalocyanine. However, under biosubstrate excess conditions and referring to the apparent reaction, we can still gain information on the different mechanistic aspects of the binding process.

ABTP binds to all biosubstrates but with different features. Interaction with both double and triple-stranded RNAs exists and occurs in a different way with respect to ct-DNA. The point of structure-specific nucleic acid-interactive drugs on the basis of the geometrical features is a very interesting

but complex aspect. In these complicate systems, a subtle change in the geometry can have important effects on the binding mode, mixed binding modes are at play and, also, different binding features could become majority depending of the experimental conditions (for instance reagents concentrations).^{[178],[373]} In the case of RNAs external/groove binding is the found active mode. The presence of a wide and swallow minor groove in these A-type polynucleotides could drive external interaction of the wide structure of ABTP. The absence of a precise orientation on the helix surface agrees with the absence of ICD signals. Also, given that the +4 charge of ABTP on the surface can balance the phosphates repulsion, and this produces the significant stabilization found in the ABTP/RNAs melting experiments.

On the other hand, in the case of ct-DNA, the CD experiments strongly indicate dye intercalation. Geometrical constraints support half intercalation which, in turn, would favour inter-strand precipitation by increasing temperature over a certain threshold (melting experiments).

The thermodynamic parameters are difficult to discuss and compare from a strictly numerical point of view in particular due to the superimposition of aggregation effects. However, they confirm the different behaviour between RNAs and DNA. Also, all parameters belong to the same line in an EEC plot indicating the consistency of the different ABTP systems.

On the whole, the dye has a complex reactivity which considers both intercalation and groove/external binding and where the thermodynamic aspects of these two possibilities can be differently balanced in the presence of the different (but always nucleotide-based) biosubstrates.

ABTP is able to externally bind to the analysed G4s. The extended inner π -system of phthalocyanines is 1.0 nm wide, and the G-tetrad is 1.5 nm.^[90] Therefore, in principle, the geometrical constraint for ABTP/G4 surface interaction is nicely fulfilled. However, in the different G4 geometries, the G-

tetrad might be differently hindered by the loops and a different contribution for the electrostatic attraction with the negatively charged loops might be at play. This is true in particular if the phthalocyanine core is functionalised with bulky positively charged residues as in the case of ABTP. The selectivity towards a particular conformation can also be due to the different distortion of the tetrad (for parallel conformations planarity is higher).

Even if more often authors claim selectivity towards parallel forms, this is not always the case. For instance, for N-methyl mesoporphyrin both preference for parallel^[374] or anti-parallel^[375] G4 sequences was demonstrated. In the here presented work, beyond a general affinity for all G4s, ABTP seems to (slightly) prefer CTA22 antiparallel telomeric form, to which it binds differently from the very similar features of the ABTP/Tel23 (hybrid) and ABTP/c-myc (parallel) systems.

Chapter VI

6. The molecular rotor BTATPE

6.1 Introduction

The use of fluorescent probes for detecting biological molecules is a widespread strategy exploited in the biomedical field.^[376] In recent years, the development of sensitive fluorescent sensors has become an interesting challenge for researchers. Useful bioprobes are “turn-on” sensors, whose fluorescence properties are activated by the interaction with the analytes.^[377] Since the emissive properties are related to the electronic distribution, promising fluorophores have been designed by mutually linking several aromatic rings, with the aim of extending the π -conjugated system. Nevertheless, extensive π systems promote aggregation phenomena, which usually quenches light emission (aggregation-caused quenching, ACQ) and limits the applicability of the probes.^[378]

In 2001, *J. Luo et al.* characterized a novel phenomenon exactly opposite to ACQ, called aggregation-induced emission (AIE): some non-emissive dyes can be induced to efficiently emit by aggregates formation.^[379]

Among other AIE luminogens (AIEgens), tetraphenylethene (TPE) derivatives have received high attention thanks to the affordable synthesis, ready functionalization, good photostability and high fluorescence quantum yields.^[380] In TPE, the olefin core (stator) is surrounded by phenyl groups (rotors). In dilute solutions, the phenyl groups undergo dynamic intramolecular rotations, which non-radiatively annihilate the excited state

and make the TPE molecule non-luminescent. Upon aggregation, the dynamic motions of the phenyl groups are greatly restricted owing to the physical constraint. The restriction of the intramolecular rotations enables the molecule to decay through a radiative pathway from the excited state and fluorescence emission is observed.^[381]

Y. Hong et al. (2011) pointed out that for substituted TPE a photo-induced E/Z isomerization process might occur (Figure 6.1).^[381] However, NMR analyses on a Z-pure solution revealed that the random rotations of the phenyl units around the single C-C bond (resulted from the photo-breaking of the double C=C bond) requires energies much higher than those normally employed in a common fluorescence experiment. Therefore, only the photo-accelerated torsional motion of the phenyl groups is considered responsible for TPE fluorescence quenching under normal experimental conditions.

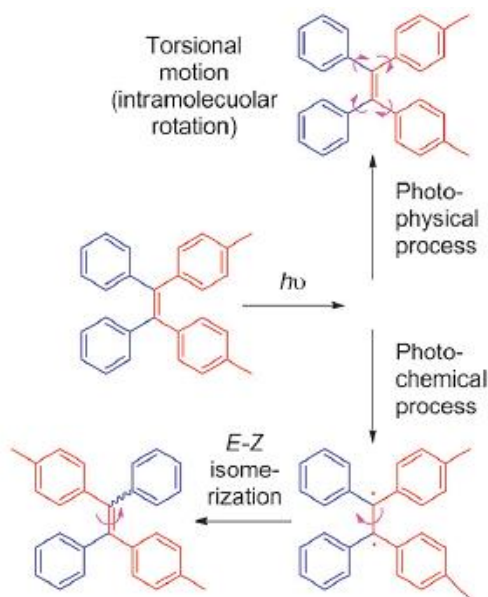


Fig. 6.1. Possible pathways of photo-induced physical and chemical processes (Y. Hong *et al.*, 2011)^[381]

Several TPE derivatives with charged and chelating groups have been prepared and used as “light-on” sensors for detecting and quantifying biopolymers. The explanation of the fluorescence enhancement induced by the addition of the biomolecules concerns the AIE properties. The interaction suppresses the intramolecular rotations of the TPE derivatives, preventing their non-radiative transitions and activating their emissive processes.

1,1,2,2-tetrakis[4-(2-triethylammonioethoxy)phenyl]ethane tetrabromide (TTAPE) was successfully employed in G-quadruplex (G4) recognition: in addition to a prominent enhancement, the emission peak of the AIEgen undergoes a noticeable bathochromic shift (λ_{em} from 400 to 492 nm), allowing easy differentiation from double stranded DNA ($\lambda_{em} = 470$ nm).^[382]

The fluorescence of two non-emissive TPE derivatives bearing alchilammonium-butoxy substituents was found to light-up in presence of natural DNA or protein BSA.^[383] However, the details of the binding mechanism were not elucidated.

Within this context, we propose the synthesis of the TPE derivative (1,2-bis(4-((triethylammonium)butoxy)phenyl)-1,2-tetraphenylethene dibromide, (BTATPE, Figure 6.2)) and the characterization of its binding properties to nucleic acids. The binding mechanism to natural DNA (ct-DNA) was studied mainly through molecular spectroscopies. The synthetic poly(dG)·poly(dC) and poly(dA)·poly(dT) DNAs were employed to investigate the selectivity towards the base pairs, synthetic double poly(rA)·poly(rU) and triple poly(rA)·2poly(rU) helix RNA were tested as well (these species will be called polyG·polyC, polyA·polyT, polyA·polyU and polyA·2polyrU for simplicity from now on).

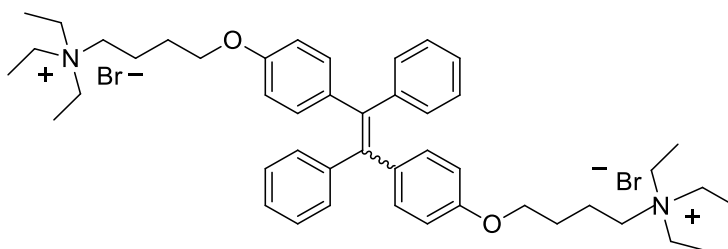


Fig. 6.2. Molecular structure of BTATPE

6.2 Synthesis

As first approach, the group of Prof. A. Pucci tried to synthesize 1,2-bis(4-(4-(N,N,N-triethylammonium)butoxy)phenyl)-1,2-diphenylethene dibromide (BTATPE) on the basis of the common procedure described by *Y. Dong et al.* (2014),^[384] i.e. by the reaction of 1,2-bis(4-hydroxyphenyl)-1,2-diphenylethene (TPE-DOH) with 1,4-dibromobutane in acetone and in the presence of K_2CO_3 . Thin layer chromatographic analyses revealed the presence of high amount of unreacted TPE-DOH, so that the synthetic approach was changed and optimized according to the reaction scheme reported in Figure 6.3.

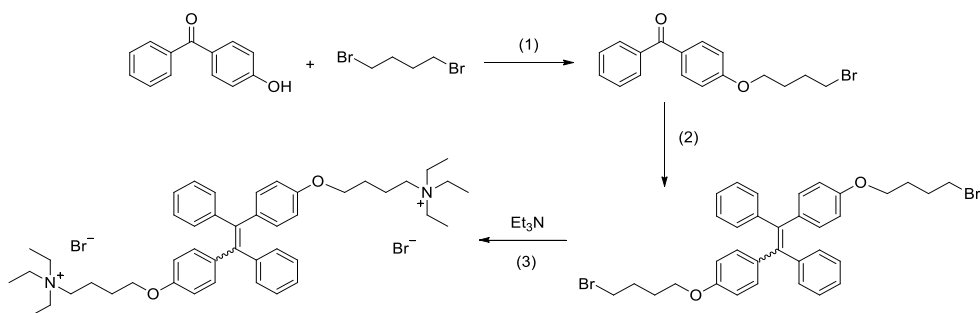


Fig. 6.3. Reaction scheme for the synthesis of BTATPE

(1) The etherification of the 4-hydroxybenzophenone to 4-(4-bromobutoxy)benzophenone was obtained in acetonitrile through the formation of the alkoxide ion in presence of K_2CO_3 , followed by the addition of a stoichiometric amount of 1,4-dibromobutane (24h reflux). The

purification was gained through recrystallization (toluene:hexane 1:2) and the product was characterized by NMR studies resulting in a 48% yield.

(2) A McMurry coupling reaction was exploited to obtain 1,2-bis(4-(4-bromobutoxy)phenyl)-1,2-diphenylethene (DBBTPE). 4-(4-bromobutoxy)benzophenone was reduced to the corresponding alkene in the presence of TiCl_4 and Zn (THF, reflux). The crude product was purified through automated flash chromatography equipped with a silica column and using a mixture of petroleum ether and dichloromethane (gradient composition, 90:10 to 20:80). Pure DBBTPE was obtained as a yellow viscous liquid with a yield of 27% (according to NMR spectroscopy). The McMurry reaction results in poor stereo-selectivity and a mixture of (E)- and (Z)-isomers is generally obtained when the substituent groups of the carbonyl unit have similar dimensions.^[385] According to the steric hindrance of the 4-bromobutoxy group, a fraction larger than 60% of (E)-DBBTPE is expected.^[386]

(3) The DBBTPE bromine atoms were substituted with triethylammonium groups by a quaternization reaction with Et_3N in THF/ H_2O (72h reflux), resulting in the final product BTATPE. The purification was performed by combining solvent extraction with Et_2O and recrystallization in CH_2Cl_2 : Et_2O (1:6). The product was obtained as a yellow sticky solid with a yield of 58%. BTATPE was characterized by the means of NMR spectroscopy and UPLC-MS analyses. The results highlighted the presence (less than 10%) of the side-product of the hydrolysis of DBBTPE (step 2). The reaction of mono hydrolysis of DBBTPE is consistent with literature reports.^{[387],[388]} The monohydrated impurity is water-soluble as well as BTATPE, so that it could not be separated.

Given the very good purity (> 90%) the final product was employed for the further binding studies.

6.3 Spectroscopic characterization

Preliminary to the binding studies, the optical properties of BTATPE were characterized in water solution under physiological conditions (NaCl 0.1 M, NaCac 2.5 mM, pH 7.0). The stability of the optical variables was checked by recording absorbance and fluorescence signals over the timescale of the experiments. Both BTATPE signals resulted to be stable over 2 hours, even under irradiation.

The UV-vis absorbance spectrum shows two characteristic absorption bands with maxima at $\lambda = 248$ nm and $\lambda = 314$ nm (Figure 6.4A). Given the possible tendency to undergo auto-aggregation, the linearity of the *Lambert and Beer* law was checked by recording absorbance spectra for increasing concentrations of BTATPE. The linear correlation between absorbance and concentration (Figure 6.4B) does not highlight evident spectral distortions. On the other hand, the ratio between the absorbance intensities at different wavelengths does not seem perfectly constant (Figure 6.4C)

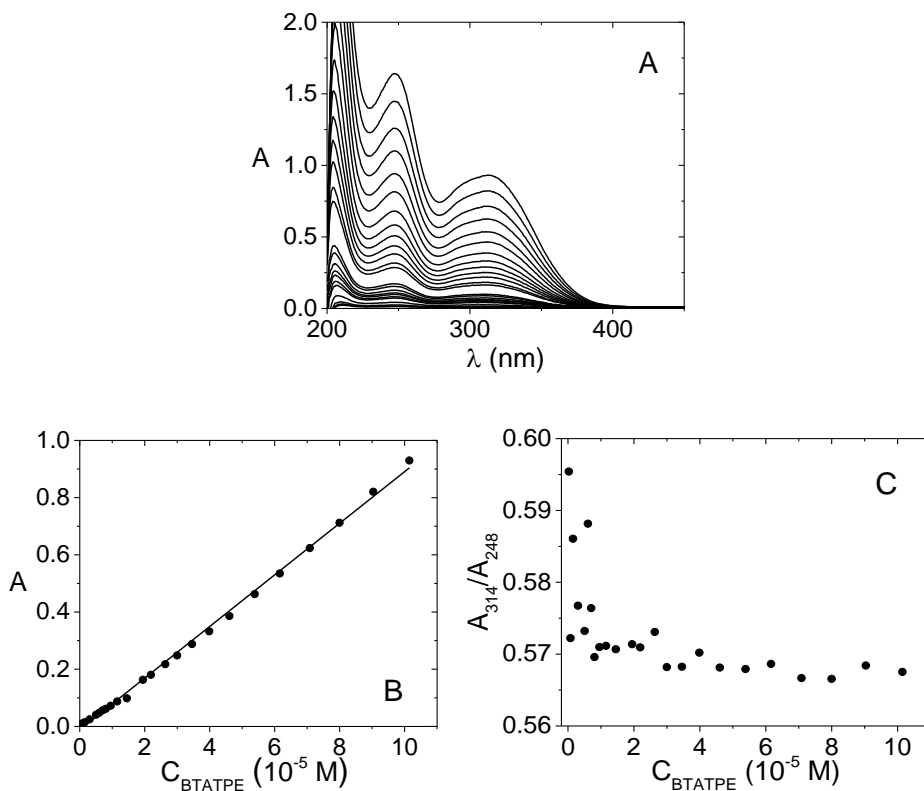


Fig. 6.4. (A) Absorbance spectra of TBATPE, (B) Lambert Beer's plot at $\lambda = 314$ nm and (C) A_{314}/A_{248} ratios (C_{BTATPE} from 2.53×10^{-7} to 1.01×10^{-4} M, NaCl 0.1 M, NaCac 2.5 mM, pH 7.0, 25.0°C)

The high sensitivity of fluorescence spectroscopy, and in particular in the case AIEgens as BTATPE, can be exploited to elucidate this topic. The 3D fluorescence spectrum of BTATPE (Figure 6.5A) shows a main emission band at $\lambda_{\text{em}} = 390$ nm when the system is excited at $\lambda_{\text{exc}} = 260$ nm and another signal at $\lambda_{\text{em}} = 473$ nm for $\lambda_{\text{exc}} > 280$ nm. The excitation of the sample at a wavelength where the polynucleotides do strongly absorb can cause non-negligible inner-filter effects and significant problems in data manipulation. Moreover, upon

the addition of ct-DNA, a strong enhancement of the emission signal at $\lambda_{em} = 473$ nm is observed and persist even for $\lambda_{exc} > 320$ nm (Figure 6.5B). This is the signal on which we focused our attention.

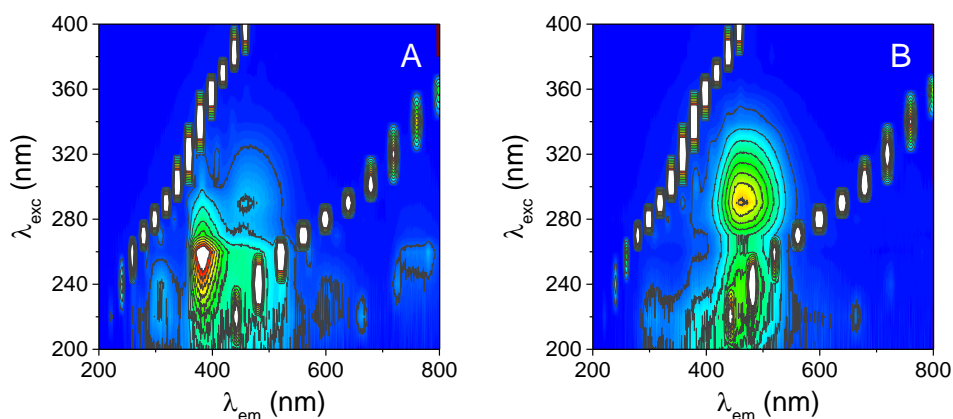


Fig. 6.5. Fluorescence 3D spectrum of (A) BTATPE 7.8×10^{-6} M and (B) BTATPE 7.5×10^{-6} M + ct-DNA 8.7×10^{-5} M (NaCl 0.1 M, NaCac 2.5 mM, pH 7.0, 25.0°C, slits exc/em 5/5 nm). Intensity scale from 0 to 500 a.u., level increment for the contour lines 50 a.u.

The presence of a fluorescence response for BTATPE alone (Figure 6.5A and 6.6) highlights that the mobility of BTATPE is restricted by the establishment of some dye-dye interactions also when the probe is alone in solution. Similar behaviour has been previously observed for TPE derivatives by changing the composition of the solvent.^[382]

At $\lambda_{exc} = 327$ nm and $\lambda_{em} = 473$ nm (Figure 6.6), considering that the standard deviation of the blank is $\sigma = 3$ (a.u.) and a limit of detection of $F_{blank} + 3\sigma$, it turns out that fluorescence can be detected until $C_{BTATPE} = 4.92 \times 10^{-7}$ M. Given that the monomer is not emissive, it can be concluded that, even under these

so diluted conditions, the likely very limited amount of aggregate is anyway able to produce some signal. This finding strengthens the “light-up” power of this AIE probe.

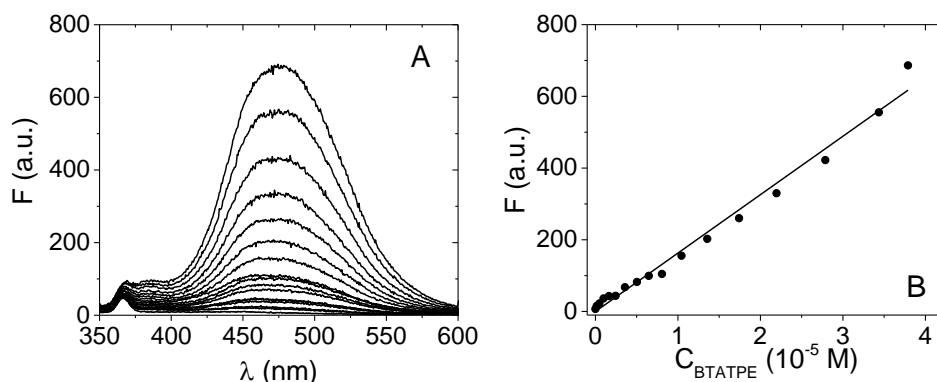


Fig. 6.6. (A) Fluorescence spectra and (B) F vs. C_{BTATPE} plot (C_{BTATPE} from 1.64×10^{-7} to 3.79×10^{-5} M, NaCl 0.1 M, NaCac 2.5 mM, pH 7.0, 25.0°C, $\lambda_{\text{exc}} = 327$ nm, $\lambda_{\text{em}} = 473$ nm, slits exc/em 5/5 nm)

6.4 Binding studies

In order to evaluate BTATPE binding affinity for different polynucleotides, spectrofluorometric titrations were performed. Different temperatures and ionic strengths were investigated. Every experiment was repeated at least twice. In addition, to optimize the signal/noise ratio, the fluorescence measurement was averaged on five runs.

Natural DNA

Note that absorbance titrations were tested and found to be inappropriate to analyse BTATPE affinity to DNA. The absorbance range of BTATPE was too

close to that of DNA to enable a robust analysis of the binding effects on the signal shapes (Figure 6.7).

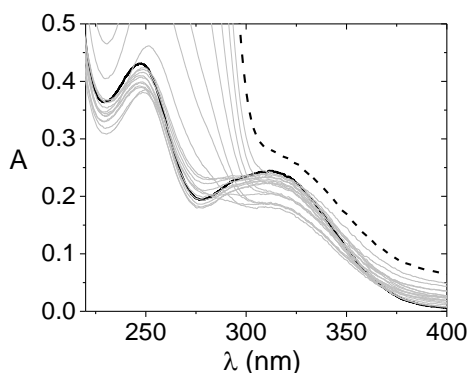


Fig. 6.7. Spectrophotometric titration of TBATPE/DNA ($C_{TBATPE} = 3.05 \times 10^{-5} M$, C_{DNA} from 0 (solid) to $2.05 \times 10^{-4} M$ (dash), NaCl 0.1 M, NaCac 2.5 mM, pH 7.0, 25.0°C)

Fluorescence is obviously the better approach to be used and fluorescence spectroscopy was indeed successfully exploited for this purpose. The significant fluorescence enhancement shown in Figure 6.5B is here evidenced again and suggests that the rotational motions of BTATPE are deeply restricted as a consequence of the interaction with ct-DNA.^[383] Figure 6.8 shows the fluorescence changes observed by titrating BTATPE with increasing amounts of ct-DNA.

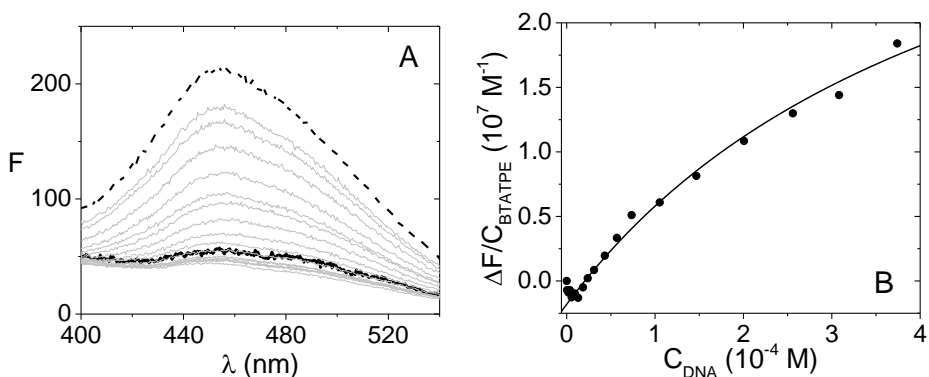


Fig. 6.8. (A) Spectrophotometric titration of TBATPE/DNA and (B) corresponding binding isotherm at $\lambda_{em} = 473 \text{ nm}$ ($C_{TBATPE} = 7.87 \times 10^{-6} \text{ M}$, C_{DNA} from 0 (solid) to $3.74 \times 10^{-4} \text{ M}$ (dash), NaCl 0.1 M, NaCac 2.5 mM, pH 7.0, 30.0°C, $\lambda_{exc} = 327 \text{ nm}$, slits exc/em 5/5 nm)

Within the approximation of a 1:1 stoichiometry model, the data were fitted with Equation 6.1.

$$\frac{\Delta F}{C_D} = \frac{\Delta\phi \cdot K \cdot [P]}{1 + K \cdot \Delta\phi} + c \quad (6.1)$$

For the detailed description of the equation refer to Chapter IV – Equation 4.4 and Appendix I. The 1:1 model could be considered as a simplified approximation and in that sense K would be an apparent constant. Note, however, that the equation above correctly fits the experimental trends. Other equations and models were tried with no evidence of significant improvements.

The results are reported in Table 6.1.

Tab. 6.1. *Equilibrium binding constants for BTATPE/DNA at different temperatures*

(NaCl 0.1 M, NaCac 2.5 mM, pH 7.0)

T (°C)	K (M ⁻¹)
17.9	$(3.7 \pm 0.2) \times 10^3$
25.0	$(2.7 \pm 0.4) \times 10^3$
30.0	$(2.2 \pm 0.3) \times 10^3$
36.6	$(1.8 \pm 0.5) \times 10^3$

The *Van't Hoff* plot (Figure 6.9) was employed in order to determine the enthalpy ΔH and the entropy ΔS variations of the binding process: we have $\Delta H = -29$ kJ/mol and $\Delta S = 33$ J/mol·K.

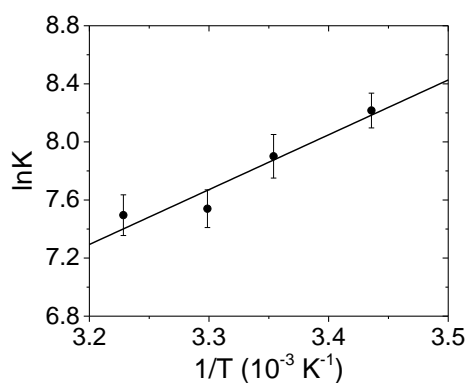


Fig. 6.9. *Van't Hoff plot for BTATPE/DNA (NaCl 0.1 M, NaCac 2.5 mM, pH 7.0)*

Given the positively charged substituents of BTATPE (total charge +2), the binding to a negatively charged polynucleotide should be connected to a significant electrostatic contribution. Therefore, the effect of the ionic strength was evaluated with titrations at different NaCl concentrations (examples in Figure 6.10A and 6.10B). The corresponding binding constants are reported in Table 6.2.

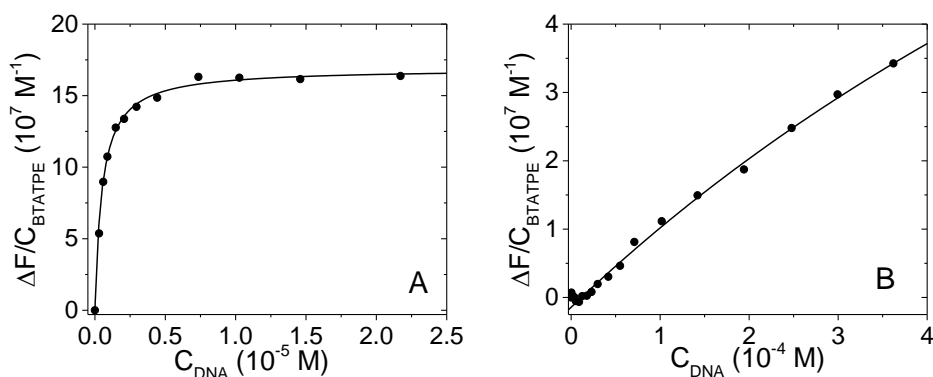


Fig. 6.10. Binding isotherm at $\lambda_{em} = 473$ nm, $\lambda_{exc} = 327$ nm, slits exc/em 5/5 nm: (A)

$C_{BTATPE} = 1.99 \times 10^{-6}$ M, C_{DNA} from 0 to 2.17×10^{-5} M, NaCac 2.5 mM, pH 7.0, 25.0°C and (B) $C_{BTATPE} = 7.87 \times 10^{-6}$ M, C_{DNA} from 0 to 3.62×10^{-4} M, NaCl 1 M, NaCac 2.5 mM, pH 7.0, 25.0°C

Tab. 6.2 Equilibrium binding constants for BTATPE/DNA at different salt content
(NaCac 2.5 mM, pH 7.0, 25.0°C)

NaCl (M)	K (M ⁻¹)
0	> 10 ⁷
0.01	(2.5 ± 0.5)×10 ⁴
0.05	(4.5 ± 0.3)×10 ³
0.1	(2.7 ± 0.4)×10 ³
0.5	(6.6 ± 0.7)×10 ²
1	(7.1 ± 0.8)×10 ²

A strong dependence on the ionic strength is here highlighted for ct-DNA binding, ranging from a quantitative reaction in the absence of NaCl to a low binding constants of $(7.1 \pm 0.8) \times 10^2$ when the NaCl content is raised to 1 M. This evidence underlines the crucial importance of the electrostatic forces in driving the interaction and the involvement of the charged BTATPE substituents in the formation of the adduct.

To explain the different behavior in the presence of different salt content we might refer to the *Record* model^[389] which takes into account that the sodium ions could either compete with the dye for the binding to the phosphate groups and/or produce a shielding effect on the electrostatic attraction between the two species. On this basis, dye interaction with the polynucleotide can be intended as a process where some of the positive counter-ions situated in the vicinity of the polynucleotide has to move far away from the ionic cloud. It can thus be written as the Equation 6.2 below:



whose equilibrium constant $K' = \{[\text{Na}^+]^m \times [\text{PD}]\} / \{[\text{P}(\text{Na}^+)_m] \times [\text{D}]\} = K \times [\text{Na}^+]^m$. On this basis we obtain Equation 6.3:

$$\log K = -m \cdot \log [\text{Na}^+] + \log K' \quad (6.3)$$

where K is the binding constant, $[\text{Na}^+]$ is the total sodium ions concentration, K' is the binding constant in the absence of electrostatic effects and m corresponds to $m'\Psi$ where m' is the number of phosphodiester residues occupied by one ligand and Ψ is the extent of DNA charge shielded by counter-ions. For DNA, $m'\Psi$ represents the number of condensed sodium ion displaced by one ligand molecule. Furthermore, the value of Ψ for DNA is equal to 0.88, so that $m \approx m'$.^[390]

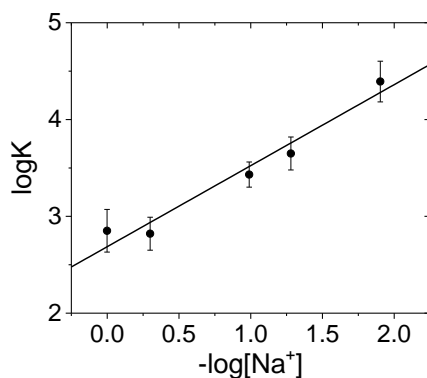


Fig. 6.11 Record's plot (*NaCl* 0-0.01-0.05-0.1-0.5 M, *NaCac* 2.5 mM, pH 7.0, 25.0°C)

Figure 6.11 collects the results: the slope of the plot corresponds to $m = 0.83$, whereas from the intercept a value of $K' = 2.68 \times 10^4 \text{ M}^{-1}$ is obtained. Note that m is lower than the actual +2 charge of BTATPE. This result agrees with the high mobility of the substituents as well as of the large dimension of the BTATPE core: the positively charged arms might be arranged relatively far from the inner electrostatic cloud (phosphodiester backbone) so that their charge is only partially detected.

However, the actual arrangement of BTATPE is quite challenging to determine. On the basis of circular dichroism (CD) measurements (Figure 6.12) we can suppose that intercalation is excluded. First, no induced CD signal is observed: it would had appeared around 312 nm which is the maximum absorbance of BTATPE. Also, the CD bands of DNA show only minor changes by the addition of the ligand and would, oppositely, had undergone significant changes upon intercalation.

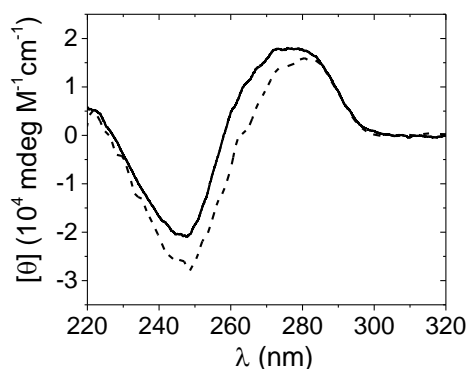


Fig. 6.12 CD spectra of DNA (solid) and DNA + BTATPE (dash) ($C_{DNA} = 7.80 \times 10^{-5} \text{ M}$, $C_{BTATPE} = 6.25 \times 10^{-5} \text{ M}$, NaCl 0.1 M, NaCac 2.5 mM, pH 7.0, 25.0°C)

Viscosity measurements were also performed (Figure 6.13). Serial and known amounts of BTATPE were added directly into the bulb containing DNA and the flow times were measured for each addition. In order to check possible dilution effects, control experiments were performed by adding same volumes of the buffered solvent to the DNA solution. The flow times (t) were used to calculate the relative viscosity (η/η_0) of the solutions, directly related to DNA elongation (Equation 6.4, see Appendix IV).

$$\left(\frac{\eta}{\eta_0}\right)^{\frac{1}{3}} = \left(\frac{t_{\text{DNA+BTATPE}} - t_{\text{solvent}}}{t_{\text{DNA}} - t_{\text{solvent}}}\right)^{\frac{1}{3}} = \frac{L}{L_0} \quad (6.4)$$

The variation of the DNA length (L) with respect to the initial value (L_0) as a function of the C_D/C_P ratio is a quantitative measurement of the effect of the ligand binding. Unfortunately, BTATPE showed also surfactant properties. Some foam was observed also by naked eyes for $C_{\text{BTATPE}}/C_{\text{DNA}} > 0.1$, so that the viscosity decrease occurring above this threshold might be not ascribable to the binding. The small ascending trend occurring at the lowest $C_{\text{BTATPE}}/C_{\text{DNA}}$ values is not robust enough to corroborate incontrovertible conclusions. However, it might be also commented that an intercalator as EtBr would had produced higher elongations even at $C_{\text{EtBr}}/C_{\text{DNA}} < 0.1$.^[391] On this basis, an external binding should again be considered the most probable option.

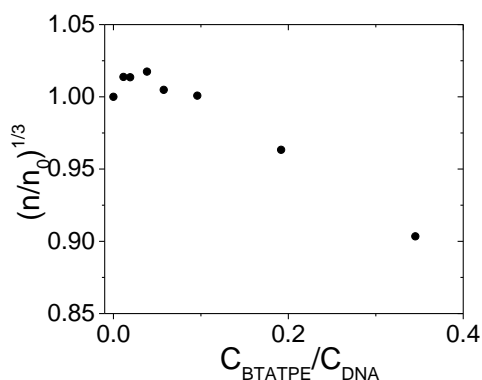


Fig. 6.13 Relative viscosity vs. C_{BTATPE}/C_{DNA} ratios plot ($C_{DNA}^{\circ} = 1.90 \times 10^{-4} M$, C_{BTATPE} from 0 to $1.23 \times 10^{-4} M$, NaCl 0.1 M, NaCac 2.5 mM, pH 7.0, 25.0°C)

polyG·polyC and polyA·polyT

The binding of BTATPE to the homopolymeric polyG·polyC and polyA·polyT was firstly studied under physiological conditions (NaCl 0.1 M, NaCac 2.5 mM, pH 7.0) and the fluorescence spectra together with the binding isotherms are reported in Figure 6.14 and Figure 6.15.

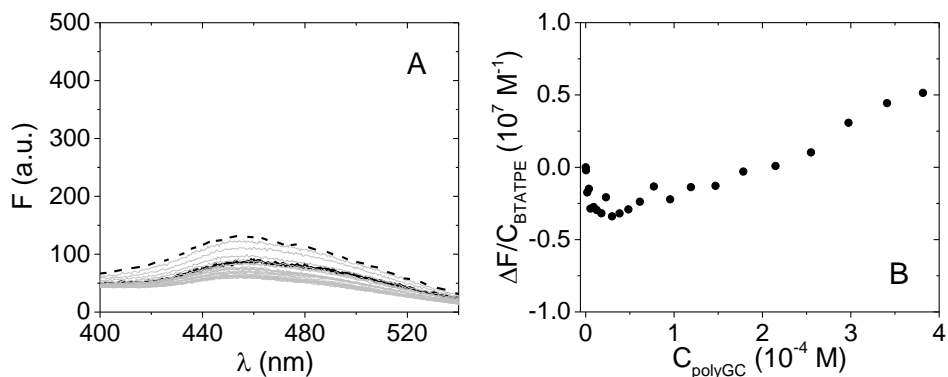


Fig. 6.14 (A) Spectrophotometric titration of TBATPE/polyG·polyC and (B) corresponding binding isotherm at $\lambda_{em} = 473$ nm ($C_{TBATPE} = 7.87 \times 10^{-6}$ M, C_{polyGC} from 0 (solid) M to 3.82×10^{-4} M (dash), NaCl 0.1 M, NaCac 2.5 mM, pH 7.0, 25.0°C, $\lambda_{exc} = 327$ nm, slits exc/em 5/5 nm)

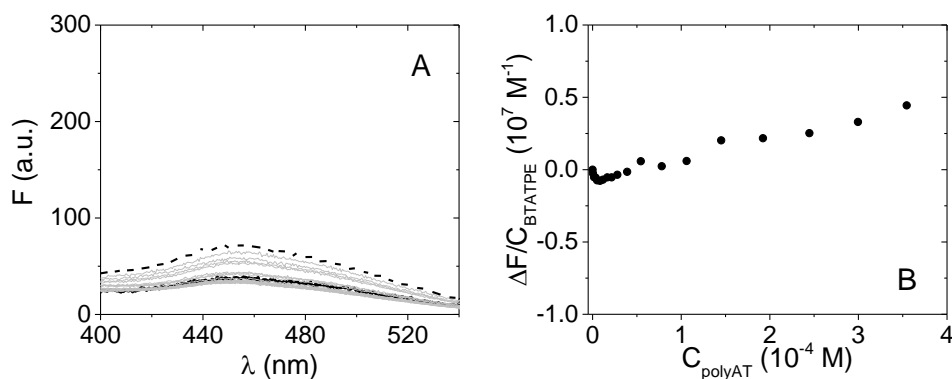


Fig. 6.15 (A) Spectrophotometric titration of TBATPE/polyA·polyT and (B) corresponding binding isotherm at $\lambda_{em} = 473$ nm ($C_{TBATPE} = 7.87 \times 10^{-6}$ M, C_{polyAT} from 0 (solid) M to 3.55×10^{-4} M (dash), NaCl 0.1 M, NaCac 2.5 mM, pH 7.0, 25.0°C, $\lambda_{exc} = 327$ nm, slits exc/em 5/5 nm)

At first sight, BTATPE does not seem to show significant affinity for none of the homopolymeric nucleotides. On the other hand, if the experiments are repeated in the absence of NaCl, the occurrence of a binding is clearly observed (Figure 6.16 and 6.17).

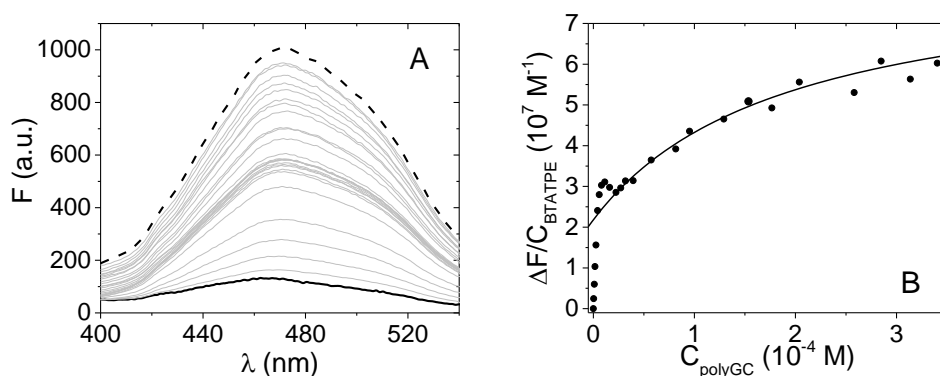


Fig. 6.16 (A) Spectrophotometric titration of TBATPE/polyG-polyC and (B) corresponding binding isotherm at $\lambda_{em} = 473$ nm ($C_{\text{TBATPE}} = 1.46 \times 10^{-5}$ M, C_{polyGC} from 0 (solid) to 3.40×10^{-4} M (dash), NaCac 2.5 mM, pH 7.0, 25.0°C, $\lambda_{exc} = 327$ nm, slits exc/em 5/5 nm)

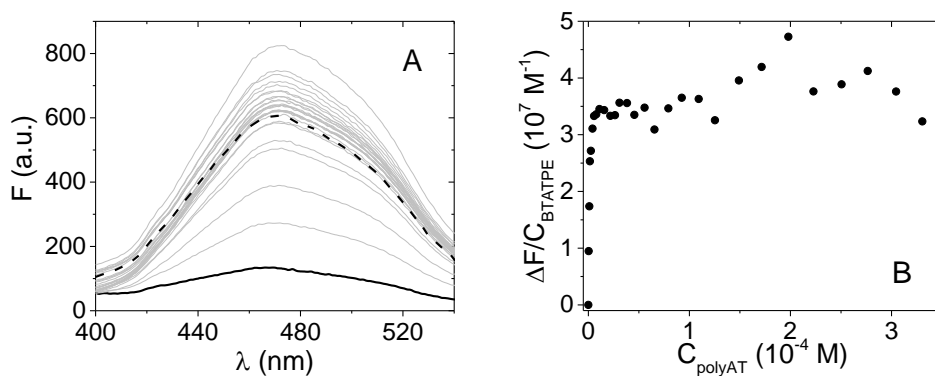


Fig. 6.17. (A) Spectrophotometric titration of TBATPE/polyA-polyT and (B) corresponding binding isotherm at $\lambda_{em} = 473$ nm ($C_{\text{TBATPE}} = 1.46 \times 10^{-5}$ M, C_{polyAT} from 0 (solid) to 3.30×10^{-4} M (dash), NaCac 2.5 mM, pH 7.0, 25.0°C, $\lambda_{exc} = 327$ nm, slits exc/em 5/5 nm)

For polyG·polyC, the binding constant calculated with Equation 6.1 in NaCac 2.5 mM results to be $(5.6 \pm 1) \times 10^3 \text{ M}^{-1}$ (K of DNA being $(4.8 \pm 0.8) \times 10^3 \text{ M}^{-1}$). Concerning polydA·polyT, the signal was particularly unstable and thus, despite the fluorescence enhancement observed, this abnormal behaviour did not allow the binding constant to be calculated robustly. On the other hand, an important result is that, in the case of synthetic DNAs, the dependence of the binding on the salt content is even stronger than that observed for ct-DNA. This behaviour would result in a higher slope of the *Record* plot, suggesting that the charged substituents might be arranged in a different way, probably closer to the phosphodiester backbone.

RNA: polyA·polyU and polyA·2polyU

Concerning the spectrofluorimetric titrations with synthetic RNA polyA·polyU and polyA·2polyU, no significant fluorescence variation is recorded for any of the RNA biotargets in NaCl 0.1 M, NaCac 2.5 mM, pH 7.0 (Figure 6.18 and 6.19).

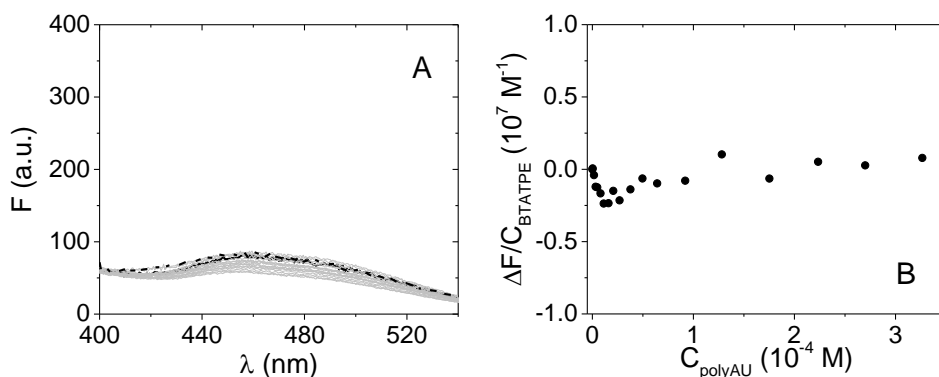


Fig. 6.18. (A) Spectrophotometric titration of TBATPE/polyA·polyU and (B) corresponding binding isotherm at $\lambda_{em} = 473 \text{ nm}$ ($C_{\text{TBATPE}} = 7.87 \times 10^{-6} \text{ M}$, C_{polyAU} from 0 (solid) to $3.27 \times 10^{-4} \text{ M}$ (dash), NaCl 0.1 M, NaCac 2.5 mM, pH 7.0, 25.0°C , $\lambda_{exc} = 327 \text{ nm}$, slits exc/em 5/5 nm)

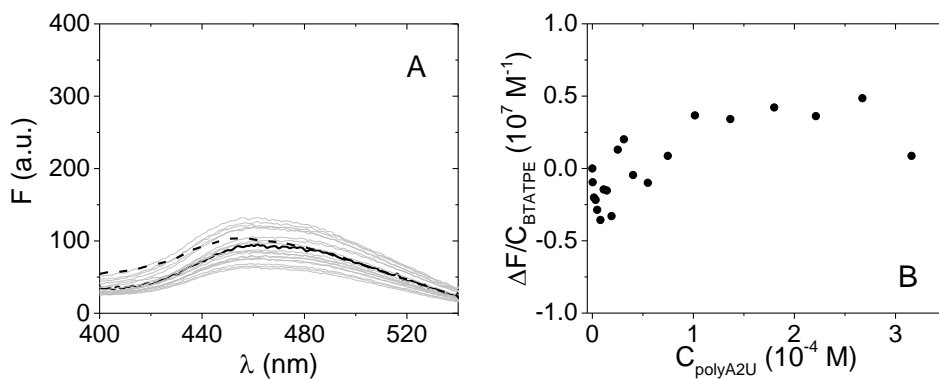


Fig. 6.19. (A) Spectrophotometric titration of TBATPE/polyA·2polyU and (B) corresponding binding isotherm at $\lambda_{em} = 473 \text{ nm}$ ($C_{\text{TBATPE}} = 7.87 \times 10^{-6} \text{ M}$, C_{polyA2U} from 0 (solid) to $3.16 \times 10^{-4} \text{ M}$ (dash), NaCl 0.1 M, NaCac 2.5 mM, pH 7.0, 25.0°C , $\lambda_{exc} = 327 \text{ nm}$, slits exc/em 5/5 nm)

The possibility of investigating the interaction with polyA·2polyU at lower salt content is ruled out by the fact that the formation of the triple helix is ensured only at NaCl 0.1 M.^[31]

6.5 UV Melting experiments

UV melting experiments allowed us to evaluate the stabilising effects induced by BTATPE on the polynucleotides' structures. The denaturation of the natural and the synthetic DNAs had to be performed in the absence of NaCl (NaCac 2.5 mM, pH 7.0), as the low salt content enables the melting temperature of ct-DNA to drop down from above 80°C to less than 60°C, ensuring the possible stabilising effect of the ligand to be better measured.

Table 6.3 reports the melting temperatures of the nucleic acids together with those of the BTATPE/polynucleotides mixtures. The T_m of ct-DNA (41.9% mole G-C and 58.1% mole A-T)^[280] is obviously located between those of its components. The higher T_m of the G-C base pairs is ascribable to the higher energy required to break the 3 H-bonds as compared to the 2 H-bonds of the A-T couple.^[171]

The stabilising effect of BTATPE on DNAs is very prominent. On the basis of the previously obtained results, the high values of ΔT_m cannot be explained with intercalation. We can hypothesise that the positively charged arms of BTATPE strongly interact with the sugar-phosphate backbone by tightening the DNA strands. This stable enlacing prevents the unfolding of the double helix. For the synthetic DNAs, the stabilisation is even stronger than that observed for ct-DNA, in agreement with the previous hypothesis speculated on the basis of the salt content dependence: the charged arms of BTATPE are proposed to be located closer to the synthetic DNA backbones, so that the

binding results tighter. On the contrary, no significant variation of the melting temperatures of the RNAs is observed upon the addition of BTATPE, neither in the absence of NaCl. These results confirm the scale of affinity previously evidenced through the spectrofluorometric titrations.

Tab. 6.3. Melting temperature of BTATPE/polynucleotide mixtures ($C_{DNA} = 2.2 \times 10^{-5} M$, $C_{polyGC} = C_{polyAT} = C_{polyAU} = C_{polyA2U} = 1.3 \times 10^{-5} M$; NaCac 2.5 mM, pH 7.0)

	polynucleotide	T_m (°C) $C_D/C_P = 0$	T_m (°C) $C_D/C_P = 1$	ΔT_m (°C)
NaCl 0 M	<i>ct-DNA</i>	56.8 ± 0.5	74.5 ± 0.5	$+17.7 \pm 1.0$
	<i>polyG·polyC</i>	67.2 ± 0.2	> 95	> +27.8
	<i>polyA·polyT</i>	37.9 ± 0.6	66.1 ± 0.2	$+28.2 \pm 0.8$
	<i>polyA·polyU</i>	36.1 ± 0.4	42.8 ± 0.4	$+6.7 \pm 0.8$
NaCl 0.1 M	<i>polyA·polyU</i>	55.5 ± 0.1	56.6 ± 0.4	$+1.1 \pm 0.5$
	<i>polyA·2polyU</i>	54.1 ± 0.4	54.6 ± 0.4	$+0.5 \pm 0.8$

6.7 Conclusions

The here presented study aims to provide a description of BTATPE binding to different nucleic acids. The AIE properties of BTATPE were exploited in the spectrofluorometric tests, as a significant enhancement of the fluorescence signal was observed upon the addition of the interacting biosubstrate.

BTATPE does bind natural DNA with a binding constant strongly dependent on the ionic strength, but persistent even when the NaCl content is raised to 1 M. The *Record* plot demonstrates that the overall charge is only partially detected (+0.8 vs. the actual +2 charge), in agreement with a picture in which the positive arms of BTATPE are mobile and located relatively far from the phosphate groups. The hypothesis of an external binding is corroborated by the circular dichroism data and by the viscosity measurements. Moreover, the binding results in a relevant thermal stabilisation of the double helix ($\Delta T_m = +17.7 \pm 1.0$ °C), suggesting that BTATPE might join the two DNA strands. This effect is even more evident in the case of the synthetic DNAs polyG·polyC and polyA·polyT. The high values of the ΔT_m (> 28°C) and the strong dependence on the salt content (even greater than that of ct-DNA) suggest that the enlacing is here tighter than that proposed for natural DNA. The spectrofluorometric tests did not highlight any strong binding neither to duplex polyA·polyU nor to triplex polyA·2polyU RNAs. This evidence was confirmed on the basis of the melting temperatures: the stabilising effect, if any, is much lower than what observed for DNA.

Of course, the fact that BTATPE is present as an E/Z mixture makes the precise determination of the geometry of the adducts very challenging. Different binding modes could occur for the different conformers and what is observed experimentally would thus be a convolution of different effects. Unfortunately, the synthesis of a pure isomer only is a not straightforward task

and would perhaps be out of the scope of a low-cost probe. However, note also that, as already claimed, a fraction larger than 60% of (E)-conformer is expected.^[386] It might be speculated that, for geometrical reasons, the E isomer might be more prone to undergo external binding with respect to the Z form. Docking pictures (Figure 6.20 left) highlight indeed the very good compatibility of the E conformation with the DNA grooves. However, groove binding cannot be excluded also for the Z conformation (Figure 6.20 right).

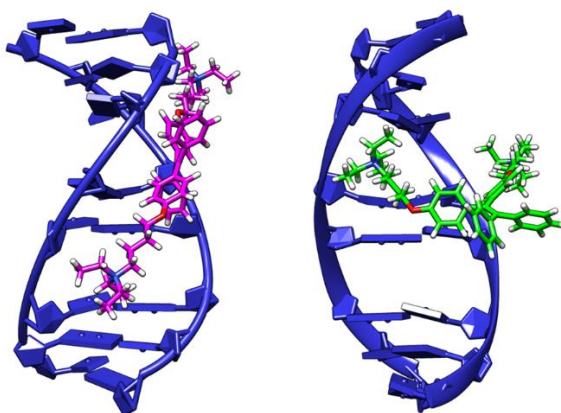


Fig. 6.20. Possible binding geometry derived from docking calculations for the E conformer (magenta) and the Z conformer (green) with the B-DNA helix

The obtained results provide hints on the relevance of the geometrical factors in driving the binding. Beyond some differences in the angle between of the base pairs plane and the helix axis, all natural DNA, polyA·polyT and polyG·polyC are arranged in a B-type conformation. Oppositely, the geometry of RNA double helix polyA·polyU is very similar to that of A-DNA, with the

groove occupied by the third strand in the case of polyA·2polyU. The results seem to indicate a preference for the B-type structure of DNA.

On the whole, we can consider the obtained results interesting and promising for further applications of BTATPE as fluorescent sensor for DNA structures. Nowadays, the employment of TPE derivatives has been focused on G4 sensors, but, at the best of our knowledge, their exploitation in the polynucleotides' recognition is scarcely investigated. Studies on nucleic acid are open to be deepened and extended to other systems, for instance other motifs containing junctions and mismatches.

Chapter VII

7. The pollutants

7.1 Introduction

Persistent Organic Pollutants (POPs) are nowadays intended as ubiquitous and, because of their lipophilicity, can bio-accumulate^[392] and condensate in the coldest parts of Earth.^[393]

Polycyclic aromatic hydrocarbons (PAHs) and their derivatives are major components of POPs both at the level of air,^[394] soil^[395] and water.^[396] They can be introduced in living organisms, where they can be metabolised or can directly interact with macromolecules (DNA, RNA, proteins).^{[397],[398],[399],[400],[401]} Most molecules of the PAHs family are classified as carcinogenic, principally due to enzymatic reactions that converts them into active metabolites.^[402] 1-Aminopyrene (1-pyNH₂, Figure 7.1A) is a common metabolite of nitro-PAHs, whose metabolic path goes through hydroxo-intermediates, which are able to covalently bind DNA.^[403] Coherently with the planar aromatic structure, 1-pyNH₂ is able to intercalate into poly- and oligo-nucleotides, the binding features being strongly dependent on the amino-residue.^[404]

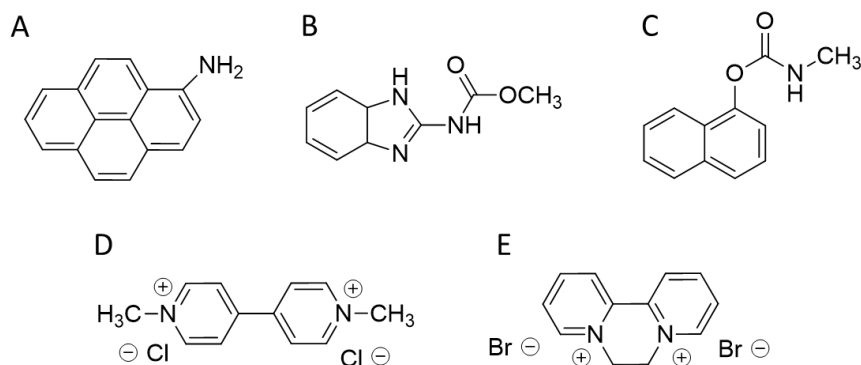


Fig. 7.1. Molecular structures of (A) 1-pyNH₂, (B) CBZ, (C) CA, (D) PQ and (E) DQ

That of pesticides is another class of POPs whose prolonged exposure was demonstrated to enhance tumour morbidity.^{[405],[406]} Carbendazim (CBZ, Figure 7.1B) and carbaryl (CA, Figure 7.1C) are widely used fungicides and insecticides, the former being also a metabolite of the benomyl fungicide. The insecticidal activity of carbamate-pesticides is related to the interference with nervous stimuli and the inhibition of the hydrolysis of acetylcholine.^[407] The same processes can produce toxic effects in the case of animals (i.e mammals and humans).^[408] Electrochemical and dye competition studies suggested intercalation of both CBZ and CA into the DNA base pairs.^{[409],[410],[411]}

Among the copious class of pesticides, also bipyridyl herbicides deserve high interest on the basis of their widespread application. These molecules are quaternary ammonium compounds marketed as contact herbicides and desiccants.^[412] The extensive use of these herbicides has been having long-lasting implications and their toxic effects affect the environment at the level of soil^[413] and water.^[414] In addition, bipyridyl herbicides are considered as responsible for detrimental effects on living organisms and their employment

is nowadays forbidden in several countries. Paraquat (PQ, Figure 7.1D) is a powerful herbicide that turns out to be extremely toxic for human beings^[415] as it can be easily stored in lungs and kidneys.^{[416],[417]} Its bioaccumulation is also supposed to be related to the onset of Parkinson's disease.^[418] PQ toxic effects are principally due to redox reactions that convert the herbicide into active free radicals.^[419] The fast oxidation of these species lead the cells to death, by means of the formation of superoxide ions O^{2-} , whose detrimental action is widely discussed.^{[420],[421]} The molecular structure of PQ is similar to that of diquat herbicide (DQ, Figure 7.1E). Prolonged exposure to this compound was demonstrated to affect kidneys, brain and the gastrointestinal tract.^[422] Conversion of DQ in toxic free radicals is supposed to take place in the eyes and this can cause the formation of cataracts.^[423] However, both the herbicides are not considered neither as carcinogenic nor as genotoxic species. At the best of our knowledge, just an example of PQ/DNA binding study is reported in the literature.^[424] PQ is proposed to weakly bind DNA groove, with no conformational change or unwinding of the double helix. However, the authors do not consider the superimposition of the spectroscopic signals, which strongly affect and limit the investigation and are, instead, carefully considered in the present study. No mechanistic study on DQ/DNA interaction is available in literature and, mostly, information on cytotoxicity come from biological analyses.^{[425],[426]} PQ has been also tested for affinity to human serum albumin (HSA).^[427] Notwithstanding, the determination of the binding details as well as the preferential binding site have been never discussed. Moreover, the crucial importance of the inner filter effects does not emerge from this studies.

On the whole, we can say that, despite the now long lasting and high interest on POPs interaction with biosubstrates, the related studies are more commonly devoted to biological aspects, whereas a detailed chemical analysis of the

mechanism of binding is still uncomplete. The spectroscopic studies are often fragmentary and devoted to a limited number of species/POP families or substrates, while quantum mechanical (QM) calculations on POP/DNA intercalated systems are relatively rare.^{[428],[429],[430]}

On this basis, within the context of the national project of research in Antarctica (PNRA), the here presented study is devoted to investigate the interaction between model organic pollutants and biosubstrates in order to provide mechanistic details on their possible toxic pathways. The experimental setup was carefully designed to ensure the reliability of the results, a crucial aspect that is sometimes underestimated in the literature. Moreover, the retention percentage on micelles and liposomes was evaluated for PQ and DQ, these tests constituting a basis for the estimation of the affinity for the cellular membrane.

7.2 1-PyNH₂, carbendazim and carbaryl binding to DNA

The experimental analysis of the binding mechanism of pyrene derivatives and carbendazim and carbaryl pesticides to natural *calx-thymus* DNA was already started during another project and only refined during this PhD. In particular, the gained experience enabled the more careful and reliable analysis of the data by carefully evaluating inner filter problems and other bias sources. Then, the binding features were further investigated by computational calculations. The experimental results are here briefly presented, highlighting their more tricky aspects.

Absorbance titrations for the pyrene derivative (1-pyNH₂ ca. 2×10^{-5} M) showed a limited spectral variation and were biased by aggregation problems of the dye (not shown). On this basis, these preliminary tests were neglected

and we focused our experiments on fluorescence titrations which may use a hundred times more diluted target species. Figure 7.2 shows the spectra recorded during a spectrofluorometric titration where DNA was added to a 1-pyNH₂ solution together with the corresponding binding isotherm.

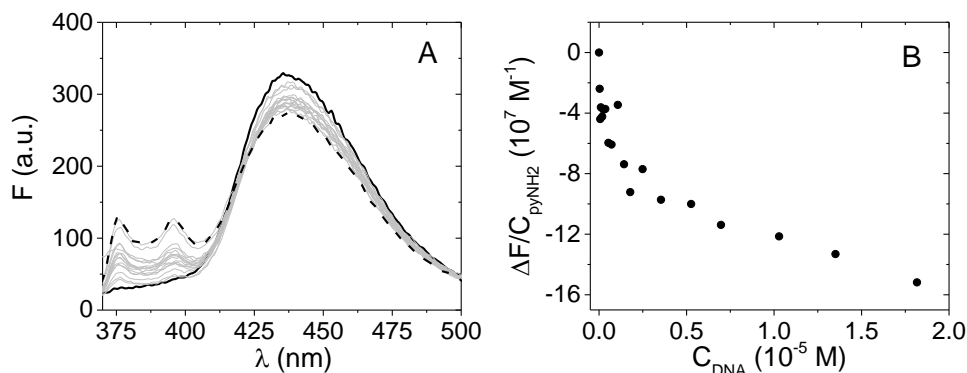


Fig. 7.2. (A) Spectrofluorometric titration of 1-pyNH₂/DNA and (B) corresponding binding isotherm at $\lambda_{em} = 440$ nm ($C_{pyNH_2} = 3.54 \times 10^{-7}$ M, C_{DNA} from 0 (solid) to 5.69×10^{-5} M (dash), NaCl 0.5 M, NaCac 2.5 mM, EtOH 1%, pH 7.0, 25.0°C, $\lambda_{exc} = 315$ nm, slits exc/em 5/5 nm)

The studied system is delicate and the fluorescence changes are not dramatic. We have carefully evaluated the possible inner-filter distortions. Fortunately, under our experimental conditions (low concentrations and exc-em wavelengths chosen), inner filter effects do not significantly affect the fluorescence read (bias lower than 0.4%). The binding constant value under conditions of DNA excess can be obtained through Equation 7.1, being $K = (3.8 \pm 0.4) \times 10^5$ M⁻¹ at 25°C.

$$\frac{C_D}{\Delta F} = \frac{1}{K\Delta\varphi} \cdot \frac{1}{[P]} + \frac{1}{\Delta\varphi} \quad (7.1)$$

Here, C_D is the total dye concentration and $[P] = C_{DNA} - [PD]$ corresponds to the free DNA concentration, $\Delta F = F - \varphi_D C_D$ and $\Delta\varphi = \varphi_{PD} - \varphi_D$ is the variation of the optical parameters upon binding. As the $[P]$ value is not exactly known and depends on K , an iterative procedure is employed until convergence of the K value. A site-size equal to one (base pairs) is supposed to apply for the model connected to the above equation: this approximation seems to hold well (linearity of the obtained plots) and agrees with the small size of the interacting (intercalating) species. The titration was repeated at different temperatures (results shown in Table 1) and the dependence of K on temperature yields the thermodynamic parameters for binding (*Van't Hoff* equation). The obtained highly negative enthalpy (-92 KJ/mol) agrees with the common signature of an intercalative binding mode.

Tab. 1. Binding constants of 1-pyNH2/DNA at different temperatures (NaCl 0.5 M, NaCac 2.5 mM, pH 7.0)

T (°C)	K (M ⁻¹)
10.0	(1.3 ± 0.4) × 10 ⁶
25.0	(3.8 ± 0.4) × 10 ⁵
37.0	(8.1 ± 0.9) × 10 ⁴

The spectroscopic analysis of the binding of carbamate-pesticides with DNA and BSA was more difficult. Scarcely soluble in water, these dyes have the

additional drawback to absorb light only in a range of wavelengths (UV) in which also the biosubstrates strongly absorb (Figure 7.3A). In the fluorescence mode, light emission can be collected over 300 nm and, in the case of CBZ, even over 600 nm, avoiding auto-absorption phenomena (Figure 7.3B). However, as excitation is in the UV, inner filter effects occur, due to increasing amounts of light-absorbing DNA during titration.

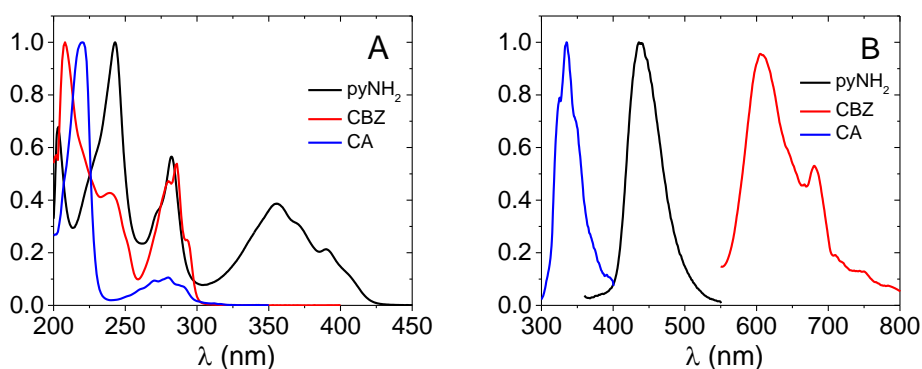


Fig. 7.3. Normalised (A) absorbance and (B) emission spectra of 1-pyNH₂ (black), CBZ (red) and CA (blue) (NaCl 0.5 M, NaCac 2.5 mM, pH 7.0, 25.0°C, $\lambda_{exc} = 315$ nm for 1-pyNH₂, $\lambda_{exc} = 225$ nm for CBZ and CA)

To limit the inner filter effects, the analysis of the data was limited to points where the DNA content was kept under a concentration threshold ($A_{DNA} < 0.1$ at λ_{exc}). Fluorescence data are anyway corrected for inner filter (see below Equation 7.3). Figure 7.4 shows the binding isotherms obtained by titrating the pesticides' solutions with DNA. The equilibrium constants found at 25°C are $(4 \pm 1) \times 10^5 \text{ M}^{-1}$ and $(3 \pm 1) \times 10^4 \text{ M}^{-1}$ for CBZ/DNA and CA/DNA respectively. In addition, ethidium bromide displacement experiments demonstrated pesticides' penetration into the DNA helix (Figure 7.5).

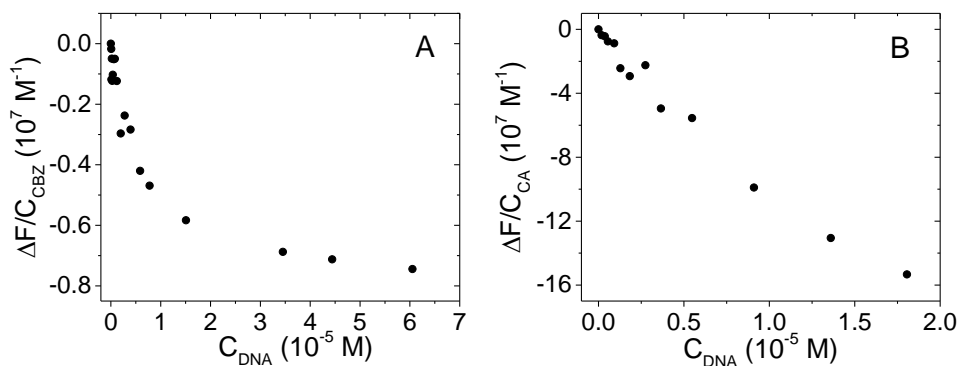


Fig. 7.4. (A) Binding isotherm of CBZ/DNA at $\lambda_{em} = 605$ nm, $C_{CBZ} = 5.10 \times 10^{-6}$ M, and (B) CA/DNA at $\lambda_{em} = 333$ nm, $C_{CA} = 1.00 \times 10^{-6}$ M. NaCl 0.5 M, NaCac 2.5 mM, EtOH 2%, pH 7.0, 25.0°C, $\lambda_{exc} = 225$ nm, slits exc/em 5/5 nm

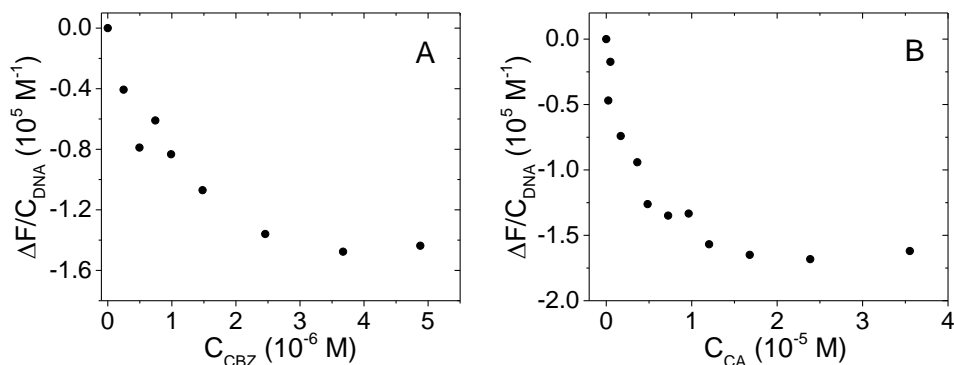


Fig. 7.5. Binding isotherms at $\lambda_{em} = 595$ nm of the EtBr-saturated DNA titrations with (A) CBZ and (B) CA ($C_{DNA} = 1.2 \times 10^{-4}$ M, $C_{EtBr} = 5.4 \times 10^{-5}$ M, C_{CBZ} from 0 to 4.89×10^{-6} M, C_{CA} from 0 to 3.55×10^{-5} M, NaCl 0.5 M, NaCac 2.5 mM, pH 7.0, 25.0°C, $\lambda_{exc} = 520$ nm, slits exc/em 5/5 nm

As anticipated, in addition to the refinement to the experimental part, computational calculations were performed with the aim of evaluating the geometry of the adducts and corroborating the experimental results.

The geometrical structures for both ground and excited states of 1-pyNH₂, CBZ and CA in water were optimized by employing a (TD)DFT approach combined with a PCM description of the solvent. The superimposition of optimized ground state conformations (in blue) with the corresponding optimized excited states (in green) is reported in Figure 7.6, while the isodensity surfaces of the electrostatic potential are shown in Figure 7.7.

As previously described in details for PZPERY (Chapter IV), twenty geometries for each adduct were arbitrarily designed and quickly screened by the semiempirical method PM6; the refined optimization of the systems were performed through (TD)DFT calculations. The results are reported in Figure 7.8.

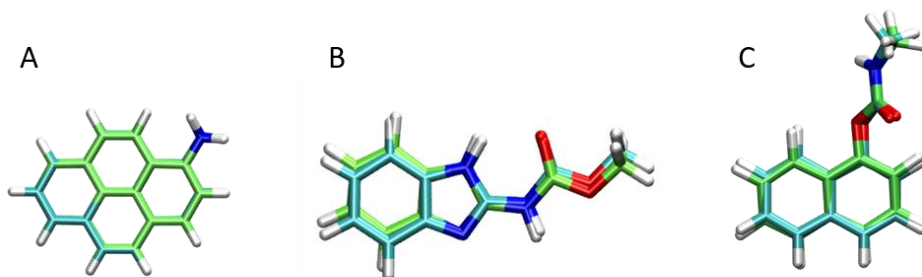


Fig. 7.6. Superimposition of optimized ground state (blue) and excited structures (green) for (A) 1-pyNH₂, (B) CBZ and (C) CA

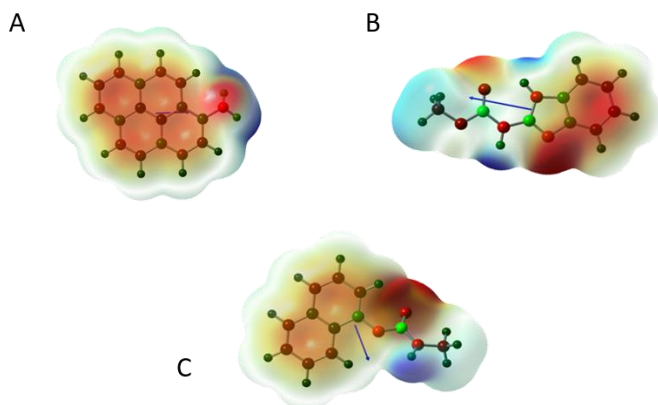


Fig. 7.7. Isodensity surfaces of electrostatic potential of (A) 1-pyNH₂, (B) CBZ and (C) CA

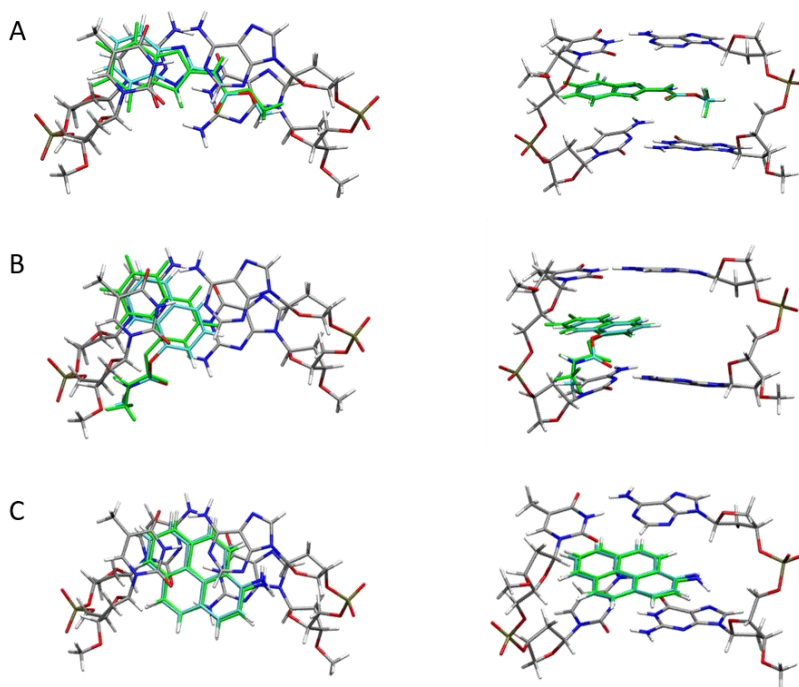


Fig. 7.8. Ground state (blue) and excited state (green) optimized structures for intercalated (A) 1-pyNH₂, (B) CBZ and (C) CA

As expected, the aromatic regions play an important role to lead the intercalation into DNA. In fact, the aromatic rings of the chromophores are aligned with those of the base pairs, suggesting π -stacking interactions. We also observe that the chain of CBZ is located into the DNA base pairs, whereas that of CA is disposed outside the pocket, stabilizing the structure through hydrogen bonds.

The Natural Transition Orbitals (NTO) provide a qualitative representation for the electronic transition density. The dominant NTO pairs ($S_0 \rightarrow S_1$) of the intercalated systems and their percent contribution to the transitions are showed in Figure 7.9, whereas the NTOs of the water solvated molecules are reported in Figure 7.10. The π - π^* nature of the transitions emerges from these data. The charge transfer is absent for the intercalated 1-pyNH₂ and for the water solvated pollutants as well.

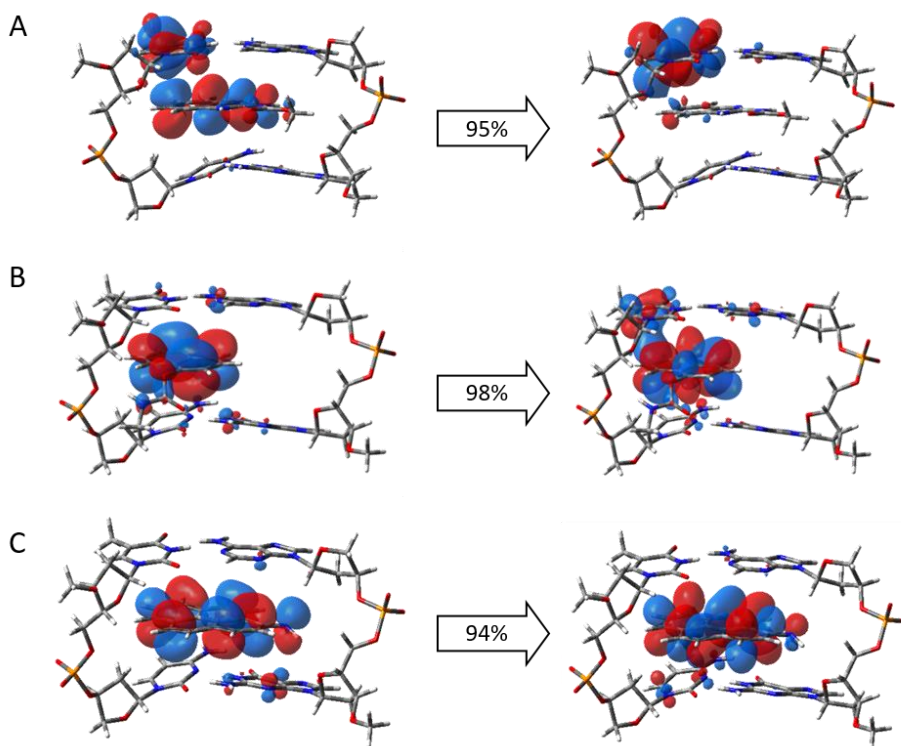


Fig. 7.9. NTO ($S_0 \rightarrow S_1$) for intercalated (A) 1-pyNH₂, (B) CBZ and (C) CA

This result agrees with the values of the dipole moments reported in Table 7.2: no significant variation is observed between the ground and the excited states. This contribution is present but still negligible in the case of CA. A strong charge transfer from the benzimidazole ring to the DNA base pairs is instead observed for the lowest excitation of CBZ. This affects the energetic states of the DNA/CBZ system and, as a consequence, we considered the second excited state (S_2) to compare the calculations with the observed excitation and emission energies. Also, moving to the spectroscopic features, we observe that both the calculated oscillator strengths and the experimental data agree that the intensity of the spectra decreases as a result of the DNA binding.

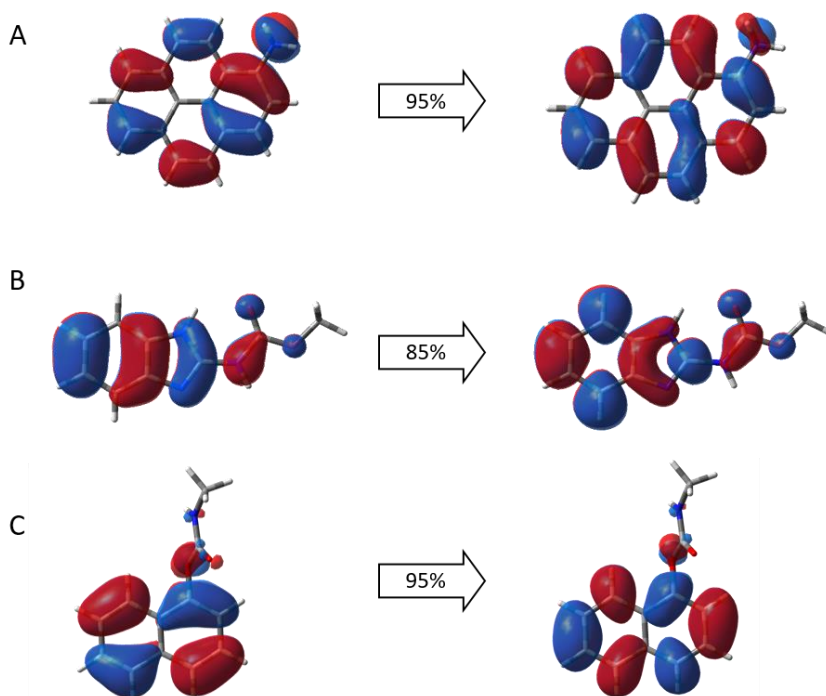


Fig. 7.10. NTO ($S_0 \rightarrow S_1$) for (A) *1-pyNH*₂, (B) *CBZ* and (C) *CA* in water

Tab. 7.2. Calculated properties for *1-pyNH*₂, *CBZ* and *CA*

	<i>1-pyNH</i> ₂		<i>CBZ</i> *		<i>CA</i>	
	water	DNA	water (+7H ₂ O)	DNA	water	DNA
Oscillator Strength	0.505	0.332	0.393	0.151**	0.147	0.060
ABS (eV)	3.54	3.43	4.90	4.76**	4.54	4.37
FLUO (eV)	3.08	2.98	4.41	4.37**	3.81	3.67

* In the case of *CBZ* explicit water molecules have been added to account for hydrogen bonding effects; ** for S_2 state

7.3 Herbicides

7.3.1 Spectroscopic characterization

The optical properties of PQ and DQ molecules were characterized under physiological conditions (NaCl 0.1 M, NaCac 2.5 mM, pH 7.0). Absorbance spectra at different concentrations were recorded for both the herbicides (Figure 7.11A and 7.12A). The unaltered spectral profile and the linearity of the *Lambert and Beer* plots indicate that the molecules do not aggregate under the explored conditions (Figure 7.11B and 7.12B).

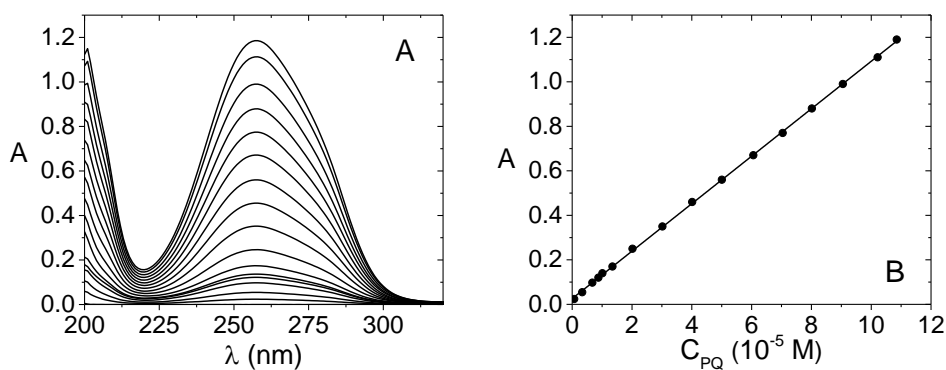


Fig. 7.11. (A) Absorbance spectra of PQ and (B) relevant Lambert Beer plot at $\lambda = 258$ nm (C_{PQ} from 4.08×10^{-7} to 1.09×10^{-4} M, NaCl 0.1 M, NaCac 2.5 mM, pH 7.0, 25.0°C), $\epsilon_{258} = 17641 \text{ M}^{-1}\text{cm}^{-1}$

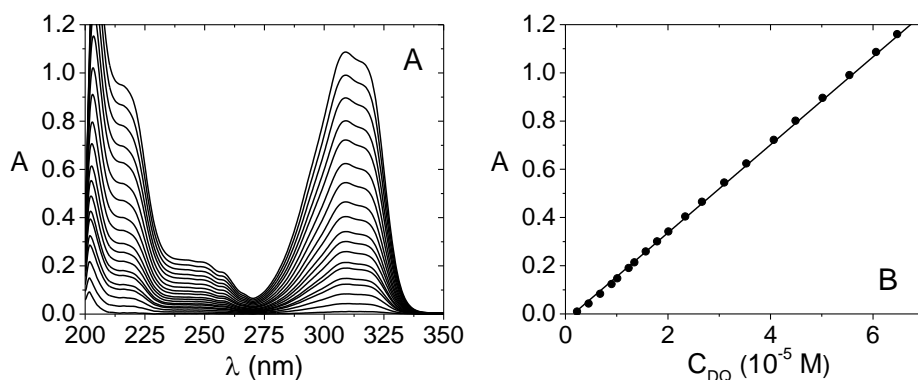


Fig. 7.12. (A) Absorbance spectra of DQ and (B) relevant Lambert Beer plot at $\lambda = 309$ nm (C_{DQ} from 2.26×10^{-7} to 6.47×10^{-5} M, NaCl 0.1 M, NaCac 2.5 mM, pH 7.0, 25.0°C). $\epsilon_{309} = 18234 \text{ M}^{-1}\text{cm}^{-1}$

The possible presence of aggregates was checked also by inspecting absorbance ratio plots, which may evidence more subtle change in the profiles (Figure 7.13). The constancy of the plotted values further confirms the absence of self-aggregation processes. The lower aggregation tendency shown here with respect to the previously analysed pollutants agrees with the +2 charge borne by PQ and DQ.

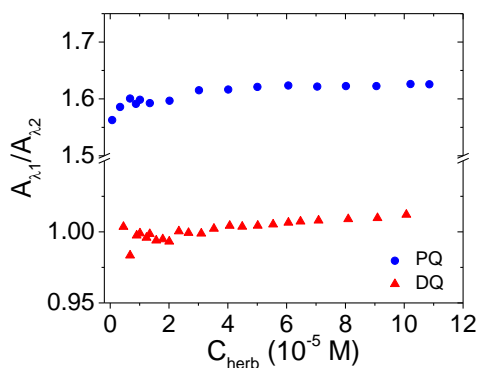


Fig. 7.13. (●) Absorbance ratio A_{258}/A_{280} for PQ (C_{PQ} from 6.76×10^{-7} to 1.09×10^{-4} M) and (▲) absorbance ratio A_{297}/A_{324} for DQ (C_{DQ} from 2.26×10^{-6} to 1.01×10^{-4} M). NaCl 0.1 M, NaCac 2.5 mM, pH 7.0, 25.0°C

7.3.2 DNA binding

In principle, the non-aggregation of the dye is a very favourable aspect for the further analysis of its interaction with the target. Nonetheless, the analysis of the binding of PQ and DQ to nucleic acids and proteins unfortunately still resulted to be very complex. The main obstacle to the spectroscopic investigation was the superimposition of the pollutants' signals with those of the biosubstrates (Figure 7.14). Under these circumstances, in the case of absorbance experiments, differential titrations in a double-beam instrument may be performed: the same amount of the titrant (DNA) is added to both the measuring and the reference cell. This procedure enables to follow the changes in the absorbance profile of the dye due to the binding and directly subtracts the contribution of the titrant. Alternatively, the titration can be done without the double addition, and the recorded signals can be mathematically corrected for the contribution of DNA. We performed some tests in both ways. Figure

7.15 shows the some examples of the spectra recorded for differential titrations.

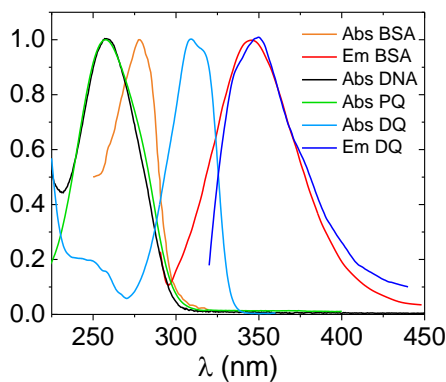


Fig. 7.14. Comparison between spectroscopic signals of PQ and DQ and those of the biotargets

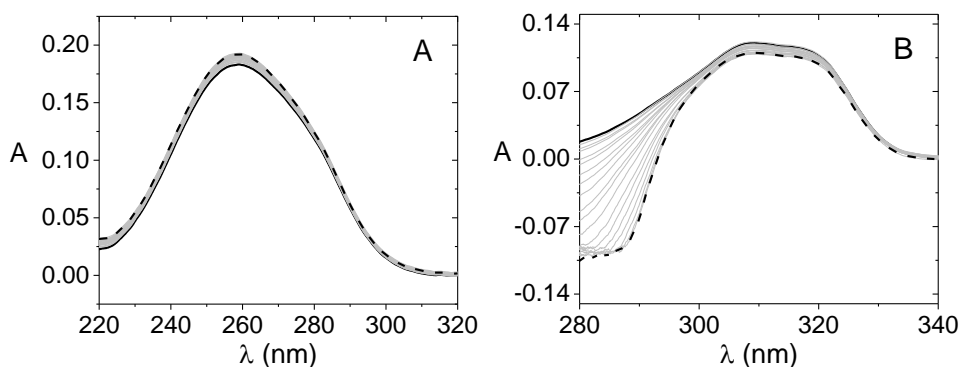


Fig. 7.15. Spectrophotometric titration of (A) PQ/DNA ($C_{PQ} = 9.30 \times 10^{-6} M$, C_{DNA} from 0 (solid) to $6.49 \times 10^{-4} M$ (dash)) and (B) DQ/DNA ($C_{DQ} = 6.87 \times 10^{-6} M$, C_{DNA} from 0 (solid) to $7.71 \times 10^{-6} M$ (dash)). NaCl 0.1 M, NaCac 2.5 mM, pH 7.0, 37.0°C

As far as the DNA content is raised and therefore high values of DNA absorbance are reached, these approaches resulted to be scarcely reliable. Note, however, that neither PQ nor DQ show significant absorbance profile changes and bathochromic effects, even for the first steps of DNA additions. This finding may be a first hint of a scarce interaction between the herbicides and DNA. In order to overcome the problem, fluorescence exchange titrations with EtBr were performed (NaCl 0.1 M, NaCac 2.5 mM, pH 7.0). Known amounts of herbicides were added directly to EtBr-saturated DNA. A decrease of emitted fluorescence at the excitation and emission wavelengths typical of intercalated EtBr would have indicated its displacement from the helix.^[199] Although the selected herbicides undoubtedly present suitable features to be considered as DNA binders, the tests do not demonstrate any significant interaction (example in Figure 7.16), meaning that intercalation is excluded. Groove binding also seems unlikely, as the penetration within the groove (and even more of a charged species) is usually still able to produce some change in the EtBr probe environment which is reflected by a signal change.

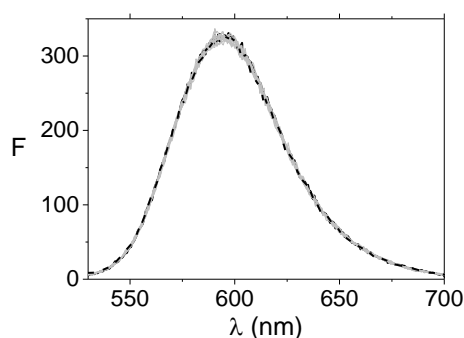


Fig. 7.16. Fluorescence exchange titration of EtBr-saturated DNA with DQ at 25.0°C ($C_{EtBr} = 9.96 \times 10^{-5} M$, $C_{DNA} = 2.43 \times 10^{-4} M$, C_{DQ} from 0 (solid) to $8.03 \times 10^{-4} M$ (dash), NaCl 0.1 M, NaCac 2.5 mM, pH 7.0, 25.0°C, $\lambda_{exc} = 510 nm$, $\lambda_{em} = 595 nm$, slits exc/em 2.5/2.5 nm)

The same conclusion emerges from the viscosity measurements carried out for the two herbicide/DNA systems at different $C_{\text{herbicide}}/C_{\text{DNA}}$ ratios. The flow times (t) were used to calculate the relative viscosity (η/η_0) of the solutions as follows (Equation 7.2, for further details refer to Chapter VI – Equation 6.4 and Appendix IV):

$$\left(\frac{\eta}{\eta_0}\right)^{\frac{1}{3}} = \left(\frac{t_{\text{DNA+BTATPE}} - t_{\text{solvent}}}{t_{\text{DNA}} - t_{\text{solvent}}}\right)^{\frac{1}{3}} = \frac{L}{L_0} \quad (7.2)$$

In both cases, the relative viscosity remains almost constant upon the addition of increasing amounts of herbicide (Figure 7.17), indicating no significant elongation of the DNA helix.^[431] This result underlines the absence of intercalation between the DNA base pairs for both PQ and DQ.

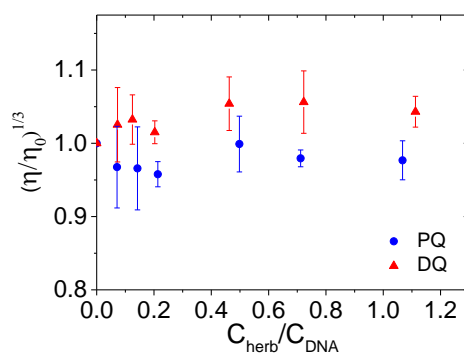


Fig. 7.17. Relative viscosity vs. $C_{\text{herb}}/C_{\text{DNA}}$ ratios plot for (●) PQ and (▲) DQ ($C^{\circ}_{\text{DNA}} = 1.77 \times 10^{-4} \text{ M}$, C_{PQ} from 0 to $1.92 \times 10^{-4} \text{ M}$, C_{DQ} from 0 to $2.0 \times 10^{-4} \text{ M}$, NaCl 0.1 M, NaCac 2.5 mM, pH 7.0, 25.0°C)

Thermal denaturation studies revealed that the thermal stability of DNA (in NaCac 2.5 mM, pH 7.0) is affected by the presence of the ligands (Figure 7.18A): a stabilising effect on the melting temperature of the polynucleotide (ΔT_m ca. $+6^\circ\text{C}$ for both PQ and DQ) is observed upon the addition of the herbicides. This result indicates that some interaction is at play. However, on the basis of the previous results, an external electrostatic interaction between the $+2$ charged PQ and DQ and the negatively charged external helix backbone may be considered as the most probable option.

The denaturation tests were repeated also in the presence of hybrid G-quadruplex Tel23, but no particular affinity was highlighted (Figure 7.18B).

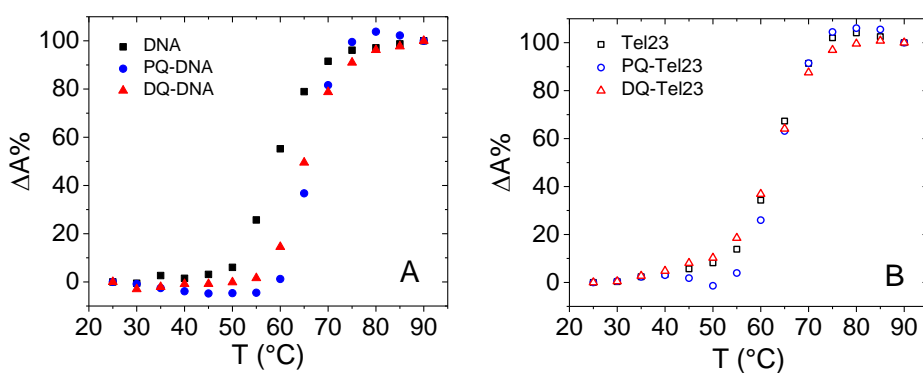


Fig. 7.18. Superimposition of melting curves for (A) (■) *ct*-DNA, (●) PQ/DNA, (▲) and DQ/DNA ($C_{DNA} = 1.14 \times 10^{-5}$ M, $C_{PQ} = 1.14 \times 10^{-5}$ M, $C_{DQ} = 1.06 \times 10^{-5}$ M, NaCac 2.5 mM, pH 7.0) and (B) (■) Tel23, (○) PQ/Tel23, (▲) and DQ/Tel23 ($C_{Tel23} = 5.50 \times 10^{-6}$ M, $C_{PQ} = 6.0 \times 10^{-6}$ M, $C_{DQ} = 5.50 \times 10^{-6}$ M, KCl 0.1 M, LiCac 2.5 mM, pH 7.0)

7.3.3 BSA binding

Spectrofluorometric titrations

Moving now to test the binding of the herbicides to proteins, absorbance approaches have to be avoided due to the already discussed experimental issues. Concerning fluorescence techniques, the superimposition of the DQ and the BSA emission signals prevented the spectroscopic analysis of the DQ/BSA system to be performed with reliability. On the contrary, in the case of PQ, spectrofluorometric titrations were carried out to highlight the possible interaction with BSA (in NaCl 0.1 M, NaCac 2.5 mM, pH 7.0). Note that inner filter effects affected the measurements: we carefully optimized the experimental conditions and, taking into account this limitation, we corrected the signals according to the Equation 7.3 below.^[192]

Figure 7.19A shows the BSA emission spectra changes observed upon the addition of increasing amounts of PQ. As cited above, PQ absorbs light at the excitation wavelength of the protein (Figure 7.14) and the occurrence of inner filter effects could be responsible for biased data. Indeed, Figure 7.19B points out evident deviations in the recorded binding isotherm (red squares) in comparison to that corrected for the inner filter effect (black points) as follows (Equation 7.3):^[192]

$$F_{\text{corr}} = F_{\text{obs}} \times 10^{\left(\frac{A_{\lambda_{\text{em}}} + A_{\lambda_{\text{exc}}}}{2}\right)} \quad (7.3)$$

Here, F_{corr} and F_{obs} are respectively the corrected and the observed fluorescence intensities, while $A_{\lambda_{\text{em}}}$ and $A_{\lambda_{\text{exc}}}$ are the absorbance values respectively at the emission and excitation wavelengths.

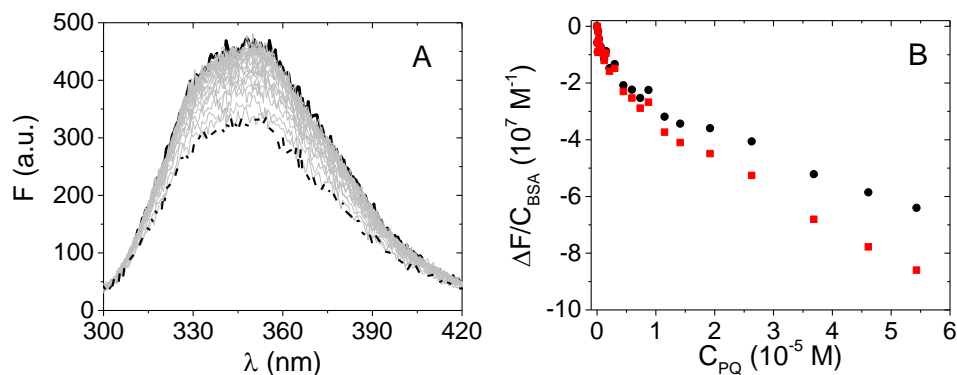


Fig. 7.19. (A) Spectrophotometric titration of PQ/BSA and (B) corresponding binding isotherm at $\lambda_{em} = 345 \text{ nm}$ ($C_{BSA} = 1.50 \times 10^{-6} \text{ M}$, C_{PQ} from 0 (solid) to $5.43 \times 10^{-5} \text{ M}$ (dash), NaCl 0.1 M, NaCac 2.5 mM, pH 7.0, 25.0°C, $\lambda_{exc} = 295 \text{ nm}$, slits exc/em 3/3 nm). Red squares refer to uncorrected fluorescence values, black points define the trend corrected according to Equation 7.3

Taking into account this unavoidable evidence, the intensities of the BSA fluorescence were always corrected according to Equation 7.3 prior to any further data analysis.

To ensure that the fluorescence decrease is really due to complex formation (and not to collisional quenching only), data recorded at different temperatures were fitted using the *Stern-Volmer* equation (Equation 7.4):

$$\frac{F_0}{F} = 1 + k_q \tau_0 = 1 + K_{SV}[Q] \quad (7.4)$$

where F_0/F corresponds to the ratio between the BSA fluorescence intensity in the absence and the presence of the quencher (PQ) respectively, K_{SV} represents the Stern-Volmer constant, $[Q]$ is the molar concentration of the

quencher, k_q is the bimolecular quenching constant and τ_0 corresponds to the average lifetime of the protein in the absence of quencher. Note that the F values must be corrected for dilution and inner filter before to be used. For static quenching, K_{SV} will be equal to the binding constant for complex formation (if the complex is non-fluorescent). Note that $[Q]$ corresponds to $[Q_{free}]$ (the molar concentration of free quencher): the evaluation of $[Q_{free}]$ requires an iterative procedure or, alternatively, just the point in large excess of quencher should be considered in the data analysis.

K_{SV} is equal to $(6.5 \pm 0.8) \times 10^3 \text{ M}^{-1}$ at 25.0°C . Being $\tau_0 = 7 \text{ ns}$ for protein BSA, k_q results beyond the upper limit for collisional quenching ($k_q = 3 \times 10^{10} \text{ M}^{-1}\text{s}^{-1}$) and should be necessarily related to the presence of some non-collisional quenching (complex formation). Moreover, the lack of dependence on temperature (Figure 7.20) confirms the non-collisional nature of the quenching process as well.

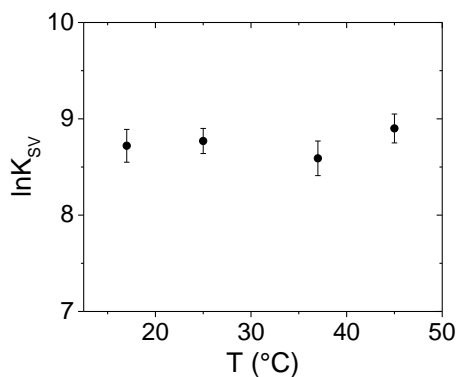


Fig. 7.20 Dependence on temperature of the Stern-Volmer constant for the PQ/BSA system (NaCl 0.1 M, NaCac 2.5 mM, pH 7.0)

Once the complex formation was ensured, the binding constants at the different temperatures were calculated by means of HypSpec® software (<http://www.hyperquad.co.uk>), which enables, through a least square procedure, to fit the data over a wavelength range according to multiple equilibria models (Figure 7.21). Note that all the spectra were previously corrected for the inner filter effect over the whole explored range, by the application of Equation 7.3 at each of the $A_{\lambda_{em}}$ and $A_{\lambda_{exc}}$ appropriate for each point of each spectrum. Tests for different models and factor analysis of the data suggest that a 1:1 binding is sufficient to describe the data set.

At 25.0°C a binding constant (K) of $(6.2 \pm 0.8) \times 10^4 \text{ M}^{-1}$ was measured.

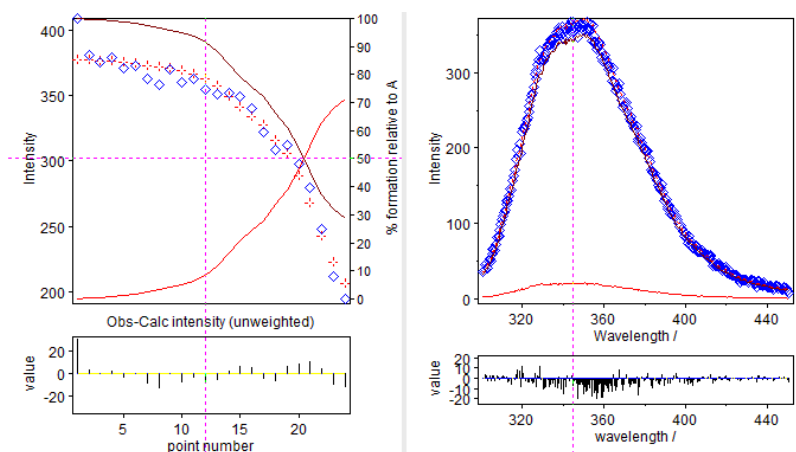


Fig. 7.21. HypSpec analysis of the fluorescence changes observed upon addition of PQ to BSA ($C_{BSA} = 1.54 \times 10^{-6} \text{ M}$, C_{PQ} from 0 to $5.12 \times 10^{-5} \text{ M}$, NaCl 0.1 M, NaCac 2.5 mM, pH 7.0, 37.0°C, $\lambda_{exc} = 295 \text{ nm}$, slits exc/em 3/3 nm). Left: titration curve at 345 nm (open diamond = experimental, cross = calculated) and species distribution (dark red = free BSA, red = PQ/BSA adduct). Right: fluorescence spectrum ((open diamond = experimental, dashed red line = calculated) and relevant deconvolution (dark red = free BSA, red = PQ/BSA adduct). The bottom panels are the residuals

The *Van't Hoff* plot (Figure 7.22) shows that the obtained *K* values do not significantly change with temperature, indicating that the enthalpy variation (ΔH) is negligible for the here analysed process; on the other hand, the entropy variation (ΔS) results to be equal to 85 J/mol·K.

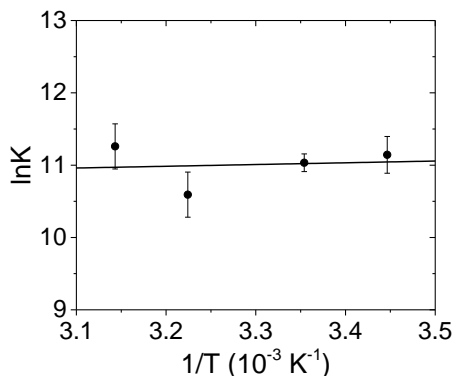


Fig. 7.22. *Van't Hoff* plot for the PQ/BSA system (NaCl 0.1 M, NaCac 2.5 mM, pH 7.0)

It is known that the sign and the order of magnitude of the thermodynamic parameters constitute a signature for the binding type (see Chapter I - Paragraph 1.3.2 and ^[118]). Interestingly, the thermodynamic parameters extracted from literature, lie on a common line (Figure 7.23). This correlation is called enthalpy-entropy compensation (EEC). EEC is a phenomenon which has also been attributed to experimental bias or intended as a simple result of thermodynamic laws.^[432] Nowadays, most of the researchers agree on EEC which is connected to the fact that, if a small molecule undergoes to more and/or tighter van der Waals contacts and H-bonds with the substrate (a process related to a more negative ΔH) this will produce a decrease in the flexibility in one or both ligand-substrate. On the whole, the reduction in the overall conformational

entropy will compensate the enthalpy decrease.^[371] Note that also hydration plays a major role: the rearrangement in the coordinated solvent molecules strongly influences, in particular, ΔS .^{[371],[370]} This strong effect and consequent variability is reflected by the change from positive to negative values for $T\Delta S$. The correlation plot of Figure 7.23 for ligand-BSA systems, yields (at 25 °C) the linear relationship $T\Delta S = \Delta H + 27 \text{ kJ mol}^{-1}$. If the value of the slope is close to one, this means that the enthalpy gain is compensated for the entropic loss. This compensation is quite always found in the case of flexible macromolecules, but significantly lower slopes can be found for stiff hosts.^[372] For the intercept of the plot, this is connected to desolvation occurring upon binding.^[433]

The thermodynamic values obtained for the PQ/BSA system (green star in Figure 7.23) agree with an electrostatics-driven process, in agreement with the charged nature of the host.

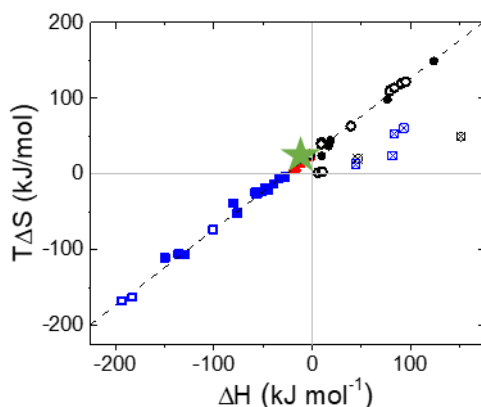


Fig. 7.23. Plot of ΔH vs. $T\Delta S$ for different ligands binding to BSA according to the bibliographic references reported in Chapter I, Table 1.1. Different points relate to: (●) = hydrophobic forces, (■) = van der Waals/H-bonding, (▲) = electrostatic. Full point refer to organic molecules, open points refer to metal complexes, the outliers have been crossed out

BSA binding site

It is known that BSA possesses two main binding sites (see Chapter I, Paragraph 1.3.2) and the evaluation of the preferential binding position is usually obtained through fluorescence competitive studies. Phenylbutazone (PB) and ibuprofen (IB) are one of the species employed respectively as site I and II marker, which were chosen for the here presented studies. Figure 7.24 shows the binding isotherms obtained by titrating BSA alone, BSA saturated with PB and BSA saturated with IB.

The negligible difference observed in the trends suggests that the binding is not selective.

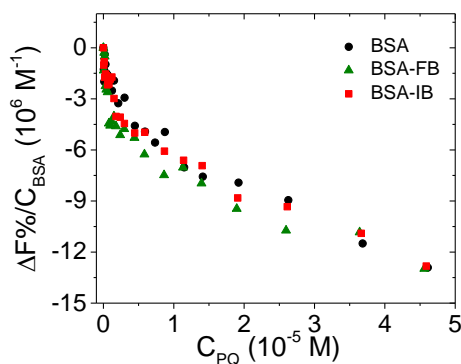


Fig. 7.24 Binding isotherm at $\lambda = 345$ nm for BSA alone and BSA/marker titrated with PQ ($C_{BSA} = 1.5 \times 10^{-6}$ M, $C_{marker} = 1.5 \times 10^{-5}$ M, C_{PQ} from 0 to 4.6×10^{-5} M, NaCl 0.1 M, NaCac 2.5 mM, pH 7.0, 25.0°C, $\lambda_{exc} = 295$ nm, slits exc/em 3/3 nm)

The same picture was also evidenced by the docking analysis (Figure 7.25): no relevant difference is observed by docking the ligand into the two different binding sites (grid score for binding site I = -26.16; grid score for binding site II = -26.46).

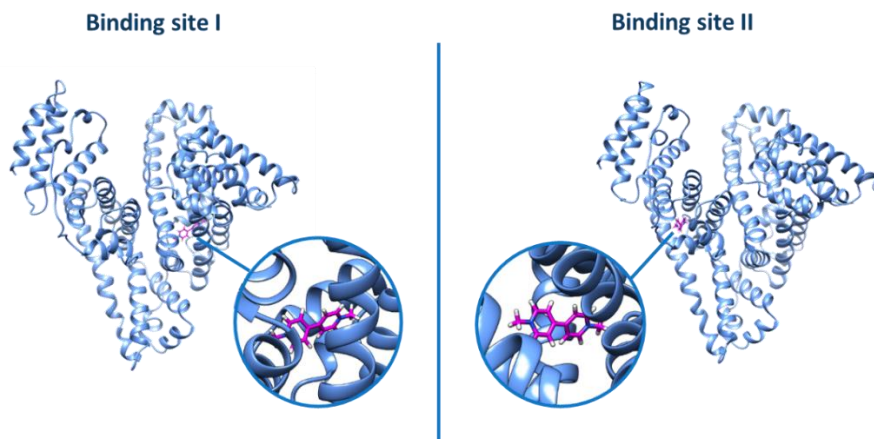


Fig. 7.25. Docking of PQ into binding site I and II of BSA

On the whole, it seems that PQ, which is a small charged species, is bound by BSA by an electrostatic, non-specific process as for the preference between site I or site II.

7.3.4 Micellar Enhanced Ultra-Filtration (MEUF) tests on surfactants and liposomes

The retention of PQ and DQ on micelles of different nature (positive, negative or neutral surface) and liposomes was studied as an indication of lipophilicity and affinity for cellular membranes. Sodium dodecyl sulphate (SDS) and dodecyl trimethyl ammonium chloride (DTAC) are used respectively for the positively and negatively charged micelles. TritonX-100 is employed for the neutral micelles, whereas 1-palmitoyl-2-oleoyl-sn-glycero-3-phosphocholine (POPC) molecules compose the liposomes (as described in Chapter III - Paragraph 3.2.7).

Micellar Enhanced Ultra-Filtration coupled with absorbance spectroscopy enables the percentage of retention (R%) on the micelles/liposomes to be measured. After the micellar phase was separated from the liquid matrix, the amount of dye adsorbed was evaluated by spectrophotometry as the difference between the initial amount and that remaining in the permeate after filtration, according to Equation 7.5:

$$R\% = \left(1 - \frac{A_{\text{final}}}{A_{\text{initial}}}\right) \times 100 \quad (7.5)$$

where A_{final} and A_{initial} are the final and the initial absorptions of the solution respectively, at the wavelength which corresponds to the maximum absorbance of the dye. Figure 7.26 shows an example of the absorbance spectra of PQ/SDS and DQ/DTAC solutions recorded before and after the ultrafiltration process.

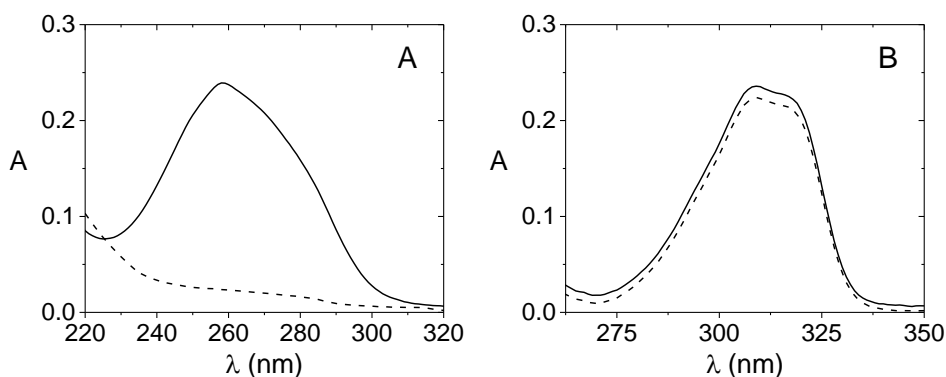


Fig. 7.26 Absorbance spectra of (A) PQ in SDS 0.01 M before (solid) and after (dash) ultrafiltration and (B) DQ in DTAC 0.01 M before (solid) and after (dash) ultrafiltration (NaCl 0.1 M, NaCac 2.5 mM, pH 7.0)

The analysis was performed at two different ionic strengths (NaCl 0.1 or 0.5 M, NaCac 2.5 mM, pH 7.0) and the obtained results are reported in Table 7.3.

Tab. 7.3. Retention percentage (R%) of the analysed herbicides on micelles and liposomes (NaCl 0.1 M and 0.5 M, NaCac 2.5 mM, pH 7.0, 25.0°C, $C_{micelles} = 0.01$ M, $C_{POPC} = 5 \times 10^{-6}$ M). Tests were performed in triplicate, errors are $\pm SD$

	PQ		DQ	
	0.1 M	0.5 M	0.1 M	0.5 M
SDS	90.4 \pm 0.6	40.8 \pm 5.0	91.0 \pm 1.1	33.5 \pm 5.1
DTAC	7.8 \pm 1.0	6.2 \pm 1.3	2.7 \pm 1.2	5.9 \pm 0.7
TritonX	10.6 \pm 2.3	18.4 \pm 2.0	15.1 \pm 0.6	14.7 \pm 0.4
POPC	5.3 \pm 1.5	3.5 \pm 1.7	5.1 \pm 2.6	5.8 \pm 1.4

As expected, the positively charged herbicides are strongly retained on the negative surface of the SDS micelles, but the increase of the salt content strongly affects the electrostatic nature of the binding, resulting in a decrease of R%. Based on electrostatics, PQ and DQ should not interact with the positive surface of DTAC. On the contrary, even if with low R%, PQ and DQ are both still retained on DTAC micelles and the retention is scarcely affected by the variation of the ionic strength. This evidence suggests the presence of some hydrophobic forces also involved in the binding. The same hint is provided by the R% values obtained for the neutral TritonX micelles. The low hydrophobicity of the systems, being $\log P_{ow} = -4.22$ for PQ^[434] and $\log P_{ow} = -4.6$ for DQ,^[435] prevents any strong affinity, but an interaction is

observed anyway. Regardless of the salt content, the adsorption on POPC liposomes results similar to what obtained for DTAC. In POPC liposomes we have the simultaneous presence of cationic R-NH₃⁺ final residues and of vicinal anionic phosphate group, together with inner neutral regions. This result indicates that the overall effect is dominated by the most external amine layer and no significant penetration beyond it occurs.

7.4 Conclusions

Details on the binding of persistent organic pollutants to biosubstrates have been here provided through the use of spectroscopic techniques, (TD)-DFT calculations and analysis of the percentage of retention on micellar aggregates and liposomes.

The highly negative enthalpic changes or the ability to displace intercalated ethidium had indicated intercalation of 1-pyNH₂, CBZ and CA between the DNA base pairs. The experimental results have been implemented with computational studies, which have both corroborated the previous evidences and enhanced the knowledge of the mechanistic details of the DNA binding process. The (TD)-DFT calculations confirm that DNA intercalation induces only small spectroscopic changes for these systems. In addition, the computational results underline the importance of the aromatic parts in driving the binding mode and determining the geometry of the adduct, giving important information on the fine properties of the systems as the charge transfer with DNA.

Oppositely, interaction with DNA is not observed in the case of PQ and DQ herbicides. The molecular structures of these systems surely fit those of common DNA binders: in principle, the small, aromatic geometry and the

presence of +2 positive charges would have suggested the possible intercalation into the DNA pocket. Despite the favourable expectations, the spectroscopic and viscosimetric measurements do not indicate any strong interaction. On the basis of the thermal denaturation tests, PQ and DQ are proposed to externally bind DNA. On the whole, PQ and DQ behave very similarly even if, despite their similarity, they are different and differently hindered species.

No DQ interaction with BSA could be spectroscopically evidenced due to the too unfavourable spectroscopic features of the partners. On the other hand, in the case of PQ interaction with BSA, fluorescence spectroscopy demonstrate that this binding does occur instead. The *Stern-Volmer* plots ensures the formation of the PQ-BSA complex (non-collisional quenching) and the binding constants could be evaluated with the Hypspec® software, being $K = (6.2 \pm 0.8) \times 10^4 \text{ M}^{-1}$ at 25.0°C. The main source of ΔG value is due to the contribution of the positive ΔS term (85 J/mol·K) with ΔH a negligible enthalpic contribution to the process: the binding is supposed to be mainly driven by electrostatic forces ($\Delta H \cong 0$, $\Delta S > 0$), even if some contribution of a hydrophobic interactions (ΔH and $\Delta S > 0$) cannot be completely ruled out. This latter, even if minority (+2 charged species), would be related to the rings present in the molecular structure and would agree with the MEUF findings. In fact, the retention percentage of PQ and DQ on different micelles/liposomes demonstrates that some hydrophobic contribution is still present. The results obtained for the PQ/BSA system are in line with the thermodynamic parameters of the PQ/HSA system measured by *G. Zhang et al.* (2007), which demonstrate that PQ binds HSA with a K binding of $4.8 \times 10^4 \text{ M}^{-1}$ (tris-HCl buffer, pH 7.4, 25.0°C), mainly through electrostatic/hydrophobic interactions.^[427] Competitive fluorescence experiments demonstrate that PQ

does not bind to a preferential BSA site, as the interaction does occur regardless of the selective marker used.

The capability of PQ to bind BSA may play a key role in the mechanism of its toxic activity. As a matter of fact, one of the main function of serum albumins is their involvement in the transport, distribution and metabolism of exogenous and endogenous substances (see Chapter I - Paragraph 1.3.1).^{[104],[436]} The interaction between PQ and BSA can therefore affect the bioavailability as well as the spreading of the herbicide in living organisms. Binding constant values of $10^4 - 10^6 \text{ M}^{-1}$ are reported as the optimal K range for the complexation of the ligands and the consequent release once reached the biotarget.^[242] The correlation between albumin's binding and bio-distribution has been highlighted by several studies. *D. Silva et al.* (2010) underlined the crucial importance of methylparathion/albumin interaction in the pesticide's toxic activity.^[437] *V. Dahiya et al.* (2017) proposed that the different solvent-dependent interaction of two organophosphate pesticides with BSA indicates the possibility of different bio-distribution of the pesticides within human body.^[438] The reversible binding to BSA has been exploited by *C. Su et al.* (2020) to enhance the thiacloprid pesticide's performance in the trunk-boring pest's control.^[439] On the whole, we can say that this study contributes to obtain a deeper comprehension of the possible toxic pathways in which the selected pollutants are involved.

Chapter VIII**8. Conclusions**

This work aims to provide useful information on the mechanistic aspects of the interaction between small molecules and biosubstrates. Molecules with different physico-chemical properties were investigated in order to test a wide variety of possible ligands, exploring the advantages and the drawbacks of each one. Several biosubstrates were employed with a focus on their geometrical features as well as on their biological functions. The use of the spectroscopic methods was extensively discussed for avoiding misuses that are sometimes reported in the literature.

Chapter IV presents the analysis of the binding of the water soluble N,N'-bis(2-(1-piperazino)ethyl)-3,4,9,10-perylenetetracarboxylic acid diimide dichloride (PZPERY) to DNA/RNA polynucleotides and G-quadruplex structures (G4). The study of the interaction was performed mainly through spectroscopic techniques, ranging from the typical absorbance measurements to FRET melting experiments. Circular dichroism and isothermal titration calorimetry tests completed the picture. Computational calculations were performed on DNA/PZPERY and G4/PZPERY systems in order to obtain information on the geometry of the adducts and deepen the knowledge of the mechanistic details of the binding. The high tendency of PZPERY to self-aggregate was highlighted and considered in the binding analyses. The binding features were found to be different in the case of natural DNA from calf thymus (ct-DNA) and synthetic RNA polynucleotide, being intercalation

evidenced for the former and groove binding demonstrated for the latter. However, the affinities are not particularly high. DFT calculations on the DNA adduct confirmed that the disruption of the aggregates occurs during the binding event and is partially responsible for the spectroscopic behaviour. PZPERY was also proposed to bind the G4 groove with higher affinity with respect to the double helical form and molecules dynamics simulations provided useful details on the lateral binding.

In *Chapter V*, the copper phthalocyanine Alcian Blue-tetrakis(methylpyridinium) chloride (ABTP) was investigated for affinity to ct-DNA, duplex and triplex RNAs and G4 DNA with different conformations. Aggregation phenomena were found to strongly occur for the ABTP molecule even under diluted conditions. In the case of ct-DNA, the spectroscopic experiments indicated intercalation, while, in the case of RNAs, external binding is the found binding mode. A structure-dependent interaction was highlighted and it was evident that, for this complex system, a subtle change in the geometry can have important effects on the binding mode. The presence of a wide and shallow minor groove in the A-type RNA could drive external interaction, being this effect missing in the case of B-type DNA. UV melting experiments were exploited to gain information on the G4 binding. Besides a general affinity for all the tested G4s, ABTP seems to slightly prefer the CTA22 antiparallel form, to which it binds differently from the very similar features of the ABTP/Tel23 (hybrid) and ABTP/c-myc (parallel) systems. The result could be ascribed to the arrangement of the G4 loops, which differently hinder the lateral G4 surface exposed to PZPERY binding.

Chapter VI reports interesting results on the newly synthesised TPE derivative (1,2-bis(4-((triethylammonium)butoxy)phenyl)-1,2-tetraphenyl ethene dibromide, BTATPE) binding to polynucleotides. The Aggregation Induced

Emission (AIE) properties of this molecular rotor were successfully exploited in the spectrofluorometric experiments. BTATPE was found to interact with natural ct-DNA, with binding constant values strongly dependent on the salt content of the medium. The same behaviour was observed for the synthetic DNAs polyG·polyC and polyA·polyT, for which this dependence is even more pronounced. Under physiological conditions, no binding affinity for duplex polyA·polyU and triplex polyA·2polyU RNA was evidenced. Circular dichroism, viscosity measurements and thermal denaturation tests confirmed an external binding of the probes to the polynucleotide with a strong preference for B-DNAs, with very strong stabilising effects in which the positively charged arms of BTATPE have a leading role.

Finally, *Chapter VII* is devoted to the analysis of some model persistent organic pollutants. Information on the binding of the selected pollutants to biosubstrates were obtained through the use of spectroscopic techniques, viscosity measurements, (TD)DFT calculations and analysis of the percentage of retention on micellar aggregates and liposomes. The superimposition of the pollutants' signals with those of the biotargets limited the potential of the spectroscopic methods, but the optimization of the experimental conditions as well as the use of mathematical correction on biased data allowed us to gain reliable results.

The computational study on the intercalation of 1-aminopyrene (1-pyNH₂), carbendazim (CBZ) and carbaryl (CA) between the DNA base pairs underlined the importance of the aromatic cores in driving the binding mode and provided useful information on the fine properties of the systems as the charge transfer with DNA. On the contrary, no strong affinity to DNA was observed for paraquat (PQ) and diquat (DQ) herbicides, for which just an electrostatic interaction is proposed. PQ does bind the bovine serum albumin

(BSA) protein instead. The binding is supposed to be electrostatically driven, even if a minority hydrophobic interaction might be involved as well. This latter finding agrees with the MEUF experiments on micelles/liposomes, which demonstrated that the electrostatic forces play a major role in leading the absorption on the tested surfaces, but a hydrophobic contribution is anyway present.

On the whole it may be concluded that the analysis of the binding mechanism of a probe/dye/drug to a biosubstrate is an important and difficult task. This is even more true in the case of small molecules which strongly undergo auto-aggregation phenomena or/and absorb light in the UV range only, with high superimposition of their own signal with that of the biosubstrate. However, the optimisation of the experimental conditions, the use of some tricks, models and data corrections enable to obtain also for these unfavourable systems a binding mode description, which is useful for the optimisation of sensors and drugs or for the better comprehension of toxic effects.

Appendices

Appendix I – Equations for a simple 1:1 model

In the case that the reaction between a polymer site (P) and a dye (D) can be expressed by the simple 1:1 relationship:



the related equilibrium constant will be:

$$K_{\text{eq}} = \frac{[PD]}{[P][D]} \quad (1.2)$$

where [PD] is the molar concentration of the polymer/dye complex, while [P] and [D] are the molar concentrations of the free polymer and dye respectively.

The total concentration of each species corresponds to the sum of the free and the complexed form:

$$C_P = [P] + [PD] \quad (1.3)$$

$$C_D = [D] + [PD] \quad (1.4)$$

If the *Lambert and Beer* law applies, for a wavelength where the free and bound dye only absorb and for a 1 cm path length cell, the overall absorbance is given by the equation:

$$A_{\text{obs}} = \varepsilon_{\text{P}}[\text{P}] + \varepsilon_{\text{PD}}[\text{PD}] \quad (1.5)$$

Expressing [D] through equation (1.4) yields:

$$\begin{aligned} A_{\text{obs}} &= \varepsilon_{\text{D}}(C_{\text{D}} - [\text{PD}]) + \varepsilon_{\text{PD}}[\text{PD}] \\ A_{\text{obs}} &= \varepsilon_{\text{D}}C_{\text{D}} - \varepsilon_{\text{D}}[\text{PD}] + \varepsilon_{\text{PD}}[\text{PD}] \\ A_{\text{obs}} - \varepsilon_{\text{D}}C_{\text{D}} &= [\text{PD}](\varepsilon_{\text{PD}} - \varepsilon_{\text{D}}) \end{aligned} \quad (1.6)$$

If one defines the difference between the observed absorbance and that expected for the free dye as $A_{\text{obs}} - \varepsilon_{\text{D}}C_{\text{D}} = \Delta A$ (where, if not known, ε_{D} is calculated by dividing the initial absorbance intensity A° of the dye solution for the dye concentration C°_{D} , and C_{D} varies at each step of the titration) and $\varepsilon_{\text{PD}} - \varepsilon_{\text{D}} = \Delta\varepsilon$, equation (2.6) can be expressed as follows:

$$[\text{PD}] = \frac{\Delta A}{\Delta\varepsilon} \quad (1.7)$$

Defining [D] with equation (1.4), the expression of the equilibrium constant (eq. 2.2) becomes:

$$K_{\text{eq}} = \frac{[\text{PD}]}{[\text{P}](C_{\text{D}} - [\text{PD}])} \Rightarrow \frac{1}{K_{\text{eq}}[\text{P}]} = \frac{C_{\text{D}}}{[\text{PD}]} - 1 \quad (1.8)$$

Introducing equation (1.7) in equation (1.8), the *Hildebrand-Benesi*^[159] equation is obtained:

$$\frac{1}{K_{\text{eq}}[P]} = \frac{C_D}{\frac{\Delta A}{\Delta \varepsilon}} - 1$$

$$\frac{C_D}{\Delta A} = \frac{1}{K_{\text{eq}}\Delta \varepsilon} \cdot \frac{1}{[P]} + \frac{1}{\Delta \varepsilon} \quad (1.9)$$

A plot of $C_D/\Delta A_{\text{Abs}}$ vs. $1/[P]$ is a straight line whose slope and intercept are equal to $1/\Delta \varepsilon K$ and $1/\Delta \varepsilon$ respectively. Therefore, K_{eq} is obtained as the intercept/slope ratio, whereas $\Delta \varepsilon$ is the intercept reciprocal.

Equation (1.9) can be rearranged as the corresponding non-linear equivalent:

$$\frac{\Delta A}{C_D} = \frac{\Delta \varepsilon \cdot K_{\text{eq}} \cdot [P]}{1 + K_{\text{eq}}[P]} \quad (1.10)$$

In both cases, an important often underestimated point is that the abscissa (free polynucleotide concentration $[P]$) is not aprioristically known and its value has to be obtained through an iterative procedure. As first approximation, for $[P] \gg [D] > [PD]$, $[P] \approx C_P$. By fitting the experimental data with equation (1.9) or (1.10) an approximate value of K_{eq} is obtained. The equilibrium constant is therefore employed to gain the quantification of the complex concentration $[PD]$, by applying equation (1.2) expressed through equations (1.3) and (1.4) as follows:

$$K_{\text{eq}} = \frac{[PD]}{(C_P - [PD])(C_D - [PD])} \quad (1.11)$$

that provides:

$$[\text{PD}] = \frac{\left(C_P + C_D + \frac{1}{K_{\text{eq}}}\right) - \sqrt{\left(C_P + C_D + \frac{1}{K_{\text{eq}}}\right)^2 - 4 \cdot C_P \cdot C_D}}{2} \quad (1.12)$$

The free polynucleotide concentration [P] can be calculated as:

$$[\text{P}] = C_P - [\text{PD}] \quad (1.3)$$

The obtained result is introduced in equation (1.9) or (1.10) and a more accurate value of K_{eq} is obtained. The process is repeated until convergence of the K_{eq} values is reached.

Analogously, in case of fluorescence experiments:

$$\frac{C_D}{\Delta F} = \frac{1}{K_{\text{eq}} \Delta \varphi} \cdot \frac{1}{[\text{P}]} + \frac{1}{\Delta \varepsilon} \Rightarrow \frac{\Delta F}{C_D} = \frac{\Delta \varphi \cdot K_{\text{eq}} \cdot [\text{P}]}{1 + K_{\text{eq}}[\text{P}]} \quad (1.13)$$

An alternative equation can be derived by expressing the equilibrium constant (equation (1.2)) through equations (1.3), (1.4) and (1.7):

$$K_{\text{eq}} = \frac{\Delta A}{\Delta \varepsilon \left(C_P - \frac{\Delta A}{\Delta \varepsilon}\right) \left(C_D - \frac{\Delta A}{\Delta \varepsilon}\right)}$$

$$\left(C_P - \frac{\Delta A}{\Delta \varepsilon}\right) \left(C_D - \frac{\Delta A}{\Delta \varepsilon}\right) = \frac{\Delta A}{\Delta \varepsilon K_{\text{eq}}}$$

$$\begin{aligned}
C_P C_D - \frac{\Delta A}{\Delta \varepsilon} (C_P + C_D) + \frac{\Delta A^2}{\Delta \varepsilon^2} &= \frac{\Delta A}{\Delta \varepsilon K_{eq}} \\
\frac{C_P C_D}{\Delta A} - \frac{1}{\Delta \varepsilon} (C_P + C_D) + \frac{\Delta A}{\Delta \varepsilon^2} &= \frac{1}{\Delta \varepsilon K_{eq}} \\
\frac{C_P C_D}{\Delta A} + \frac{\Delta A}{\Delta \varepsilon^2} &= \frac{1}{\Delta \varepsilon} (C_P + C_D) + \frac{1}{\Delta \varepsilon K_{eq}} \tag{1.15}
\end{aligned}$$

Such an equation enables K_{eq} and $\Delta \varepsilon$ to be obtained in an iterative way. Namely, disregarding the $(\Delta A/\Delta \varepsilon)^2$ term on a first approximation, $\Delta \varepsilon$ can be calculated from the reciprocal of the slope of the straight line fitting the experimental $C_P C_D/\Delta A$ vs. $(C_P + C_D)$. This $\Delta \varepsilon$ value will be used to re-evaluate the $C_P C_D/\Delta A + (\Delta A/\Delta \varepsilon)^2$ term and so on, until the convergence of the K_{eq} values is reached.

Likewise, for fluorescence experiments:

$$\frac{C_P C_D}{\Delta F} + \frac{\Delta F}{\Delta \varphi^2} = \frac{1}{\Delta \varphi} (C_P + C_D) + \frac{1}{\Delta \varphi K_{eq}} \tag{1.15}$$

Appendix II – Models for different stoichiometries

The reaction between a ligand (dye, D) and an active binding site (S) of a polymer (P) can be described as follows:



And the corresponding equilibrium constant is:

$$K_{SC} = \frac{[SD]}{[S][D]} \quad (2.2)$$

where [SD] is the molar concentration of the polymer/dye complex, while [S] and [D] are the molar concentrations of the free binding sites and the free dye respectively.

The total concentration of the polymer is defined as C_P , which may expressed in nucleotides or in base pairs (the base pairs option has been used all along this thesis). If B is the number of binding sites for each base pairs, then:

$$[S]_0 = C_P B \quad (2.3)$$

Considering that each binding site is independent from the others, at each step of the titration the concentration of the sites corresponds to the sum of the free and the complexed form:

$$[S]_0 = [S] + [SD] \quad (2.4)$$

We then define the fraction of the saturated binding site as follows:

$$r = \frac{[SD]}{C_P} \quad (2.5)$$

Consequently, by expressing equation (2.2) through equation (2.5), we obtain:

$$[S] = \frac{r \cdot C_P}{K_{SC} \cdot [D]} \quad (2.6)$$

If equation (2.4) is expressed in terms of equations (2.3), (2.5) and (2.6), after rearrangement the *Scatchard*^[160] equation is obtained:

$$\frac{r}{[D]} = -K_{SC} \cdot r + K_{SC} \cdot B \quad (2.7)$$

Equation (2.7) represents a straight line, whose slope corresponds to $-K_{SC}$ and the intercept is equal to $K_{SC}B$.

The reciprocal of B yields the number of the binding sites and can be obtained by means of a spectroscopic titration. Note that r and $[D]$ can be expressed through equations (2.8) and (2.9), in which the SD complex can be considered as the PD complex of Appendix I.

$$[D] = C_D - [SD] = C_D - \frac{\Delta A}{\Delta \epsilon} \quad (2.8)$$

$$r = \frac{[SD]}{C_P} = \frac{\Delta A}{C_P \Delta \epsilon} \quad (2.9)$$

By introducing equations (2.3) and (2.9) in equation (2.2) considering $C_P = [S] + [SD]$, and equations (2.3) and (2.5) in equation (2.2) considering $C_P/\gamma = [S] + [DS]$ and it can be demonstrated that, for isolate binding of the dye, i.e. $r \rightarrow 0$, $K_{sc}B = K$, with K the equilibrium constant of the binding defined in Appendix I.

Actually, the linearity supposed by equation (2.7) is rarely fully obeyed. This might happen only in case a single class of independent sites is present on the polymer that, moreover, have to be saturated in ordered way, without any empty space between an occupied site and the following, i.e. when $B = 1$. When the sites are not independent and cooperativity effects are present, gap that cannot be occupied are formed and the *Scatchard* equation can no longer provide a correct model for the equilibrium. The K_{SC} value is no longer a constant, but a function of polynucleotide saturation. More precisely, K_{SC} increases for positive and decreases for negative cooperativity, producing curved *Scatchard* plot with opposite concavities.^[440]

This behaviour was rationalised by J. D. *Mc Ghee* and P. H. *Von Hippel* (1974) through rigorous mathematical models that introduce correcting factors into the *Scatchard* equation, on the basis of cooperativity and probabilistic models. These authors demonstrated that the *Scatchard* plot should display a positive deviation from linearity at the end of the titration curve, i.e. for high values of r . Owing to this phenomenon, due to site overlapping, the intercept on the X-axis is larger than B . Its value, $1/n$, is related to B through the relationship $n = (1/B+1)/2$.^[161]

Appendix III – Fluorescence

Fluorescence is defined as the emission of light from the first excited state upon irradiation with appropriate wavelengths.^[192]

The fluorescence quantum yield is the ratio of the number of photons emitted to the number absorbed:

$$\Phi = \frac{\text{n emitted photons}}{\text{n absorbed photons}} = \frac{F}{I_0 - I} \quad (3.1)$$

where F is the fluorescence emission, while I_0 and I are the intensity of the incident and the emitted light beam respectively.

Given that I_0 can be defined through the *Lambert and Beer* law as $I = I_0 \cdot e^{-2.3\epsilon bC}$, equation (3.1) can be expressed as:

$$F = \Phi \cdot I_0 \cdot e^{-2.3\epsilon bC} \quad (3.2)$$

where ϵ is the molar absorption coefficient ($M^{-1}cm^{-1}$), b is the optical path length (cm) and C is the molar concentration of the chromophore (M).

For low values of ϵ and/or C , the exponential can be approximated with the first order term of *Taylor's* expansion, resulting in a linear correlation between F and C :

$$F = 2.3 \cdot \Phi \cdot I_0 \cdot b \cdot C \quad (3.3)$$

Appendices

As the detector is oriented at 90° with respect to the light source, just a portion of light will be detected. Considering this feature, an instrumental parameter called K has to be introduced:

$$F = K \cdot 2.3 \cdot \Phi \cdot I_0 \cdot b \cdot C \quad (3.4)$$

K , φ , I_0 and b values are constant and can be gathered in the ϕ parameter.

The expression of fluorescence is therefore obtained as:

$$F = \varphi \cdot C \quad (3.5)$$

All the above means that the linear relationship between fluorescence signal and concentration is not straightforward and more complicated than the analogous *Lambert-Beer's* law which applies in the case of absorbance measurements. The experimental conditions for fluorescence need to be carefully chosen and direct proportionality needs to be checked prior to any subsequent data analysis based on the fact that Equation (3.5) will hold.

Appendix IV – Viscosity

The viscosity of a liquid flowing through a capillary viscometer can be expressed through the *Poiseuille's* law:

$$\eta = \frac{\pi \cdot P \cdot r^4 \cdot t}{8 \cdot V \cdot l} \quad (4.1)$$

where P is the pressure applied on the liquid, r is the radius of the of the capillary, t represents the flow time, V is the volume of the solution and l is the length of the capillary.

The applied pressure corresponds to:

$$P = \rho \cdot h \cdot g \quad (4.2)$$

where ρ is the density of the solution, h is the difference between the height reached by the liquid in the two branches of the viscometer and g is the gravitational acceleration.

Introducing equation (4.2) into equation (4.1) yields:

$$\eta = \frac{\pi \cdot \rho \cdot h \cdot g \cdot r^4 \cdot t}{8 \cdot V \cdot l} \quad (4.3)$$

However, the quantification of h, r, V, l is quite difficult to ensure and the expression of the viscosity as a relative feature is therefore preferred. The viscosity of the sample is compared to the viscosity of a reference as:

Appendices

$$\frac{\eta_{\text{sample}}}{\eta_{\text{reference}}} = \frac{\pi \cdot \rho_{\text{sample}} \cdot h \cdot g \cdot r^4 \cdot t_{\text{sample}}}{8 \cdot V \cdot l} \times \frac{8 \cdot V \cdot l}{\pi \cdot \rho_{\text{ref}} \cdot h \cdot g \cdot r^4 \cdot t_{\text{ref}}} \quad (4.4)$$

The h , r , V and l terms are constant. Moreover, as the amount of analyte is very low, ρ_{sample} can be assumed as equal to $\rho_{\text{reference}}$. Equation (4.4) can be thus simplified and the relative viscosity will be expressed as:

$$\frac{\eta_{\text{sample}}}{\eta_{\text{reference}}} = \frac{t'_{\text{sample}}}{t'_{\text{reference}}} = \frac{t_{\text{sample}} - t_{\text{solvent}}}{t_{\text{reference}} - t_{\text{solvent}}} \quad (4.5)$$

Appendix V – The effect of charged peripheral substituents on the interaction of Cu(II)-phthalocyanine complexes with polynucleotides

The ABTP binding properties were compared with those of another copper phthalocyanine, Cu(II)-phthalocyanine-3,4',4'',4'''-tetrasulfonic acid tetrasodium salt (CuPCTS), which, oppositely to ABTP, has four negatively charged substituents (Figure 1).

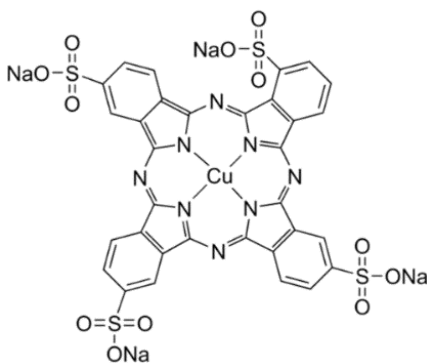


Fig. 1. *Molecular structure of CuPCTS*

Absorbance and circular dichroism titrations reveal that under physiological conditions (NaCl 0.1 M, NaCac 2.5 mM, pH 7.0) CuPCTS does not interact with ct-DNA (Figure 2A and 2B).

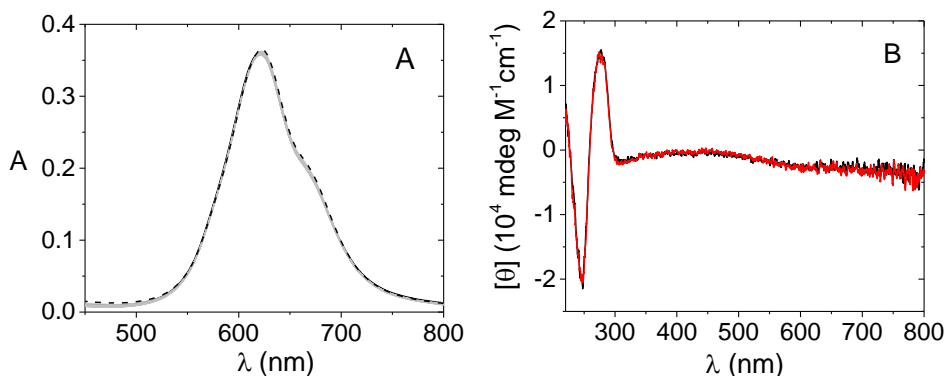


Fig. 2. (A) Absorbance titration of CuPCTS/DNA ($C_{\text{CuPCTS}} = 6.37 \times 10^{-6} \text{ M}$, C_{DNA} from 0 (black) to $5.68 \times 10^{-4} \text{ M}$ (red)) and (B) CD spectra of CuPCTS/DNA ($C_{\text{DNA}} = 5.15 \times 10^{-5} \text{ M}$, C_{CuPCTS} 0 M (black) – $2.29 \times 10^{-6} \text{ M}$ (red)); NaCl 0.1 M, NaCac 2.5 mM, pH 7.0, 25.0 °C

As the positively charged phthalocyanine ABTP does bind DNA, the results demonstrate that the charged substituents play a major role in leading the interaction with the biosubstrate.

Therefore, CuPCTS was tested in NaCl 1 M in order to decrease the electrostatic repulsion with the phosphate groups. Under this conditions, an indicative spectral change (as for ABTP, see Chapter V) is observed at approximately $\lambda = 680 \text{ nm}$ (Figure 3A). The values of the binding constants were calculated with Hypspec® software and the dependence on temperature (*Van't Hoff* plot) is showed in Figure 3B.

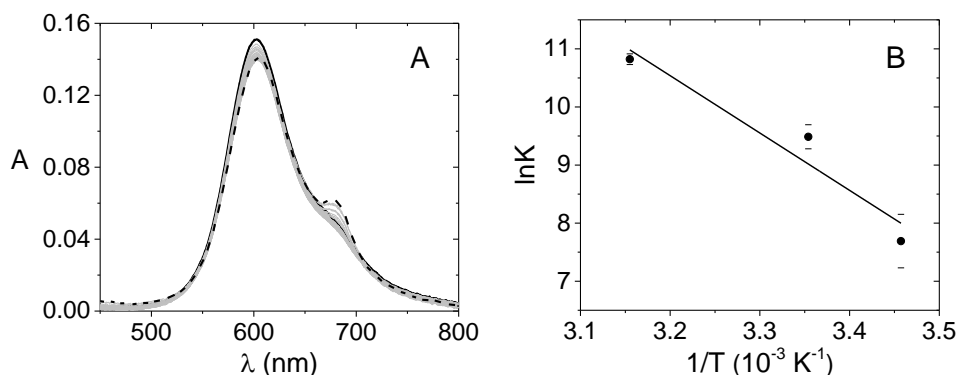


Fig. 3. (A) Absorbance titration of CuPCTS/DNA ($C_{\text{CuPCTS}} = 6.37 \times 10^{-6} \text{ M}$, C_{DNA} from 0 (solid) to $4.25 \times 10^{-4} \text{ M}$ (dash), 45.0°C) and (B) Van't Hoff plot; NaCl 1 M, NaCac 2.5 mM, pH 7.0

Interestingly, if the test in NaCl 1 M is repeated in the presence of double helix RNA poly(rA)·poly(rU), no spectral change occurs (Figure 4). This evidence highlights the binding selectivity: CuPCTS interacts with B-type DNA, but it does not bind A-type RNA under the same conditions.

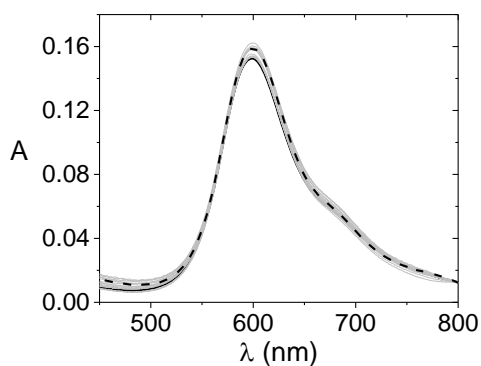


Fig. 4. Absorbance titration of CuPCTS/ polyA·polyU ($C_{\text{CuPCTS}} = 6.37 \times 10^{-6} \text{ M}$, C_{polyAU} from 0 (solid) to $4.03 \times 10^{-4} \text{ M}$ (dash), NaCl 1 M, NaCac 2.5 mM, pH 7.0, 25.0°C)

Appendix VI – The Record equation

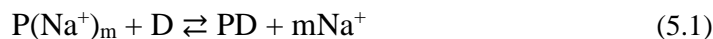
This equation was first derived by *M. T. Record* (1978)^[389] on the basis of a theory that assimilates polynucleotides in solution to negatively charged cylinders, surrounded by a positive counterions atmosphere.

If the ligand is positively charged, the binding is a reaction occurring between ions of opposite charges since the polynucleotide backbone is negatively charged due to the presence of the phosphate groups of the DNA backbone.

Therefore, upon dye interaction with the polynucleotide, some of the positive counterions situated in the vicinity of the polynucleotide has to move far away from the ionic cloud.

At first sight it might seem obvious that, for instance, a +1 positively charged dye intercalating into DNA will expulse one Na⁺ counterion molecule. Nevertheless, the complexity of such systems makes the charge balance not so easy to quantify. Therefore, the equilibrium constant dependence on salt concentration can give interesting information on ion shielding and dye penetration into the helix.

If P(Na⁺)_m indicates a DNA site with its counterions, D the dye, PD the DNA/dye complex and m the number of Na⁺ ions displaced, if a simple 1:1 binding model can be assumed, the complexation reaction can be written as:



whose equilibrium constant is:

$$K' = \frac{[PD][\text{Na}^+]^m}{[P(\text{Na}^+)_m][D]} \quad (5.2)$$

that is:

$$K' = K[\text{Na}^+]^m \quad (5.3)$$

where K is the binding equilibrium constant expressed as $[\text{PD}]/([\text{P}]\times[\text{D}])$.

The logarithmic form of equation (5.3) is:

$$\begin{aligned} \log K' &= \log K + m \cdot \log[\text{Na}^+] \\ \log K &= \log K' - m \cdot \log[\text{Na}^+] \end{aligned} \quad (5.4)$$

The intercept of the plot yields $\log K'$, K' being defined as the binding constant in the absence of electrostatic effects. The slope m corresponds to $m'\psi$, where m' the number of ions pairs formed between ligand and phosphodiester residues and ψ is the extent of DNA charge shielded by counterions. The value of ψ is made by a shielding contribution (ψ_s) and by a contribution from ion condensation (ψ_c). Being for DNA $\psi \approx \psi_c$, it turns out that $m'\psi$ represents the number of condensed sodium ion displaced by one dye molecule. Moreover, the value of ψ for DNA being equal to 0.88^[441], it follows that $m' \approx m$.

Bibliography

- [1] R. E. Dickerson, H. R. Drew, B. N. Conner, R. M. Wing, A. V. Fratini, M. L. Kopka, *Science (80-)*. **1982**, DOI 10.1126/science.7071593.
- [2] J. Watson, F. Crick, *Nature* **1953**.
- [3] R. E. Franklin, R. G. Gosling, *Acta Crystallogr.* **1953**, DOI 10.1107/s0365110x53001939.
- [4] L. L. Albert, A. L. Lehninger, *Lehninger Principles of Biochemistry / David L. Nelson, Michael M. Cox*, **2005**.
- [5] B. J. Pages, D. L. Ang, E. P. Wright, J. R. Aldrich-Wright, *Dalt. Trans.* **2015**, *44*, 3505–3526.
- [6] W. Saenger, *Principles of Nucleic Acid Structure*, **1984**.
- [7] T. Umehara, S. Kuwabara, S. Mashimo, S. Yagihara, *Biopolymers* **1990**, *30*, 649–656.
- [8] J. C. Wang, *Proc. Natl. Acad. Sci. U. S. A.* **1979**, *76*, 200–203.
- [9] R. E. Dickerson, A. Klug, *J. Mol. Biol.* **1983**, *166*, 419–441.
- [10] A. H. J. Wang, G. J. Quigley, F. J. Kolpak, J. L. Crawford, J. H. Van Boom, G. Van Der Marel, A. Rich, *Nature* **1979**, *282*, 680–686.
- [11] T. Biver, B. García, J. M. Leal, F. Secco, E. Turriani, *Phys. Chem. Chem. Phys.* **2010**, *12*, 13309–13317.
- [12] P. D. Leslie A. Pray, *Nat. Educ.* **2008**, DOI 10.1016/S1571-0661(05)82577-0.
- [13] A. Rich, S. Zhang, *Nat. Rev. Genet.* **2003**, DOI 10.1038/nrg1115.
- [14] M. McCall, T. Brown, O. Kennard, *J. Mol. Biol.* **1985**, *183*, 385–396.
- [15] S. Arnott, E. Selsing, *J. Mol. Biol.* **1974**, *88*, 551–552.
- [16] W. Szybalski, H. Kubinski, P. Sheldrick, *Cold Spring Harb. Symp. Quant. Biol.* **1966**, *31*, 123–127.
- [17] J. Aymami, M. Coll, C. A. Frederick, A. H. J. Wang, A. Rich, *Nucleic Acids Res.* **1989**, DOI 10.1093/nar/17.8.3229.
- [18] V. P. Chuprina, *Nucleic Acids Res.* **1987**, DOI 10.1093/nar/15.1.293.
- [19] P. T. Lang, S. R. Brozell, S. Mukherjee, E. F. Pettersen, E. C. Meng, V. Thomas, R. C. Rizzo, D. A. Case, T. L. James, I. D. Kuntz, *Rna* **2009**, *15*, 1219–1230.
- [20] A. Rich, D. R. Davies, *J. Am. Chem. Soc.* **1956**, *78*, 3548–3549.
- [21] A. Varshavsky, *Cell* **2006**, *127*, 1295–1297.
- [22] A. L. Wang, C. C. Wang, *Mol. Biochem. Parasitol.* **1986**, *21*, 269–276.
- [23] G. Hutvagner, P. D. Zamore, *Curr. Opin. Genet. Dev.* **2002**, *12*, 225–232.
- [24] T. Biver, F. Secco, M. Venturini, *Arch. Biochem. Biophys.* **2005**, *437*, 215–223.
- [25] A. M. Katz, I. S. Tolokh, S. A. Pabit, N. Baker, A. V. Onufriev, L. Pollack, *Biophys. J.* **2017**, *112*, 22–30.
- [26] G. Felsenfeld, A. Rich, *BBA - Biochim. Biophys. Acta* **1957**, *26*, 457–468.

- [27] R. Sinha, G. S. Kumar, *J. Phys. Chem. B* **2009**, *113*, 13410–13420.
- [28] F. Qiao, T. R. Cech, *Nat. Struct. Mol. Biol.* **2008**, *15*, 634–640.
- [29] C. C. Esau, B. P. Monia, *Adv. Drug Deliv. Rev.* **2007**, *59*, 101–114.
- [30] G. Felsenfeld, D. R. Davies, A. Rich, *J. Am. Chem. Soc.* **1957**, DOI 10.1021/ja01565a074.
- [31] B. Garcia, J. M. Leal, V. Paiotta, S. Ibeas, R. Ruiz, F. Secco, M. Venturini, *J. Phys. Chem. B* **2006**, *110*, 16131–16138.
- [32] T. Hermann, E. Westhof, *Curr. Opin. Biotechnol.* **1998**, DOI 10.1016/S0958-1669(98)80086-4.
- [33] T. V. Chalikian, J. Völker, A. R. Srinivasan, W. K. Olson, K. J. Breslauer, *Biopolymers* **1999**, *50*, 459–471.
- [34] S. Dasari, P. Bernard Tchounwou, *Eur. J. Pharmacol.* **2014**, *740*, 364–378.
- [35] L. Strekowski, B. Wilson, *Mutat. Res. - Fundam. Mol. Mech. Mutagen.* **2007**, *623*, 3–13.
- [36] H. Ihmels, D. Otto, *Top. Curr. Chem.* **2005**, *258*, 161–204.
- [37] H. S. B. N. Sangeetha Gowda K.R., Blessy Baby Mathew, C.N. Sudhamani, *Biomed. Biotechnol.* **2014**, *Vol. 2 No.*, 1–9.
- [38] M. J. Waring, *J. Mol. Biol.* **1965**, *13*, 269–282.
- [39] T. Biver, F. Secco, M. R. Tinè, M. Venturini, *Arch. Biochem. Biophys.* **2003**, *418*, 63–70.
- [40] J. Sartorius, H. J. Schneider, *J. Chem. Soc. Perkin Trans. 2* **1997**, 2319–2327.
- [41] L. Li, J. Lu, W. Zhou, H. Li, X. Yang, *J. Photochem. Photobiol. B Biol.* **2013**, *123*, 32–40.
- [42] W. D. Wilson, R. L. Jones, *Intercalating Drugs: DNA Binding and Molecular Pharmacology*, **1981**.
- [43] J. B. Chaires, *Arch. Biochem. Biophys.* **2006**, *453*, 26–31.
- [44] J. B. Chaires, *Biopolymers* **1997**, *44*, 201–215.
- [45] T. Record, D. P. D. E. Haseth, **1976**, 145–158.
- [46] M. Waring, *J. Mol. Biol.* **1970**, *54*, 247–279.
- [47] A. S. Biebricher, I. Heller, R. F. H. Roijmans, T. P. Hoekstra, E. J. G. Peterman, G. J. L. Wuite, *Nat. Commun.* **2015**, *6*, 1–12.
- [48] J. B. Chaires, *Curr. Opin. Struct. Biol.* **1998**, *8*, 314–320.
- [49] L. H. Hurley, *Nat. Rev. Cancer* **2002**, *2*, 188–200.
- [50] G. S. Khan, A. Shah, Zia-Ur-Rehman, D. Barker, *J. Photochem. Photobiol. B Biol.* **2012**, *115*, 105–118.
- [51] S. Neidle, *Nat. Prod. Rep.* **2001**, *18*, 291–309.
- [52] F. Hamy, U. Asseline, J. Grasby, S. Iwai, C. Pritchard, G. Slim, P. J. G. Butler, J. Karn, M. J. Gait, *J. Mol. Biol.* **1993**, DOI 10.1006/jmbi.1993.1129.
- [53] J. C. François, T. Saison-Behmoaras, C. Hélène, *Nucleic Acids Res.* **1988**, DOI 10.1093/nar/16.24.11431.
- [54] A. Biancardi, T. Biver, F. Secco, B. Mennucci, *Phys. Chem. Chem. Phys.* **2013**, *15*, 4596–4603.
- [55] C. M. Nunn, E. Garman, S. Neidle, *Biochemistry* **1997**, *36*, 4792–4799.
- [56] I. Haq, J. E. Ladbury, B. Z. Chowdhry, T. C. Jenkins, J. B. Chaires, *J. Mol.*

- Biol.* **1997**, 271, 244–257.
- [57] C. Bailly, J. B. Chaires, *Bioconjug. Chem.* **1998**, 9, 513–538.
- [58] S. M. Nelson, L. R. Ferguson, W. A. Denny, *Mutat. Res. - Fundam. Mol. Mech. Mutagen.* **2007**, 623, 24–40.
- [59] M. A. A. F. d. C. T. Carrondo, M. Coll, J. Aymami, A. H. J. Wang, G. A. van der Marel, J. H. van Boom, A. Rich, *Biochemistry* **1989**, 28, 7849–7859.
- [60] M. L. Kopka, C. Yoon, D. Goodsell, P. Pjura, R. E. Dickerson, *Proc. Natl. Acad. Sci. U. S. A.* **1985**, 82, 1376–1380.
- [61] H. Diebler, F. Secco, M. Venturini, *Biophys. Chem.* **1987**, 26, 193–205.
- [62] H. J. Li, D. M. Crothers, *J. Mol. Biol.* **1969**, 39, 461–477.
- [63] M. Bengtsson, *Nucleic Acids Res.* **2003**, 31, 45e – 45.
- [64] M. Eigen, K. Tamm, *Zeitschrift für Elektrochemie* **1962**, 66, 93–107.
- [65] D. F. Bradley, M. K. Wolf, *Proc. Natl. Acad. Sci.* **1959**, 45, 944–952.
- [66] K. E. Erkkila, D. T. Odom, J. K. Barton, *Chem. Rev.* **1999**, 99, 2777–2795.
- [67] D. E. Graves, L. M. Velea, *Curr. Org. Chem.* **2005**, 4, 915–929.
- [68] R. Nanjunda, W. D. Wilson, *Curr. Protoc. Nucleic Acid Chem.* **2012**, 1–20.
- [69] C. Zimmer, *Prog. Nucleic Acid Res. Mol. Biol.* **1975**, DOI 10.1016/S0079-6603(08)60122-1.
- [70] W. Müller, *Eur. J. ...* **1975**, 54, 267–277.
- [71] W. Müller, D. M. Crothers, *J. Mol. Biol.* **1968**, 35, 251–290.
- [72] E. Tuite, B. Nordén, *J. Am. Chem. Soc.* **1994**, 116, 7548–7556.
- [73] R. Haselkorn, *Science (80-.)*. **1964**, 143, 682–684.
- [74] S. Burge, G. N. Parkinson, P. Hazel, A. K. Todd, S. Neidle, *Nucleic Acids Res.* **2006**, 34, 5402–5415.
- [75] D. Sen, W. Gilbert, *Nature* **1988**, DOI 10.1038/334364a0.
- [76] M. W. Kilpatrick, A. Torri, D. S. Kang, J. A. Engler, R. D. Wells, *J. Biol. Chem.* **1986**, 261, 11350–11354.
- [77] C. Platella, C. Riccardi, D. Montesarchio, G. N. Roviello, D. Musumeci, *Biochim. Biophys. Acta - Gen. Subj.* **2017**, 1429–1447.
- [78] W. E. Wright, V. M. Tesmer, K. E. Huffman, S. D. Levene, J. W. Shay, *Genes Dev.* **1997**, 11, 2801–2809.
- [79] S. T. D. Hsu, P. Varnai, A. Bugaut, A. P. Reszka, S. Neidle, S. Balasubramanian, *J. Am. Chem. Soc.* **2009**, 131, 13399–13409.
- [80] K. W. Lim, P. Alberti, A. Guédin, L. Lacroix, J. F. Riou, N. J. Royle, J. L. Mergny, A. T. Phan, *Nucleic Acids Res.* **2009**, 37, 6239–6248.
- [81] Z. F. Wang, M. H. Li, S. T. D. Hsu, T. C. Chang, *Nucleic Acids Res.* **2014**, DOI 10.1093/nar/gku083.
- [82] A. Ambrus, D. Chen, J. Dai, T. Bialis, R. A. Jones, D. Yang, *Nucleic Acids Res.* **2006**, 34, 2723–2735.
- [83] F. B. Howard, J. Frazier, H. T. Miles, *Biopolymers* **1977**, 16, 791–809.
- [84] K. N. Luu, A. T. Phan, V. Kuryavyi, L. Lacroix, D. J. Patel, *J. Am. Chem. Soc.* **2006**, 128, 9963–9970.
- [85] J. L. Mergny, C. Helene, *Nat. Med.* **1998**, 4, 1366–1367.
- [86] C. Harley B., A. Fatcher B., C. Greider W., *Nature* **1990**, 345, 458–460.
- [87] A. De Cian, L. Lacroix, C. Douarre, N. Temime-Smaali, C. Trentesaux, J. F.

- Riou, J. L. Mergny, *Biochimie* **2008**, *90*, 131–155.
- [88] D. Sun, B. Thompson, B. E. Cathers, M. Salazar, S. M. Kerwin, J. O. Trent, T. C. Jenkins, S. Neidle, L. H. Hurley, *J. Med. Chem.* **1997**, *40*, 2113–2116.
- [89] R. T. Wheelhouse, D. Sun, H. Han, F. X. Han, L. H. Hurley, *J. Am. Chem. Soc.* **1998**, *120*, 3261–3262.
- [90] H. Yaku, T. Fujimoto, T. Murashima, D. Miyoshi, N. Sugimoto, *Chem. Commun.* **2012**, *48*, 6203–6216.
- [91] S. N. Georgiades, N. H. Abd Karim, K. Suntharalingam, R. Vilar, *Angew. Chemie - Int. Ed.* **2010**, *49*, 4020–4034.
- [92] A. Arola, R. Vilar, *Curr. Top. Med. Chem.* **2008**, 1405–1415.
- [93] N. Busto, P. Calvo, J. Santolaya, J. M. Leal, A. Guédin, G. Barone, T. Torroba, J. L. Mergny, B. García, *Chem. - A Eur. J.* **2018**, *24*, 11292–11296.
- [94] S. Neidle, *Nat. Rev. Chem.* **2017**, *1*, 1–10.
- [95] D. Monchaud, A. Granzhan, N. Saettel, A. Guédin, J. L. Mergny, M. P. Teulade-Fichou, *J. Nucleic Acids* **2010**, DOI 10.4061/2010/525862.
- [96] C. Pérez-Arnaiz, N. Busto, J. Santolaya, J. M. Leal, G. Barone, B. García, *Biochim. Biophys. Acta - Gen. Subj.* **2018**, *1862*, 522–531.
- [97] Q. Cao, Y. Li, E. Freisinger, P. Z. Qin, R. K. O. Sigel, Z. W. Mao, *Inorg. Chem. Front.* **2017**, *4*, 10–32.
- [98] J. E. Reed, A. A. Arnal, S. Neidle, R. Vilar, *J. Am. Chem. Soc.* **2006**, *128*, 5992–5993.
- [99] D. Monchaud, M. P. Teulade-Fichou, *Org. Biomol. Chem.* **2008**, *6*, 627–636.
- [100] C. Rajput, R. Rutkaite, L. Swanson, I. Haq, J. A. Thomas, *Chem. - A Eur. J.* **2006**, *12*, 4611–4619.
- [101] T. M. Ou, Y. J. Lu, J. H. Tan, Z. S. Huang, K. Y. Wong, L. Q. Gu, *ChemMedChem* **2008**, *3*, 690–713.
- [102] X. M. He, D. C. Carter, *Nature* **1992**, DOI 10.1038/358209a0.
- [103] Y. Zhang, K. Zhou, Y. Lou, D. Pan, J. Shi, *J. Biomol. Struct. Dyn.* **2017**, *1102*, 1–10.
- [104] R. E. Olson, D. D. Christ, *Annu. Rep. Med. Chem.* **1996**, *31*, 327–336.
- [105] W. M. Pardridge, *Am. J. Physiol. - Endocrinol. Metab.* **1987**, DOI 10.1152/ajpendo.1987.252.2.e157.
- [106] Y. J. Hu, Y. Liu, X. H. Xiao, *Biomacromolecules* **2009**, *10*, 517–521.
- [107] M. H. Tarhoni, T. Lister, D. E. Ray, W. G. Carter, *Biomarkers* **2008**, *13*, 343–363.
- [108] A. Sułkowska, M. Maciazek-Jurczyk, B. Bojko, J. Równicka, I. Zubik-Skupień, E. Temba, D. Pentak, W. W. Sułkowski, *J. Mol. Struct.* **2008**, *881*, 97–106.
- [109] J. Tian, J. Liu, Z. Hu, X. Chen, *Interactions* **2005**, *1*, 21–23.
- [110] D. C. Carter, J. X. Ho, *Adv. Protein Chem.* **1994**, *45*, 153–176.
- [111] G. Zhang, A. Wang, T. Jiang, J. Guo, *J. Mol. Struct.* **2008**, *891*, 93–97.
- [112] G. Sudlow, D. J. Birkett, D. N. Wade, *Mol. Pharmacol.* **1975**, *11*, 824–832.
- [113] S. K. Pawar, S. Jaldappagari, *J. Pharm. Anal.* **2019**, *9*, 274–283.
- [114] J. F. Neault, A. Benkirane, H. Malonga, H. A. Tajmir-Riahi, *J. Inorg.*

- Biochem.* **2001**, *86*, 603–609.
- [115] M. Jiang, M. X. Xie, D. Zheng, Y. Liu, X. Y. Li, X. Chen, *J. Mol. Struct.* **2004**, *692*, 71–80.
- [116] M. C. Manning, *Expert Rev. Proteomics* **2005**, *2*, 731–743.
- [117] I. M. Klotz, *Ann. N. Y. Acad. Sci.* **1973**, *226*, 18–35.
- [118] P. D. Ross, S. Subramanian, *Biochemistry* **1981**, *20*, 3096–3102.
- [119] G. Zhang, N. Zhao, X. Hu, J. Tian, *Spectrochim. Acta - Part A Mol. Biomol. Spectrosc.* **2010**, *76*, 410–417.
- [120] X. Le Han, F. F. Tian, Y. S. Ge, F. L. Jiang, L. Lai, D. W. Li, Q. L. Yu, J. Wang, C. Lin, Y. Liu, *J. Photochem. Photobiol. B Biol.* **2012**, *109*, 1–11.
- [121] X. Le Han, P. Mei, Y. Liu, Q. Xiao, F. L. Jiang, R. Li, *Spectrochim. Acta - Part A Mol. Biomol. Spectrosc.* **2009**, *74*, 781–787.
- [122] Y. Z. Zhang, X. Xiang, P. Mei, J. Dai, L. L. Zhang, Y. Liu, *Spectrochim. Acta - Part A Mol. Biomol. Spectrosc.* **2009**, *72*, 907–914.
- [123] Y. Z. Zhang, B. Zhou, X. P. Zhang, P. Huang, C. H. Li, Y. Liu, *J. Hazard. Mater.* **2009**, *163*, 1345–1352.
- [124] Y. Z. Zhang, H. R. Li, J. Dai, W. J. Chen, J. Zhang, Y. Liu, *Biol. Trace Elem. Res.* **2010**, *135*, 136–152.
- [125] M. Asadi, Z. Asadi, L. Zarei, S. B. Sadi, Z. Amirghofran, *Spectrochim. Acta - Part A Mol. Biomol. Spectrosc.* **2014**, *133*, 697–706.
- [126] X. X. Cheng, Y. Lui, B. Zhou, X. H. Xiao, Y. Liu, *Spectrochim. Acta - Part A Mol. Biomol. Spectrosc.* **2009**, *72*, 922–928.
- [127] Y. J. Hu, Y. Ou-Yang, C. M. Dai, Y. Liu, X. H. Xiao, *Mol. Biol. Rep.* **2010**, *37*, 3827–3832.
- [128] J. hua Shi, D. qi Pan, M. Jiang, T. T. Liu, Q. Wang, *J. Photochem. Photobiol. B Biol.* **2016**, DOI 10.1016/j.jphotobiol.2016.09.025.
- [129] J. hua Shi, D. qi Pan, X. xiou Wang, T. T. Liu, M. Jiang, Q. Wang, *J. Photochem. Photobiol. B Biol.* **2016**, *162*, 14–23.
- [130] Y. Ni, R. Zhu, S. Kokot, *Analyst* **2011**, *136*, 4794.
- [131] J. H. Shi, K. L. Zhou, Y. Y. Lou, D. Q. Pan, *Spectrochim. Acta - Part A Mol. Biomol. Spectrosc.* **2018**, *188*, 362–371.
- [132] J. H. Shi, Q. Wang, D. Q. Pan, T. T. Liu, M. Jiang, *J. Biomol. Struct. Dyn.* **2017**, *35*, 1529–1546.
- [133] G. F. Shen, T. T. Liu, Q. Wang, M. Jiang, J. H. Shi, *J. Photochem. Photobiol. B Biol.* **2015**, *153*, 380–390.
- [134] J. H. Shi, Y. Y. Zhu, J. Wang, J. Chen, Y. J. Shen, *Spectrochim. Acta - Part A Mol. Biomol. Spectrosc.* **2013**, *103*, 287–294.
- [135] X. Wang, L. Zou, C. Mi, H. Yu, M. Dong, Y. Teng, *J. Environ. Sci. Heal. - Part A Toxic/Hazardous Subst. Environ. Eng.* **2020**, *55*, 318–325.
- [136] X. Wei, Y. Yang, J. Ge, X. Lin, D. Liu, S. Wang, J. Zhang, G. Zhou, S. Li, *J. Inorg. Biochem.* **2020**, *202*, 110857.
- [137] S. Neidle, L. H. Pearl, J. V. Skelly, *Biochem. J.* **1987**, *243*, 1–13.
- [138] P. Giri, G. S. Kumar, *Arch. Biochem. Biophys.* **2008**, *474*, 183–192.
- [139] J. A. Bordelon, K. J. Feierabend, S. A. Siddiqui, L. L. Wright, J. T. Petty, *J. Phys. Chem. B* **2002**, *106*, 4838–4843.

- [140] T. Urathamakul, D. J. Waller, J. L. Beck, J. R. Aldrich-Wright, S. F. Ralph, *Inorg. Chem.* **2008**, *47*, 6621–6632.
- [141] A. Terenzi, C. Ducani, L. Male, G. Barone, M. J. Hannon, *Dalt. Trans.* **2013**, *42*, 11220–11226.
- [142] P. Ragazzon, J. B. Chaires, *Methods* **2007**, *43*, 313–323.
- [143] A. Adams, *Med. Chem. Rev. - Online* **2005**, *1*, 405–412.
- [144] S. J. Berners-Price, L. Ronconi, P. J. Sadler, *Prog. Nucl. Magn. Reson. Spectrosc.* **2006**, *49*, 65–98.
- [145] Y. Iwasaki, M. Kimura, A. Yamada, Y. Mutoh, M. Tateishi, H. Arai, Y. Kitamura, M. Chikira, *Inorg. Chem. Commun.* **2011**, *14*, 1461–1464.
- [146] A. Blake, A. R. Peacocke, *Biopolymers* **1968**, *6*, 1225–1253.
- [147] L. S. Lerman, *J. Mol. Biol.* **1961**, *3*, 18–30.
- [148] T. Biver, *Appl. Spectrosc. Rev.* **2012**, *47*, 272–325.
- [149] A. Tingle, *J. Am. Chem. Soc.* **1918**, DOI 10.1021/ja02239a001.
- [150] S. Hanlon, L. Wong, G. R. Pack, *Biophys. J.* **1997**, *72*, 291–300.
- [151] A. G. Cherstvy, *J. Phys. Chem. B* **2007**, *111*, 12933–12937.
- [152] J. Liu, W. J. Mei, L. J. Lin, K. C. Zheng, H. Chao, F. C. Yun, L. N. Ji, *Inorganica Chim. Acta* **2004**, *357*, 285–293.
- [153] M. Sirajuddin, S. Ali, A. Badshah, *J. Photochem. Photobiol. B Biol.* **2013**, *124*, 1–19.
- [154] S. Aydinoglu, A. Pasti, T. Biver, B. Mennucci, *Phys. Chem. Chem. Phys.* **2019**, *21*, 20606–20612.
- [155] T. Nowicka-Jankowska, *J. Inorg. Nucl. Chem.* **1971**, *33*, 2043–2050.
- [156] T. Biver, S. Aydinoglu, D. Greco, F. Macii, *Monatshefte fur Chemie* **2018**, *149*, 175–183.
- [157] R. Bondi, T. Biver, L. Dalla Via, F. Guarra, M. Hyeraci, C. Sissi, L. Labella, F. Marchetti, S. Samaritani, *J. Inorg. Biochem.* **2020**, *202*, 110874.
- [158] S. J. Leach, H. A. Scheraga, *J. Am. Chem. Soc.* **1960**, *82*, 4790–4792.
- [159] H. A. Benesi, J. H. Hildebrand, *J. Am. Chem. Soc.* **1949**, DOI 10.1021/ja01176a030.
- [160] B. Y. G. Scatchard, *Ann. New York Acad. Sci.* **1949**, 660–672.
- [161] J. D. McGhee, P. H. von Hippel, *J. Mol. Biol.* **1974**, DOI 10.1016/0022-2836(74)90031-X.
- [162] R. Thomas, *Experientia* **1951**, DOI 10.1007/BF02154543.
- [163] R. Thomas, *BBA - Biochim. Biophys. Acta* **1954**, DOI 10.1016/0006-3002(54)90163-8.
- [164] R. Thomas, *Gene* **1993**, *135*, 77–79.
- [165] C. R. Stewart, *Biopolymers* **1968**, *6*, 1737–1743.
- [166] J. L. Mergny, G. Duval-Valentin, C. H. Nguyen, L. Perrouault, B. Faucon, M. Rougée, T. Montenay-Garestier, E. Bisagni, C. Hélène, *Science (80-.)*. **1992**, DOI 10.1126/science.256.5064.1681.
- [167] J. M. Y, A. Phan, L. Lacroix, **1998**, *435*, 74–78.
- [168] J. L. Mergny, L. Lacroix, *Oligonucleotides* **2003**, *13*, 515–537.
- [169] P. D. Lawley, *Biochim. Biophys. Acta* **1956**, *21*, 481–488.
- [170] A. Rich, M. Kasha, *J. Am. Chem. Soc.* **1960**, DOI 10.1021/ja01508a057.

- [171] P. Yakovchuk, E. Protozanova, M. D. Frank-Kamenetskii, *Nucleic Acids Res.* **2006**, *34*, 564–574.
- [172] C. Schildkraut, S. Lifson, *Biopolymers* **1965**, *3*, 195–208.
- [173] A. Kellett, Z. Molphy, C. Slator, V. McKee, N. P. Farrell, *Chem. Soc. Rev.* **2019**, *48*, 971–988.
- [174] A. Guédin, L. Lacroix, J. L. Mergny, *Methods Mol. Biol.* **2010**, DOI 10.1007/978-1-60327-418-0_2.
- [175] W. D. Wilson, F. A. Tanius, M. Fernandez-Saiz, C. T. Rigl, *Methods Mol. Biol.* **1997**, *90*, 219–240.
- [176] R. Palchaudhuri, P. J. Hergenrother, *Curr. Opin. Biotechnol.* **2007**, *18*, 497–503.
- [177] C. V. Kumar, E. H. Asuncion, *J. Am. Chem. Soc.* **1993**, *115*, 8547–8553.
- [178] W. D. Wilson, L. Ratmeyer, M. Zhao, L. Strekowski, D. Boykin, *Biochemistry* **1993**, *32*, 4098–4104.
- [179] M. A. Husain, T. Sarwar, S. U. Rehman, H. M. Ishqi, M. Tabish, *Phys. Chem. Chem. Phys.* **2015**, *17*, 13837–13850.
- [180] F. Guarra, N. Busto, A. Guerri, L. Marchetti, T. Marzo, B. García, T. Biver, C. Gabbiani, *J. Inorg. Biochem.* **2020**, *205*, DOI 10.1016/j.jinorgbio.2020.110998.
- [181] T. Biver, A. Boggioni, B. García, J. M. Leal, R. Ruiz, F. Secco, M. Venturini, *Nucleic Acids Res.* **2009**, *38*, 1697–1710.
- [182] C. Tanford, *Adv. Protein Chem.* **1968**, DOI 10.1016/S0065-3233(08)60401-5.
- [183] M. Barbi, S. Lepri, M. Peyrard, N. Theodorakopoulos, *Phys. Rev. E - Stat. Physics, Plasmas, Fluids, Relat. Interdiscip. Top.* **2003**, *68*, 1–14.
- [184] J. Marmur, P. Doty, *J. Mol. Biol.* **1961**, DOI 10.1016/S0022-2836(61)80023-5.
- [185] J. L. Mergny, L. Lacroix, *Curr. Protoc. Nucleic Acid Chem.* **2009**, 1–15.
- [186] J. L. Mergny, J. Li, L. Lacroix, S. Amrane, J. B. Chaires, *Nucleic Acids Res.* **2005**, *33*, 1–6.
- [187] B. Juskowiak, *Anal. Bioanal. Chem.* **2011**, *399*, 3157–3176.
- [188] A. Marini, A. Muñoz-Losa, A. Biancardi, B. Mennucci, *J. Phys. Chem. B* **2010**, *114*, 17128–17135.
- [189] D. Suh, J. B. Chaires, *Bioorganic Med. Chem.* **1995**, *3*, 723–728.
- [190] S. A. Latt, J. C. Wohlleb, *Chromosoma* **1975**, *52*, 297–316.
- [191] S. M. Yarmoluk, S. S. Lukashov, M. Y. Losytskyy, B. Akerman, O. S. Korniyushyna, *Spectrochim. Acta - Part A Mol. Biomol. Spectrosc.* **2002**, *58*, 3223–3232.
- [192] J. R. Lakowicz, *Principles of Fluorescence Spectroscopy*, **2006**.
- [193] A. Biancardi, T. Biver, A. Marini, B. Mennucci, F. Secco, *Phys. Chem. Chem. Phys.* **2011**, *13*, 12595–12602.
- [194] A. Biancardi, T. Biver, A. Burgalassi, M. Mattonai, F. Secco, M. Venturini, *Phys. Chem. Chem. Phys.* **2014**, *16*, 20061–20072.
- [195] Y. Hong, *Methods Appl. Fluoresc.* **2016**, 022003, 22003.
- [196] M. Kubista, R. Sjöback, S. Eriksson, B. Albinsson, *Analyst* **1994**, *119*, 417–

- 419.
- [197] F. J. Meyer-Almes, D. Porschke, *Biochemistry* **1993**, *32*, 4246–4253.
- [198] J. Olmsted, D. R. Kearns, *Biochemistry* **1977**, *16*, 3647–3654.
- [199] J. B. Lepecq, C. Paoletti, *J. Mol. Biol.* **1967**, *27*, 87–106.
- [200] A. R. Morgan, J. S. Lee, D. E. Pulleyblank, N. L. Murray, D. H. Evans, *Nucleic Acids Res.* **1979**, DOI 10.1093/nar/7.3.547.
- [201] W. C. Tse, D. L. Boger, *Acc. Chem. Res.* **2004**, *37*, 61–69.
- [202] T. Marzo, D. Cirri, L. Ciofi, C. Gabbiani, A. Feis, N. Di Pasquale, M. Stefanini, T. Biver, L. Messori, *J. Inorg. Biochem.* **2018**, *183*, 101–106.
- [203] T. Förster, *Ann. Phys.* **1948**, DOI 10.1002/andp.19484370105.
- [204] A. W. Nguyen, P. S. Daugherty, *Nat. Biotechnol.* **2005**, *23*, 355–360.
- [205] T. Simonsson, R. Sjöback, *J. Biol. Chem.* **1999**, *274*, 17379–17383.
- [206] A. De Cian, L. Guittat, M. Kaiser, B. Saccà, S. Amrane, A. Bourdoncle, P. Alberti, M. P. Teulade-Fichou, L. Lacroix, J. L. Mergny, *Methods* **2007**, *42*, 183–195.
- [207] A. De Rache, J. L. Mergny, *Biochimie* **2015**, *115*, 194–202.
- [208] S. L. Noer, S. Preus, D. Gudnason, M. Aznauryan, J. L. Mergny, V. Birkedal, *Nucleic Acids Res.* **2016**, *44*, 464–471.
- [209] V. V. Didenko, *Biotechniques* **2001**, *31*, 1106–1121.
- [210] D. Renčiuk, J. Zhou, L. Beaurepaire, A. Guédin, A. Bourdoncle, J. L. Mergny, *Methods* **2012**, *57*, 122–128.
- [211] P. Murat, Y. Singh, E. Defrancq, *Chem. Soc. Rev.* **2011**, *40*, 5293–5307.
- [212] T. Kurucsev, M. Kubista, *Q. Rev. Biophys.* **1992**, *25*, 51–170.
- [213] K. S. Dahl, A. Pardi, I. Tinoco, *Biochemistry* **1982**, *21*, 2730–2737.
- [214] M. Górecki, F. Zinna, T. Biver, L. Di Bari, *J. Pharm. Biomed. Anal.* **2017**, *144*, 6–11.
- [215] A. Rodger, *Circular Dichroism and Linear Dichroism*, **2014**.
- [216] A. Cotton, *J. Phys. Théorique Appliquée* **1896**, DOI 10.1051/jphystap:018960050023700.
- [217] L. Rosenfeld, *Zeitschrift für Phys.* **1929**, *52*, 161–174.
- [218] A. Koslowski, N. Sreerama, R. W. Woody, in *Circ. Dichroism Princ. Appl.*, **2000**.
- [219] I. Tinoco, R. W. Woody, *J. Chem. Phys.* **1964**, *40*, 160–165.
- [220] N. Berova, L. Di Bari, G. Pescitelli, *Chem. Soc. Rev.* **2007**, *36*, 914–931.
- [221] J. Kypr, I. Kejnovská, D. Renčiuk, M. Vorlíčková, *Nucleic Acids Res.* **2009**, *37*, 1713–1725.
- [222] T. Šmidlehner, I. Piantanida, G. Pescitelli, *Beilstein J. Org. Chem.* **2017**, *14*, 84–105.
- [223] S. Allenmark, *Chirality* **2003**, *15*, 409–422.
- [224] B. Nordén, T. Kurucsev, *J. Mol. Recognit.* **1994**, *7*, 141–155.
- [225] P. E. Schipper, B. Nordén, F. Tjerneld, *Chem. Phys. Lett.* **1980**, *70*, 17–21.
- [226] R. Lyng, T. Hård, B. Norden, *Biopolymers* **1987**, *26*, 1327–1345.
- [227] R. F. Pasternack, E. J. Gibbs, J. J. Villafranca, J. J. Villafranca, *Biochemistry* **1983**, *22*, 5409–5417.
- [228] O. Buchardt, T. Koch, M. Wirth, B. Nordén, P. E. Nielsen, *J. Am. Chem.*

- Soc.* **1988**, DOI 10.1021/ja00211a038.
- [229] N. C. Garbett, P. A. Ragazzon, J. O. B. Chaires, *Nat. Protoc.* **2007**, *2*, 3166–3172.
- [230] B. García, J. M. Leal, R. Ruiz, T. Biver, F. Secco, M. Venturini, *J. Phys. Chem. B* **2010**, *114*, 8555–8564.
- [231] M. Zama, S. Ichimura, *Biopolymers* **1970**, *9*, 53–63.
- [232] M. Rowley, J. J. Kulagowski, A. P. Watt, D. Rathbone, G. I. Stevenson, R. W. Carling, R. Baker, G. R. Marshall, J. A. Kemp, A. C. Foster, et al., *J. Med. Chem.* **1997**, *40*, 4053–4068.
- [233] M. K. Bijsterbosch, *Nucleic Acids Res.* **2000**, *28*, 2717–2725.
- [234] B. Rizzuti, R. Bartucci, A. L. Pey, R. Guzzi, *Arch. Biochem. Biophys.* **2019**, *676*, 108123.
- [235] M. J. Banker, T. H. Clark, J. A. Williams, *J. Pharm. Sci.* **2003**, *92*, 967–974.
- [236] J. Oravcová, B. Böhs, W. Lindner, *J. Chromatogr. B Biomed. Appl.* **1996**, *677*, 1–28.
- [237] C. Pérez-Arnaiz, J. Leal, N. Busto, M. C. Carrión, A. R. Rubio, I. Ortiz, G. Barone, B. Díaz De Greñu, J. Santolaya, J. M. Leal, et al., *Inorg. Chem.* **2018**, *57*, 6124–6134.
- [238] J. B. Whitlam, K. F. Brown, *J. Pharm. Sci.* **1981**, *70*, 146–150.
- [239] K. P. Campbell, D. H. MacLennantll, A. Jorgensen, *J. Biol. Chem.* **1983**, *258*, 11267–11273.
- [240] F. Zsila, Z. Bikádi, M. Simonyi, *Biochem. Pharmacol.* **2003**, *65*, 447–456.
- [241] D. Rocco, L. K. Batchelor, G. Agonigi, S. Braccini, F. Chiellini, S. Schoch, T. Biver, T. Funaioli, S. Zacchini, L. Biancalana, et al., *Chem. - A Eur. J.* **2019**, 1–17.
- [242] T. Topală, A. Bodoki, L. Oprean, R. Oprean, *Clujul Med.* **2014**, *87*, 5.
- [243] M. Zhu, L. Wang, Y. Wang, J. Zhou, J. Ding, W. Li, Y. Xin, S. Fan, Z. Wang, Y. Wang, *Int. J. Environ. Res. Public Health* **2018**, *15*, DOI 10.3390/ijerph15010116.
- [244] A. Ray, B. Koley Seth, U. Pal, S. Basu, *Spectrochim. Acta - Part A Mol. Biomol. Spectrosc.* **2012**, *92*, 164–174.
- [245] J. Jayabharathi, V. Thanikachalam, M. Venkatesh Perumal, *J. Lumin.* **2012**, *132*, 707–712.
- [246] B. Valeur, *Molecular Fluorescence - Principles and Applications*, **2001**.
- [247] L. K. Fraiji, D. M. Hayes, T. C. Werner, *J. Chem. Educ.* **1992**, *69*, 424–428.
- [248] J. R. Lakowicz, G. Weber, *Biochemistry* **1973**, *12*, 4161–4170.
- [249] F. Macii, G. Salvadori, R. Bonini, S. Giannarelli, B. Mennucci, T. Biver, *Spectrochim. Acta - Part A Mol. Biomol. Spectrosc.* **2019**, *223*, 117313.
- [250] M. R. Eftink, C. A. Ghiron, *Anal. Biochem.* **1981**, *114*, 199–227.
- [251] H. S. Geethanjali, D. Nagaraja, R. M. Melavanki, R. A. Kusanur, *J. Lumin.* **2015**, *167*, 216–221.
- [252] S. S. Lehrer, *Biochemistry* **1971**, *10*, 3254–3263.
- [253] W. R. Ware, *J. Phys. Chem.* **1962**, *66*, 455–458.
- [254] N. Tayeh, T. Rungassamy, J. R. Albani, *J. Pharm. Biomed. Anal.* **2009**, *50*, 107–116.

- [255] J. R. Alcala, E. Gratton, F. G. Prendergast, *Biophys. J.* **1987**, *51*, 597–604.
- [256] J. M. Beechem, L. Brand, *Ann. Rev. Biochem.* **1985**, *54*, 43–71.
- [257] A. A. Franich, M. D. Živković, J. Milovanović, D. Arsenijević, A. Arsenijević, M. Milovanović, M. I. Djuran, S. Rajković, *J. Inorg. Biochem.* **2020**, *210*, 111158.
- [258] T. Töpala, A. Pascual-Álvarez, M. Á. Moldes-Tolosa, A. Bodoki, A. Castiñeiras, J. Torres, C. del Pozo, J. Borrás, G. Alzuet-Piña, *J. Inorg. Biochem.* **2020**, *202*, 110823.
- [259] C. Q. Jiang, M. X. Gao, J. X. He, *Anal. Chim. Acta* **2002**, *452*, 185–189.
- [260] J. A. Molina-Bolívar, F. Galisteo-González, C. Carnero Ruiz, M. Medina-O'Donnell, A. Parra, *J. Mol. Liq.* **2015**, *208*, 304–313.
- [261] P. Sathyadevi, P. Krishnamoorthy, E. Jayanthi, R. R. Butorac, A. H. Cowley, N. Dharmaraj, *Inorganica Chim. Acta* **2012**, *384*, 83–96.
- [262] C. Y. Gao, X. Qiao, Z. Y. Ma, Z. G. Wang, J. Lu, J. L. Tian, J. Y. Xu, S. P. Yan, *Dalt. Trans.* **2012**, *41*, 12220–12232.
- [263] A. L. de Andrade Querino, J. T. da Silva, J. T. Silva, G. M. Alvarenga, C. H. da Silveira, M. T. Q. de Magalhães, O. A. Chaves, B. A. Iglesias, R. Diniz, H. Silva, *J. Biol. Inorg. Chem.* **2019**, *24*, 1087–1103.
- [264] A. M. Queiroz, A. V. Mezacasa, D. E. Graciano, W. F. Falco, J. C. M'Peko, F. E. G. Guimarães, T. Lawson, I. Colbeck, S. L. Oliveira, A. R. L. Caires, *Spectrochim. Acta - Part A Mol. Biomol. Spectrosc.* **2016**, *168*, 73–77.
- [265] Y. J. Hu, Y. Liu, X. S. Shen, X. Y. Fang, S. S. Qu, *J. Mol. Struct.* **2005**, *738*, 143–147.
- [266] Q. Guo, J. Yuan, J. Zeng, *Biotechnol. Biotechnol. Equip.* **2014**, *28*, 333–341.
- [267] M. Gharagozlou, D. M. Boghaei, *Spectrochim. Acta - Part A Mol. Biomol. Spectrosc.* **2008**, *71*, 1617–1622.
- [268] Y. Liu, Y. Z. Zhang, B. Zhou, C. X. Zhou, X. L. Ding, Y. X. Liu, *J. Fluoresc.* **2008**, *18*, 109–118.
- [269] Y. Q. Wang, H. M. Zhang, G. C. Zhang, W. H. Tao, S. H. Tang, *J. Lumin.* **2007**, *126*, 211–218.
- [270] S. Awasthi, N. T. Saraswathi, *RSC Adv.* **2016**, *6*, 90739–90753.
- [271] Y. Ni, S. Su, S. Kokot, *Anal. Chim. Acta* **2006**, *580*, 206–215.
- [272] F. Ding, N. Li, B. Han, F. Liu, L. Zhang, Y. Sun, *Dye. Pigment.* **2009**, *83*, 249–257.
- [273] C. Dufour, O. Dangles, *Biochim. Biophys. Acta - Gen. Subj.* **2005**, *1721*, 164–173.
- [274] Y. Ni, X. Zhang, S. Kokot, *Spectrochim. Acta - Part A Mol. Biomol. Spectrosc.* **2009**, *71*, 1865–1872.
- [275] C. Ràfols, S. Amézqueta, E. Fuguet, E. Bosch, *J. Pharm. Biomed. Anal.* **2018**, *150*, 452–459.
- [276] L. Alderighi, P. Gans, A. Ienco, D. Peters, A. Sabatini, A. Vacca, *Coord. Chem. Rev.* **1999**, 311–318.
- [277] T. Biver, F. Criscitiello, F. Di Francesco, M. Minichino, T. Swager, A. Pucci, *RSC Adv.* **2015**, *5*, 65023–65029.
- [278] F. Donati, A. Pucci, G. Ruggeri, *Phys. Chem. Chem. Phys.* **2009**, *11*, 6276–

- 6282.
- [279] F. Khalili, A. Henni, A. L. L. East, *J. Chem. Eng. Data* **2009**, *54*, 2914–2917.
- [280] J. Marmur, P. Doty, *J. Mol. Biol.* **1962**, *5*, 109–118.
- [281] T. Biver, F. Secco, M. R. Tinè, M. Venturini, A. Bencini, A. Bianchi, C. Giorgi, *J. Inorg. Biochem.* **2004**, DOI 10.1016/j.jinorgbio.2004.06.005.
- [282] G. Felsenfeld, S. Z. Hirschman, *J. Mol. Biol.* **1965**, *13*, 407–427.
- [283] A. Ambrus, D. Chen, J. Dai, R. A. Jones, D. Yang, *Biochemistry* **2005**, *44*, 2048–2058.
- [284] A. Łęczkowska, J. Gonzalez-Garcia, C. Perez-Arnaiz, B. Garcia, A. J. P. White, R. Vilar, *Chem. - A Eur. J.* **2018**, *24*, 11785–11794.
- [285] A. R. De La Faverie, A. Guédin, A. Bedrat, L. A. Yatsunyk, J. L. Mergny, *Nucleic Acids Res.* **2014**, *42*, 1–8.
- [286] L. J. Aaldering, V. Poongavanam, N. Langkjær, N. A. Murugan, P. T. Jørgensen, J. Wengel, R. N. Veedu, *ChemBioChem* **2017**, *18*, 755–763.
- [287] T. Biver, N. Busto, B. García, J. M. Leal, L. Menichetti, F. Secco, M. Venturini, *J. Inorg. Biochem.* **2015**, *151*, 115–122.
- [288] F. J. Hoyuelos, B. García, J. M. Leal, N. Busto, T. Biver, F. Secco, M. Venturini, *Phys. Chem. Chem. Phys.* **2014**, *16*, 6012–6018.
- [289] *All About Albumin*, **1995**.
- [290] P. C. Griffiths, N. Hirst, A. Paul, S. M. King, R. K. Heenan, R. Farley, *Langmuir* **2004**, *20*, 6904.
- [291] S. Aydinoglu, T. Biver, F. Secco, M. Venturini, *Colloids Surfaces A Physicochem. Eng. Asp.* **2014**, *461*, 303.
- [292] M. J. Frisch, G. W. Trucks, H. E. Schlegel, G. E. Scuseria, M. A. Robb, J. R. Cheeseman, G. Scalmani, V. Barone, G. A. Petersson, F. O., et al., *Gaussian, Inc., Wallingford CT*, **2016**.
- [293] H. P. Spielmann, D. E. Wemmer, J. P. Jacobsen, *Biochemistry* **1995**, *34*, 8542–8553.
- [294] E. Cancès, B. Mennucci, J. Tomasi, *J. Chem. Phys.* **1997**, *107*, 3032–3041.
- [295] J. Tomasi, B. Mennucci, R. Cammi, *Chem. Rev.* **2005**, *105*, 2999–3093.
- [296] M. Caricato, B. Mennucci, J. Tomasi, F. Ingrosso, R. Cammi, S. Corni, G. Scalmani, *J. Chem. Phys.* **2006**, *124*, 124520.
- [297] R. L. Martin, *J. Chem. Phys.* **2003**, *118*, 4775–4777.
- [298] M. S., **1995**, DOI 10.3367/ufnr.0168.199805j.0591.
- [299] J. Wang, R. M. Wolf, J. W. Caldwell, P. A. Kollman, D. A. Case, *J. Comput. Chem.* **2004**, *25*, 1157–1174.
- [300] J. Wang, W. Wang, P. A. Kollman, D. A. Case, *J. Mol. Graph. Model.* **2006**, *25*, 247–260.
- [301] A. T. Guy, T. J. Piggot, S. Khalid, *Biophys. J.* **2012**, *103*, 1028–1036.
- [302] D. Van Der Spoel, E. Lindahl, B. Hess, G. Groenhof, A. E. Mark, H. J. C. Berendsen, *J. Comput. Chem.* **2005**, *26*, 1701–1718.
- [303] B. Hess, C. Kutzner, D. Van Der Spoel, E. Lindahl, *J. Chem. Theory Comput.* **2008**, *4*, 435–447.
- [304] G. Bussi, D. Donadio, M. Parrinello, *J. Chem. Phys.* **2007**, *126*, 0141001/1–

- 014101/7.
- [305] T. Darden, D. York, L. Pedersen, *J. Chem. Phys.* **1993**, *98*, 10089–10092.
- [306] D. T. Moustakas, P. T. Lang, S. Pegg, E. Pettersen, I. D. Kuntz, N. Brooijmans, R. C. Rizzo, *J. Comput. Aided. Mol. Des.* **2006**, *20*, 601–619.
- [307] F. Würthner, *Chem. Commun.* **2004**, *4*, 1564–1579.
- [308] B. E. Hardin, H. J. Snaith, M. D. McGehee, *Nat. Photonics* **2012**, *6*, 162–169.
- [309] M. G. Debije, P. P. C. Verbunt, *Adv. Energy Mater.* **2012**, *2*, 12–35.
- [310] G. Li, Y. Zhao, J. Li, J. Cao, J. Zhu, X. W. Sun, Q. Zhang, *J. Org. Chem.* **2015**, *80*, 196–203.
- [311] F. Donati, A. Pucci, C. Cappelli, B. Mennucci, G. Ruggeri, *J. Phys. Chem. B* **2008**, *112*, 3668–3679.
- [312] T. H. Rehm, M. R. Stojković, S. Rehm, M. Škugor, I. Piantanida, F. Würthner, *Chem. Sci.* **2012**, *3*, 3393–3397.
- [313] Z. Xu, W. Cheng, K. Guo, J. Yu, J. Shen, J. Tang, W. Yang, M. Yin, *ACS Appl. Mater. Interfaces* **2015**, *7*, 9784–9791.
- [314] Z. Xu, K. Guo, J. Yu, H. Sun, J. Tang, J. Shen, K. Müllen, W. Yang, M. Yin, *Small* **2014**, *10*, 4087–4092.
- [315] M. Franceschin, E. Pascucci, A. Alvino, D. D’Ambrosio, A. Bianco, G. Ortaggi, M. Savino, *Bioorganic Med. Chem. Lett.* **2007**, *17*, 2515–2522.
- [316] S. M. Kerwin, G. Chen, J. T. Kern, P. W. Thomas, *Bioorganic Med. Chem. Lett.* **2002**, *12*, 447–450.
- [317] A. Rangan, O. Y. Fedoroff, L. H. Hurley, *J. Biol. Chem.* **2001**, *276*, 4640–4640.
- [318] L. Rossetti, M. Franceschin, A. Bianco, G. Ortaggi, M. Savino, *Bioorganic Med. Chem. Lett.* **2002**, *12*, 2527–2533.
- [319] L. Rossetti, M. Franceschin, S. Schirripa, A. Bianco, G. Ortaggi, M. Savino, *Bioorganic Med. Chem. Lett.* **2005**, *15*, 413–420.
- [320] H. Han, D. R. Langley, A. Rangan, L. H. Hurley, *J. Am. Chem. Soc.* **2001**, *123*, 8902–8913.
- [321] L. Rao, J. D. Dworkin, W. E. Nell, U. Bierbach, *J. Phys. Chem. B* **2011**, *115*, 13701–13712.
- [322] M. H. Li, Q. Luo, X. G. Xue, Z. S. Li, *J. Mol. Model.* **2011**, *17*, 515–526.
- [323] G. W. Collie, R. Promontorio, S. M. Hampel, M. Micco, S. Neidle, G. N. Parkinson, *J. Am. Chem. Soc.* **2012**, *134*, 2723–2731.
- [324] F. Guarra, T. Marzo, M. Ferraroni, F. Papi, C. Bazzicalupi, P. Gratteri, G. Pescitelli, L. Messori, T. Biver, C. Gabbiani, *Dalt. Trans.* **2018**, *47*, 16132–16138.
- [325] T. H. Rehm, M. R. Stojković, S. Rehm, M. Škugor, I. Piantanida, F. Würthner, *Chem. Sci.* **2012**, *3*, 3393–3397.
- [326] J. Gershberg, M. Radić Stojković, M. Škugor, S. Tomić, T. H. Rehm, S. Rehm, C. R. Saha-Möller, I. Piantanida, F. Würthner, *Chem. - A Eur. J.* **2015**, *21*, 7886–7895.
- [327] Y. Bin Ruan, A. F. Li, J. S. Zhao, J. S. Shen, Y. B. Jiang, *Chem. Commun.* **2010**, *46*, 4938–4940.

- [328] D. Görl, X. Zhang, F. Würthner, *Angew. Chemie - Int. Ed.* **2012**, *51*, 6328–6348.
- [329] F. Würthner, Z. Chen, V. Dehm, V. Stepanenko, *Chem. Commun.* **2006**, *4*, 1188–1190.
- [330] B. Wang, C. Yu, *Angew. Chemie - Int. Ed.* **2010**, *49*, 1485–1488.
- [331] K. Balakrishnan, A. Datar, T. Naddo, J. Huang, R. Oitker, M. Yen, J. Zhao, L. Zang, *J. Am. Chem. Soc.* **2006**, *128*, 7390–7398.
- [332] K. Balakrishnan, A. Datar, R. Oitker, H. Chen, J. Zuo, L. Zang, *J. Am. Chem. Soc.* **2005**, *127*, 10496–10497.
- [333] M. W. Freyer, E. A. Lewis, *Methods Cell Biol.* **2008**, *84*, 79–113.
- [334] T. Uno, K. Hamasaki, M. Tanigawa, S. Shimabayashi, *Inorg. Chem.* **1997**, *36*, 1676–1683.
- [335] T. Biver, A. Boggioni, F. Secco, E. Turriani, M. Venturini, S. Yarmoluk, *Arch. Biochem. Biophys.* **2007**, *465*, 90–100.
- [336] F. Macii, C. P. Arnaiz, L. Arrico, N. Busto, B. Garcia, T. Biver, *J. Inorg. Biochem.* **2020**, *212*, 111199.
- [337] J. B. Chaires, *Annu. Rev. Biophys.* **2008**, *37*, 135–151.
- [338] A. Biancardi, A. Bungalassi, A. Terenzi, A. Spinello, G. Barone, T. Biver, B. Mennucci, *Chem. - A Eur. J.* **2014**, *20*, 7439–7447.
- [339] M. Zuffo, A. Guédin, E. D. Leriche, F. Doria, V. Pirota, V. Gabelica, J. L. Mergny, M. Freccero, *Nucleic Acids Res.* **2018**, *46*, 115.
- [340] O. Y. Fedoroff, M. Salazar, H. Han, V. V. Chemeris, S. M. Kerwin, L. H. Hurley, *Biochemistry* **1998**, *37*, 12367–12374.
- [341] H. L. Lightfoot, T. Hagen, N. J. Tatum, J. Hall, *FEBS Lett.* **2019**, *593*, 2083–2102.
- [342] D. Yang, K. Okamoto, *Future Med. Chem.* **2010**, *2*, 619–646.
- [343] E. W. White, F. Tanious, M. A. Ismail, A. P. Reszka, S. Neidle, D. W. Boykin, W. D. Wilson, *Biophys. Chem.* **2007**, *126*, 140–153.
- [344] M. Bončina, Č. Podlipnik, I. Piantanida, J. Eilmes, M. P. Teulade-Fichou, G. Vesnaver, J. Lah, *Nucleic Acids Res.* **2015**, *43*, 10376–10386.
- [345] W. Tuntiwechapikul, T. Taka, M. Béthencourt, L. Makonkawkeyoon, T. Randall Lee, *Bioorganic Med. Chem. Lett.* **2006**, *16*, 4120–4126.
- [346] S. Vasimalla, S. Sato, F. Takenaka, Y. Kurose, S. Takenaka, *Bioorganic Med. Chem.* **2017**, *25*, 6404–6411.
- [347] M. Franceschin, C. M. Lombardo, E. Pascucci, D. D’Ambrosio, E. Micheli, A. Bianco, G. Ortaggi, M. Savino, *Bioorganic Med. Chem.* **2008**, *16*, 2292–2304.
- [348] C. Pivetta, L. Lucatello, A. Paul Krapcho, B. Gatto, M. Palumbo, C. Sissi, *Bioorganic Med. Chem.* **2008**, *16*, 9331–9339.
- [349] J. Lopes-Nunes, J. Carvalho, J. Figueiredo, C. I. V. Ramos, L. M. O. Lourenço, J. P. C. Tomé, M. G. P. M. S. Neves, J. L. Mergny, J. A. Queiroz, G. F. Salgado, et al., *Bioorg. Chem.* **2020**, *100*, 103920.
- [350] G. Loebbert, *Ullmann’s Encycl. Ind. Chem.* **2012**, 619–671.
- [351] S. Q. Lomax, *Stud. Conserv.* **2005**, *50*, 19–29.
- [352] J. E. Scott, J. Dorling, *Histochemie* **1965**, *5*, 221–233.

- [353] J. E. Scott, *Histochemie* **1973**, *37*, 379–380.
- [354] J. E. Scott, *Histochemie* **1972**, *32*, 191–212.
- [355] J. E. Scott, *Histochemie* **1970**, DOI 10.1007/BF00304219.
- [356] L. B. Josefsen, R. W. Boyle, *Theranostics* **2012**, *2*, 916–966.
- [357] M. Machacek, A. Cidlina, V. Novakova, J. Svec, E. Rudolf, M. Miletin, R. Kučera, T. Simunek, P. Zimcik, *J. Med. Chem.* **2015**, *58*, 1736–1749.
- [358] N. Sekkat, H. Van Den Bergh, T. Nyokong, N. Lange, *Molecules* **2012**, *17*, 98–144.
- [359] T. Arslan, M. Buğrahan Ceylan, H. Baş, Z. Biyiklioglu, M. Senturk, *Dalt. Trans.* **2019**, *49*, 203–209.
- [360] N. A. Kasyanenko, R. A. Tikhomirov, V. M. Bakulev, V. N. Demidov, E. V. Chikhirzhina, E. B. Moroshkina, *ACS Omega* **2019**, *4*, 16935–16942.
- [361] T. Keleş, B. Barut, A. Özel, Z. Biyiklioglu, *Dye. Pigment.* **2019**, *164*, 372–383.
- [362] C. J. Churukian, M. Frank, R. W. Horobin, *Biotech. Histochem.* **2000**, *75*, 147–150.
- [363] C. Bazzicalupi, M. Ferraroni, F. Papi, L. Massai, B. Bertrand, L. Messori, P. Gratteri, A. Casini, *Angew. Chemie - Int. Ed.* **2016**, *55*, 4256–4259.
- [364] H. Isago, H. Fujita, *J. Porphyr. Phthalocyanines* **2018**, *22*, 102–111.
- [365] K. M. Kadish, K. M. Smith, R. Guilard, *The Porphyrin Handbook: Multiporphyrins, Multiphthalocyanines and Arrays*, **2012**.
- [366] T. Biver, N. Eltugral, A. Pucci, G. Ruggeri, A. Schena, F. Secco, M. Venturini, *Dalt. Trans.* **2011**, *40*, 4190–4199.
- [367] R. M. Kenney, K. E. Buxton, S. Glazier, *Biophys. Chem.* **2016**, *216*, 9–18.
- [368] C. Qin, F. Kang, W. Zhang, W. Shou, X. Hu, Y. Gao, *Water Res.* **2017**, *123*, 58–66.
- [369] X. Qu, J. Ren, P. V. Riccelli, A. S. Benight, J. B. Chaires, *Biochemistry* **2003**, *42*, 11960–11967.
- [370] A. I. Dragan, C. M. Read, C. Crane-Robinson, *Eur. Biophys. J.* **2017**, *46*, 301–308.
- [371] U. Ryde, *Medchemcomm* **2014**, *5*, 1324–1336.
- [372] W. Kenji, T. Mizutani, M. Hideki, K. Susumu, *Chem. - A Eur. J.* **2003**, *9*, 2368–2380.
- [373] M. R. Beccia, T. Biver, A. Pardini, J. Spinelli, F. Secco, M. Venturini, N. Busto Vázquez, M. P. Lopez Cornejo, V. I. Martin Herrera, R. Prado Gotor, *Chem. - An Asian J.* **2012**, *7*, 1803–1810.
- [374] J. M. Nicoludis, S. P. Barrett, J. L. Mergny, L. A. Yatsunyk, *Nucleic Acids Res.* **2012**, *40*, 5432–5447.
- [375] D. Zhao, X. Dong, N. Jiang, D. Zhang, C. Liu, *Nucleic Acids Res.* **2014**, *42*, 11612–11621.
- [376] R. B. Thompson, *Fluorescence Sensors and Biosensors*, **2005**.
- [377] D. Li, X. Tian, A. Wang, L. Guan, J. Zheng, F. Li, S. Li, H. Zhou, J. Wu, Y. Tian, *Chem. Sci.* **2016**, *7*, 2257–2263.
- [378] B. Guo, X. Cai, S. Xu, S. M. A. Fateminia, J. Liu, J. Liang, G. Feng, W. Wu, B. Liu, *J. Mater. Chem. B* **2016**, *4*, 4690–4695.

- [379] J. Luo, Z. Xie, Z. Xie, J. W. Y. Lam, L. Cheng, H. Chen, C. Qiu, H. S. Kwok, X. Zhan, Y. Liu, et al., *Chem. Commun.* **2001**, 18, 1740–1741.
- [380] G. Yu, G. Tang, F. Huang, *J. Mater. Chem. C* **2014**, 2, 6609–6617.
- [381] Y. Hong, J. W. Y. Lam, B. Z. Tang, *Chem. Soc. Rev.* **2011**, 40, 5361–5388.
- [382] Y. Hong, M. Häußler, J. W. Y. Lam, Z. Li, K. K. Sin, Y. Dong, H. Tong, J. Liu, A. Qin, R. Renneberg, et al., *Chem. - A Eur. J.* **2008**, 14, 6428–6437.
- [383] H. Tong, Y. Hong, Y. Dong, M. Häußler, J. W. Y. Lam, Z. Li, Z. Guo, Z. Guo, B. Z. Tang, *Chem. Commun.* **2006**, 3705–3707.
- [384] Y. Dong, W. Wang, C. Zhong, J. Shi, B. Tong, X. Feng, J. Zhi, Y. Dong, *Tetrahedron Lett.* **2014**, 55, 1496–1500.
- [385] M. P. Fleming, J. E. McMurry, in *Org. Synth.*, **2003**.
- [386] Y. D. Lim, D. W. Seo, S. H. Lee, H. H. Ju, T. W. Hong, D. M. Kim, H. C. Ju, W. G. Kim, *Int. J. Hydrogen Energy* **2013**, 38, 7667–7673.
- [387] J. L. Kurz, L. C. Kurz, *Isr. J. Chem.* **1985**, 26, 339–348.
- [388] J. L. Kurz, J. Lee, M. E. Love, S. Rhodes, *J. Am. Chem. Soc.* **1986**, 108, 2960–2968.
- [389] M. T. Record, C. F. Anderson, T. M. Lohman, *Q. Rev. Biophys.* **1978**, 11, 103–178.
- [390] N. Busto, J. Valladolid, C. Aliende, F. A. Jalón, B. R. Manzano, A. M. Rodríguez, J. F. Gaspar, C. Martins, T. Biver, G. Espino, et al., *Chem. - An Asian J.* **2012**, 7, 788–801.
- [391] X. Liang, X. Zou, L. Tan, W. Zhu, *J. Inorg. Biochem.* **2010**, 104, 1259–1266.
- [392] M. Lorenzo, J. Campo, Y. Picó, *TrAC - Trends Anal. Chem.* **2018**, 137.
- [393] A. Lo Giudice, P. Casella, V. Bruni, L. Michaud, *Ecotoxicology* **2013**, 22, 240.
- [394] S. Ben Hassine, B. Hammami, W. Ben Ameer, Y. El Megdiche, B. Barhoumi, M. R. Driss, *Bull. Environ. Contam. Toxicol.* **2014**, 93, 375–382.
- [395] J. S. Seo, Y. S. Keum, R. M. Harada, Q. X. Li, in *J. Agric. Food Chem.*, **2007**, pp. 5383–5389.
- [396] P. Amoatey, M. S. Baawain, *Water Environ. Res.* **2019**, 91, 1272–1287.
- [397] K. L. Harris, L. D. Banks, J. A. Mantey, A. C. Huderson, A. Ramesh, *Expert Opin. Drug Metab. Toxicol.* **2013**, 1465–1480.
- [398] J. Beyer, G. Jonsson, C. Porte, M. M. Krahn, F. Ariese, *Environ. Toxicol. Pharmacol.* **2010**, 224–244.
- [399] J. Zhang, W. Chen, B. Tang, W. Zhang, L. Chen, Y. Duan, Y. Zhu, Y. Zhu, Y. Zhang, *RSC Adv.* **2016**, 6, 23622–23633.
- [400] C. Xu, J. Gu, X. Ma, T. Dong, X. Meng, *Spectrochim. Acta - Part A Mol. Biomol. Spectrosc.* **2014**, 125, 391–395.
- [401] A. Wolfe, G. H. Shimer, T. Meehan, *Biochemistry* **1987**, 26, 6392–6396.
- [402] D. Sar, B. Kim, F. Ostadhossein, S. K. Misra, D. Pan, *Chem. Rec.* **2018**, 18, 619–658.
- [403] M. Stiborová, M. Moserová, V. Černá, R. Indra, M. Dračinský, M. Šulc, C. J. Henderson, C. R. Wolf, H. H. Schmeiser, D. H. Phillips, et al., *Toxicology* **2014**, 318, 1–12.

- [404] R. G. Harvey, N. E. Geacintov, *Acc. Chem. Res.* **1988**, *21*, 66–73.
- [405] M. C. R. Alavanja, M. R. Bonner, *J. Toxicol. Environ. Heal. - Part B Crit. Rev.* **2012**, *15*, 238–263.
- [406] C. Coscollà, A. López, A. Yahyaoui, P. Colin, C. Robin, Q. Poinsignon, V. Yusà, *Sci. Total Environ.* **2017**, 584–585.
- [407] T. R. Fukuto, in *Environ. Health Perspect.*, **1990**, p. 245.
- [408] B. A. Golomb, *Proc. Natl. Acad. Sci. U. S. A.* **2008**, DOI 10.1073/pnas.0711986105.
- [409] Y. Xiong, T. F. Kang, L. P. Lu, *J. Solid State Electrochem.* **2013**, *17*, 129–136.
- [410] G. Zhang, X. Hu, P. Fu, *J. Photochem. Photobiol. B Biol.* **2012**, *108*, 53–61.
- [411] T. F. Kang, Y. Xiong, R. Xue, S. Y. Cheng, *Anal. Lett.* **2013**, *46*, 1255–1266.
- [412] M. Eddleston, in *Crit. Care Toxicol.*, **2016**.
- [413] A. S. R. Juo, O. O. Oginni, *J. Environ. Qual.* **1978**, *7*, 9–12.
- [414] J. E. Barbash, G. P. Thelin, D. W. Kolpin, R. J. Gilliom, *J. Environ. Qual.* **2001**, *30*, 831–845.
- [415] Y. Yin, X. Guo, S. L. Zhang, C. Y. Sun, *Biomed. Environ. Sci.* **2013**, 509–512.
- [416] L. L. Smith, *Hum. Exp. Toxicol.* **1987**, *6*, 31–36.
- [417] S. J. Kim, H. W. Gil, J. O. Yang, E. Y. Lee, S. Y. Hong, *Nephrol. Dial. Transplant.* **2009**, *24*, 1226–1232.
- [418] J. K. Andersen, *Neurotox. Res.* **2003**, *5*, 307–312.
- [419] A. Adam, L. L. Smith, G. M. Cohen, *Biochem. Pharmacol.* **1990**, *40*, 1533–1539.
- [420] J. S. Bus, J. E. Gibson, *Environ. Health Perspect.* **1984**, *55*, 37–46.
- [421] J. R. Richardson, Y. Quan, T. B. Sherer, J. T. Greenamyre, G. W. Miller, *Toxicol. Sci.* **2005**, *88*, 193–201.
- [422] R. Vanholder, F. Colardyn, J. De Reuck, M. Praet, N. Lameire, S. Ringoir, *Am. J. Med.* **1981**, *70*, 1267–1271.
- [423] A. Pirie, J. R. Rees, N. J. Holmberg, *Exp. Eye Res.* **1970**, *9*, 204–218.
- [424] F. Jafari, S. Moradi, A. Nowroozi, K. Sadrjavadi, L. Hosseinzadeh, M. Shahlaei, *New J. Chem.* **2017**, *41*, 14188–14198.
- [425] S. Gupta, H. E. Kleiner, L. K. Rogers, S. S. Lau, C. V. Smith, *Redox Rep.* **1997**, *3*, 31–29.
- [426] Q. Zhang, C. Wang, W. Liu, X. Zhang, S. Zhuang, *Environ. Chem. Lett.* **2012**, *10*, 35–39.
- [427] G. Zhang, Y. Wang, H. Zhang, S. Tang, W. Tao, *Pestic. Biochem. Physiol.* **2007**, *87*, 23–29.
- [428] P. Kathuria, P. Sharma, M. N. Abendong, S. D. Wetmore, *Biochemistry* **2015**, *54*, 2414–2428.
- [429] F. Ahmadi, K. Ghanbari, *Ecotoxicol. Environ. Saf.* **2014**, *106*, 136–145.
- [430] F. Ahmadi, B. Jafari, M. Rahimi-Nasrabadi, S. Ghasemi, K. Ghanbari, *Toxicol. Vitro.* **2013**, *27*, 641–650.
- [431] G. Cohen, H. Eisenberg, *Biopolymers* **1969**, *8*, 45–55.

- [432] S. Khrapunov, *Curr. Protein Pept. Sci.* **2018**, DOI 10.2174/1389203719666180521092615.
- [433] Y. Inoue, D. Jing, *J. Am. Chem. Soc.* **1993**, *115*, 10637–10644.
- [434] R. F. Platford, *Chemosphere* **1983**, *12*, 1107–1111.
- [435] C. Tomlin, *The Pesticide Manual*, **2003**.
- [436] Y. Gou, F. Yang, H. Liang, *Curr. Top. Med. Chem.* **2016**, *9*, 996–1008.
- [437] D. Silva, C. M. Cortez, J. Cunha-Bastos, S. R. W. Louro, *Toxicol. Lett.* **2004**, *147*, 53–61.
- [438] V. Dahiya, B. Chaubey, A. K. Dhaharwal, S. Pal, *Pestic. Biochem. Physiol.* **2017**, *139*, 92–100.
- [439] C. Su, S. Liu, S. Cao, S. Yin, C. Zhou, S. Gao, C. Jia, Y. Ji, Y. Liu, *J. Nanobiotechnology* **2020**, *18*, 165.
- [440] C. R. Cantor, P. R. Schimmel, *Biophys. Chem. Part III* **1980**.
- [441] T. Schelhorn, S. Kretz, H. W. Zimmermann, *Cell. Mol. Biol.* **1992**.

List of publications

1. S. Aydinoglu, T. Biver, D. Greco, F. Macii, “*Mechanistic details on Pd(II)/5,10,15,20-tetrakis(1-methyl-4-pyridyl)-porphyrine complex formation and reactivity in the presence of DNA*”, Monatshefte fuer Chemie, 149 (2018), 175–183. DOI: 10.1007/s00706-017-2057-y
2. F. Macii, G. Salvadori, Bonini R., S. Giannarelli, B. Mennucci, T. Biver, “*Binding of model polycyclic aromatic hydrocarbons and carbamate-pesticides to DNA, BSA, micelles and liposomes*”, Spectrochimica Acta Part A: Molecular and Biomolecular Spectroscopy, 223 (2019), 117313. DOI: 10.1016/j.saa.2019.117313
3. F. Macii, C. Perez-Arnaiz, L. Arrico, N. Busto, B. Garcia, T. Biver, “*Alcian blue pyridine variant interaction with DNA and RNA polynucleotides and G-quadruplexes: changes in the binding features for different biosubstrates*”, Journal of Inorganic Biochemistry, 212 (2020), 111199. DOI: 10.1016/j.jinorgbio.2020.111199
4. F. Macii, T. Biver, “*Spectrofluorimetric Analysis of the Binding of a Target Molecule to Serum Albumin: Tricky Aspects and Tips*”, Journal of Inorganic Biochemistry, (2020), 111305. DOI: 10.1016/j.jinorgbio.2020.111305
5. F. Macii, L. Cupellini, M. Stifano, J. Santolaya, C. Perez-Arnaiz, A. Pucci, G. Barone, B. Garcia, N. Busto, T. Biver, “*Combined spectroscopic and theoretical analysis of the binding of a water-soluble perylene diimide to DNA/RNA polynucleotides and G-quadruplexes*”, submitted to Organic & Biomolecular Chemistry
6. F. Macii, R. Detti, F. R. Bloise, S. Giannarelli, T. Biver, “*Spectroscopic analysis of the binding features of paraquat and diquat herbicides to biosubstrates*”, submitted to International Journal of Environmental Research and Public Health

Participation to conferences with oral and poster contributions

1. XXX International Symposium on Metal Complexes 2018, 3rd – 7th June 2018, Firenze (Italy)

POSTER PRESENTATION: “*DNA and RNA binding tests of highly positively or negatively charged phtalocyanines*” (L. Arrico, T. Biver, L. Di Bari, F. Macii)

BEST POSTER AWARD WINNER

2. Chemistry for the future 2018, 4th – 6th July 2018, Pisa (Italy)

POSTER PRESENTATION: “*Solution properties and ct-DNA binding tests of a perylene diimide with promising anticancer activity*” (F. Macii, T. Biver, L. Di Bari, B. Mennucci, A. Pucci)

3. XIV International Symposium on Inorganic Biochemistry, 5th – 9th September 2018, Wroklaw (Poland)

ORAL PRESENTATION: “*The effect of charged peripheral substituents on the interaction of Cu(II)-phtalocyanine complexes with biosubstrates*” (L. Arrico, T. Biver, L. Di Bari, F. Macii)

BEST ORAL PRESENTATION AWARD WINNER

4. XXXVI Convegno Interregionale TUMA 2018, 4th – 5th October 2018, Pisa (Italy)

POSTER PRESENTATION: “*Studio delle interazioni fra acidi nucleici e complessi Cu(II)-ftalocianina di interesse biomedico*” (F. Macii, L. Arrico, L. Di Bari, T. Biver)

5. XL National Congress on Calorimetry, Thermal Analysis and Applied Thermodynamic, 17th – 19th December 2018, Pisa (Italy)

ORAL PRESENTATION: “*Thermodynamic analysis of the interaction between two Cu(II)-phtalocyanine complexes and nucleic acids*” (F. Macii, L. Arrico, L. Di Bari, T. Biver)

6. XXXI International Symposium on Metal Complexes 2019, 11th – 14th June 2019, Debrecen (Hungary)

POSTER PRESENTATION: “*Investigation on the Alcian Blue-tetrakis(methylpyridinium) chloride reactivity in presence of DNA, RNA, G-quadruplex structures and BSA*” (F. Macii, C. Pérez Arnaiz, N. Busto, B. García, T. Biver)

7. Chemistry for the future 2019, 3rd – 5th July 2019, Pisa (Italy)

POSTER PRESENTATION: “*Binding affinity of PZPERY to double helix DNA and G-quadruplex structures*” (F. Macii, C. Pérez Arnaiz, A. Macrì, N. Busto, A. Pucci, B. Mennucci, B. García, T. Biver)

8. Innovative Researches in Pharmaceutical and Environmental Sciences IRPES2019, 27th November 2019, Pisa (Italy)

POSTER PRESENTATION: “*Spectroscopic and computational investigation on the binding affinity of a perylene diimide derivative to polynucleotides*” (F. Macii, C. Pérez Arnaiz, J. Santolaya, A. Pucci, B. Mennucci, G. Barone, B. Garcia, T. Biver)

Other contributions to conferences

1. XXXI International Symposium on Metal Complexes 2019, 11th – 14th June 2019, Debrecen (Hungary)

POSTER CONTRIBUTION: “*Thermodynamic analysis of POPs interaction with biosubstrates*” (T. Biver, R. Detti, S. Giannarelli, F. Macii)

2. Innovative Researches in Pharmaceutical and Environmental Sciences IRPES2019, 27th November 2019, Pisa (Italy)

POSTER CONTRIBUTION: “*Synthesis of a TPE derivative and investigation on its interaction with DNA and RNA*” (A. Macrì, F. Macii, G. Iasilli, P. Minei, A. Pucci, T. Biver)

Participation to workshops and schools

1. IV Computer Aided Drug Design Summer School, 8th – 13th July 2019, Pisa (Italy)
 2. Workshop: Computational methods and NMR spectroscopy: a powerful synergy for chemistry, materials science and biology, 10th December 2019, Pisa (Italy)
 3. Just a peek into the multifaced world of drugs, 22nd – 26th June 2020, Telematic PhD Week organized by Department of Pharmacy (UniPi)
- Member of the Organizing Committee of Chemistry for the future 2019, 3rd – 5th July 2019, Pisa (Italy)